TECTONO-THERMAL HISTORY MODELING AND RESERVOIR SIMULATION STUDY OF THE NENANA BASIN, CENTRAL ALASKA: IMPLICATIONS FOR REGIONAL TECTONICS AND GEOLOGIC CARBON SEQUESTRATION

By

Nilesh C. Dixit, B.Tech., M.Sc.

A Dissertation Submitted in Partial Fulfillment of the Requirements

for the Degree of

Doctor of Philosophy

In

Geophysics

University of Alaska Fairbanks

May 2017

APPROVED:

Dr. Catherine Hanks, Committee Chair
Dr. Bernard Coakley, Committee Member
Dr. Mohabbat Ahmadi, Committee Member
Dr. Paul McCarthy, Committee Member
Dr. Paul McCarthy, Chair
    Department of Geosciences
Dr. Paul Layer, Dean
    College of Natural Science and Mathematics
Dr. Michael Castellini, Dean of the Graduate School

Abstract

Central Interior Alaska is an active tectonic deformation zone highlighted by the complex interactions of active strike-slip fault systems with thrust faults and folds of the Alaska Range fold-and-thrust belt. This region includes the Nenana basin and the adjacent Tanana basin, both of which have significant Tertiary coal-bearing formations and are also promising areas (particularly the Nenana basin) with respect to hydrocarbon exploration and geologic carbon sequestration.

I investigate the modern-day crustal architecture of the Nenana and Tanana basins using seismic reflection, aeromagnetic and gravity anomaly data and demonstrate that the basement of both basins shows strong crustal heterogeneity. The Nenana basin is a deep (up to 8 km), narrow transtensional pull-apart basin that is deforming along the left-lateral Minto Flats fault zone. The Tanana basin has a fundamentally different geometry and is a relatively shallow (up to 2 km) asymmetrical foreland basin with its southern, deeper side controlled by the northern foothills of the central Alaska Range. NE-trending strike-slip faults within the Tanana basin are interpreted as a zone of clockwise crustal block rotation.

Seismic refection data, well data, fracture data and apatite fission track data further constrain the tectonic evolution and thermal history of the Nenana basin. The Nenana basin experienced four distinct tectonic phases since Late Paleocene time. The basin initiated as a narrow half-graben structure in Late Paleocene with accumulation of greater than 6000 feet of sediments. The basin was then uplifted, resulting in the removal of up to 5000 feet of Late

Paleocene sediments in Eocene to Oligocene time. During Middle to Late Miocene time, left lateral strike-slip faulting was superimposed on the existing half-graben system. Transtensional deformation of the basin began in the Pliocene. At present, Miocene and older strata are exposed to temperatures $> 60^0C$ in the deeper parts of the Nenana basin.

Coals have significant capacity for sequestering anthropogenic CO_2 emissions and offer the benefit of enhanced coal bed methane production that can offset the costs associated with the sequestration processes. In order to do a preliminary assessment of the CO_2 sequestration and coal bed methane production potential of the Nenana basin, I used available surface and subsurface data to build and simulate a reservoir model of subbituminous Healy Creek Formation coals. The petroleum exploration data were also used to estimate the state of subsurface stresses that are critical in modeling the orientation, distribution and flow behavior of natural coal fractures in the basin. The effect of uncertainties within major coal parameters on the total CO_2 sequestration and coal bed methane capacity estimates were evaluated through a series of sensitivity analyses, experimental design methods and fluid flow simulations. Results suggest that the mature, unmineable Healy Creek Formation coals of the Nenana basin can sequester up to 0.41 TCF of CO_2 while producing up to 0.36 TCF of CH_4 at the end of 44-year forecast. However, these volumes are estimates and they are also sensitive to the well type, pattern and cap rock lithology.

I used a similar workflow to evaluate the state of *in situ* stress in the northeastern North Slope province of Alaska. The results show two distinct stress regimes across the northeastern North Slope. The eastern Barrow Arch exhibits both strike-slip and normal stress regimes.

Along the northeastern Brooks Range thrust front, an active thrust-fault regime is present at depths up to 6000 ft but changes to a strike-slip stress regime at depths greater than 6000 ft.

Table of Contents

x

xi

List of Figures

List of Tables

List of Appendices

Acknowledgements

It is about five years since I first arrived at UAF and became part of a very challenging but exciting project on Alaska's interior basins. As years went by, I felt very fortunate to have had the wonderful opportunities to work with my advisor, Prof. Catherine Hanks and learn enormously from her outstanding academic experience. She has been the most influential person in my doctorate study, who provided continuous encouragement towards my research and taught me how to do quality research under minimal guidance. She showed me the ways to express my ideas confidently (speak up, slow down!), to write clearly and concisely in an academic style (keep it simple!) and to implement stringent work plans to meet dissertation goals (crack the whip!). Her energy, mentoring skills and discipline have been indispensable to my transformation into a skilled professional and as a better person over these past five years. I am also truly grateful for all the hard work, time and energy she has put into providing me with strong financial support and many career opportunities through the Imperial Barrel Program, many conferences and seminars. For me, she is a wonderful academic role model and an outstanding mentor. Thank you so much for changing my life in a positive direction!

I am especially grateful to my dissertation committee members who guided me through all these years. To Prof. Mohabbat Ahmadi, I truly appreciate your work ethic, energy and willingness to perform reservoir simulation studies with me during last year's holiday season and for passing on your knowledge about CO_2 sequestration. Thank you for giving me a chance to work with you on the Shublik resource play project in the summer of 2014. I would like to thank Prof. Paul McCarthy for giving me the incredible opportunities to gain wider breadth of experience as a teaching assistant/instructor under your guidance and to develop a thorough

understanding of sedimentary geology through your classes and stimulating field studies. He was incredibly patient with me and never got upset over my mistakes during my graduate study. I would also like to thank Prof. Bernard Coakley, who kept me on my toes and challenged me to think in new and creative ways. I really appreciate his continuous encouragement in all aspects of my research and support in funding the software licenses. I am honored to have such supportive and truly outstanding committee members. I thank you all for your enjoyable and stimulating collaboration and valuable time.

Many thanks to Carla Tomsich who made a significant contribution at the start of the project with her expertise in potential field modeling, field work and sample preparations. You are an amazing person! A very special thanks goes out to Prof. Anupma Prakash, without whose support I would not be here in Alaska. I have had the great pleasure of working with Prof. Obadare Awoleke, Prof. Carl Tape and Prof. Wes Wallace, who all provided insightful questions, great advice and their time in revising my papers. Sincere thanks to Douglas Moore (ConocoPhillips), Tom Morahan (PRA), Jim Mery (Doyon Limited), Kenneth Papp (GMC), Kiran Kumar Venepalli (CMG) and Mallory Phillips (PRA) who made significant contributions to the project data and provided helpful comments. I am greatly indebted to all faculty, who taught me the fundamental principles of geology, geophysics and geochronology that allowed me to pursue a broader innovative and creative scientific approach in my research. I am also grateful to the staff at the Department of Geosciences, especially Jochen, Ellen and Barbara, for their timely help with printing, paperwork and paychecks.

My time in Alaska was full of adventures and full of good memories largely due to my roommates Arvind and Olaniyi, and my other close friends, Ibrahim and Celso (you are the best, guys!). To every one of them, thank you so much for all the hiking trips, parties, get togethers, coffee breaks, scientific discussions, road trips, late night chats and political debates. These were some of the best days of my life and I will always cherish our memories until forever. To all my wonderful friends in all of the Geoscience communities at UAF, thank you for your friendship and bringing endless happiness throughout my life.

And lastly, I am very thankful to my parents Chandrakant and Shubhangi, my brother Umesh and my sister-in-law Trupti for giving me freedom in the first place, for inspiring me to pursue my dreams, for their unconditional emotional and financial support in all difficult times and for believing in me. Though I was thousands of miles away from home, I always knew that I

had my family to count on when the times were rough. You all have always been my strength and I love you all dearly.

Most importantly, the best outcome from past three years is finding my best friend, my wonderful girlfriend- Katie and my three adorable guinea pigs (females) - Bingley, Darcy and Lizzy. They have been an incredible inspiration with their unconditional love during the critical times of my dissertation. To Katie- you made me believe that anything was possible through hard work, dedication and determination. You are an amazing and beautiful young woman with exceptional talent, who has instilled confidence in me and pushed me to the next level. During all good and bad times, we both learned a lot about science and life that helped to strengthen our commitment to each other over the last three years. I love you so much.

1 Introduction and Statement of Problem

1.1 Introduction and Motivation

In Alaska, the majority of petroleum exploration is focused on the North Slope and in Cook Inlet. However, in recent years, the relatively unexplored Tertiary coal basins of Interior Alaska have become hydrocarbon exploration targets. Nenana basin is one of several coal basins in Interior Alaska and it is located 60 miles southwest of the city of Fairbanks. The Nenana basin holds an estimated 250 million barrels of recoverable oil, up to 1 trillion cubic feet of recoverable natural gas and contains up to 8 billion short tons of identified coal resources (Merritt, 1986, Doyon Limited, 2015). Despite the four exploration wells that have been drilled in the basin, it still remains largely underexplored for oil and gas. In addition, recent carbon sequestration studies on CO_2 storage capacity of Interior Alaska suggest that Tertiary-age lignite to subbituminous coals of the Nenana coal province had a significant potential for long-term storage of anthropogenic CO_2 emissions in the region (Stevens and Bank, 2007; Shellenbaum and Clough, 2010).

However, despite recent exploration efforts, our understanding of the present-day tectonic deformation style, timing of faulting and subsequent evolution of the Nenana basin remain speculative and poorly understood. A better understanding of the Tertiary development of the Nenana basin region can aid in the exploration of the basin by constraining the timing of trap formation vs. timing of hydrocarbon generation as well as by constraining the present-day thermal maturity of source rocks in the basin. Additionally, this information can be used to evaluate the CO_2 sequestration capacity of the coals addressed in this research.

1

1.2   Regional Geology of Interior Alaska

Three major regional structural features characterize the neotectonics of Central Interior Alaska. From north to south, these are: the Kaltag-Tintina fault system, the Alaska Range fold-and-thrust belt, and the Denali Fault system (Page et al., 1995; Bemis and Wallace, 2007; Lesh and Ridgway, 2007) (Figure 1-1). The Tintina fault is a steeply dipping dextral strike-slip fault that extends through central Alaska and separates deformed North American crustal rocks in the north from the accreted Yukon-Tanana Terrane rocks of Interior Alaska (Till et al., 2007). Murphy and Mortensen (2003) suggested there was at least 450 km of dextral displacement along the Tintina fault in Late Cretaceous or Early Tertiary time. Since Early Tertiary time, slip on the Tintina fault system has been minimal (Brogan et al., 1975). At its western end, the Tintina fault splays into the Kaltag fault (Till et al., 2007).
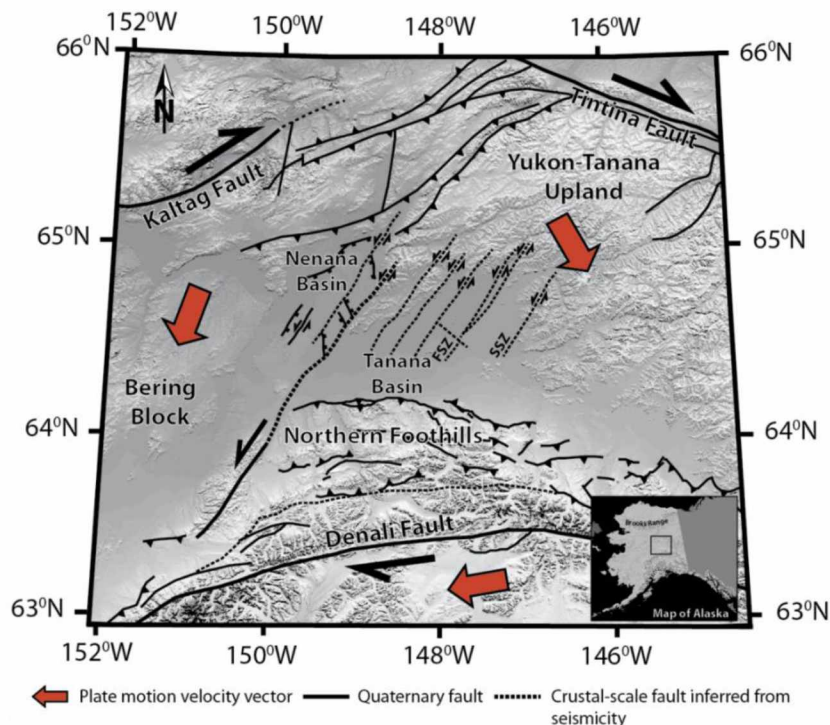
Figure 1-1 Simplified tectonic setting of the central Interior Alaska

Another prominent structural feature of central Alaska is the Denali fault (Figure 1-1). It is an active intraplate, dextral strike-slip fault that arcs through the Alaska Range and accommodates dextral shear strain resulting from the oblique plate convergence to the south (Eberhart-Phillips et al., 2003; Matmon et al., 2006) (Figure 1-1). The Denali Fault is reported to have 350 km of right-lateral strike-slip displacement along it and extends steeply through the crust as deep as ~30 km (Lanphere, 1978; Fisher et al., 2007). At present, the Denali Fault is the boundary of the counterclockwise rotating block of south-central Alaska, separating Wrangelia from the Yukon-Tanana Terrane (Nokleberg et al., 1985).

Seismological evidence suggests that three, northeast-trending, sinistral strike-slip seismic zones exist between these two regional dextral strike-slip fault systems and they include the Minto Flats seismic zone (MFSZ), the Fairbanks seismic zone (FSZ) and Salcha seismic zone (SSZ) (Page et al., 1995; Ratchkovski and Hansen, 2002) (Figure 1-1). The presence of these active seismic zones indicates a broad crustal zone of dextral shear deformation that extends from the Tintina fault in the north to the Denali fault to the south and accommodates clockwise rotation of crustal blocks in this region (Page et al., 1995).

South of this crustal shear zone, the Alaska Range is a transpressional orogen with north-vergent thrusting along the northern foothills fold-and-thrust belt and strike-slip faulting along the Denali fault to the south (Cross and Freymueller, 2008). To the north of the foothills, contractional deformation continues into the Tanana foreland basin (Ridgway et al., 2007).

1.3 Significant Questions Specific to the Tectonic Setting of the Nenana Basin Province Addressed by This Dissertation

The Nenana and Tanana basins are located within the dextral shear zone between the Denali and Tintina fault systems, and to the north of the central Alaska Range (Page et al., 1995; Ridgway et al., 2007) (Figure 1-1). Topographically, the basins are expressed as the low-lying swampy area of about 23,500 km^2 south and west of the Yukon-Tanana Upland. Based on gravity and seismic reflection data, the Nenana basin has been interpreted as an extensional half-graben associated with high-angle normal faulting across the Minto fault (Barnes, 1961; Kirschner, 1994; Van Kooten et al., 2012). However, recent crustal seismicity studies of Interior Alaska have suggested that the Nenana basin is bounded by two major active northeast-striking sinistral strike-slip faults (Ratchkovski and Hansen, 2002; Ruppert et al., 2008; Tape et al., 2013) (Figure 1-1). These basin-bounding faults form a seismic zone that is interpreted as the eastern edge of a diffuse plate boundary between the Bering plate to the west and North American plate to the east (Cross and Freymueller, 2008).

In contrast, the Tanana basin, immediately east of the Nenana basin, is a Neogene transpressional foreland basin actively forming and deforming in response to regional transpressional deformation in south-central Alaska (Bemis and Wallace, 2007; Lesh and Ridgway, 2007). Unlike the Nenana basin, no useful seismic reflection data have been acquired for the Tanana basin, so the subsurface structure of the Tanana basin remains poorly understood.

Both of these basins largely contain Tertiary non-marine sedimentary strata deposited uncomformably on early Paleozoic to Proterozoic Yukon-Tanana Terrane basement schist

4

(Ridgway et al., 2007, Van Kooten et al., 2012) (Figure 1-2). The Tertiary sedimentary strata include: 1) Late Paleocene Formation (mainly present in the Nenana basin), 2) Miocene Usibelli Group, 3) Pliocene Nenana Gravel, and 4) Quaternary surficial and unconsolidated deposits. The Usibelli Group is further subdivided into five formations: the Healy Creek, Sanctuary, Suntrana, Lignite Creek and Grubstake formations (Wahrhaftig et al., 1969). The major thermally mature to marginally mature coal-bearing units of the Nenana basin are in the Late Paleocene and Healy Creek Formations (Van Kooten et al., 2012).

Stratum		Color Code	Thickness (ft) (Nunivak 1)	Lithology (Nunivak 1) 0 GR (gAPI) 200	Depositional Setting
Age	Formation				
Tertiary / Neogene / Pliocene	Nenana Gravel		4500'		Braided fluvial-alluvial fan
Tertiary / Neogene / Late — USIBELLI GROUP Upper Miocene	Grubstake Fm.		550'		Lacustrine
Middle	Lignite Creek Fm.		840'		High-sinuosity mixed load fluvial
	Suntrana Fm.		960'		Distal sandy braided fluvial
Early — Lower Miocene	Sanctuary Fm.		1020'		Lacustrine
	Healy Creek Fm.		1990'		Proximal gravelly braided fluvial
Paleogene / Oligocene Eocene					
Paleo-cene	Paleocene Fm.		975'		Fluvial-lacustrine-alluvial fan
Paleozoic	Basement Schist				

Figure 1-2 Generalized stratigraphy of the Nenana basin

1.3.1 What is the modern-day crustal architecture of the Nenana and Tanana basins?

Regionally, the Nenana and Tanana basins are located in a crustal deformation zone characterized by complex interactions between regional crustal scale dextral strike-slip faults active northeast-striking sinistral faults, and the active fold-and-thrust belt growing the Alaska Range. A detailed knowledge of the crustal architecture and structural history of these two basins is crucial for investigating the interplay between the intra-plate stress field and the development of regional structural features in Interior Alaska.

Although the geology and structures along the northern and southern margins of the Nenana and Tanana basins have been studied extensively in the past, the present-day crustal structure and internal geometries of both basins are poorly understood. In addition, published information on the basement structure of the Nenana and Tanana basins is sparse. This region, especially the Nenana basin, is still considered a largely underexplored "frontier" area for hydrocarbon exploration and many gaps remain in our understanding of the extent of sedimentary sequences and present-day deformation style of the region that may have implications for the distribution of reservoir rocks, source rock maturation and hydrocarbon entrapment. Consequently, the understanding of the crustal structure of these basins is a key to understanding the tectonic and thermal history of each basin and the region as a whole.

.

1.3.2 How did the Nenana basin evolve over time?

The Nenana basin of central Interior Alaska has been tectonically active since the Late Paleocene, as suggested by deformed Late Paleocene sediments within the basin (Van Kooten et

al., 2012). However, little has been published about the timing and extent of tectonic deformation associated with the evolution of the basin since Late Paleocene. The basin was formed on Paleozoic basement rocks of the Yukon-Tanana terrane and contains Tertiary non-marine sediments that are more than 18,000 ft in thickness (AOGCC, 2015). Determining the tectonic development of the Nenana basin has been difficult due to lack of outcrops, limited exploration well data and scarcity of publicly available seismic reflection data. Based on gravity data, numerous studies have suggested that the Nenana basin is presently an extensional graben complex (Barnes, 1961; Kirschner, 1994; Van Kooten et al., 2012) although recent work suggests that the basin is a transtensional basin (Tape et al., 2015). However, these studies did not provide any information on how the basin initiated, and the timing of faulting and fault block exhumation rates within the basin.

A clear understanding of the evolution of the thermal regime is of critical importance to hydrocarbon generation and maturation modeling of a basin (Ziegler, 1994). No such thermal history data were available for the Nenana basin. As a result, a lack of detailed structural and thermal studies of the basin had made the development of a cohesive tectono-thermal model of the Nenana basin difficult.

1.4   Geologic CO_2 Sequestration Potential of the Nenana Basin

Over 30% of the electricity used in central Interior Alaska is generated by 6 coal-fired power plants located in the vicinity of the Nenana basin (Figure 1-3). In 2007, about 1.46 million metric tons of CO_2 emissions in the Fairbanks North Star Borough originated from these coal-fired power plants. Long term sequestration of CO_2 in Interior Alaska thus will be necessary

7

under the Clean Power Plan (CPP) if coal is to continue to be a viable energy source in the future.

Subsurface, unmineable coal seams are attractive CO2 reservoirs because they preferentially adsorb CO_2 as well as store it in coal matrix and fractures, providing a mechanism to sequester CO2 and significantly reduce anthropogenic CO_2 emissions. An additional benefit is that, in gas-saturated coal beds, injected CO_2 displaces the adsorbed methane (CH_4) molecules and allows production of displaced CH_4 without need of reservoir pressure depletion. Enhanced coal bed methane recovery (ECBM) can therefore help offset costs associated with the CO_2 sequestration. However, to successfully achieve long-term CO_2 storage as well as production of large volumes of CH_4 from the coal seams, precise geologic characterization of the CO_2 storage site is required. As a result, selection of a potential storage site involves a wide range of geological, reservoir and economic considerations to minimize risks associated with CO_2 leakage and to ensure economical CH_4 recovery. To evaluate the technical feasibility and economic viability of the Nenana basin as a potential CO_2 storage site, it is important to address the issues that fall into the following categories:

1. Tectonic setting and state of *in situ* stress (site selection)

2. CO_2 storage and CH_4 production capacity (storage capacity), and

3. Potential for and risk of CO_2 leakage (caprock integrity)
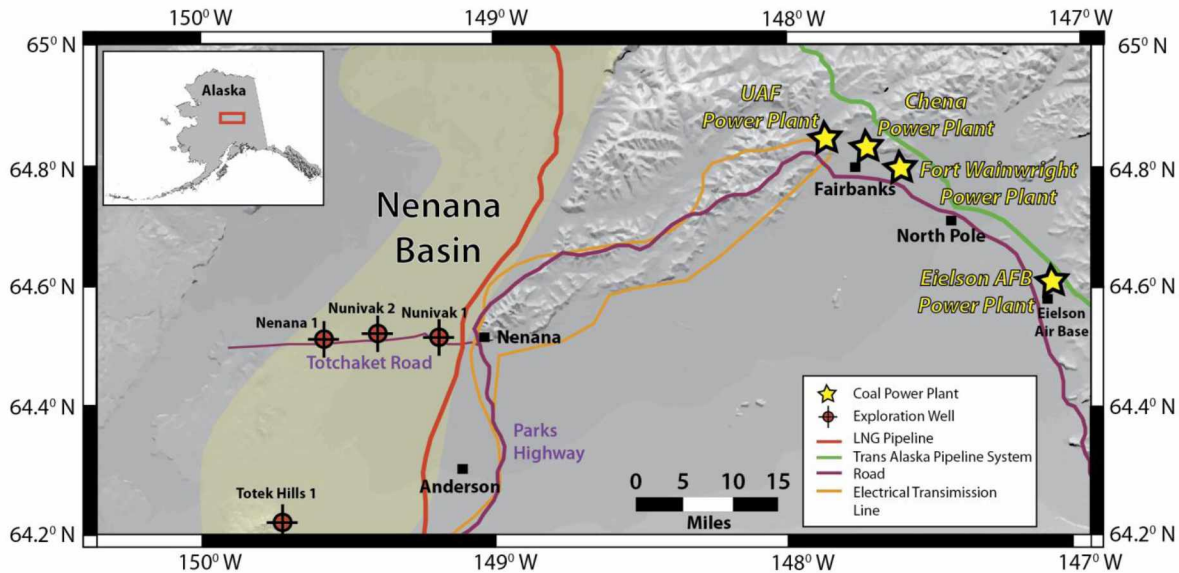
Figure 1-3 Location of the coal-fired power plants relative to the Nenana basin in Interior Alaska

1.4.1 How can subsurface exploration data be used to determine the in situ state in a basin? How does the state of stress relate to the active tectonic regime?

The state of in situ stresses in the subsurface controls the orientation, distribution and flow behavior of both natural and induced fractures. Consequently, knowledge of the state of stress is essential to provide confidence in the integrity of the CO_2 confining zone as well as well stability (Zoback, 1992). Fractured reservoirs such as coals are particularly sensitive to stresses induced by pore pressure build up and subsequent reactivation of preexisting fractures and faults during CO_2 injection. This could compromise containment of CO_2 by inducing leakage along reactivated faults and fractures and could also increase risk of induced seismicity through abnormal pressure build-ups.

Consequently, identification of the active tectonic regime and associated state of stress in a coal reservoir is of primary importance to ensure safe CO_2 injection pressures and to determine

the possibility of CO_2 leakage for a potential injection site. Tectonic stress regime at any depth can be estimated by the quantification of the relative magnitudes of pore pressure, P_p, vertical stress, S_v, maximum horizontal principle stress, S_{Hmax}, and minimum horizontal principle stress, S_{hmin}, with the assumption that the Earth's surface is traction free (Bell, 1996) (Figure 1-4). The estimated S_{Hmax} orientations can be used to further identify the present-day permeability trends in deeper coal seams as the natural fractures parallel to the S_{Hmax} orientation tend to be open (Brudy and Zoback, 1999). Once the state of stress is estimated, the resulting information can be used to identify safe sites for the CO_2 injection project, to calculate CO_2 injection pressures and to investigate risk of induced seismicity in the region.
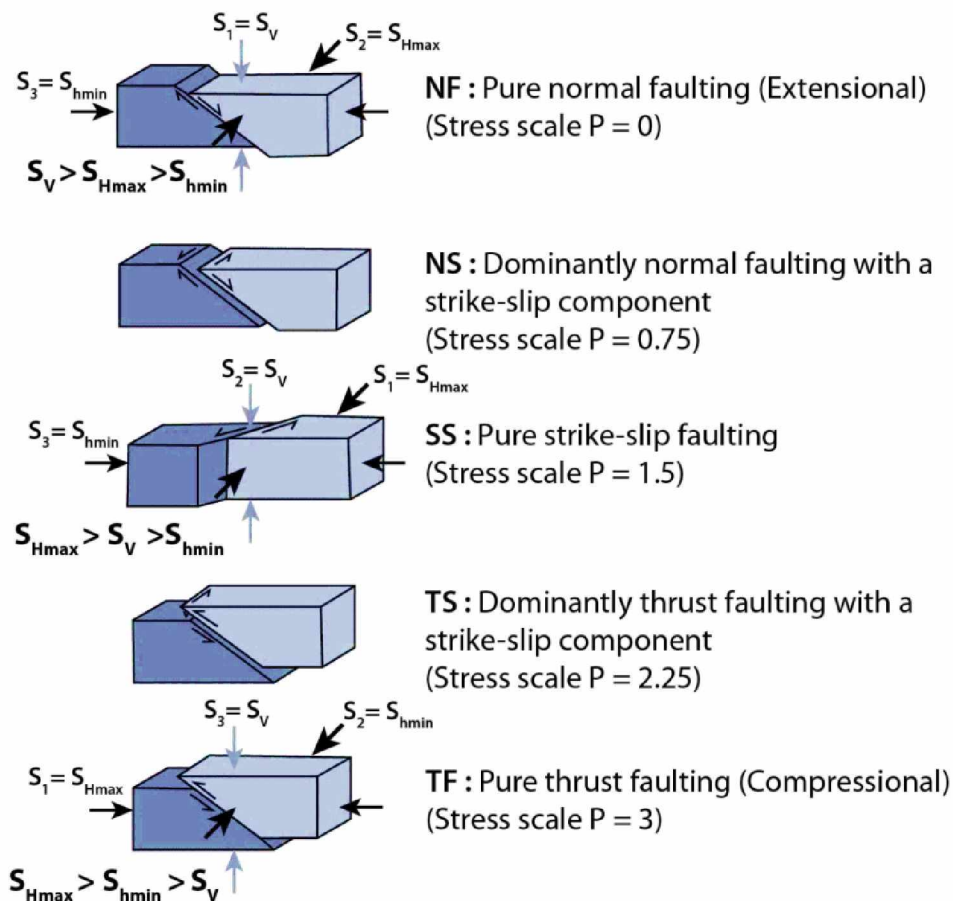
Figure 1-4 Tectonic stress regimes inferred from the relative stress magnitudes

1.4.2 What is the CO_2 sequestration capacity of the Nenana Basin?

Nenana basin is the most promising geologic CO_2 storage site in Interior Alaska. The basin contains about 8 billion short tons of subsurface coal resources and is located relatively close to oil and gas pipelines as well as coal-fired power plants operating in the region (Merritt, 1986, Doyon Limited, 2015). Several studies in the past had investigated the CO_2 storage capacity of the Nenana basin coals that occur at depths less than 3000 ft. These studies were based on basic assumptions regarding coal parameters such as coal rank, coal density and coal thickness. However, these CO_2 sequestration studies did not consider the effects of uncertainties associated with coal reservoir properties and possible coal bed methane production via CO_2 injection scenarios.

Recent CO_2-ECBM reservoir simulation and field studies have shown that the CO_2 storage and ECM production capacity of a target coal reservoir largely depends on key parameters such as coal maturity, coal permeability, coal adsorption capacity, water saturation, caprock lithology, in-situ gas content, coal geomechanical properties and CO_2 injection and CH_4 production pressures (Flores, 2004; Hernandez et al., 2006; Seidle, 2011). In addition, heterogeneities in these coal properties often result in a wide range of uncertainties in the estimates of CO_2-ECBM capacity of a sequestration site. It is therefore important to account for the reservoir heterogeneity associated with coal properties to provide accurate constraints on the CO2 sequestration and ECBM production capacity estimates of the Nenana basin.

1.5 Dissertation Format

In addition to this introduction, the dissertation consists of four different chapters which represent a series of refereed papers. Each chapter is a standalone paper which is either already accepted for publication, in review or in preparation for submission in peer-reviewed journals. Consequently some repetition of the content of the chapters is unavoidable.

Chapter 1 describes the regional crustal framework of the Nenana and Tanana basins located in Interior Alaska using integrated potential field and geologic data. This paper is currently under revision for publication in Journal of Geophysical Research-Solid Earth under the title "Crustal structure of the Nenana basin and Tanana basin, central Alaska: constraints from integration of gravity, magnetic and seismic reflection data." This paper provides new insights into the upper crustal framework of the Nenana and Tanana basins and highlights the distinct tectonic deformation styles of these two basins. I conducted the majority of potential field modeling and interpretation of data outlined in Chapter 1. My co-author, Ms. Tomsich, assisted in the field and with sample lithology descriptions. My co-author, Dr. Hanks, was largely responsible for providing funding for this research and assisted in the development of the ideas in the manuscript and in manuscript preparation. Additional co-authors include Dr. Wallace and Dr. Coakley, who helped to develop concepts, provided technical expertise and critiqued the manuscript.

Chapter 2 focuses on the distinct episodes of tectonic deformation and associated thermal regimes of the Nenana basin since the Late Paleocene. This paper has been accepted and is currently under revision for publication in Canadian Journal of Earth Sciences under the title "Cenozoic tectonic and thermal history of the Nenana basin, central Interior Alaska: new

constraints from seismic reflection data, fracture history and apatite fission-track analyses." The paper investigates the Tertiary tectonic deformation history of the Nenana basin and illustrates how basin subsidence and uplift events influenced the thermal regimes of the basin by integrating seismic reflection and well data with fracture data and apatite fission track analyses. I performed the majority of the basin modeling, data interpretation and writing. This paper is co-authored with Alec Rizzo, who performed the fracture data analyses and interpretations and Dr. Hanks, who provided funding, supervised both projects and contributed to the development of manuscript. My other co-authors are Dr. McCarthy and Dr. Coakley, who provided editorial and research guidance.

Chapter 3 outlines the methodology that I used to derive the state of in situ stresses in the basin, using the northeastern North Slope of Alaska as an example. This paper is in press in American Association of Petroleum Geologists (AAPG) Bulletin under the title "In situ stress variations associated with regional changes in tectonic setting, Northeastern Brooks Range and eastern North Slope of Alaska." This paper developed a workflow using existing methodologies for estimating the magnitudes of the present-day in situ stresses in areas with minimal core log data. This method was then used in Chapter 4 to evaluate the tectonic stress regimes at a potential CO_2 storage site in the Nenana basin. I did the majority of the exploration data analysis, developed the methodology to interpret the tectonic stress regimes and performed data interpretation and writing. My co-authors on this paper are Dr. Hanks, who assisted in data interpretation and in manuscript preparation, Dr. Ahmadi, who provided funding and helped with the manuscript revision and, Dr. Wallace and Dr. Dare, who provided technical expertise and research guidance.

Chapter 4 discusses the technical feasibility of sequestering anthropogenic CO_2 with simultaneous recovery of coal bed methane in the mature, subbituminous coals of the Nenana basin. This paper is in press for publication in Natural Resources Research Journal under the title "Preliminary study of the carbon sequestration and enhanced coal bed methane production potential of subbituminous to high-volatile bituminous coals of the Healy Creek Formation, Nenana basin, Interior Alaska." This paper evaluates the uncertainties within major reservoir parameters through a series of sensitivity analyses, experimental design methods and fluid flow simulations and examines how these uncertainties influence the total CO_2 sequestration and coal bed methane capacity estimates of the Nenana basin. I conducted the majority of the work on Chapter 4 including reservoir modeling, data interpretation and writing. My co-author on this paper, Dr. Ahmadi, was largely responsible for developing the ideas and concepts for the reservoir simulation scenarios that are used in this paper. Additional co-authors include Dr. Hanks, who provided funding and helped in discussing uncertainty analyses and in revising the manuscript, and Dr. Dare, who assisted in designing experimental design methods and in manuscript preparation.

Detailed descriptions of the rock lithologies, magnetic susceptibilities, vitrinite reflectances and apatite fission track analyses on cuttings from the Nunivak 1 and Nenana 1 wells have been published as Division of Geological and Geophysical Survey (DGGS) Geologic Material Center data file (Dixit and Tomsich, 2014). Appendix 7-A and Appendix 7-B detail the present-day stress magnitudes used to develop the tectonic stress regime maps for the northeastern North Slope province and at the top of the Shublik Formation, respectively.

1.6   References

Alaska Oil and Gas Conservative Commission (AOGCC). (2015). Digital well history files, doa.alaska.gov/ogc/publicdb.html. Accessed September, 2015.

Barnes, D. F. (1961). Gravity low at Minto Flats, Alaska, in U.S. Geological Survey, Geological survey research 1961, Short papers in the geologic and hydrologic sciences, Articles 293-435: U.S. Geological Survey Professional Paper, 254-257.

Bell, J. S. (1996). In situ stresses in sedimentary rocks (part 2): applications of stress measurements: Geoscience Canada, 23, 135-153.

Bemis, S. P., and Wallace, W. K. (2007). Neotectonic framework of the north-central Alaska Range foothills, in K. D. Ridgway, J. M. Trop, J. M. G. Glen, and J. M. O'Neill (Eds.), Tectonic growth of a collisional continental margin: Crustal evolution of southern Alaska, Geological Society of America Special Paper, 431, 549-572.

Brogan, G. E., Cluff, L. S., Korringa, M. K., and Slemmons, D. B. (1975). Active faults of Alaska, Tectonophysics, 29, 73–85.

Brudy, M., and Zoback, M. D. (1999). Drilling- induced tensile wall-fractures: implications for determination of in situ stress orientation and magnitude, International Journal of Rock Mechanics and Mining Sciences, 36, 191-215.

Cross, R. S., and Freymueller, J. T. (2008). Evidence for and implications of a Bering plate based on geodetic measurements from the Aleutians and western Alaska: Journal of Geophysical Research, 113, B07405, doi:10.1029/2007JB005136.

Dixit, N. C., and Tomsich, C. S. (2014). Apatite fission track, magnetic susceptibility, and vitrinite reflectance analyses on cuttings from the Nunivak #1 and Nenana #1 wells, Alaska. Division of Geological & Geophysical Surveys Geologic Materials Center Data Report, 422 (1), p. 891, doi:10.14509/27042.

Doyon Limited. (2015). Alaska onshore rift basins, Nenana and Yukon Flats. http://doyonoil.com/Content/pdfs/NenanaBasin3DSeismic.pdf. Accessed November, 2015.

Eberhart-Phillips, D., Haeussler, P. J., Freymueller, J. T., Frankel, A. D. et al. (2003). The 2002 Denali fault earthquake, Alaska: a large magnitude, slip-partitioned event, Science, 300, 1113–1118.

Fisher, M. A., Pellerin, L., Nokleberg, W. J., Ratchkovski, N. A., and Glen, J. M. G. (2007). Crustal structure of the Alaska Range orogen and Denali fault along the Richardson Highway, in Tectonic Growth of a Collisional Continental Margin: Crustal Evolution of Southern Alaska, edited by K. D. Ridgway et al., Geological Society of America Special Papers., 431, 43–53, doi:10.1130/2007.2431(03).

Flores, R. M. (2004). Coalbed methane in the Powder River Basin, Wyoming and Montana: An assessment of the Tertiary-Upper Cretaceous coalbed methane total petroleum system. U.S. Geological Survey Digital Data Series, DDS-69-C, Chapter 2.

Hernandez, G., Bello, R., McVay D. et al. (2006). Evaluation of the technical and economic feasibility of CO_2 sequestration and enhanced coal-bed-methane recovery in Texas low-rank coals. Society of Petroleum Engineers Journal, doi:10.2118/100584-MS.

Kirschner, C. E. (1994). Interior basins of Alaska, in Plafker, G., and Berg, H. D., eds., The geology of Alaska: Boulder, Colorado, Geological Society of America, Geology of North America, G-1, 469–493.

Lanphere, M. A. (1978). Displacement history of the Denali fault system, Alaska and Canada. Canadian Journal of Earth Sciences, 15, 817 – 822.

Lesh, M. E., and Ridgway, K. D. (2007). Geomorphic evidence of active transpressional deformation in the Tanana foreland basin, south -central Alaska, in K. D. Ridgway, J. M. Trop, J. M. G. Glen, and J. M. O'Neill (Eds.), Tectonic growth of a collisional continental margin: Crustal evolution of southern Alaska, The Geological Society of America Special Paper, 431, 573-593.

Matmon, A., Schwartz, D. P., Haeussler, P. J., Finkel, R., Lienkaemper, J. J., Stenner, H. D., and

Dawson, T. E. (2006). Denali fault slip rates and Holocene–late Pleistocene kinematics of central

Alaska: Geology, 34, 645–648.

Merritt, R. D. (1986). Coal geology and resources of the Nenana Basin, Alaska. Alaska Division

of Geological & Geophysical Surveys, Public-data File 086-74, p. 71.

Murphy, D. C. and Mortensen, J. K. (2003). Late Paleozoic and Mesozoic features constrain

displacement on Tintina fault and limit large-scale orogen-parallel displacement in the northern

Cordillera [abstract]: Geological Association of Canada-Mineralogical Association of Canada-

Society of Economic Geologists, Vancouver, p. 151.

Nokleberg, W. J., Jones, D. L., and Silberling, N. J. (1985). Origin and tectonic evolution of the

Maclaren and Wrangellia terranes, eastern Alaska Range, Alaska: Geological Society of America

Bulletin, 96, 1251–1270.

Page, R. A., Plafker, G. and Pulpan, H. (1995). Block rotation in east-central Alaska: a

framework for evaluating earthquake potential, Geology, 23 (7), 629-632.

Ratchkovski, N. A., and Hansen, R. (2002). New constraints on tectonics of Interior Alaska:

earthquake locations, source mechanisms, and stress regime, Bulletin of the Seismological

Society of America, 92 (3), 998-1014.

Ridgway, K. D., Thoms, E. E., Layer, P. W., Lesh, M. E., White, J. M., and Smith, S. V. (2007). Neogene transpressional foreland basin development of the north side of the central Alaska Range, Usibelli Group and Nenana Gravel, Tanana Basin. In K. D. Ridgway, and others (Eds.), Tectonic Growth of a Collisional Continental Margin—Crustal evolution of southern Alaska, Geological Society of America Special Paper, 431, 507–547.

Ruppert, N. A., Ridgway, K. D., Freymueller, J. T., Cross, R. S., and Hansen, R. A. (2008). Active tectonics of Interior Alaska - Seismicity, GPS geodesy, and local geomorphology, in J. T. Freymueller, P. J. Haeussler, R. L. Wesson, and G. Ekström (Eds.), Active Tectonics and Seismic Potential of Alaska: Washington, D.C., American Geophysical Union, Geophysical Monograph, 179, 109-133.

Seidle, J. (2011). Fundamentals of Coalbed Methane Reservoir Engineering. PennWell Corporation, Tulsa, Oklahoma.

Shellenbaum, D. P., and Clough, J. G. (2010). Alaska geologic carbon sequestration potential estimate: Screening saline basins and refining coal estimates. West Coast Regional Carbon Sequestration Partnership, DOE Contract No. DE-FC26-05NT42593.

Stevens, S., and Bank, G. (2007). Alaska geologic CO_2 storage potential: Preliminary scoping estimate for deep coal seams, WESTCARB Project draft report, p. 7.

Tape, C. H., West, M. E., Silwal, V., and Ruppert, N. A. (2013). Earthquake nucleation and triggering on an optimally oriented fault, Earth and Planetary Science Letters, 363, 231–241.

Till, A. B., Roeske, S. M., Bradley, D. C., Friedman, R., and Layer, P. W. (2007). Early Tertiary ranstension-related deformation and magmatism long the Tintina fault system. Alaska.In: Till, A. B., Roeske, S. M., Foster, D. A., and Sample, J. (eds.) Exhumation and Continental Strike-Slip Fault Systems. Geological Society of America Special Paper 434, 233–264, doi: 10.1130/2007.2434(11).

Van Kooten, G. K., Richter, M. and Zippi, P. A. (2012). Alaska's Interior rift basins: A new frontier for discovery, Oil and Gas Journal, p. 10.

Wahrhaftig, C., Wolfe, J. A., Leopold, E. B., and Lanphere, M. A. (1969). The coal-bearing group in the Nenana coal field, Alaska, U.S. Geological Survey Bulletin, 1274, 1-30.

Ziegler, P. A. (1994). Cenozoic rift system of Western and Central Europe: an overview. Geol. Mijnbow, 73, 99-127.

Zoback, M. L. (1992). First and second order patterns of stress in the lithosphere: the World Stress Map Project: Journal of Geophysical Research, 97, 11703- 11728.

2 Crustal structure of the Nenana basin and Tanana basin, central Alaska: constraints from integration of gravity, magnetic and seismic reflection data[1]

2.1 Abstract

The scarcity of surface exposures, subsurface geologic data and seismic data within the Nenana and Tanana basins of central Alaska has made a detailed structural investigation of these basins difficult. Using available aeromagnetic, gravity and seismic reflection data with other geophysical information, we constrained nine two-dimensional potential field models that provide new insights into the subsurface structure of both basins. Our results highlight the major differences between the two basins. We interpret the Nenana basin as a deep (up to 8 km), narrow Cenozoic basin that formed in an oblique-extensional tectonic regime within the Minto Flats fault zone (MFFZ). We integrate results from potential field modeling with published models of the basin, and present two refined tectonic models that explain the distribution and geometries of intrabasinal faults, as well as regional subsidence. Our modeling supports a "transtensional pull-apart" model over a "pure strike-slip" model. The adjacent Tanana basin has a fundamentally different geometry. Our potential field models indicate this basin is relatively shallow, with depths of up to 2 km. It is actively forming in a compressional tectonic setting dominated by north-directed thrusting along the central Alaska Range and northeast-oriented strike-slip faulting in central Interior Alaska. We present three models for the development of the Tanana basin in this setting: 1) chevron-fold type deformation model, 2) foreland flexural model and 3) dextral shear deformation model. Our analysis finds that no single model can fully explain the formation of the Tanana basin, and additional structural complexities exist that require further investigation.

---

[1] Dixit, N.C., Hanks, C.L., Tomsich, C.S., Wallace, W.K., and Coakley, B.J. (2016). Crustal structure of the Nenana basin and Tanana basin, central Alaska: constraints from integration of gravity, magnetic and seismic reflection data, Journal of Geophysical Research – Solid Earth (in revision).

2.2 Introduction

Central Interior Alaska is a broad zone of active deformation characterized mainly by a dextral shear zone between two regional east-west-trending dextral strike-slip fault systems-the Denali fault to the south and the Tintina fault to the north. South of the Denali fault, compressional deformation related to the Alaska Range dominates (Page et al., 1995, Lesh and Ridgway, 2007; Ruppert et al., 2008) (Figure 2-1). Beginning in early Cenozoic time, tectonic deformation in Interior Alaska produced several basins that share similar sedimentary sequences but differ in geometries and underlying basement structure (Frost and Stanley, 1991; Ridgway et al., 2007; Van Kooten et al., 2012; Wartes et al., 2013). A better understanding of lateral variations in the crustal structure and overlying sedimentary cover of these basins is necessary to determine the tectonic origin of these basins and their subsequent evolution. This in turn has implications for resource exploration in the region.

The Nenana and Tanana basins are situated along the northern flank of the central Alaska Range and cover a low-lying swampy area of about 23500 km^2 south and west of the Yukon-Tanana Upland (Figure 2-2). Several shallow gravity and outcrop field studies have documented the extent and geometry of these basins, as well as estimated the thickness of sedimentary fill in each basin (Barnes, 1961; Kirschner, 1994, Lesh and Ridgway, 2007; Van Kooten et al., 2012). Van Kooten and others (2012) interpreted seismic reflection profiles from the Nenana basin that revealed a northeast-trending asymmetric half-graben with up to 8 km of Cenozoic sedimentary fill. They constrained the sediment ages using the palynomorph data collected from exploration wells drilled in the Nenana basin (Gerry Van Kooten, written communication, 2014). More recently, an exploration drilling program conducted by Doyon Limited provided additional information on the basement structure of the Nenana basin that suggests the basin consists of two

distinct depocenters with a relatively steep eastern flank and more gently sloping western flank (Van Kooten et al., 2012; Doyon Limited, 2015). In contrast, the Tanana basin, immediately east of the Nenana basin, is relatively unexplored. While subsurface data from the Tanana basin is lacking, ~2 km of Neogene sedimentary strata are exposed immediately south of the Tanana basin in the Northern Foothills of the central Alaska Range (Péwé et al., 1966; Wahrhaftig, 1987; Bemis and Wallace, 2007; Lesh and Ridgway, 2007; Bemis et al., 2012, Brennan and Ridgway, 2015) (Figure 2-2). Stratigraphic, structural and geomorphic analyses of these exposed Neogene sediments and structures suggest that the Tanana basin is a Neogene transpressional foreland basin actively forming and deforming in response to northward propagation of the Northern Foothills fold-and-thrust belt (Bemis and Wallace, 2007; Lesh and Ridgway, 2007; Ridgway et al., 2007; Bemis et al., 2012).

Although detailed geological and structural studies have been previously carried out along the southern margin of both basins, little is known about the basement structure and the deformation of the overlying Cenozoic sedimentary cover within the basins. Only four exploration wells have been drilled in Cenozoic non-marine rocks of the Nenana basin and no deep well has been drilled into the Tanana basin (Figure 2-2). Most recent exploration efforts have documented the extent and geometry of the sedimentary sequences in the Nenana basin using seismic reflection data (Van Kooten et al., 2012; Doyon Limited, 2015). However, these seismic profiles did not image the basement structure in the deeper areas of the basin and were sparsely spaced. No useful seismic reflection data have been acquired for the Tanana basin. The basement depth across the Tanana basin, therefore, remains highly speculative. As a result, the

crustal framework of these two basins, the response of the underlying basement to Cenozoic tectonics and the resulting impact on basin geometry and filling history are poorly constrained.

To fill this gap, we integrate regional magnetic and gravity data with the available seismic and well data and use the resulting models to delineate the internal basin geometry and crustal framework of these two basins. These models can be used to constrain the upper crustal basin structure and define major boundaries between the sedimentary and the underlying basement units; identify the possible location of intrusive bodies; identify possible active geologic structures; and delineate the extent and geometry of the sedimentary units to better understand the nature of faulting within the basin sediments as well as deformation style of the basement.

Results of our investigation help to constrain the modern-day tectonic setting of the Nenana basin and Tanana basin, which is critical in unraveling the structural development of the region since the early Cenozoic period.

2.3   Geophysical Data

2.3.1   Residual Aeromagnetic Data

Figure 2-3 shows the residual merged aeromagnetic anomaly map for the Fairbanks Quadrangle area. This map was constructed from merged aeromagnetic surveys (Veach, 1973) that were conducted during the years 1971-to1973. Data were acquired along 1-mile-spaced flight lines at a height of about 305m. We used the corrected, digitally compiled and gridded data (Meyer, 2008) for our magnetic data modeling. The locations of the magnetic anomaly profiles for our potential field models are shown in Figure 2-3.

The initial aeromagnetic data processing was performed by Peterson, Grant & Watson Limited which was contracted by the Northwest Geophysical Associates according to the following: 1) data interpolation on the original aeromagnetic survey data with the minimum curvature algorithm to construct digitalized contour data with the final grid cell size of 1 km; 2) the differences at the survey boundaries were reduced by adjusting the survey datum levels and a composite grid map of magnetic anomalies was constructed; and 3) these adjusted grids were draped at a level of 304 m above the terrain using GEOSOFT software (Meyer and Saltus, 1995). Saltus and others (1999) performed a regional/residual field separation to delineate the effects of shallow local magnetic sources in the upper crust and presented an updated version of the Alaska aeromagnetic anomaly grid. In addition, the gridded aeromagnetic data sets were merged together after the long wavelength component, defined by the International Geomagnetic Reference Field (IGRF 1972) was removed. Combining data of Meyer and Saltus (1995) and digital elevation models (DEM), Meyer (2008) subsequently published a digitally compiled, aeromagnetic anomaly map of the Nenana and Tanana basins at a scale of 1:250,000 and a contour interval of 5 nT. A recent version of the regional merged aeromagnetic anomaly map for the Fairbanks Quadrangle area (modified from Meyer, 2008) is shown in Figure 2-3.

Both Nenana and Tanana basins are marked by a number of major positive and negative magnetic anomalies, with values ranging from -75 to 350 nT. Short wavelength, high amplitude anomalies of up to 350 nT are observed mainly to the north of the Northern Foothills fold-and-thrust belt and in the central part of the Tanana basin. These magnetic anomalies clearly trend northeast-southwest, parallel to mapped structures (Figure 2-3).

2.3.2 Gravity Data

Figure 2-4 shows the most recent complete Bouguer anomaly map for the Fairbanks Quadrangle area. To better understand and model the gravity anomaly patterns caused by shallow sources with contrasting densities in the two basins, we separated the regional and residual gravity field components using the complete Bouguer gravity anomaly map of Meyer (2008). The low-density root of the topographically high central Alaska Range is removed with well-constrained assumptions: (1) depth to isostatic root (Moho) at sea level = 35-45 km (Veenstra et al., 2006), and (2) average density of basement masses = 2.6-2.7 g/cm^3 (Simpson et al., 1986; Veenstra et al., 2006). To estimate the regional gradient from the complete Bouguer gravity anomaly map (Meyer, 2008), we applied a two-dimensional surface fitting technique to the observed gravity values measured across nine gravity profiles. The residual gravity anomaly values for each profile were obtained by subtracting the estimated regional gradient from the observed gravity along the profile. The residual gravity anomalies are the result of lateral density contrasts at a shallow crustal level and serve as the basis for our gravity modeling (Figure 2-5).

The residual gravity anomalies in our study area reveal two distinct gravity regions- the Nenana gravity low and the Tanana gravity low (Figure 2-5). Both basins are associated with negative anomalies, up to 55 mGal in magnitude for the Nenana basin and up to 25 mGal for the Tanana basin. Short-wavelength anomaly lows indicate shallow sources with low densities that are surrounded by denser crystalline rocks (Lowrie, 2007). The presence of thick successions of low-density Neogene sedimentary rocks in the subsurface of this region (Ridgway et al., 2007; Van Kooten et al., 2012) may explain the observed gravity lows over the two basins. We test this hypothesis in a later section of this paper.

26

2.3.3 Seismic Reflection and Well Data

In addition to gravity and magnetic data, subsurface and surface geologic data were used to determine the density and magnetic susceptibility of different rock types, major geological boundaries, and the spatial distribution of the main lithological units. These data include four seismic reflection lines, drill chips and well log files of four exploration wells, geologic maps and outcrop studies conducted in the vicinity of the Nenana and Tanana basins (Figure 2-2; Wahrhaftig et al.; 1969, Merritt, 1985, Lesh and Ridgway, 2007, Ridgway et al., 2007; Stanley and Lillis, 2011, Tomsich et al., 2011; Van Kooten et al., 2012). For our study, we interpreted seismic reflection data (courtesy of ConocoPhillips) on the southern part of the Nenana basin. The seismic data include four 2D, time-migrated seismic profiles (T1, T2, T3 and T4) that extend up to 4.5 sec in two-way-traveltimes (T.W.T.), corresponding to approximately 9.5 km of depth in the subsurface. Seismic data has been integrated with well log data to construct a depth to basement map. Most recently, Doyon Limited published a series of additional 2D & 3D seismic reflection profiles acquired for oil and gas exploration in the Nenana basin (Van Kooten et al., 2012; Doyon Limited, 2015). We integrated the available published seismic data with 2D seismic profiles provided by ConocoPhillips. The resulting seismic framework for the basin was then used to identify major stratigraphic sequences and the structural features in the Nenana basin as well as to augment our gravity and magnetic interpretation for the basin.

No seismic reflection data is available for the Tanana basin. However, several geophysical studies of crustal sections in central Alaska based on regional deep seismic refraction, receiver function, gravity and aeromagnetic data analyses provide valuable constraints on the crustal structure of the Tanana basin (Barnes, 1961; Grantz et al., 1991; Fisher et al., 2004; Veenstra, 2006; Brennan et al. 2011). We integrated the published geophysical crustal

27

sections of these studies with available geological data from sparsely distributed shallow

subsurface and water well drill logs (Golder Associates, 2000; WELTS, 2010) to develop basin-

scale gravity and magnetic models of the basement structure of the Tanana basin.

2.3.4 Seismicity

Several studies on past and present earthquakes in Interior Alaska outline zones of active

crustal deformation in Interior Alaska (Ruppert et al., 2008; Tape et al., 2013). Figure 2-6 shows

areas of seismicity in the Nenana and Tanana basins based on relocated earthquake events. The

seismicity has been interpreted to occur within a series of northeast-trending shear zones that are

thought to have formed in response to strain caused by large-scale dextral strike-slip motion on

the Denali and Tintina fault systems. These shear zones have been interpreted to accommodate

regional shortening resulting from possible crustal block rotation within the shear zone between

the Denali and Tintina faults, far-field effects of the ongoing collision of the Yakutat microplate

in the south and the interaction between the Bering block and the North American Plate to the

west (Page et al., 1995, Eberhart-Phillips et al., 2006; Ruppert et al., 2008, Brennan and

Ridgway, 2015). It should be noted that while seismicity is the best indicator of regional stress

and structural grain at greater depths (depths up to 30 km), it does not always reflect the

structures or localized state of stress at shallow crustal levels (depths < 6 km) (Fisher et al., 2004;

Dixit et al., 2015).

2.3.5 Rock Property Measurements

Gravity and magnetic anomalies observed at the surface are caused by lateral variations

in bulk densities and magnetic susceptibilities of the underlying lithologic units (Grantz et al.,

1991; Fuis, 1998; Saltus et al., 2007). To model the gravity and magnetic anomalies, it is

necessary to make assumptions about rock densities and magnetic susceptibilities for unknown

rock units in the subsurface. Table 2-1 summarizes observed and averaged magnetic susceptibility and rock density values for all modeled lithologic units in our study area.

2.4   Methodology

We used GM-SYS, a 2D gravity and magnetic interactive forward modeling software, to generate subsurface models that honor the observed residual gravity and residual magnetic anomaly data as well as the known distribution and physical properties of major geologic units. The model constrains the subsurface position, shape, thicknesses, physical properties and depths of these units. Modeled blocks are assumed to have constant densities and magnetic susceptibilities.

Observed gravity and magnetic anomalies at the surface can result from several Earth models, many of which may not be geologically realistic. To remove this inherent ambiguity in determining realistic potential field sources, an initial potential field model was developed in GM-SYS and it was further constrained by existing geophysical and geological data, assuming each structural/lithologic block to extend to infinity in a direction perpendicular to the profile. In GM-SYS software, the joint modeling for calculated gravity and magnetic responses was performed using the methods of Talwani et al. (1959) and Talwani and Heirzler (1964). Forward gravity and magnetic models were then generated, based on algorithms described by Won and Bevis (1987) and Rasmussen and Pedersen (1979). This potential field model was then used to estimate a hypothetical potential field signature that was compared to the observed residual gravity and magnetic data. The geometries of the assumed geophysical source values were then iteratively modified to obtain a best fit between the observed and calculated values of both gravity and magnetic anomaly data.

For the final potential field models of the Nenana basin and Tanana basin, the intrabasement sources were attributed to Proterozoic to Early Paleozoic Yukon-Tanana Terrane schist (regional schist sequences) and Late Paleozoic Totatlanika Schist underlying the basin sequences. A suite of Late Cretaceous to Early Tertiary mafic and plutonic intrusions into the basement were modeled as separate higher-density bodies similar to those seen at the surface and inferred in published geophysical cross-sections for Interior Alaska (Grantz et al., 1991; Wilson et al., 1998; Hanks and Holdmann, 2013). Sedimentary sequences that are exposed in Interior Alaska and are incorporated into the model include: Late Paleocene and older sediments, Miocene Usibelli Group strata, Pliocene Nenana Gravel, and Quaternary and younger surficial deposits (Wahrhaftig et al., 1969; Thoms, 2000; Ridgway et al., 2007). Table 2-1 shows the representative densities and magnetic susceptibilities assigned to each modeled unit.

Our gravity and magnetic anomaly profiles show the best of the possible solutions that are well-constrained by seismic reflection data and the available sources of other geophysical and geologic data. The errors in the least square fitting between the observed and computed profiles were 0.7% for gravity and 31% for the magnetic data. The misfit for gravity and magnetic profiles could be the result of local changes in rock densities and uncertainty about the direction of magnetization (Saltus and Blakely, 2011). It, however, can be improved by splitting sources into a large number of homogeneous bodies with variable densities and magnetization properties. However, the degree of heterogeneity within the source body is hard to constrain and relies mostly on the consistency with the available geologic and geophysical data for the area and geologic concepts.

2.5 Results and Discussion

2.5.1 Interpretation of Gravity Anomalies

The calculated residual gravity anomaly data indicate three prominent features in the study area (Figure 2-5). These are 1) a narrow northeast-trending zone of a large negative gravity anomaly over the entire Nenana basin, 2) a broad, low-amplitude zone of east-to-west trending negative gravity anomaly within the southern part of the Tanana basin, and 3) several northeast-trending belts of positive gravity anomalies within the Tanana basin.

The northeast-trending gravity low (-28 to -42 mGal) over the Nenana basin extends the entire length of the basin and coincides with the mapped structural boundaries of the Nenana basin (Figures 2-2 and 2-5). This large, aerially extensive gravity low can be subdivided into two distinct gravity lows that are coincident with two mapped depocenters (Van Kooten et al., 2012). A relative positive anomaly, with amplitude higher than 19 mGal, separates the two gravity lows and may indicate a buried basement arch. The western margin of the Nenana basin is marked by a northeast-trending, relatively high-amplitude oval-shaped negative gravity anomaly (12 to 20 mGal) and may be associated with a northeast-striking buried structural high. A pronounced gravity high with a steep gradient (up to 130 mGal) defines the eastern margin of the northern depocenter of the Nenana basin (Figure 2-2) and coincides with the mapped trace of the Minto fault. The high-amplitude Bouguer anomaly observed along the footwall of the Minto fault (Figure 2-4) matches well with the surface exposures of Yukon-Tanana schist in this part of the Yukon-Tanana Upland. This correlation may reflect the large contrast in densities of rocks on both sides of the Minto fault in the northern part of the Nenana basin. In contrast to the northern depocenter, the eastern side of the southern depocenter shows no significant gravity expression, indicating that rocks on both sides of the Minto fault in this area may have similar rock densities.

31

The gravity signature of the Tanana basin is more complex, but overall reflects a significantly shallower sedimentary basin. Immediately north of the Northern Foothills fold-and-thrust belt, several east-to-west trending negative gravity anomalies have low amplitudes (up to 8 mGal) and are widely spaced. These gravity lows lie within the Tanana basin and suggest a wide, shallow source deeper than 1 km. The western margin of the Tanana basin is marked by a dramatic increase in the gravity gradient and correlates well with the westward-dipping Minto fault that defines the eastern boundary of the Nenana basin. Localized gravity highs are found in the central part of the Tanana basin; these highs may be related to high-density basement rocks exposed in the area (Frost and Stanley, 1991).

2.5.2 Interpretation of Magnetic Anomalies

The magnetic anomalies in our study area are dominated by northeast-trending anomalies that parallel similar trends seen in the gravity anomalies (Figure 2-3). In the Nenana basin, magnetic anomaly values are low (< 0 nT) along the inferred basin axis and reflect the presence of thick sedimentary rocks with low magnetic susceptibilities. These narrow, subdued magnetic anomalies coincide well with pronounced gravity lows (-28 mGal and -42 mGal) measured over the Nenana basin.

To the east, positive magnetic anomalies of varying gradients and wavelengths are oriented northeast- and east-west. These moderately high anomalies (up to 35 nT) correspond to gravity highs, suggesting thin sedimentary cover in the Tanana basin (Hanks and Holdmann, 2013).

Two prominent magnetic anomalies show a magnetic dipole with amplitudes of 275 nT and 400

nT, respectively, on the south side paired with a magnetic low of -75 nT and -85 nT on the north

side. The presence of a strong magnetic high to the south of a magnetic source at this latitude

suggests remnant magnetization played a role in forming these magnetic dipoles. We suggest that

these bipolar anomalies are produced by magnetic bodies with normal polarity and higher

magnetic susceptibilities located at very shallow depths in the Tanana basin. Gravity anomalies

over these prominent magnetic patterns have only slightly more positive amplitudes. The gravity

anomaly patterns associated with these bipolar magnetic anomalies also suggest that the sources

of the magnetic anomalies have somewhat higher densities than surrounding rocks.

2.5.3   Integrated Potential Field Models
Nine profiles were selected roughly perpendicular to the strike of major geologic

structures and the gradients of the prominent anomalies (Figure 2-2). Four profiles (T1 to T4)

entirely lie within the southern part of the Nenana basin and coincide with 2D seismic profiles

(courtesy of ConocoPhillips) (Figure 2-7). The northwestern segments of four additional profiles

(T5 to T8) extend from the northwestern margin of the northern Nenana basin to the eastern and

southern margin of the Tanana basin and transect the inferred geologic boundary between the

two basins (Hanks and Holdmann, 2013). Profile T9 is a south-to-north profile that starts at the

Northern Foothills of the central Alaska Range, extending northward across the basin and ends in

the Yukon-Tanana Upland, north of the Tanana basin (Figure 2-2).

Using the interactive forward modeling feature of the Geosoft GM-SYS software, we

developed nine 2D forward potential field models of the geologic structures along the profiles

outlined in Figures 2-2 and 2-8. The aeromagnetic data were modeled for only five selected

profiles (T1, T2, T3, T5 and T7), due to the availability of magnetic susceptibility data and

geologic information about the nature of bedrock in the study area. As discussed earlier, the 2D

forward models are geologically simplistic models for the upper 10 km of the shallow crustal

structure and basin geometries. We acknowledge here that gravity and magnetic anomaly

interpretations are non-unique solutions and carry large uncertainties. We strove to find the most

viable solutions by using all available data for the subsurface (See Saltus and Blakely, 2011).

Below we discuss the two basins separately due to variations in their basement structure

as well as available geological and geophysical information for each basin.

Nenana Basin

The basement structure of the southern Nenana basin is well constrained by 2D seismic

data (Figure 2-7). The data, combined with the 2D potential field models for the Nenana basin,

show Cenozoic sedimentary fill as thick as ~6 km (-28 mGal) along the southern part and ~8 km

(-42 mGal) along the northern part of the basin (Figure 2-8). Based on density variations, we

modeled the sedimentary rock sequences of the Nenana basin in four rock packages: 1) Late

Paleocene and older sediments (up to ~2100 m thick), 2) Miocene Usibelli Group sediments (up

to ~4 km thick), 3) Pliocene Nenana Gravel (up to ~1300m thick), and 4) Quaternary surficial

deposits (up to ~500 m thick) (Table 2-1). The changes in thicknesses of these sedimentary units

observed on potential field models of the basin are well constrained by regional seismic

reflection profiles and well log data.

Eastern Nenana Basin Margin

Our potential field models indicate that the sedimentary fill thickens along the eastern and northeastern flank of the basin to as much as 7 km against the Minto fault- a prominent north-east striking left-lateral fault bounding the northern depocenter of the Nenana basin (Transect T4, Figure 2-8d). The Minto fault is modeled as a steep, west-dipping (~76^0 dip with strike of 10^0) oblique-extensional fault that juxtaposes the Cenozoic sediments of the basin against more dense Precambrian to Paleozoic quartz mica schists of the Yukon-Tanana terrane that underlie most of the basin to the west and in the south (Tape et al., 2015; this study; Transects T1, T2 and T3, Figure 2-8). A strong contrast in gravity and magnetic anomalies along the northeastern flank of the Nenana basin is attributed to the main trace of the Minto fault with east-side up. Our interpretation is consistent with mapped seismic lineaments of the Minto fault in previous geophysical investigations (Van Kooten et al., 2012; Tape et al., 2013) and geomorphic analyses (Frohman, 2015; Koehler, 2013). Numerous northwest-striking normal faults that are oblique to, but do not cross, the Minto fault have been mapped within the Nenana basin (Doyon Limited, 2015) (Figure 2-2). For the sake of simplicity, we do not show these secondary normal faults in our potential field model; however, we do acknowledge their presence in the context of basin formation processes. It is likely that the northern depocenter experiences rapid subsidence along the northeastern segment of the Minto fault and secondary extension occurs along the normal faults that are highly oblique to the main Minto fault trace, further controlling the basin geometry in this region. The Nenana basin gradually deepens from south to north over a distance of 60 km, after which it reaches the maximum depth 7 km to the north of the Nunivak #1 well site (Transects T3 and T4, Figure 2-8c,d). Our potential field model shows that the southern depression of the Nenana basin, hereafter referred as the

"southern depocenter" (Transects T1, T2 and T3, Figure 2-8a,b,c), is bounded to its southeastern margin by a fairly steep northwest-dipping Minto fault, consistent with the previously published models of the Nenana basin (Barnes, 1961; Kirschner, 1994; Van Kooten et al., 2012, Doyon Limited, 2015).

The smooth, fairly uniform gradients of the gravity and magnetic anomalies observed along the eastern margin of the Nenana basin between Transects T2 and T3 (Figure 2-8b,c) suggest that no significant lateral rock density and magnetic susceptibility contrast exists across the Minto fault. These smooth curvilinear anomaly gradients across the Minto fault support little or no dip-slip motion on the trace of the fault. This observation is consistent with a zone of weak seismicity that has been observed between 30 and 60km south-southwest of the town of Nenana (Figure 2-6, Fletcher, 2002). Within this area, the Minto fault may form a localized left-restraining step-over along which lateral and vertical displacement decreases (Figure 2-7). Alternatively, the break in the seismicity along the Minto fault can be explained by the presence of highly oblique northwest-striking faults that accommodate oblique slip on the Minto fault (Figures 2-6 and 2-7). Northwest-striking oblique faults have been documented to the west of the Minto fault, and they appear to accommodate the sinistral motion component locally (Dixit and Hanks, 2015; Doyon Limited, 2015). Tape et al. (2015) also identified northwest-striking faults (Event K, fault strike – 150^0) to the east of the Minto fault that suggests ongoing secondary extension in a region between Transects T2 and T3 (Figure 2-8b,c).

The basin shallows gradually to the southwest. The Totek Hills High is a prominent structural high in this area and is a notable feature on seismic data with the depth to basement

36

(~1 km) well-constrained at the Totek Hills #1 well site (Figures 2-7 and 2-9). This structural

high is bounded by two anomaly lows (Transects T1 and T4, Figure 2-8a,d). Our modeling

results also suggest that the northern edge of the Totek Hills block is defined by a steeply

dipping reverse fault (Figure 2-7 and Transect 4, Figure 2-8d). This is consistent with seismic

reflection data and outcrop exposures of the Usibelli Group in the hills (Wilson et al., 1998; Dixit

and Hanks, 2015).

Western Basin Margin

The western margin of the Nenana basin is characterized by a major, northeast-trending

high amplitude positive magnetic anomaly (~30 nT). We modeled this magnetic high, hereafter

called the Nenana High, as the result of a buried basement high that plunges smoothly to the

southwest (Figures 2-7 and 2-8c). A relatively high gravity anomaly (10 mGal) coincides directly

with this magnetic anomaly and supports the interpretation of a basement high at a shallow depth

along the western margin of the Nenana basin. The depths to the basement computed from the

seismic reflection data and well analysis of Unocal Nenana #1 well (estimated basement depth ~

1 km) agree with our interpretation and further indicate that the basement surface gradually

shallows up over the western flank of the Nenana basin.

On the west side and parallel to this northeast-trending Nenana High is a low amplitude (-

30 nT) magnetic anomaly (Figure 2-3). This magnetic low is roughly coincident with a structural

low that is evident in the seismic reflection data collected across the area (Figure 2-7). Thickness

estimates for the sedimentary sequences, calculated from the seismic data, amount to as much as

1800 m within this structural low, here after called the "southwestern Nenana sub-basin" (Figure

2-9). A gravity low (~ - 18 mGal) observed over this area further supports interpretation of a localized depocenter filled with the low-density sedimentary rocks (Figures 2-8b,c and 2-9).

In addition, the recently published structural map for the Nenana basin by Doyon Limited (2015) shows a structural low between the Transects T6 and T7 (Figure 2-8f,g) with depths of up to 3.5 km. The depression bounds the Nenana High to the northwest. Our potential field models do not directly constrain this "northwestern Nenana sub-basin" (Figure 2-9); however, we note that the existence of this sub-basin indicates an opening of the Nenana basin along the Kantishna River in the north and provides structural constraints on the basin-forming processes along the western margin of the Nenana basin.

Intrusive Rock Bodies

Intrusive bodies with high densities and magnetic susceptibilities were modeled to resolve short wavelength magnetic highs observed at the western margin, central part and along the eastern margin of the Nenana basin (Figure 2-8). Late Cretaceous and Tertiary intrusions ranging in size from small plutons to batholiths are exposed throughout the Yukon-Tanana Upland and are thought to be present in the subsurface throughout the Yukon-Tanana terrane in the southeastern part of the Fairbanks Quadrangle (Foster and Keith, 1994). The potential field data shows isolated circular and belt-like short-wavelength, low to moderately high amplitude gravity and magnetic anomalies in the study area. They were interpreted and modeled as intrusions. The compositions of these intrusive rocks are between mafic to felsic (Hansen and Dusel-Bacon, 1998; Nokleberg and Richter, 2007). The magnetic susceptibility of Cretaceous granites such as the Walker Fork pluton exposed in the Yukon-Tanana Upland ranges from 0.003

to 0.030 SI (Werdon et al., 2001); a magnetic susceptibility of 0.005-0.009 SI and bulk density of 2.75-2.9 g/cm^3 were used to model potential intrusive rocks in our study area. Misfits observed between the calculated and observed magnetic anomalies over the modeled source bodies in the Nenana basin area could be related to heterogeneous compositions of intrusive rocks and surrounding basement assemblage and/or uncertainties associated with the rock geometries, and lack of magnetic data as these younger rocks may still preserve remanence.

Tanana Basin

In contrast to the Nenana basin, the potential field data for Tanana basin is consistent with a broad and shallow basin (Figures 2-8 and 2-9). The depth-to-basement inferred from our potential field analysis suggests that the sedimentary cover of the Tanana basin thickens from ~900 m along the northern margin of the basin against the Yukon-Tanana Upland to ~1.5 km in the south, immediately north of the Northern Foothills fold-and-thrust belt.

Our integrated potential field models have identified three distinct geologic provinces within the Tanana Basin: the Northern Foothills fold-and-thrust belt province in the south (Domain II), the central Tanana Lowland and the southern margin of the Yukon-Tanana Upland in the north (Domain I) (Figure 2-5). A depth to basement map is shown in Figure 2-9.

Northern Foothills Fold-and-Thrust Belt Province/Southern Tanana basin

The Northern Foothills fold-and-thrust belt province extends northward from the northern limit of the foothills on the north side of the Alaska Range into the southern Tanana Lowland. Based on observed gravity and magnetic anomaly signatures for the area, we modeled two

principle rock units: 1) the Tertiary sedimentary sequences of the Tanana basin with low densities and low magnetic susceptibilities that are interpreted to be the source of gravity and magnetic anomaly lows; and 2) dense to very dense Precambrian Yukon-Tanana schists with metamorphic grades varying locally between greenschist and amphibolite facies, and younger greenschist facies Paleozoic rocks such as the Totatlanika Schist that are interpreted to be the source of prominent magnetic and gravity anomalies (Table 2-1). The magnetic anomaly pattern over the northern foothills of the Alaska Range shows a broad east-west-trending, low amplitude negative anomaly (up to 25 nT). This pattern is roughly parallel to the fold axes in the foothills (Figures 2-3 and 2-8). Our preferred interpretation for this magnetic low are the contrasting properties posed by a thick cover of weakly magnetic Neogene sediments (up to ~2 km thick) that are well exposed on the northern flank of the central Alaska Range (Bemis, 2004). We tested this hypothesis by assigning an average density of 2.24 g/cm^3 and magnetic susceptibility averaging 0.00015 SI to the Neogene sedimentary sequences and basement rocks to values of 2.67 g/cm^3 and 0.0005 SI respectively, up to a depth of 7.5 km. The resulting potential field models provided the best fit to the observed anomaly data as expected (Figure 2-8).

Further to the east, a prominent magnetic high (~60nT) that extends across the Japan Hills has been interpreted in our potential field models as a positive anomaly produced by the exposed Totatlanika Schist (Andreasen et al., 1964) (Figure 2-2). These authors suggested that the Pliocene Nenana Gravel in this area was possibly eroded away or pinched out along the crest of the Japan Hills and was too thin to produce measurable positive magnetic anomalies at this site.

Ridgway et al. (2007) suggested that the southern part of the Tanana basin is actively deforming due to flexural subsidence related to northward propagation of the Neogene Northern Foothills fold-and-thrust belt of the central Alaska Range. In this interpretation, the Pliocene Nenana gravel was deposited in a proximal foredeep along the northern edge of the thrust front. We used this interpretation to model the east-west-trending negative amplitude (~ 30 nT) magnetic anomaly observed north of the thrust front (Figures 2-3 and 2-9). Our potential field models for this area show that the depth to the basement of the Tanana foredeep increases to the south, and suggests Neogene sediments reach a maximum thickness of ~1.5 km in the deepest part of the basin (Figure 2-9).

Central Tanana Lowland

The central Tanana Lowland is modeled to accommodate a prominent northeast-trending belt of significantly high amplitude magnetic anomalies (~500 nT) that cross the lowland south of the Wood River Buttes and Clear Creek Butte (Figure 2-3). The source of these intense magnetic anomalies corresponds to mafic and ultramafic rocks exposed in the vicinity of the Wood River Buttes (Frost et al., 2002) (Figure 2-2). These rocks are composed mainly of diorite and serpentinized peridotite and are interpreted as an ophiolite included in Seventymile terrane in central Alaska (Péwé et al., 1966; Dusel-Bacon and Harris, 2003). The anomaly can be modeled as a shallow (maximum 3 km deep) serpentinized body with a thickness of 1600 m and extending as far as 15 km southward of the Wood River Buttes (Transects T5 and T8 in Figure 2-8). The limited size of the magnetic anomalies indicates that the anomalous rocks are discontinuous.

According to Frost et al. (2002), the exposed rocks at Clear Creek Butte are composed of Yukon-Tanana schist of Precambrian age. Further to the south in the Tanana basin, the hills surrounding Blair Lakes project through the sedimentary cover. These topographic salients are also composed of Yukon-Tanana schist (Péwé et al., 1966). The magnetic lineations observed over Blair Lakes trend northward and show positive low amplitudes (~25 nT) with broad gradients (Figure 2-3). Based on a similar pattern observed at Japan Hills, we interpret that the positive magnetic anomalies observed at Blair Lakes are mainly produced by near-surface schistose basement rocks.

Northern Tanana basin

Predominantly northeast and east-trending magnetic anomalies characterize the northern part of the Tanana basin immediately south of the Yukon-Tanana Upland (Figure 2-3). A set of northeast-trending magnetic anomalies (~150 nT) that are dominant along the northwestern margin of the Tanana basin were modeled as a result of exposed high density mineralized and amphibolite facies pelitic schist of the Yukon-Tanana Upland (average density of 2.65 g/cm^3 with magnetic susceptibility of 0.0005 SI). The trends for the positive gravity anomalies observed over this area are also consistent with our interpretation of northeast-ward structural trends of high density schist that crops out in the Yukon-Tanana Upland (Wilson et al., 1998). Further to the south, in the vicinity of the town of Nenana, an anomalous negative magnetic anomaly (~60 nT) with a steep anomaly gradient that overlies the well exposed schist of the Yukon-Tanana Upland was modeled as a dike-like intrusive body with an average density of 2.77 g/cm^3 and magnetic susceptibility of 0.005 SI (Transects T7 and T8 in Figure 2-8). We interpret this body to represent mafic plutonic rocks that intruded the Yukon-Tanana Upland in

Late Cretaceous or in Early Tertiary time (Dusel-Bacon and Till, 1993). The early Tertiary igneous rocks are typically reverse polarized, causing a negative magnetic anomaly (Roe and Stone, 1993).

The northern part of the Tanana basin is generally characterized by a belt of east-to-west-trending, positive low amplitude magnetic anomalies (up to 25 nT) (Figure 2-3). These anomalies have gravity lows associated with them (up to 12 mGal), which suggests localized relatively thicker sedimentary cover in the northern part of the Tanana basin. The basement rocks composed of the Yukon-Tanana schist along the northern margin of the Tanana basin is modeled at a depth of about ~500m but shallows rapidly to the north against the uplands (Figures 2-8i and 2-9). Geomorphic studies by Lesh and Ridgway (2007) suggest that the drainage pattern of the Tanana basin exhibits northward dipping of the basement surface of the Tanana basin along its northern margin. We interpret the northern margin of the Tanana basin as a structural low bounded to the north by the topography of the Yukon-Tanana Upland.

The northern part of the Tanana basin is further characterized by a series of possibly active northeast-striking regional-scale sinistral strike-slip faults (Page et al., 1995; Frohman, 2015) in addition to previously mapped faults along the southern edge of the Yukon-Tanana Upland (Newberry et al., 1996). The interpretation of the active northeast-striking strike-slip faults (Page et al., 1995; Frohman, 2015) is solely based on the distribution of deep seismicity data and no fault traces have yet been identified in Pliocene and younger sedimentary deposits. This is likely due to dense vegetation and prolonged snow cover, sedimentary processes following snow melt, and inaccessibility of terrain. To remove ambiguities associated with

vertical displacements along fault surfaces and for the simplicity of our potential field models, we have modeled these northeast-striking faults as vertical to steeply dipping pure strike-slip structures (Newberry et al., 1996) that extend throughout the upper crust (Transects T6 to T9, Figure 2-8).

2.6 Implications of Joint Modeling for Crustal Scale Evolution of Tanana and Nenana Basins

2.6.1 Tanana Basin

Various tectonic models have been proposed for the formation and evolution of the Tanana basin based on outcrop mapping, seismicity and geodetic studies. Page et al. (1995) first suggested that the basement underlying the Tanana basin was actively deforming by a series of northeast-striking left-lateral faults, with motion on these faults accommodating clockwise rotation of crustal blocks in a dextral shear zone of the Denali and Tintina fault systems. Their hypothesis was based on the kinematics of faults inferred from seismic and paleomagnetic data. They further postulated that these left-lateral faults offset the thrust front of the Alaska Range and proposed about 15^0 clockwise rotation of the fault blocks relative to the strike of the Denali fault by calculating the amount of offsets observed at the thrust front in east-central Alaska. This model does not explicitly propose a mechanism for the formation of the Tanana basin itself.

The presence of east-trending contractional structures in the southern Tanana basin has been recognized only recently (Ratchkovski and Hansen, 2002; Bemis and Wallace, 2007; Lesh and Ridgway, 2007; Ridgway et al., 2007). Ridgway et al. (2007) incorporated these observations into a model of the modern-day Tanana basin as a northward-migrating foreland-basin related to the northern Alaska Range thrust belt. However, this model does not account for

the observed left-lateral strike slip motion on the northeast-trending faults in the northern Tanana basin.

Based on joint modeling, the Tanana basin can be divided into two distinct domains with different basement characteristics. Domain I comprises the northern Tanana basin and is underlain by northwest-striking active faults; Domain II is composed of the southern Tanana basin and the leading edge of the northern Alaska Range fold-and-thrust belt. The boundary between the two domains is the Tanana High. We propose several alternative models that explain the character of these domains and their interaction. These proposed models do not contradict but rather complement the previously published tectonic models of the Tanana basin by Page et al. (1995) and Ridgway et al. (2007).

Our models include: (1) crustal-scale chevron-style folding within a pure shear zone; (2) foreland-related deformation and development of a flexural forebulge along the Tanana High; or, (3) crustal-scale dextral shear deformation with differential block rotation and development of structural highs in the areas of overlap. Each of these models is discussed in more detail below.

Initial Configuration

Based on the available structural, geochemical and seismicity data, Wallace and Ruppert (2012) restored the Late Cretaceous average strike direction of north-northeast-striking and northeast-striking left lateral faults in the Fairbanks area to approximately $N13^0E$ (Figure 2-10). We use this orientation as our starting configuration in all of our models.

There is not much geological or geophysical evidence for Quaternary slip along the Tintina fault that bounds the Yukon-Tanana Upland in the north. Active seismicity decreases and dies out across the Yukon-Tanana Upland north of Fairbanks (Plafker and Berg, 1994; Ruppert et al., 2008). Consequently, we model the Yukon-Tanana Upland as a rigid backstop to the deforming region of the Tanana basin in the south.

Model 1--Chevron Fold Deformation, Initiated by Crustal Shortening

This model explains the development of a basement high in the central Tanana basin as crustal-scale chevron folding around a vertical fold axis (Figure 2-11). In this model, the hinge of the fold coincides with the Tanana High, with folding accommodated by flexural slip on the northeast-trending left-lateral strike slip faults in Domain I and northwest-trending right-lateral strike slip faults in Domain II. Horizontal strain is accommodated by shortening and uplift in the hinge region of the orocline while strain in the limb regions is accommodated by flexural slip between rotating crustal blocks (De Sitter, 1958; Ramsay, 1967). In this model, the faults/flexural slip planes in Domain I are pinned against a rigid backstop. Shortening will cause clockwise rotation in the northern limbs, counterclockwise rotation in the southern limbs in Domain II and overlap zones along the fold hinge (Tanana High). Key consequences of this model are:

1. the northern and southern limbs rotate in opposite directions;

2. the northern limb and southern limb rotate relative to the Yukon-Tanana Upland at different velocities (V_1 and V_2);

3. A large extensional gap occurs at the western edge of the southern limb (Domain II) as a result of an increased rotation rate relative to the northern limb.

In this model, the northeast-striking left lateral faults of Domain I correspond to those defined by active seismicity. The presence of right lateral, northwest striking faults in basement underlying Domain II is not well documented, but northwest-striking right-lateral faults have been mapped in the northern foothills of the Alaska Range (Bemis et al., 2012).

Model 2--Foreland Basin Related to Loading by the Alaska Range Fold-and-Thrust Belt

This model expands on the model proposed by Ridgeway et al. (2002; 2007), but incorporates the northeast striking faults observed in Domain I. In this model, the southern part of the basin (Domain II, Figure 2-12) is the leading edge of the thick-skinned fold and thrust belt of the Alaska Range that is encroaching on and deforming the proximal foreland basin sediments. In this model, the Tanana High may be either the forebulge of the foreland basin (DeCelles and Giles, 1996) or, alternatively, may be a high related to an underlying blind thrust at the leading edge of the northern Alaska Range fold-and-thrust belt.

In this model, north-south directed shortening in Domain II causes contemporaneous left-lateral strike-slip displacements on the northeast-striking fault systems of Domain I. These results in clockwise rotation of fault blocks in Domain I around a pole of rotation located at the Yukon-Tanana Upland in the north.

Model 3: Dextral Shear Between the Denali and Tintina Faults

This model builds upon the model proposed by Page et al. (1995). They postulated that the clockwise rotation of basement blocks underlying the Tanana basin in a dextral shear zone

between the Denali and Tintina faults, was driven by north-northwestward compression resulting from the Pacific-North American plate convergence in the south. Their hypothesis, however, provides no explanation for the Tanana High and also requires significant right-lateral slip on the Tintina fault, which is not evident in the geologic and geophysical data collected for this region (Plafker and Berg, 1994; Trop et al., 2004; Ruppert et al., 2008).

In our modified version of Page et al.'s (1995) model (Figure 2-13) we suggest that the strain partitioning within the dextral shear zone between the Denali and Tintina faults is not regionally homogenous but is subdivided between Domain I and II, with the Tanana High acting as a structural break or crustal discontinuity between the two. Due to the limited amount of observed motion on the Tintina Fault, the Yukon-Tanana Upland is considered to be a rigid backstop.

In this model, crustal blocks in Domain I rotate clockwise about a vertical axis located in the Yukon-Tanana Upland in the north. This rotation is accommodated by left-lateral strike slip motion on northwest-trending faults. This interpretation is supported by Wallace and Ruppert (2012), who concluded that the faults in Domain I have experienced about 27^0 regional clockwise rotation since the Late Cretaceous to their present-day position of N40^{0}E.

To the south of the Tanana High, similarly oriented left-lateral strike-slip faults are proposed for Domain II. In this model, ongoing dextral slip on the Denali Fault (Fletcher 2002; Biggs et al., 2007) results in left-lateral slip along these faults and counterclockwise rotation of the intervening crustal blocks, but to a lesser amount than that seen in Domain I. Differential

rotation of Domain I and II has resulted in local shortening and uplift along their boundary and formation of the Tanana High.

All three of the proposed models provide an explanation for the present-day geometry of the Tanana basin; the presence of an intra-basin basement high along the basin axis; and a zone of left-lateral strike-slip faults in the north. Discriminating between the three models requires more information on the presence or absence of significant strike slip faults in the southern part of the basin as well as the geometry and character of structures that are causing the Tanana High.

2.6.2 Nenana Basin

To date, only a few studies have interpreted the structure of the Nenana basin. A thick sedimentary, basin-like structure for the Nenana basin was first recognized by Barnes (1961) during U.S. Geological Survey's petroleum investigations in the Minto Flats region of Alaska. Kirschner in 1994, further modeled the gravity gradients across the Minto Flats and proposed that the Nenana basin was an extensional half-graben or graben complex associated with high-angle normal faulting. However, in the absence of fault exposures at the surface and subsurface geophysical data, no definite evidence for an extensional half-graben-related development of the Nenana basin had been found at that time. Only in the course of the regional hydrocarbon exploration project led by Doyon Limited since 2009 have new seismic and potential field data been acquired that provide insight into the subsurface structure of the basin. In their interpretation of the structural and geohistory models of the Nenana basin, the basin is asymmetrical, with a relatively gently sloping northwestern flank and a steeper southeast margin that is actively subsiding (Van Kooten et al., 2012). In 2015, Doyon Limited published the first structural map at the top of the Healy Creek formation for the Nenana basin using seismic

reflection data. Their structural mapping shows a northeast-trending half-graben complex that is bound to the east by a regional northwest-dipping, northeast-striking normal fault.

Recent crustal seismicity studies of interior Alaska have shown that the Nenana basin contains major seismically active northeast-trending left-lateral strike-slip fault zones (Ratchkovski and Hansen, 2002; Ruppert et al., 2008; Tape et al., 2013). Tape et al. (2015) used this seismological evidence to suggest that the formation of the Nenana basin can be described as a transtensional pull-apart basin that is situated between two basin-bounding active left-lateral faults within the Minto Flats fault zone (MFFZ).

Nenana Basin: Extensional Graben versus Strike-Slip Pull-Apart System

There is clear distinction in the datasets used to develop the "extensional half-graben" model proposed in the previous studies (Barnes, 1961; Kirschner, 1994; Van Kooten et al., 2012, Doyon Limited, 2015) and the "transtensional strike-slip" model proposed by Tape et al. (2015).

1. "Extensional half-graben" model by Van Kooten et al. (2012) and Doyon Limited (2015) is established as the result of shallow seismic reflection interpretations that show actual basin-forming extensional structures in more detail locally and at shallow crustal depths of up to 8 km. In this model, the Minto fault is interpreted as a northwest-dipping, extensional normal fault that forms an asymmetric half-graben along the eastern margin of the Nenana basin. Recent geomorphic evidence presented by Frohman (2015) suggests significant vertical displacement along the Minto fault in this area and further, supports the idea that the Nenana basin is undergoing active extensional deformation at the east margin. In contrast to the normal faulting, Tape et al. (2015) used deep seismicity data to

interpret Minto fault as a sinistral, pure strike-slip fault that extends throughout the upper crust at depths between 10 km and 30 km. Their interpretation of left-lateral strike-slip displacement along the Minto fault is further supported by the identification of shear fractures along the east margin of the Nenana basin by Rizzo (2015).

In this sense, although the formation of the Nenana basin is dominated by extensional rifting at a local scale and at a shallow crustal depth, these extensional structures are overprinted by strike-slip faulting at a regional scale and at a deeper depth. We suggest that pure strike-slip motion along the Minto fault occurs only at a deeper crustal level, whereas the fault at higher structural levels generally involves oblique-extensional motion.

2. One of the most noteworthy features of the "extensional half-graben" mapped by Doyon Limited (2015) is the existence of asymmetric dual depocenters that are separated by an intra-basin horst structure. In contrast, the "transtensional strike-slip" model presented by Tape et al. (2015), considers a pull-apart depression dominated by a single depocenter. Recognition of dual depocenters in the basin therefore suggests that a simple transtensional strike-slip model alone cannot explain the formation of the Nenana basin. Recent studies of pull-apart basins show that dual depocenters are the most prominent features of asymmetric strike-slip pull apart systems (Katzman et al., 1995; Sims et al., 1999; Dooley et al., 2007; Wu et al., 2009). Their sandbox modeling efforts show that the dual depocenters can develop in both transtensional as well as pure strike-slip pull-apart basins between two basin-bounding master faults.

It is possible that the dual depocenter geometry observed in the Nenana basin is influenced by either the transtensional or pure strike-slip displacement along the master basin-bounding strike-slip faults (Minto Faults and Fault 2) that extend into deeper crustal levels of the Nenana basin.

3. Seismic reflection profiles interpreted by Doyon Limited (2015) display a series of northwest-striking normal faults that cut across the Nenana basin and terminate against master basin-bounding northeast-striking faults. Despite their existence, their role in basin formation processes remains poorly understood in both the "extensional half-graben" and the "transtensional strike-slip" models proposed by the previous authors. In more recent seismic interpretations, Dixit and Hanks (2015) have identified northwest-striking faults as transverse faults in the southern part of the Nenana basin. Their interpretation of transverse faulting is further supported by the fault kinematic study performed by Rizzo (2015), indicating a combined dip-slip and strike-slip motion along these northwest-striking transverse faults bounding the southern depocenter of the basin.

   In the present-day setting, the northwest-striking intrabasinal transverse faults could possibly accommodate the ongoing oblique-extensional motion along the main northeast-striking strike-slip faults in the basin. Thus, it is likely that much of the basin subsidence and basin growth is accommodated along the northwest-striking intrabasinal transverse and normal faults, allowing the depocenters to develop in the basin.

4. In the "transtensional strike-slip" model, Tape et al. (2015) have further mapped a few major northeast-striking pure strike-slip faults that define the western margin of the Nenana basin (subregions N, W and SW of Tape et al., 2015). In contrast, the

52

"extensional half-graben" complex presented by Doyon Limited (2015) suggests that these northeast-striking faults show pure dip-slip motion within Tertiary deposits of the Nenana basin at depths up to 8 km. However, recent seismic interpretations of major northeast-striking faults along the western margin of the Nenana basin by Dixit and Hanks (2015) define components of both strike-slip and dip-slip movement along these northeast-striking faults. We prefer the later model of oblique-extensional faulting based on the available seismicity, GPS velocities and fault kinematics data (Ruppert et al., 2008; Rizzo, 2015).

It is possible that the oblique-extension observed within a fault system at a shallow crustal depth could be a result of localized extension along a shallow crustal detachment layer (Bertotti et al., 2000) and the obliquity of basin-bounding crustal fault segments to north-northwest-directed regional compression (Ratchkovski and Hansen, 2002).

Our study yields a subsurface image of the Nenana basin basement surface in its present-day tectonic setting (Figure 2-9). In order to explain this current geometry, we combine our potential field models with previously published geophysical and geological data from the Nenana basin and examine two possible models for the formation and evolution of the Nenana basin: 1) transtensional pull-apart model and 2) pure strike-slip pull-apart model. Our models complement the models proposed in the previous basin studies and provide alternate hypotheses regarding how basin-forming extensional structures interact in a strike-slip regime in the Nenana basin.

Transtensional Pull-Apart Basin

This model builds upon a model proposed by Dixit and Hanks (2015). In this model, the Nenana basin initiated during Paleocene time as a single depression within an extensional half-graben system (Figure 2-14a). This is supported by the asymmetry of the basin and early basin fill (Van Kooten et al., 2012). This half-graben structure was subsequently modified by later left-lateral strike-slip faulting in a transtensional stress regime since the late Miocene (See Dixit and Hanks, 2015) (Figure 2-14b).

As transtension initiated, the basin started opening and deforming along a step over zone between the left-lateral strike-slip faults (in this case, Minto fault and Fault 2). As the transtensional deformation continued, a cross-basin strike-slip fault formed connecting left-lateral master faults. The intra-basin high developed across this cross-basin strike-slip fault above the center of the basin, further dividing the basin in dual opposing depocenters (northern and southern Nenana depocenters). Each of the depocenters is bounded on one side by the basin-bounding major oblique extensional fault. In addition, sub-basins observed along the western margin could represent a series of incipient half-grabens that developed in response to transtensional motion (See Wu et al., 2009).

Recent GPS geodetic and seismological studies confirm that the deformation zone between the Minto fault and Fault 2 marks the eastern edge of a diffuse plate boundary between the Bering plate and North American plate (Cross and Freymueller, 2008). It is possible that these plates began to move after initial formation of the Nenana basin in Paleocene time with a transtensional component that continues to the present-day.

Pure Strike-Slip Basin

This model expands on the idea of the Nenana basin originating as a pure strike-slip basin proposed by Tape et al. (2015). In this model, the Nenana basin initiated as a single rhomb-shaped pull-apart depression between two main left-lateral strike-slip faults (Minto Fault and Fault 2; Figure 2-15a). As the basin evolved over time, an intrabasinal structural high developed along a cross-basin left-lateral strike-slip fault that linked the two main basin-bounding strike-slip faults (Figure 2-15b). This high divided the original single depocenter into two isolated sub-basins. This model is similar to the pure strike-slip pull-apart basin model proposed by Sims et al. (1999). Their pure strike-slip model for an asymmetric basin suggests that a localized zone of extension develops over a releasing bend that evolves over a basal ductile decollement.

Beaudoin (1994) proposed that the lower crust (9-20 km) beneath the Yukon-Tanana terrane is in a ductile regime and accommodates the differential movement between the upper crust and upper mantle in this region. For the Nenana basin, it is possible that the brittle rocks in the upper crust are detached along a ductile decollement in the lower crust, further influencing the tectonic deformation within the basin.

Model Comparison

Both models suggest that a deep, asymmetric pull-apart basin with dual depocenters similar to the Nenana basin can be formed in either transtensional or pure strike-slip dominated system. Both models recognize a significant component of strike-slip deformation in the Nenana basin related to the two major basin-bounding master faults.

However, based on the previous studies, we find that the "pure strike-slip" model for the Nenana basin is the more speculative of the two models. Tape et al. (2015) suggested that large-scale movement would need to be transferred to the pure strike-slip MFFZ to form a narrow, deep pull-apart structure like the Nenana basin. Such a large-scale offset along the MFFZ has not been documented. It is possible that the horizontal displacement along the main fault zone can be accommodated by either the cross-basin strike-slip fault or by the normal to oblique-slip transfer faults that connect the parallel master faults and thus decrease the observed displacement along the main faults (Cunningham and Mann, 2007). Alternatively, a large magnitude of horizontal strain along the fault zone can be accommodated by ductile deformation in the lower crust, and so there may not be apparent large-scale lateral displacement along the fault surfaces (Dauteuil and Mart, 1998). In the absence of regional kinematic data from the crustal shear zones in Interior Alaska, the role of ductile decollement in distributing strain in the lower crust remains poorly understood. In addition, the pure strike-slip basin model does not explain the presence of sub-basins observed along the western margin of the Nenana basin.

In contrast to the pure strike-slip basin model, the two phase model for the evolution of the Nenana basin explains the basin geometry and the presence of younger subbasins to the northwest without calling upon major left-lateral strike slip motion on the Minto fault. This model is supported by fault kinematics studies on the southeast basin shoulder (Rizzo, 2015) that indicate that there was early dip-slip motion on the fault followed by strike slip motion. This model is also consistent with regional geodetic studies (Cross and Freymueller, 2008) that suggest that the MFFZ is a zone of differential lateral plate motion accommodating oblique-extensional regimes across the Nenana basin in central interior Alaska.

2.7   Conclusions

Analysis of regional gravity and magnetic anomaly data, in combination with geological, seismic reflection and seismicity data, constrain the upper crustal structure of the Nenana and Tanana basin in central Alaska. Potential field modeling shows that although the Nenana basin and Tanana basin appear contiguous and are underlain by crustal rocks of similar compositions, the two basins differ significantly in crustal geometry and age. The Nenana basin is a narrower and deeper (12-15 km wide and up to 8 km deep) depression that contains sediments estimated to be as old as Paleocene age, whereas the Tanana basin is a significantly wider and shallower basin filled with sediments that probably date to Miocene and younger ages.

Three distinct structural provinces have been identified in the Tanana basin based on 1) the northern strike-slip province characterized by northeast-striking crustal-scale strike-slip faults, 2) a central province associated with strong gravity and magnetic character that is attributed to the regional basement high, the Tanana High, and 3) a southern fold-and-thrust province displaying a well-defined anomaly low associated with the deepening of basement along the northern edge of the active thrust front of the central Alaska Range. Three alternative structural models for the Tanana basin that explain these observations include: 1) crustal-scale chevron folding with the hinge region correlating with the Tanana High; 2) foreland basin with the Tanana High either a forebulge or a blind thrust;, and 3) differential dextral shear along crustal scale left lateral strike slip faults.. Although each of these models will explain the occurrence of the Tanana High, the currently available geological and geophysical evidence is not sufficient to support any single model.

The modern-day structural configuration of the Nenana basin is interpreted as an oblique-extensional pull-apart zone (Tape et al., 2015; Dixit and Hanks, 2015) that is significantly different from the compressional-type setting (Ridgway et al., 2007) preferred for the Tanana basin, further indicating two distinct zones of crustal deformation in central Alaska.

Our two proposed tectonic models feature the Nenana basin in more detail than previous studies (Van Kooten et al., 2012; Tape et al., 2015), as bounded by two well-defined, crustal-scale oblique-extensional master faults that form a pull-apart rift zone either 1) in pure strike-slip or 2) in transtensional regional settings. Our analysis, in addition to previous geodetic (Cross and Freymueller, 2008) and fault kinematic (Rizzo, 2015) studies supports the "transtensional pull-apart" model for the Nenana basin formation. However, we suggest that a comprehensive study involving, 1) a detailed quantification of fault-slip data to provide greater understanding of relative displacements and strain partitioning across the faults in the basin-scale transtensional shear zone, and 2) detailed crustal studies to investigate the effect of ductile deformation in the lower crust on the mechanics of transtensional pull-apart basin formation is required to better understand the structural development of the Nenana basin within this pull-apart setting.

2.8   References

Andreasen, G. E., Wahrhaftig, C., and Zietz, I. (1964). Aeromagnetic reconnaissance of the east-central Tanana Lowland, Alaska: U.S. Geological Survey Geophysical Investigations Map, 447, 2 sheets, scale 1:125,000.

Athey, J. E., Newberry, R. J., Werdon, M. B., Freeman, L.K., Smith, R. L., and Szumigala, D. J. (2006). Bedrock geologic map of the Liberty Bell area, Fairbanks A-4 Quadrangle, Bonnifield mining district, Alaska: Report of Investigation RI 2006-2 V 1.0.1, State of Alaska, Department of Natural Resources, Division of Geological & Geophysical Surveys (DGGS), Fairbanks, AK, USA.

Barnes, D. F. (1961). Gravity low at Minto Flats, Alaska, in U.S. Geological Survey, Geological survey research 1961, Short papers in the geologic and hydrologic sciences, Articles 293-435: U.S. Geological Survey Professional Paper, 254-257.

Beaudoin, B. C. (1994). Lower-crustal deformation during terrane dispersion along strike-slip faults, Tectonophysics, 232, 257-266.

Bemis, S. P. (2004). Neotectonic Framework of the North-Central Alaska Range Foothills, M.S. Thesis, University of Alaska Fairbanks, Fairbanks, AK, USA.

Bemis, S. P., and Wallace, W. K. (2007). Neotectonic framework of the north-central Alaska Range foothills, in K. D. Ridgway, J. M. Trop, J. M. G. Glen, and J. M. O'Neill (Eds.), Tectonic growth of a collisional continental margin: Crustal evolution of southern Alaska, Geological Society of America Special Paper, 431, 549-572.

Bemis, S. P., Carver, G. A., and Koehler, R. D. (2012). The Quaternary thrust system of the northern Alaska Range, Geosphere, 8(1), 196-205, doi: 10.1130/GES00695.1.

Bertotti, G., Podlachikov, Y. Y., and Daehler, A. (2000). Dynamic link between the level of ductile crustal flow and style of normal faulting of brittle crust, Tectonophysics, 320, 195–218, doi:10.1016/S0040-1951(00)00045-7.

Biggs, J., Wright, T., Lu, Z., and Parsons, B. (2007). Multi-interferogram method for measuring interseismic deformation: Denali Fault, Alaska, Geophysical Journal International, 170, 1165–1179, doi: 10.1111/j.1365-246X.2007.03415.

Brennan, P. R. K., Gilbert, H., and Ridgway, K. D. (2011). Crustal structure across the central Alaska Range: Anatomy of a Mesozoic collisional zone, Geochemistry, Geophysics, Geosystems, 12 (4), doi:10.1029/2011GC003519.

Brennan, P. R. K., and Ridgway, K. D. (2015). Detrital zircon record of Neogene exhumation of the central Alaska Range: A far-field upper plate response to flat-slab subduction, Geological Society of America Bulletin, doi:10.1130/B31164.1.

Cross, R. S., and Freymueller, J. T. (2008). Evidence for and implications of a Bering plate based on geodetic measurements from the Aleutians and western Alaska, Journal of Geophysical Research, 113, B07405, doi:10.1029/2007JB005136.

Cunningham, D., and Mann, P. (Eds.) (2007). Tectonics of Strike-Slip Restraining and Releasing Bends, Geological Society, London, Special Publication, 290.

Dauteuil, O., and Mart, Y. (1998). Analogue modelling of faulting pattern, ductile deformation, and vertical motion in strike-slip fault zones, Tectonics, 17, 303-310.

De Sitter, L. U. (1958). Boudins and parasitic folds in relation to cleavage and folding, Geologie en Mijnbouw, 20, 277-286.

DeCelles, G., and Giles, K. N. (1996). Foreland basin systems, Basin Research, 8, 105–123.

Dixit, N. C., and Tomsich, C. S. (2014). Apatite fission track, magnetic susceptibility, and vitrinite reflectance analyses on cuttings from the Nunivak #1 and Nenana #1 wells, Alaska Division of Geological & Geophysical Surveys Geologic Materials Center Data Report, 422, 1, doi:10.14509/27042.

Dixit, N.C., Hanks, C. L., Wallace, W. K., Ahmadi, M., and Awoleke, O. (2015). In situ stress variations at the northeastern Brooks Range and eastern North Slope of Alaska: Implications for regional changes in tectonic setting [abs], The Geological Society of America Cordilleran Section 111th Annual Meeting, Anchorage, Alaska, Paper 20-4, 11-13May, 2015.

Dixit, N. C., and Hanks, C. L. (2015). Cenozoic structural framework and tectono-sedimentary evolution of the southern Nenana basin, Alaska [abs]: Implications for conventional and unconventional hydrocarbon exploration, The American Association of Petroleum Geologists Annual Convention and Exhibition, Denver, Colorado, 3 June 2015.

Dooley, T., Monastero, F. C., and McClay, K. R. (2007). Effects of a weak crustal layer in a

transtensional pull-apart basin: results from a scaled physical modeling study [abs], Eos 88 (52),

Abstract V53F–04.

Doyon Limited (2015). Alaska onshore rift basins, Nenana and Yukon Flats,

http://doyonoil.com/Content/pdfs/NenanaBasin3DSeismic.pdf

(Accessed April 2015).

Dusel-Bacon, C., and Till, A. B. (Eds.) (1993). Geologic studies in Alaska by the U.S.

Geological Survey, U.S. Geological Survey Bulletin, 2068, 250.

Dusel-Bacon, C., and Harris, A. G. (2003). New occurrences of Late Paleozoic and Triassic

fossils from the Seventymile and Yukon-Tanana terranes, east-central Alaska, with comments on

previously published occurrences in the same area, in J. P. Galloway, studies by the U.S.

Geological Survey in Alaska, 2001, U.S. Geological Survey Professional Paper, 1678, 5-30.

Eberhart-Phillips, D., Christensen, D. H., Brocher, T. M., Hansen, R., Ruppert, N. A.,

Haeussler, P. J., and Abers, G. A. (2006). Imaging the transition from Aleutian subduction to

Yakutat collision in central Alaska, with local earthquakes and active source data, Journal of

Geophysical Research, 111, B11303, doi:10.1029/2005JB004240.

Fisher, M. A., Ratchkovski, N. A., Nokleberg, W. J., Pellerin, L., and Glen, J. M. G. (2004). Geophysical data reveal the crustal structure of the Alaska Range orogen within the aftershock zone of the Mw 7.9 Denali fault earthquake, Seismological Society of America Bulletin, 94, 107-131, doi: 10.1785/0120040613.

Fletcher, H. (2002). Crustal Deformation in Alaska Measured using the Global Positioning system, Ph.D. Thesis, University of Alaska Fairbanks, Fairbanks, Alaska, USA.

Foster, H. L., and Keith, T. E. C. (1994). Geology of the Yukon-Tanana area of east-central Alaska, in G. Plafker, and H. C. Berg, The Geology of Alaska, Geological Society of America, 205-240.

Frohman, R. A. (2015). Identification and evolution of tectonic faults in the greater Fairbanks area, Alaska, Master's Thesis, University of Alaska Fairbanks, Fairbanks, Alaska, USA.

Frost, G. M., and Stanley, R. G. (1991). Compiled geologic and Bouguer gravity map of the Nenana Basin area, central Alaska, U.S. Geological Survey Open-File Report, 91-562, 30, 2 sheets, scale 1:250,000.

Frost, G. M., Barnes, D. F., and Stanley, R. G. (2002). Geologic and isostatic gravity map of the Nenana basin area, central Alaska, U.S. Geological Survey Geologic Investigations Series Map, 2543, 16, 2 sheets, scale 1:250,000.

Fuis, G. S. (1998). West margin of North America: A synthesis of recent seismic transects, Tectonophysics, 288, 265–292.

Grantz, A., Moore, T. E., and Roeske, S. (1991). Gulf of Alaska to Arctic Ocean: Centennial Continent/Ocean Transect #15, TRA-A3, The Geological Society of America, 2 sheets.

Golder Associates (2000). Drill log for shallow boreholes along the proposed Intertie from Fairbanks to Healy, Report to Golden Valley Electrical Association.

Hanks, C., and Holdmann, G. (Eds.) (2013). Using modeling to assess CO_2 sequestration, engineering, environmental and economic issues related to a proposed coal-to-liquids plant in Interior Alaska, Prepared for the U.S. Air Force by the Geophysical Institute and the Alaska Center for Energy and Power, University of Alaska Fairbanks, 1-222.

Hansen, V. L., and Dusel-Bacon, C. (1998). Structural and kinematic evolution of the Yukon -Tanana upland tectonites, east-central Alaska: A record of late Paleozoic to crustal assembly, Geological Society of America Bulletin, 110, 211–230.

Katzman, R., ten Brink, U. S., and Lin, J. (1995). Three-dimensional modeling of pull-apart basins: Implications for the tectonics of the Dead Sea Basin, Journal of Geophysical Research, 100, 6295–6312, doi:10.1029/94JB03101.

Kirschner, C. E. (1994). Interior basins of Alaska, in G. Plafker, and H. C. Berg (Eds.), The

Geology of Alaska, Geological Society of America, The Geology of North America, G-1, 469–

493.

Koehler, R. D. (2013). Quaternary Faults and Folds (QFF), Alaska Division of Geological &

Geophysical Surveys Digital Data Series 3,

http://maps.dggs.alaska.gov/qff/. doi:10.14509/24956

Lesh, M. E., and Ridgway, K. D. (2007). Geomorphic evidence of active transpressional

deformation in the Tanana foreland basin, south -central Alaska, in K. D. Ridgway, J. M. Trop, J.

M. G. Glen, and J. M. O'Neill (Eds.), Tectonic growth of a collisional continental margin:

Crustal evolution of southern Alaska, The Geological Society of America Special Paper, 431,

573-593.

Lowrie, W. (2007). Fundamentals of Geophysics, 2nd edition, Cambridge University Press, New

York, 390.

Merritt, R. D. (1985). Coal Atlas of the Nenana Basin, Alaska, Alaska Division of Geological &

Geophysical Surveys Public-data File, 85-41, 197, scale 1: 250,000, 5 sheets.

Meyer, J. F. Jr., and Saltus, R. W. (1995). Merged aeromagnetic map of interior Alaska: U.S.

Geological Survey Geophysical Investigations Map, 1014, 2 sheets, scale 1:500,000.

Meyer, J. F. Jr. (2008). Total Intensity Magnetic Anomaly Map of the Nenana Basin, Alaska,

Division of Natural Resources Oil and Gas Conservation Commission, Sheet 4 of 4.

Newberry, R. J., Bundtzen, T. K., Clautice, K. H., Combellick, R. A., Douglas, T., Laird, G. M.,

Liss, S. A., Pinney, D. S., Reifenstuhl, R. R., and Solie, D. N. (1996). Preliminary geologic map

of the Fairbanks Mining District, Alaska, Alaska Division of Geological & Geophysical Surveys

Public Data File, 96-16, 17, sheet 1, scale 1:63,360.

Nokleberg, W. J., and Richter, D. H. (2007). Origin of narrow terranes and adjacent major

terranes occurring along the Denali fault in the Eastern and Central Alaska Range, Alaska, in

Tectonic growth of a collisional continental margin—Crustal evolution of southern Alaska,

Geological Society of America Special Paper, 431, 129–154.

Page, R. A., Biswas, N. N., Lahr, J. C., and Pulpan, H. (1995). Seismicity of continental Alaska,

in D. B. Slemmons, E. R. Engdahl, M. D. Zoback, and D. D. Blackwell (Eds.), Neotectonics of

North America: Boulder, Colorado, Geological Society of America, Decade Map Volume 1.

Page, R. A., Plafker, G., and Pulpan, H. (1995). Block rotation in east-central Alaska: a

framework for evaluating earthquake potential, Geology, 23 (7), 629-632.

Péwé, T. L., Wahrhaftig, C., and Weber, F. R. (1966). Geologic Map of the Fairbanks

quadrangle, Alaska, U.S. Geological Survey Miscellaneous Geologic Investigations Map, 455, 5,

Sheet 1, scale 1:250,000.

Plafker, G., and Berg, H. C. (1994). Review of the geology and tectonic evolution of Alaska, in G. Plafker, and H. C. Berg (Eds.), The Geology of Alaska: Boulder, Colorado, Geological Society of America, The Geology of North America, G-1, 989-1,021.

Ramsay, J. G. (1967). Folding and Fracturing of Rocks, McGraw-Hill, New York.

Rasmussen, R., and L. B. Pedersen (1979), End corrections in potential field modeling, Geophysical Prospecting, 29, 749-760.

Ratchkovski, N. A., and Hansen, R. (2002). New constraints on tectonics of Interior Alaska: earthquake locations, source mechanisms, and stress regime, Bulletin of the Seismological Society of America, 92 (3), 998-1014.

Ridgway, K. D., Thoms, E. E., Layer, P. W., Lesh, M. E., White, J. M., and Smith, S. V. (2007). Neogene transpressional foreland basin development of the north side of the central Alaska Range, Usibelli Group and Nenana Gravel, Tanana Basin, in K. D. Ridgway, and others (Eds.), Tectonics Growth of a Collisional Continental Margin—Crustal evolution of southern Alaska, Geological Society of America Special Paper, 431, 507–547.

Rizzo, A. J. (2015). Natural fracture character and distribution adjacent to the Nenana basin, central Alaska, Master's Thesis, University of Alaska Fairbanks, Fairbanks, Alaska, USA.

Roe, J. T., and Stone, D. B. (1993). Paleomagnetism of the Fairbanks basalts, Interior Alaska, in

D. N. Solie, and F. Tannian (Eds.), Short Notes on Alaskan Geology, Alaska Division of

Geological & Geophysical Surveys Professional Report, 113, 61-69. doi:10.14509/2311.

Ruppert, N. A., Ridgway, K. D., Freymueller, J. T., Cross, R. S., and Hansen, R. A. (2008).

Active tectonics of Interior Alaska - Seismicity, GPS geodesy, and local geomorphology, in J. T.

Freymueller, P. J. Haeussler, R. L. Wesson, and G. Ekström (Eds.), Active Tectonics and

Seismic Potential of Alaska: Washington, D.C., American Geophysical Union, Geophysical

Monograph, 179, 109-133.

Saltus, R. W., Connard, G. G., and Hill, P. L. (1999). Alaska aeromagnetic compilation, digital

grids and survey data, U.S. Geological Survey Open-File Report, 99-502.

Saltus, R. W., Hudson, T. L., and Wilson, F. H. (2007). The geophysical character of southern

Alaska - implications for crustal evolution, in K. D. Ridgway, J. M. Trop, J. M. G. Glen, and J.

M. O'Neill (Eds.), Tectonic Growth of a Collisional Continental Margin: Crustal Evolution of

Southern Alaska, Geological Society of America Special Paper, 431, 1-20, doi:

10.1130/2007.2431(01).

Saltus, R. W., and Blakely, R. J. (2011). Unique geologic insights from "non-unique" gravity and

magnetic interpretation, GSA Today, 21 (12), 4-10.

Simpson, R. W., Jachens, R. C., Blakely, R. J., and Saltus, R. W. (1986). A new isostatic residual gravity map of the conterminous United States with a discussion on the significance of isostatic residual anomalies, Journal of Geophysical Research, 91, 8348-8372.

Sims, D., Ferrill, D. A., and Stamatakos, J. A. (1999). Role of ductile décollement in the development of pull-apart basins: Experimental and natural examples, Journal of Structural Geology, 21, 533–554, doi: 10.1016/S0191-8141(99)00010-3.

Stanley, R. G., and Lillis, P. G. (2011). Preliminary interpretation of Rock-Eval pyrolysis and vitrinite reflectance results from the Nunivak 1 well in the Nenana basin, central Alaska (abs.), Program with Abstracts, 2011 Western Region Meeting, May 6–14, 2011, Anchorage, Alaska, Society of Petroleum Engineers and Pacific Section, American Association of Petroleum Geologists, 87–88.

Talwani, M., Worzel, J. L., and Landisman, M. (1959). Rapid Gravity Computations for two-dimensional bodies with application to the Mendocine Submarine Fracture Zone, Journal of Geophysical Research, 64, 49-61.

Talwani, M., and Heirtzler, J. R. (1964). Computation of magnetic anomalies caused by two-dimensional structures of arbitrary shape, Computers in the mineral industries, Part 1, Stanford University Publication Geological Sciences, 9, 464-480.

Tape, C. H., West, M. E., Silwal, V., and Ruppert, N. A. (2013). Earthquake nucleation and triggering on an optimally oriented fault, Earth and Planetary Science Letters, 363, 231–241.

Tape, C. H., Silwal, V., Ji, C., Keyson, L., West, M. E., and Ruppert, N. A. (2015). Transtensional tectonics of the Minto Flats fault zone and Nenana basin, central Alaska, Bulletin of the Seismological Society of America, 105 (4), 2081-2100.

Thoms, E. E. (2000). Late Cenozoic unroofing sequence and foreland basin development of the central Alaska Range: Implications from the Nenana Gravel, M.S. Thesis, 215, University of Alaska Fairbanks, Fairbanks, Fairbanks, Alaska, USA.

Tomsich, C. S., Hanks, C. L., and Coakley, B. J. (2011). Basement depth and stratigraphic thickness solutions from modelled gravity data for the Tanana and Nenana basins and implications for CO_2 sequestration (Abs.), American Association of Petroleum Geologists Pacific section meeting, Anchorage, Alaska, 90125, 8-11 May, 2011.

Trop, J. M., Ridgway, K. D., and Sweet, A. R. (2004). Stratigraphy, palynology, and provenance of the Colorado Creek basin: Oligocene transpressional tectonics along the central Denali fault system, Canadian Journal of Earth Sciences, 41, 457-480.

Van Kooten, G. K., Richter, M., and Zippi, P. A. (2012). Alaska's Interior rift basins: A new frontier for discovery, Oil and Gas Journal, 10.
http://www.doyon.com/lands/oil_gas/DoyonNenanaOGJ.pdf

Veach, N. J. (1973). Aeromagnetic map, southeastern part of Fairbanks Quadrangle, Alaska, Alaska Division of Geological & Geophysical Surveys Alaska Open-File Report 8, 5, 1 sheet, scale 1:250,000, doi:10.14509/175.

Veenstra, E., Christensen, D. H., Abers, G. A., and Ferris, A. (2006). Crustal thickness variation in south-central Alaska, Geology, 34(9), 781-784.

Wahrhaftig, C., Wolfe, J. A., Leopold, E. B., and Lanphere, M. A. (1969). The coal-bearing group in the Nenana coal field, Alaska, U.S. Geological Survey Bulletin, 1274, 1-30.

Wahrhaftig, C. (1987). The Cenozoic section at Suntrana Creek, in M. L. Hill (Eds.), Geological Society of America, Cordilleran Section, Centennial Field Guide, 1, 445–450.

Wallace, W. K., and Ruppert, N. A. (2012). Young tectonics of a complex plate boundary zone: Indentation, rotation, and escape in Alaska (Abs.), American Geophysical Union fall meeting, San Francisco, CA, T14A-08, 3 December, 2012.

Wartes, M. A., Gillis, R. J., Herriott, T. M., Stanley, R. G., Helmold, K. P., Peterson, C. S., and Benowitz, J. A. (2013). Summary of 2012 reconnaissance field studies related to the petroleum geology of the Nenana Basin, interior Alaska, Alaska Division of Geological & Geophysical Surveys Preliminary Interpretive Report 2013-2, 13, doi:10.14509/24880.

WELTS (2010). Alaska Department of Natural Resources Well Log Tracking System. www.navmapsalaska.gov/welts.

Werdon, M. B., Newberry, R. J., and Szumigala, D. J. (2001). Bedrock geologic map of the Eagle A-2 Quadrangle, Fortymile mining district, Alaska, Alaska Division of Geological & Geophysical Surveys Preliminary Interpretive Report 2001-3B, 1 sheet, scale 1:63,360. doi:10.14509/2670

Wilson, F. H., Dover, J. H., Bradley, D. C., Weber, F. R., Bundtzen, T. K., and Haeussler, P. J. (1998). Geologic map of Central (Interior) Alaska, U.S. Geological Survey Open-File Report 98-133-A, 62, 3 sheets.

Won, I. J., and Bevis, M. (1987). Computing the gravitational and magnetic anomalies due to a polygon, Algorithms and Fortran subroutines, Geophysics, 52, 232-238.

Wu, J. E., McClay, K., Whitehouse, P., and Dooley, T. (2009). 4D analogue modelling of transtensional pull-apart basins, Marine and Petroleum Geology, 26 (8), 1608-1623, doi: 10.1016/j.marpetgeo.2008.06.007.
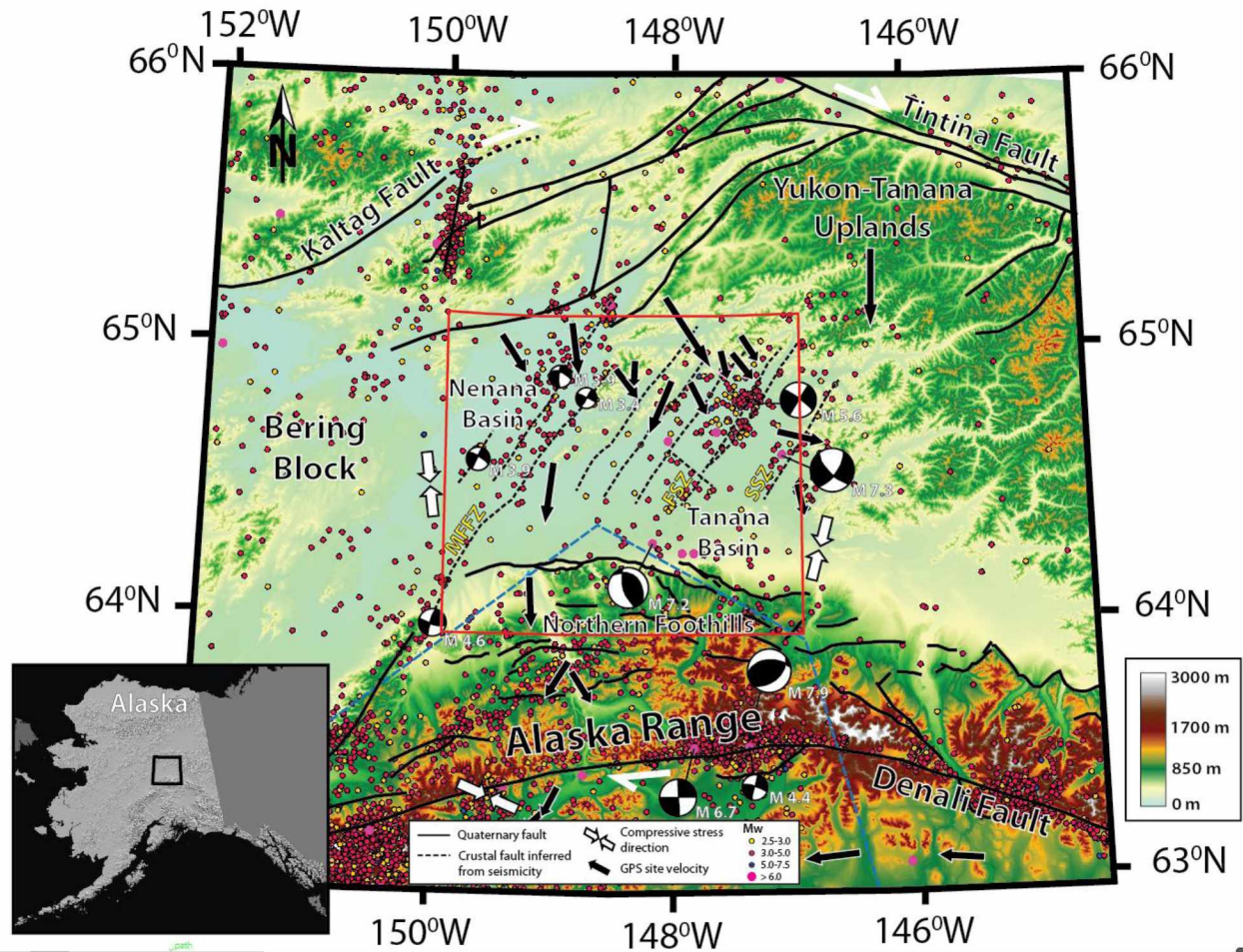
Figure 2-1 Simplified tectonic map of central Alaska

The simplified tectonic map showing the location of the study area (marked in red) relative to major active crustal structures and the distribution of major faults (Koehler, 2013) in the region. The blue dotted line marks the flat-slab region showing the subducted extent of the Yakutat microplate. Horizontal velocity vectors relative to stable North America are inferred from the GPS velocities available for the region (Fletcher, 2002). Earthquake fault place solution data is modified from Ruppert et al. (2008).
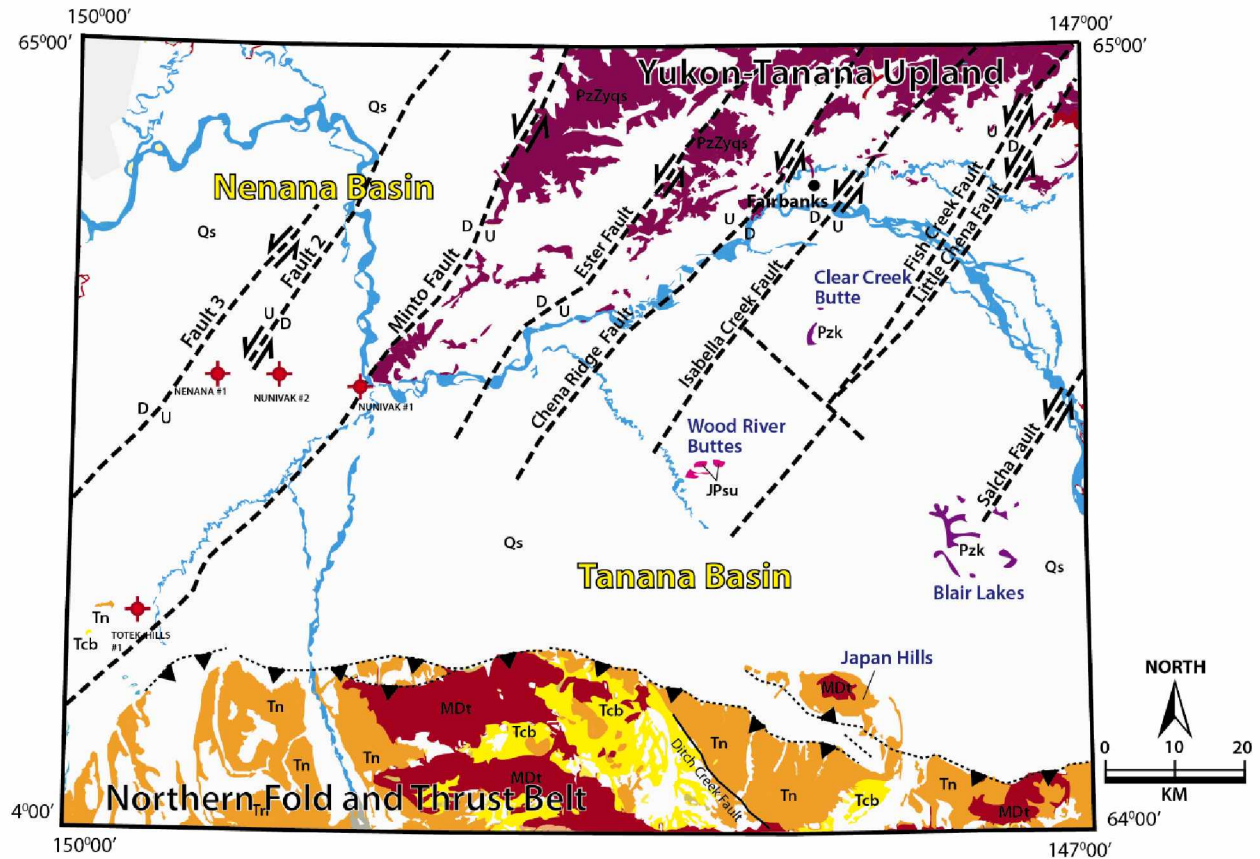
Figure 2-2 Geologic map of the central Interior Alaska

Geologic map of central Interior Alaska, showing the Cenozoic-age Nenana and Tanana basins and exposed geology, including major lithologic units and regional fault systems. Solid black lines in the Nenana basin are based on seismic data and indicate fault patterns at the top of Healy Creek Formation, (Van Kooten et al., 2012; Doyon Limited, 2015; this study); dashed black lines indicate high-angle faults observed in surface outcrops in the Fairbanks area and inferred based on active seismicity (Ruppert et al., 2008; Frohman, 2015; this study). Quaternary thrust faults (black dotted line with thrust symbols) define the northern limit of the Northern Foothills fold-and-thrust belt of the central Alaska Range (Bemis, 2004). Dashed dark blue lines indicate the locations of profiles for the geophysical models developed in this study. Geologic map modified from Wilson et al. (1998).
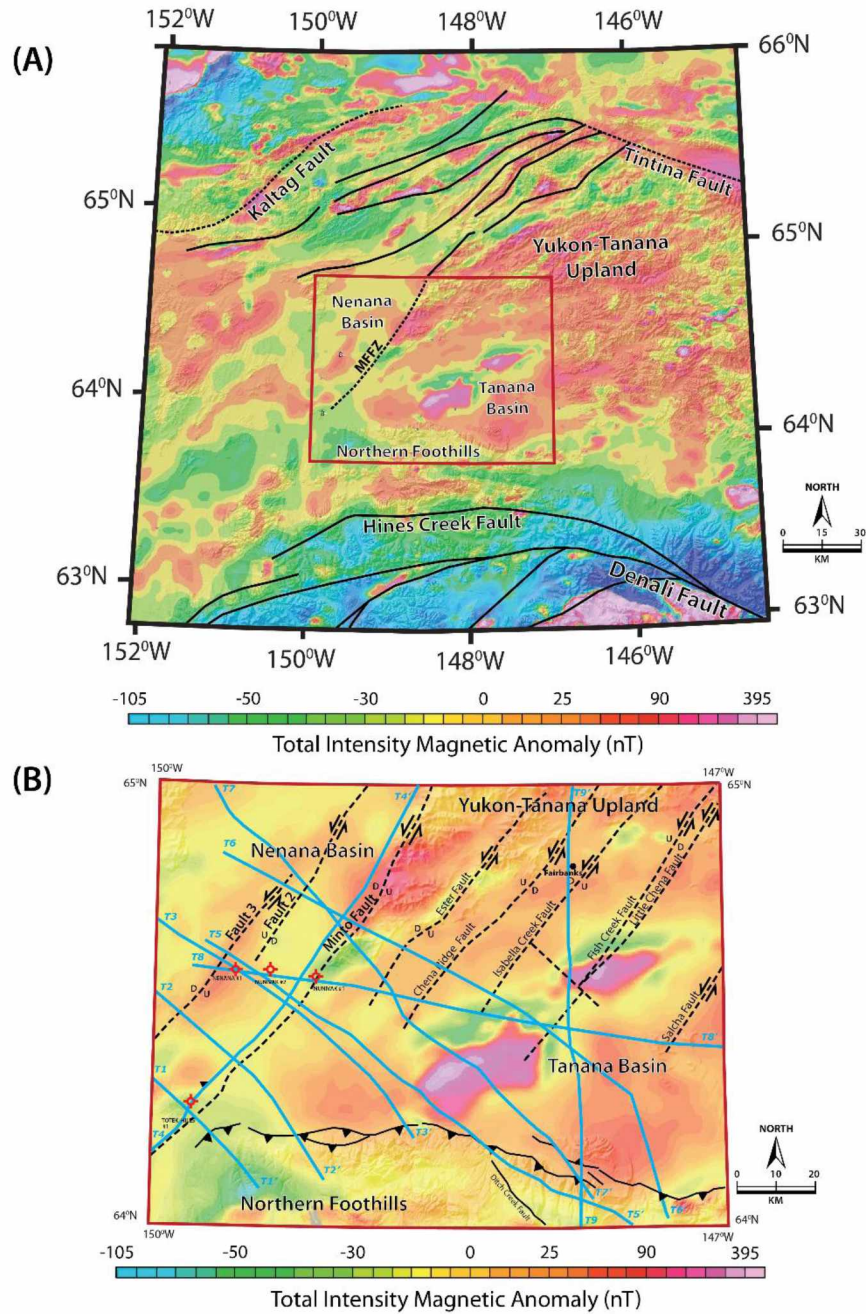
Figure 2-3 Total intensity magnetic anomaly map of the (A) central Interior Alaska and (B) Fairbanks Quadrangle

Total intensity magnetic anomaly maps showing major structural features from Figure 2

(modified from Meyer, 2008). Solid blue lines indicate the geophysical transects; red stars

represent well locations.
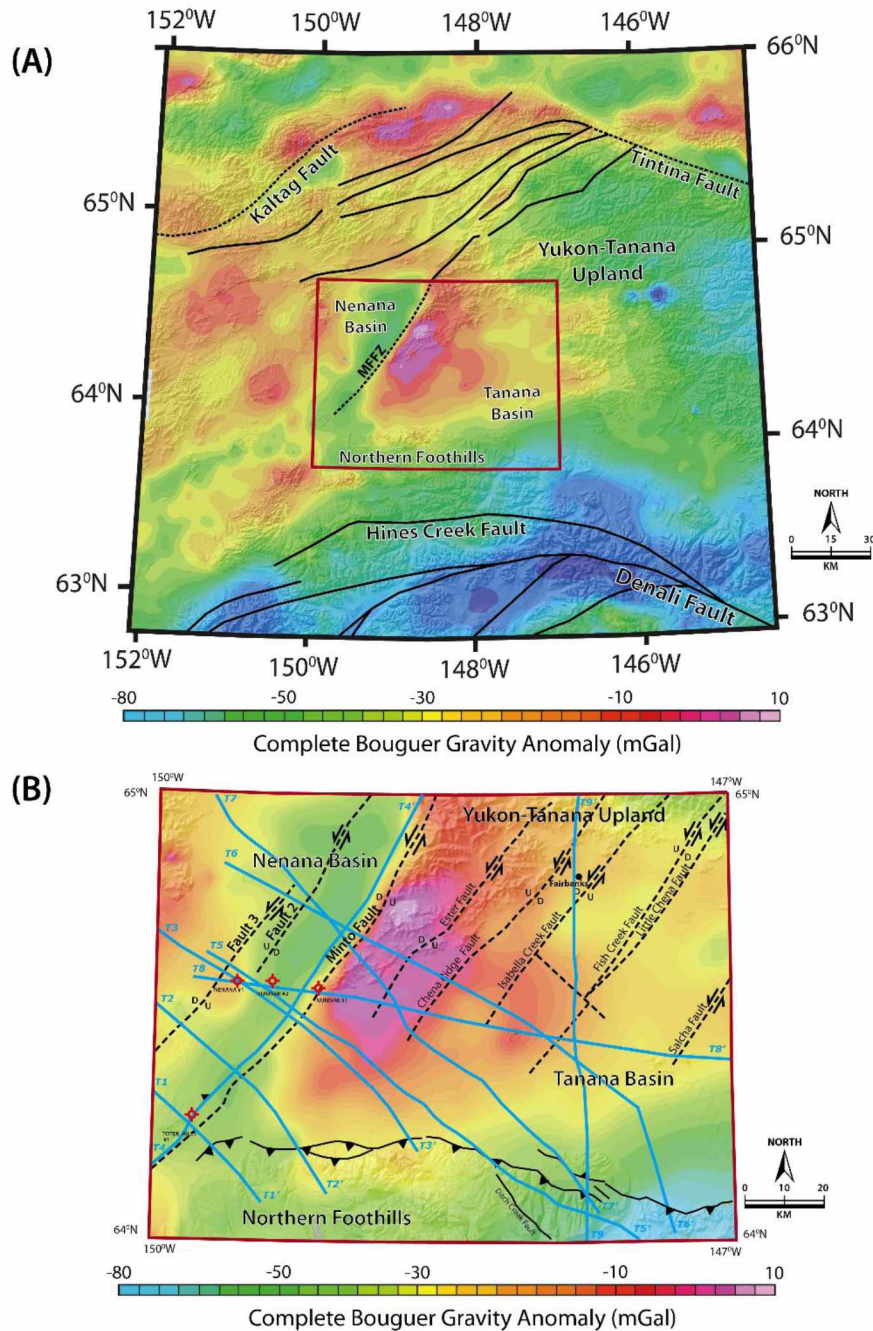
Figure 2-4 Complete Bouguer gravity anomaly of the (A) central Interior Alaska and (B) Fairbanks Quadrangle

Complete Bouguer gravity anomaly maps showing major structural features from Figure 2 (modified from Meyer, 2008). Solid blue lines indicate the geophysical transects; red stars represent well locations.
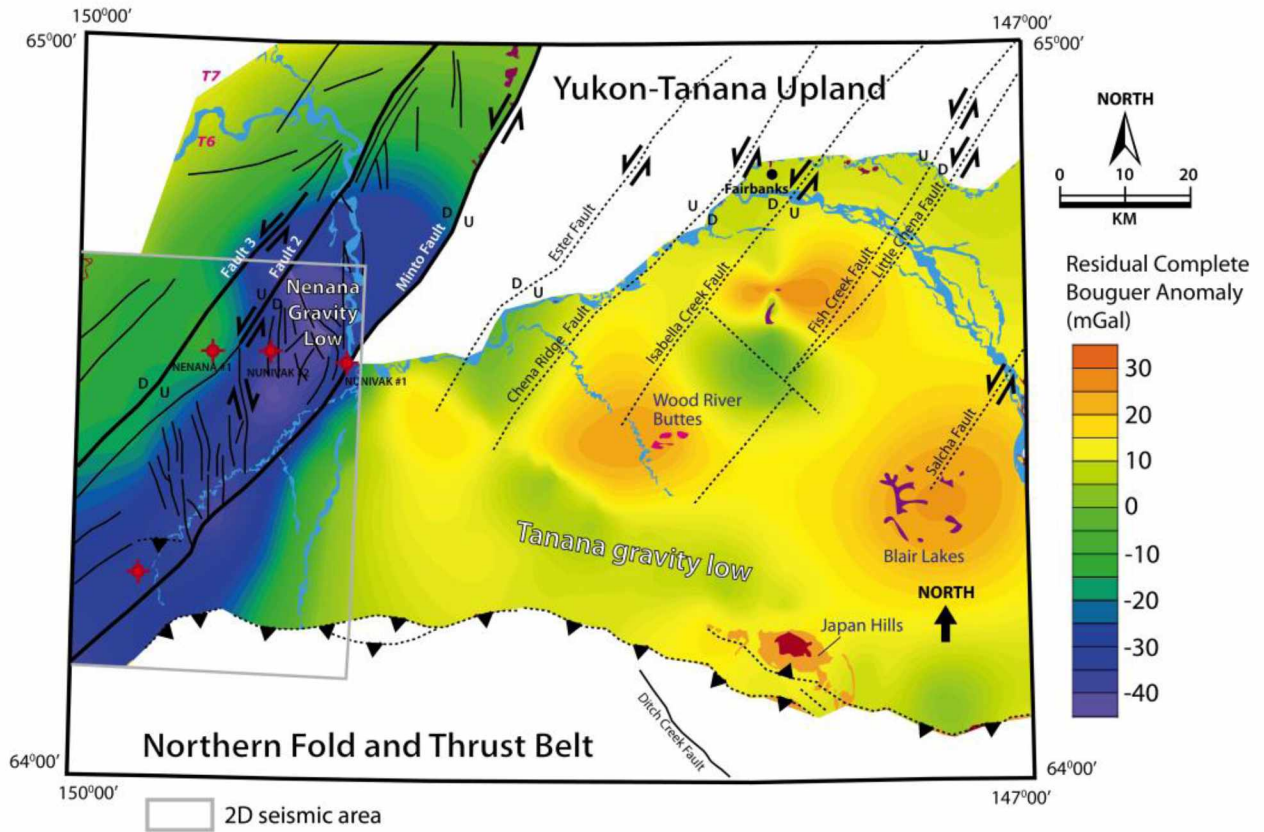
Figure 2-5 Residual complete Bouguer gravity anomaly map

Calculated residual complete Bouguer gravity anomaly map of the study area. The anomaly was

calculated by isolating long wavelength anomalies. Resulting short-wavelength anomalies

reflect sources at a shallow subsurface level. In general, positive gravity anomalies are associated

with near-surface metamorphic basement and intrusive igneous rocks; gravity lows are

associated with low-density sedimentary rocks and unconsolidated sediments.
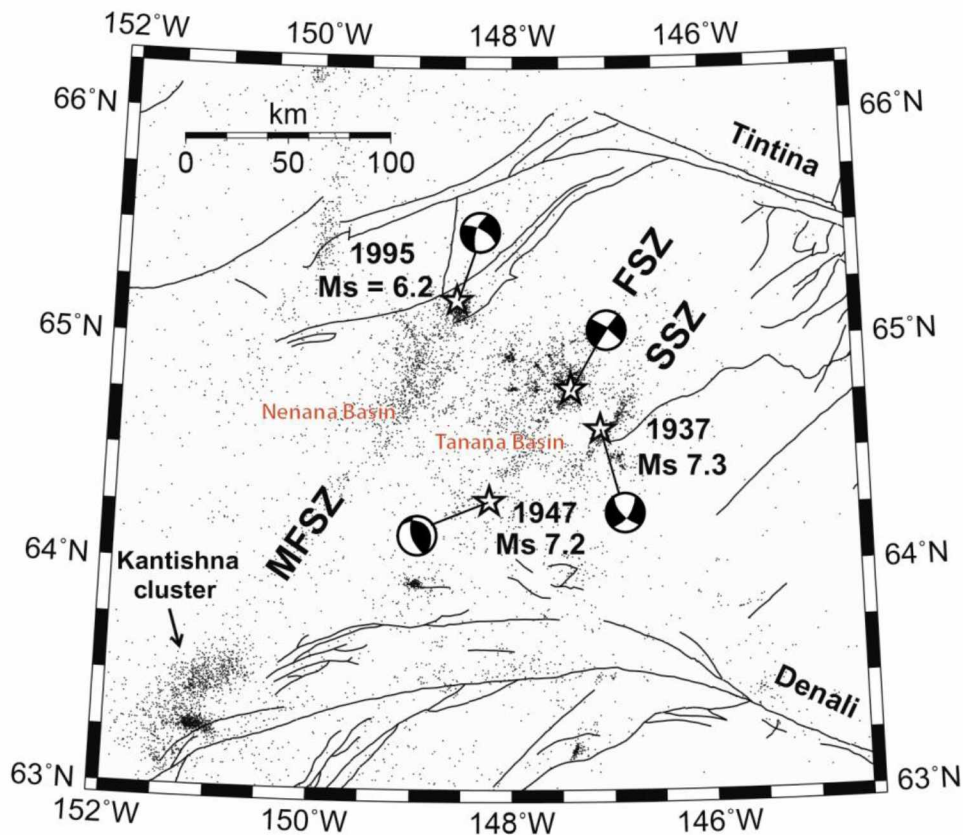
Figure 2-6 Earthquake density map showing distribution of earthquakes (1990-1996)

Major active regional seismic trends include: (1) east-trending, pure right-lateral strike-slip of the Denali fault system (2) east-trending, pure right-lateral strike-slip of the Tintina-Kaltag fault system; (3) three north northeast-trending left-lateral strike-slip seismic zones between the Tintina-Kaltag fault system in the north and Denali fault-system in the south--the Minto Flats Seismic Zone (MFSZ) , the Fairbanks Seismic Zone (FSZ) and the Salcha Seismic Zone (SSZ); and (4) a zone of east-trending thrust faults on the northern and western side of the central Alaska Range,. Earthquakes with magnitudes of 7 and greater are shown by stars. Map modified from Fletcher, 2002, with additional fault-plane solution data from Page et al. (1995). All these shallow earthquakes likely represent the strain distribution along the crustal structures in response to a regional, north to northwest-directed shortening resulting from the plate collision in the south (Eberhart et al., 2006).
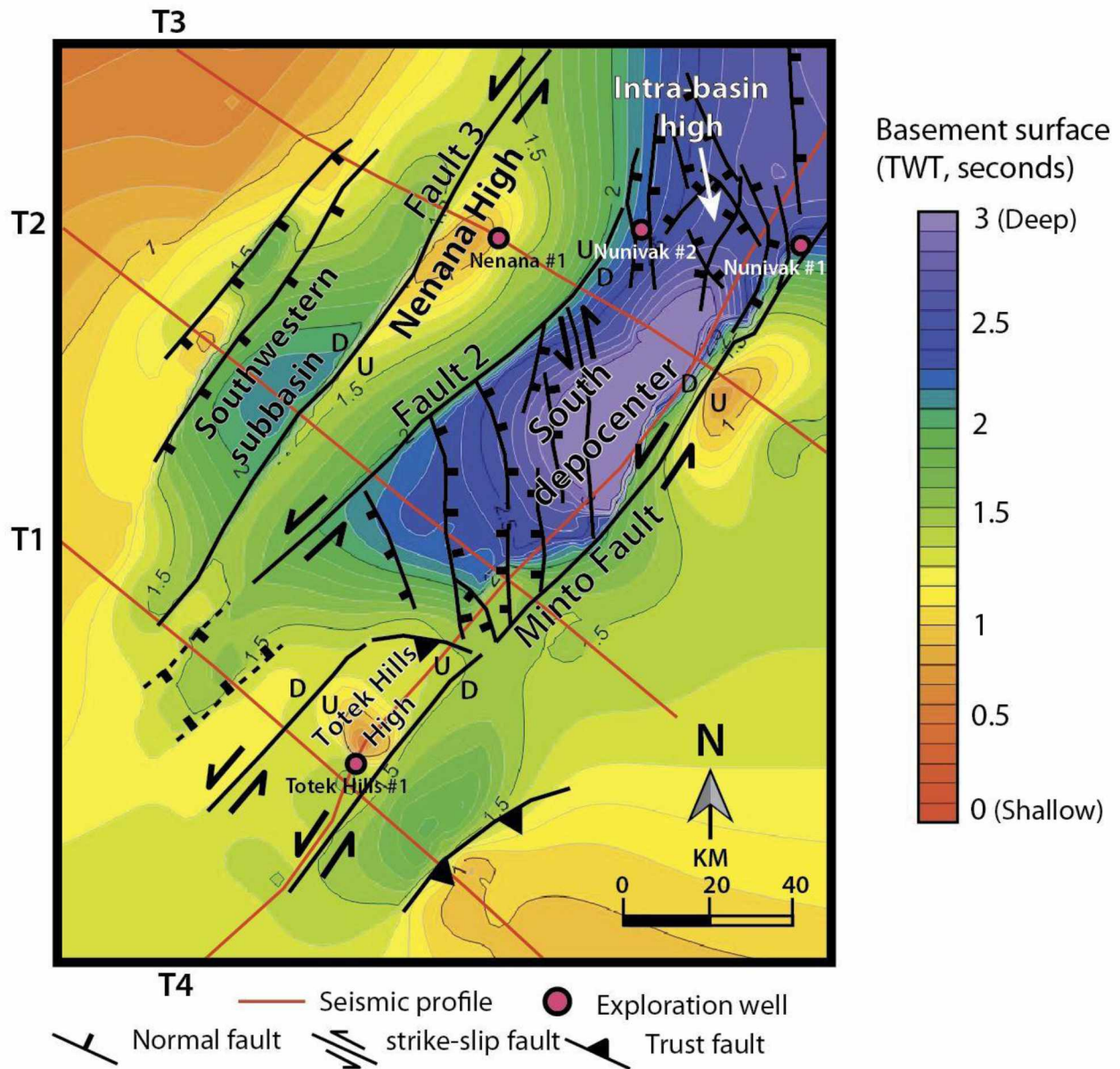
Figure 2-7 Top of basement depth map for the southern Nenana basin

Top of basement map for the southern Nenana Basin showing the distribution of faults and major

structural features discussed in text. Map is in two-way travel time and based on the

interpretation of 2D seismic profiles (white lines) and published structural data by Dixit and

Hanks (2015) and Doyon Limited (2015). Well locations shown in red.
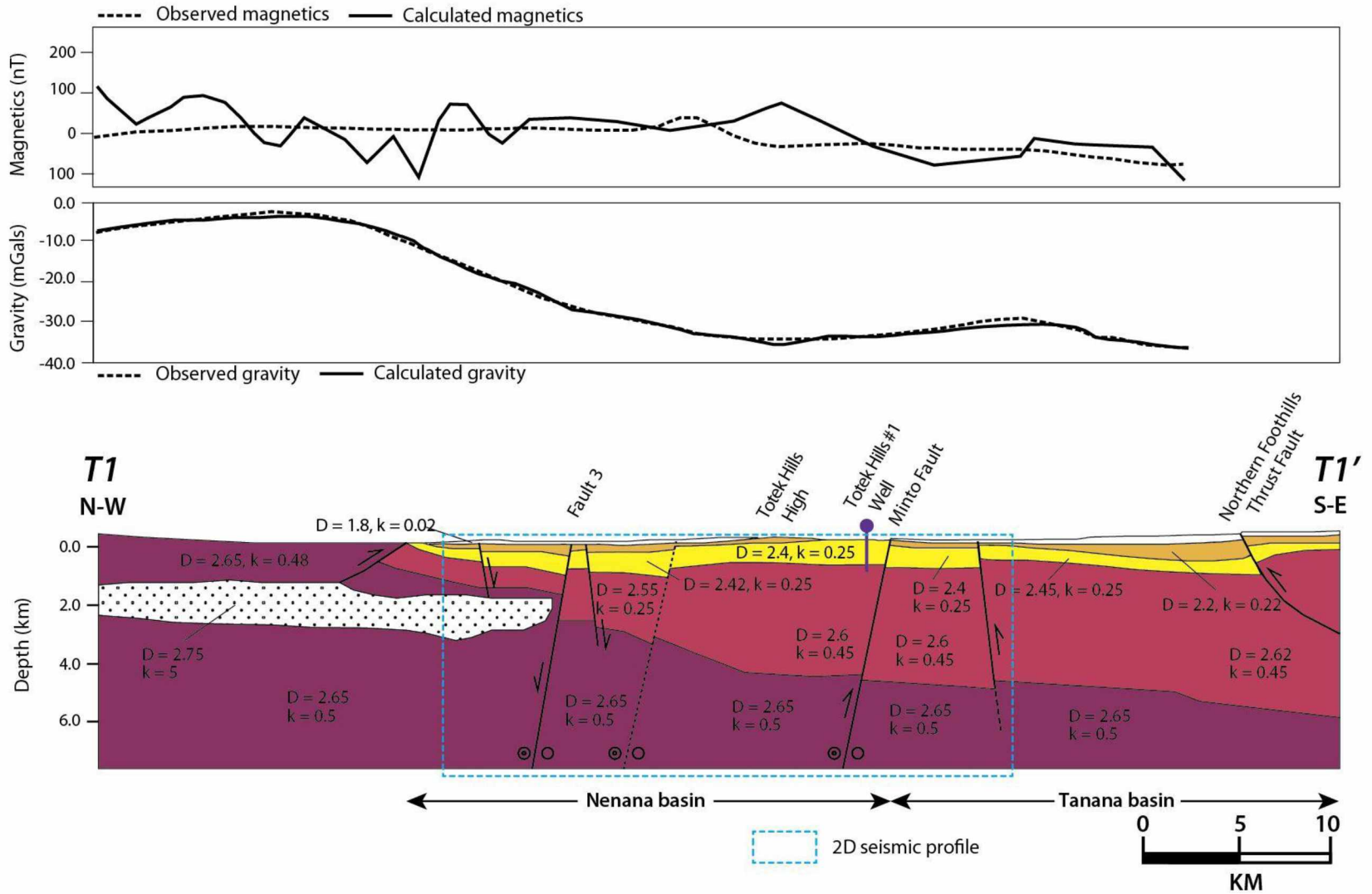
Figure 2-8 Potential field models developed for both the Nenana and Tanana basins

(a) Residual gravity and magnetic anomaly model along profile T1.
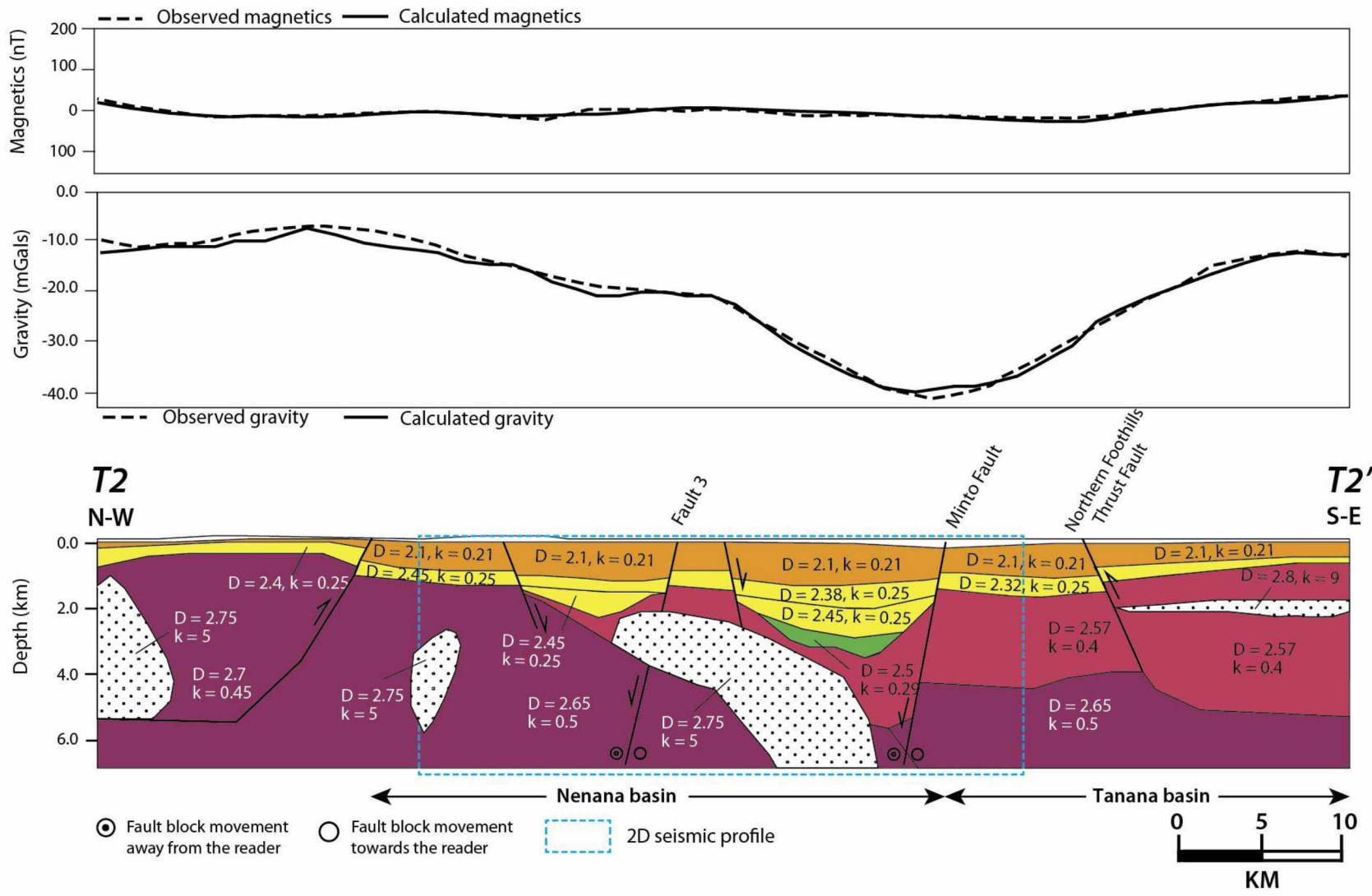
Figure 2-8 cont.

(b) Residual gravity and magnetic anomaly model along profile T2.
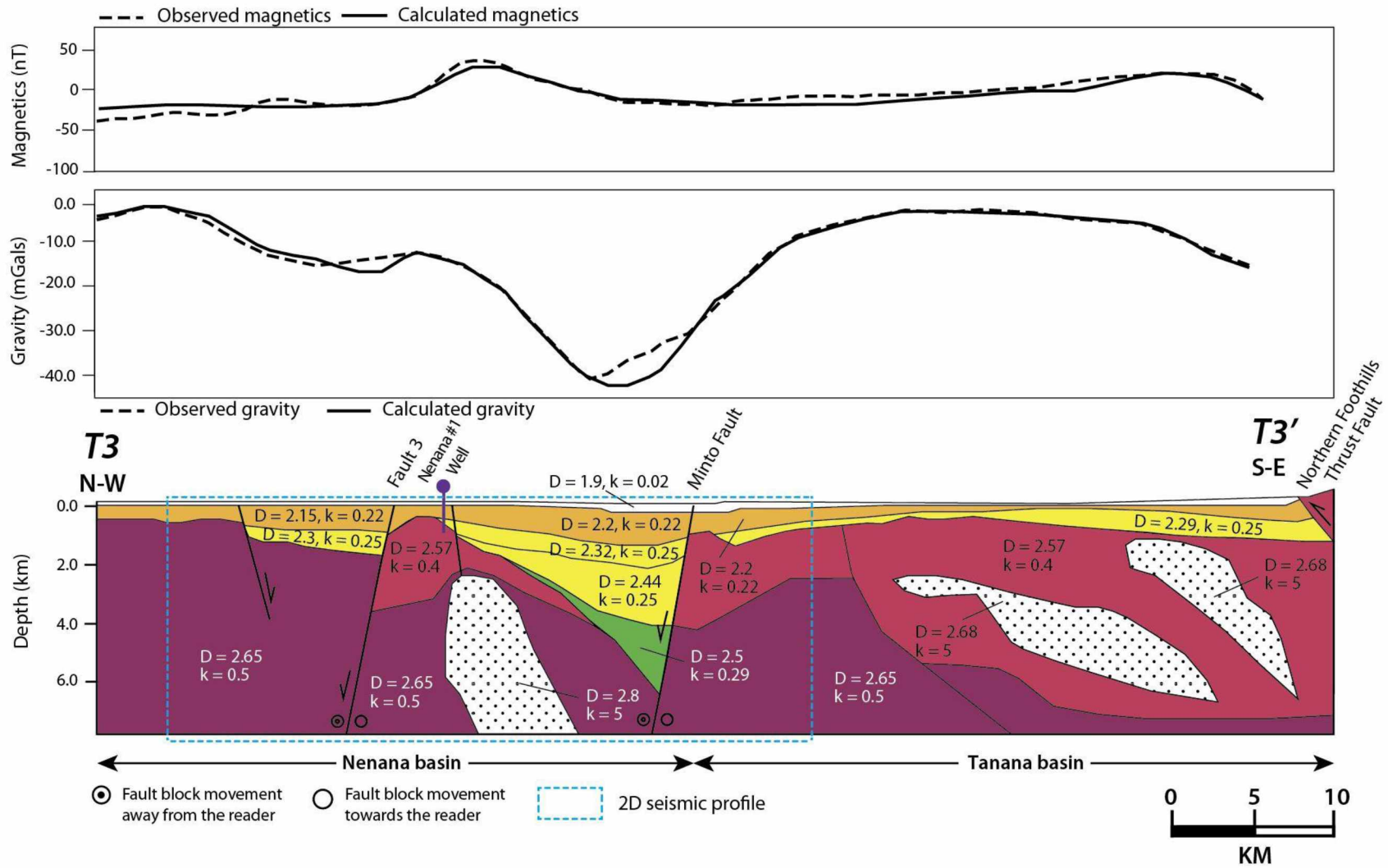
Figure 2-8 cont.

(c) Residual gravity and magnetic anomaly model along profile T3.
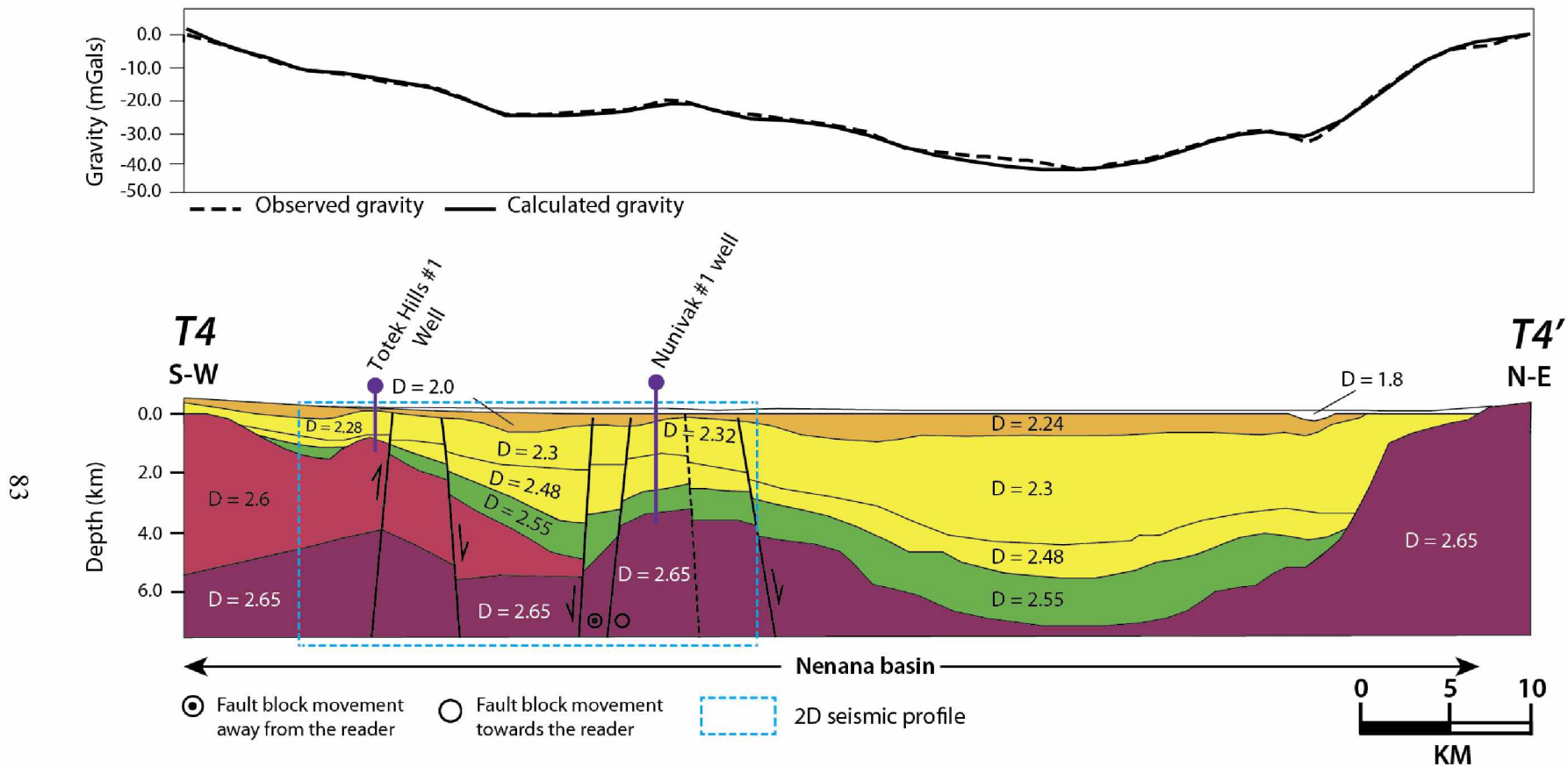
Figure 2-8 cont.

(d) Residual gravity anomaly model along profile T4.
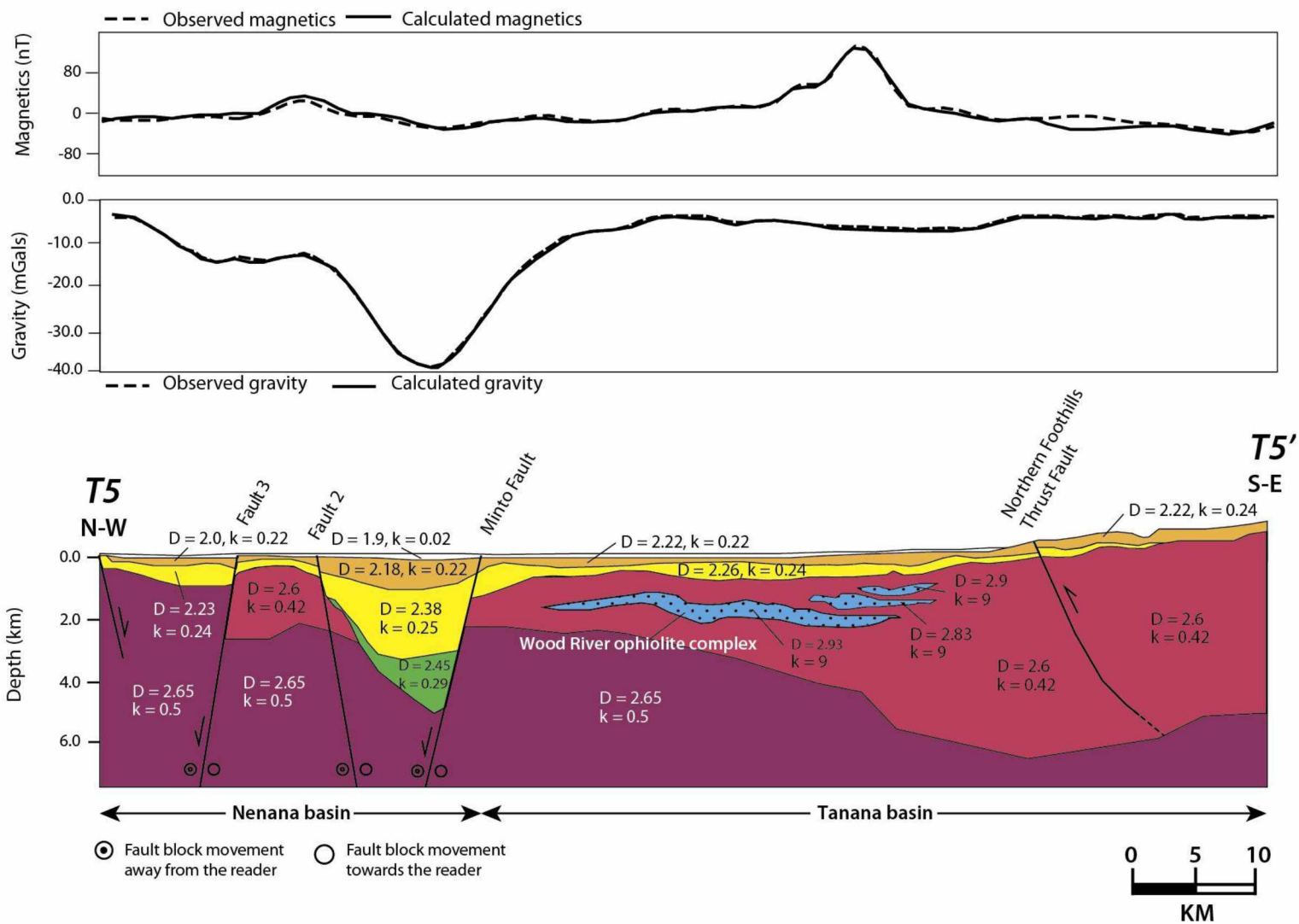
Figure 2-8 cont.

(e) Residual gravity and magnetic anomaly model along profile T5.
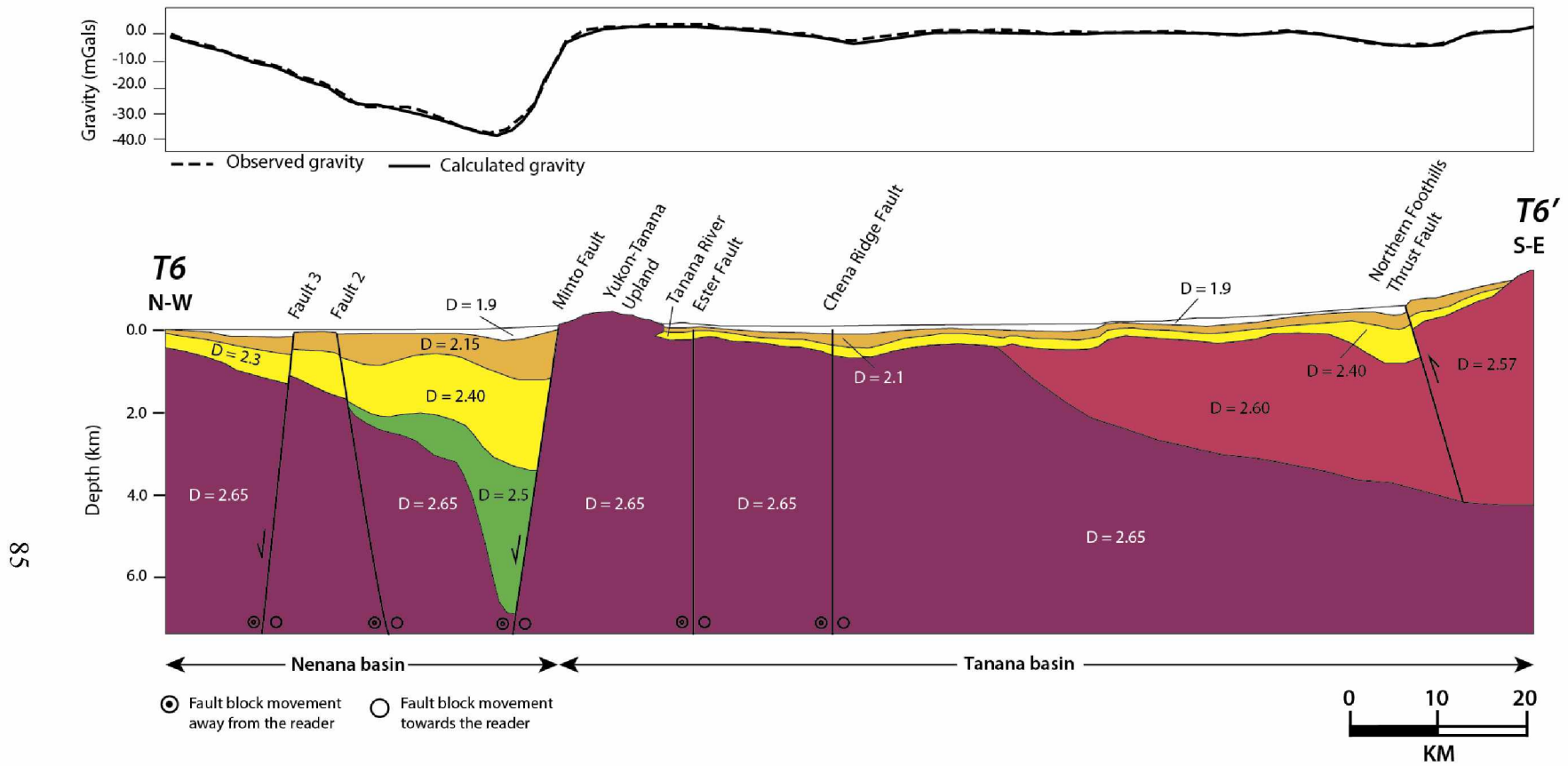
Figure 2-8 cont.

(f) Residual gravity anomaly model along profile T6.
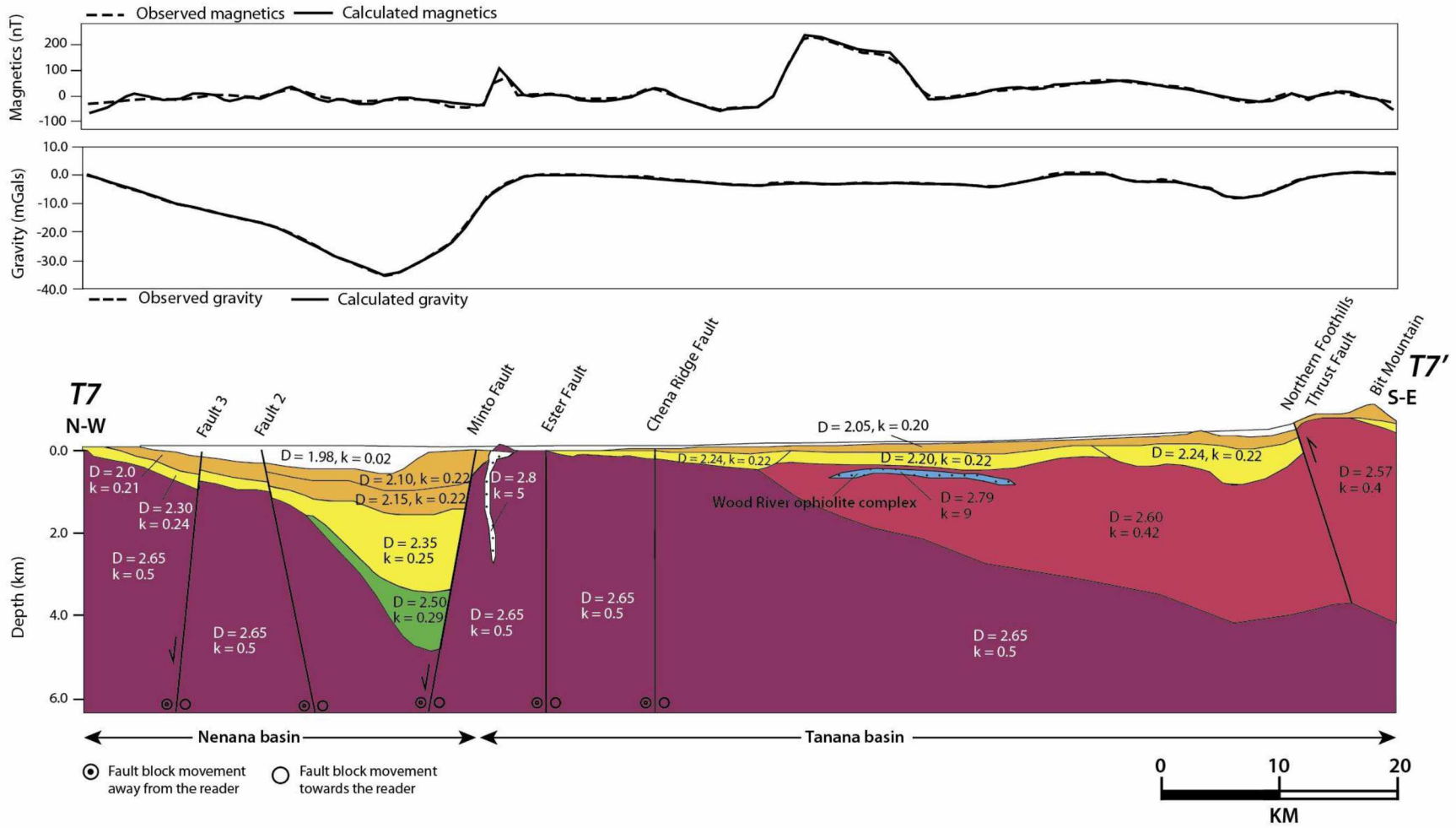
Figure 2-8 cont.

(g) Residual gravity and magnetic anomaly model along profile T7.
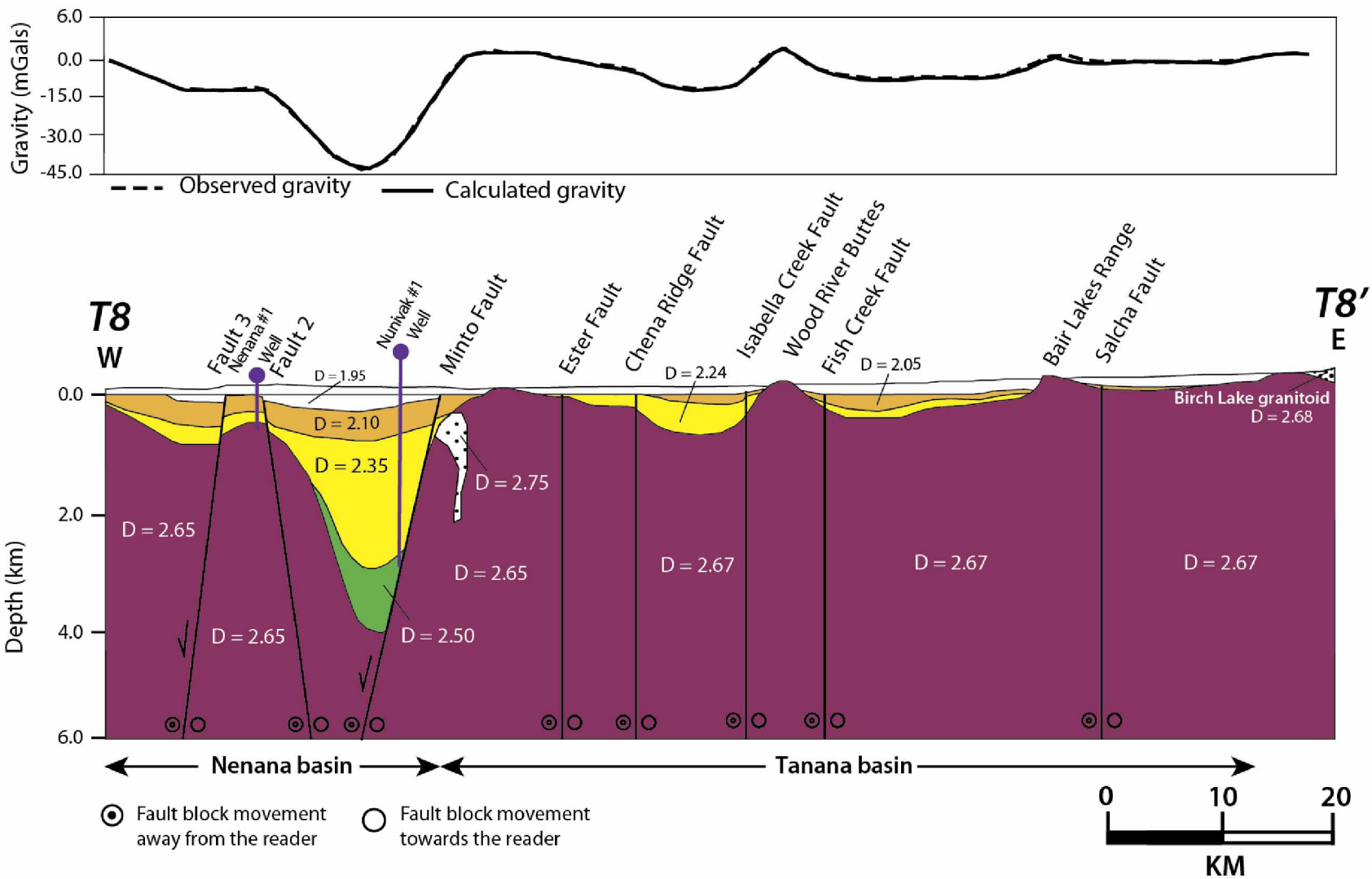
Figure 2-8 cont.

(h) Residual gravity anomaly model along profile T8.
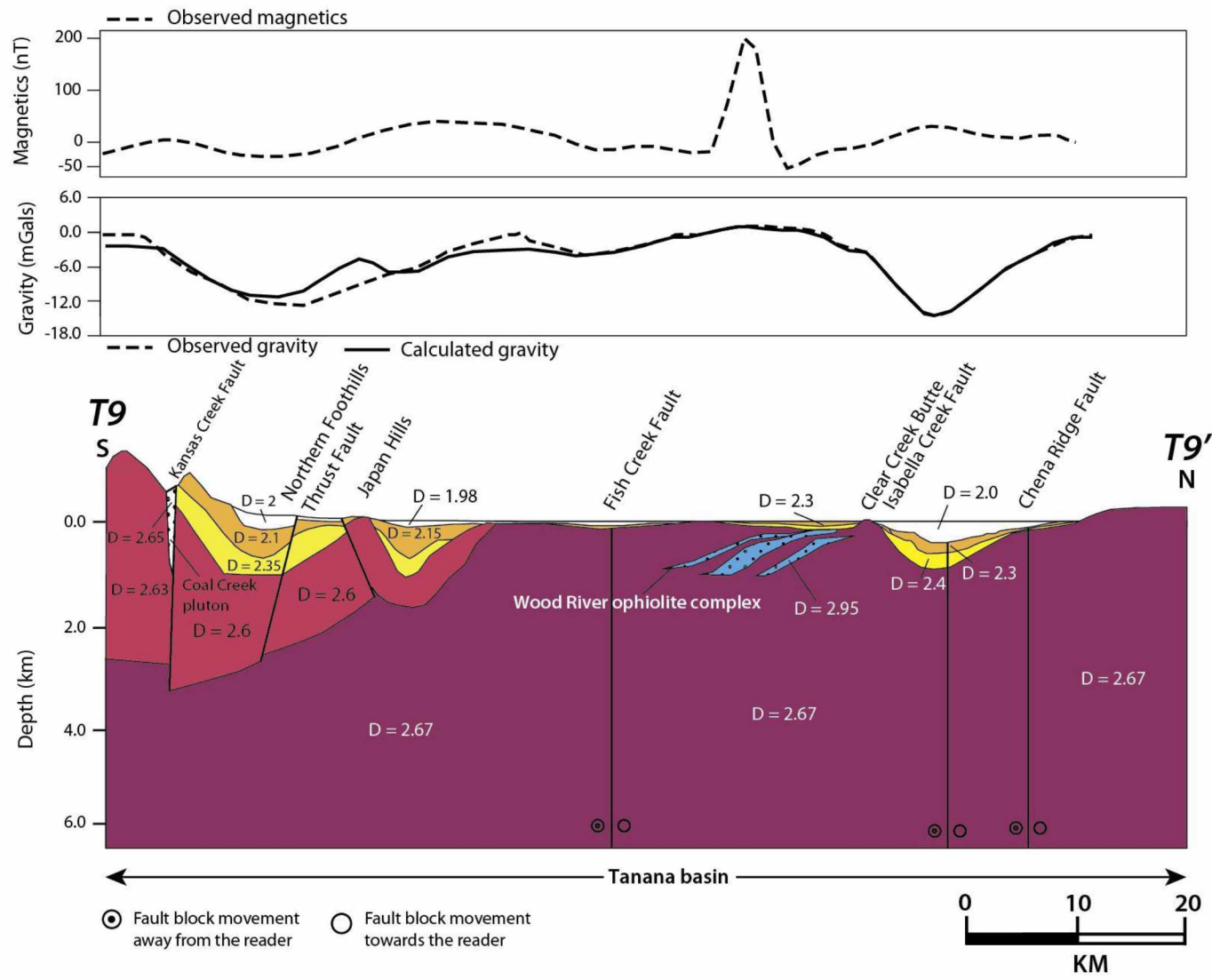
Figure 2-8 cont.

(i) Residual gravity anomaly model along profile T9.

Profile locations shown in Figure 2-2. The upper panels show observed (dotted black line) and calculated (solid black line), gravity and magnetic anomaly curves. The lower panel shows the potential field model with individual source bodies colored by lithology and labeled with density (kg/m^3) and magnetic susceptibility (x 10^3 SI). Blue dotted line shows the limit of seismic reflection data in our study area. Table 2-1 summarizes measured average magnetic susceptibility and rock density values for modeled lithologic units in our study area.
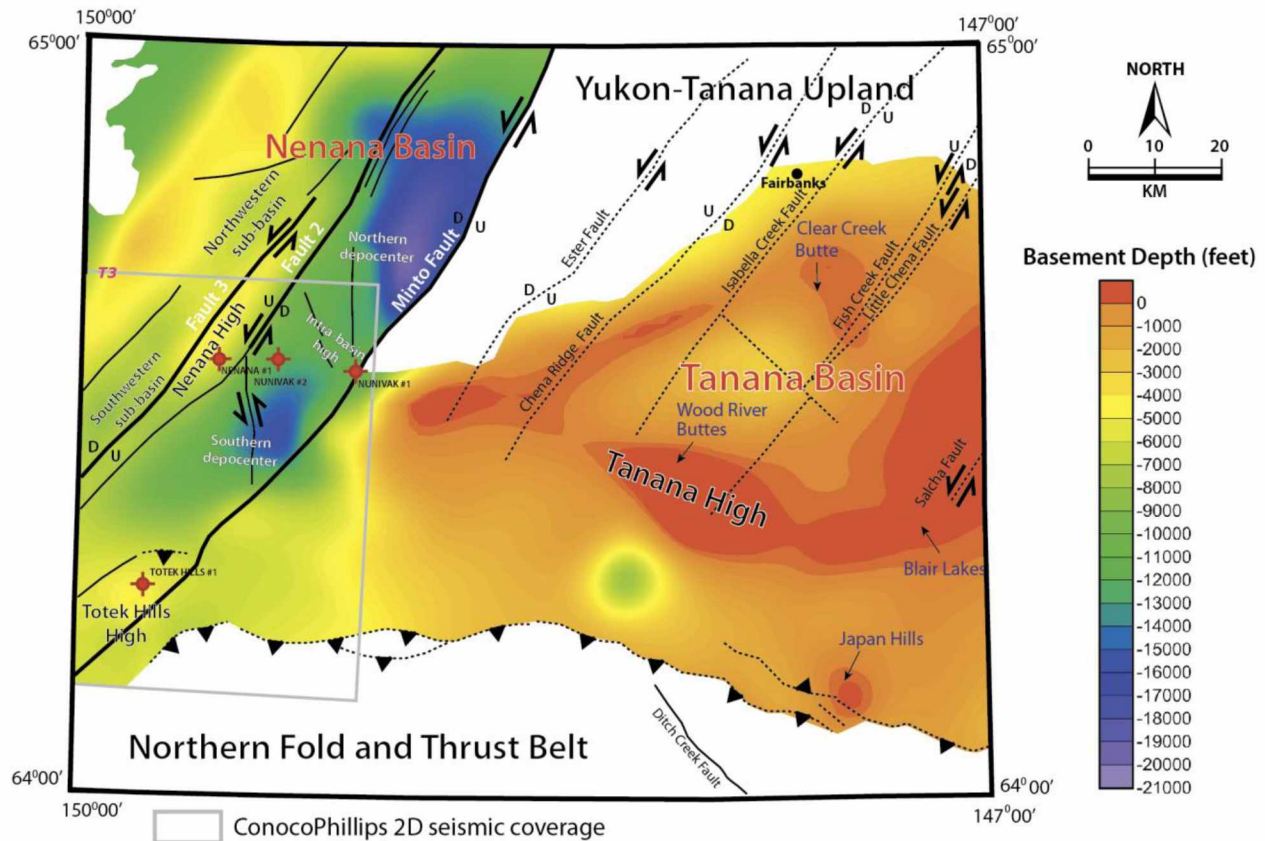
Figure 2-9 Modelled basement depth map using integrated seismic and potential field models of the basins

Grey box indicates the extent of seismic reflection profile data interpreted for basement depths in the southern part of the Nenana basin. In general, the modeled gravity and magnetic anomaly data suggest that there are some similarities between the two adjacent basins but also several significant differences. While the composition of the crust underlying the two basins is similar, the distribution and thicknesses of the overlying sedimentary sequences vary greatly. Overall, the sedimentary fill in the Nenana basin is significantly thicker (up to 8 km) and probably older than that in the Tanana basin (up to 2 km thick).
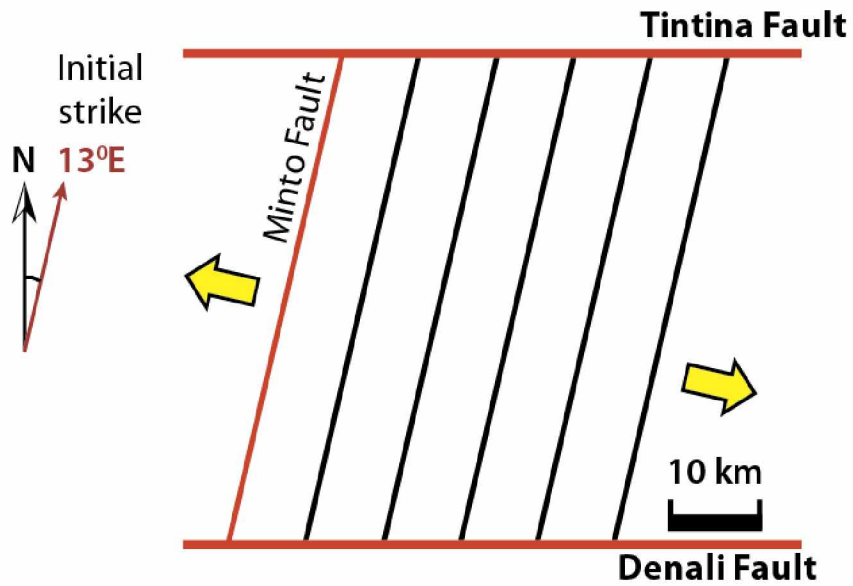
Figure 2-10 Late Cretaceous fault configuration in the study area

Schematic illustrating initial fault configuration with parallel fault blocks, restored from observed regional plate motion vectors (Wallace and Ruppert, 2012). The restored fault direction for the Late Cretaceous is approximately $N13^0E$.
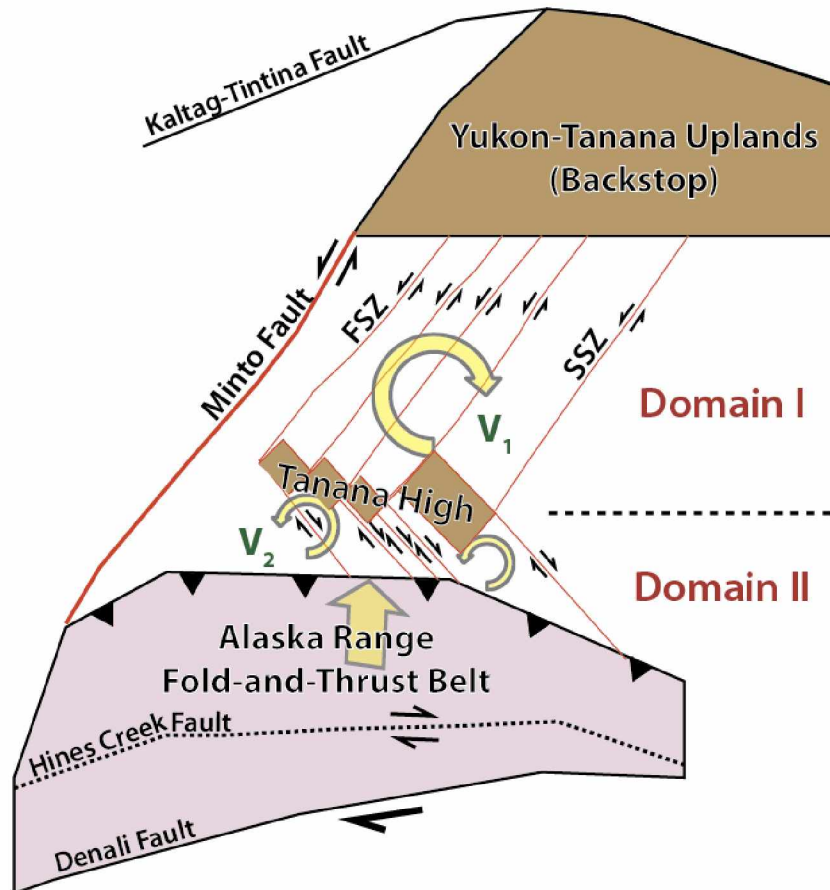
Figure 2-11 Chevron folding-type basement deformation model of the Tanana basin
Fault blocks in Domain I rotate clockwise facilitated by left lateral strike slip motion on northeast strike faults; fault blocks in Domain II rotate counterclockwise facilitated by right-lateral strike slip motion on northwest striking faults. Areas of crustal overlap (orange rectangles) represent the location of Tanana High. North-south shortening is caused by northward migrating thrust belt of the Alaska Range. The locations of the strike-slip faults are shown by red lines; arrows indicate the sense of motion across the faults. Rotational symbols indicate proposed rotation directions of fault blocks in each domain. V_1 and V_2 are the rotational velocities of Domain I and Domain II respectively. In this model, V_2 is greater than V_1. FFZ-Fairbanks Seismic Zone; SSZ-Salcha Seismic Zone.

92
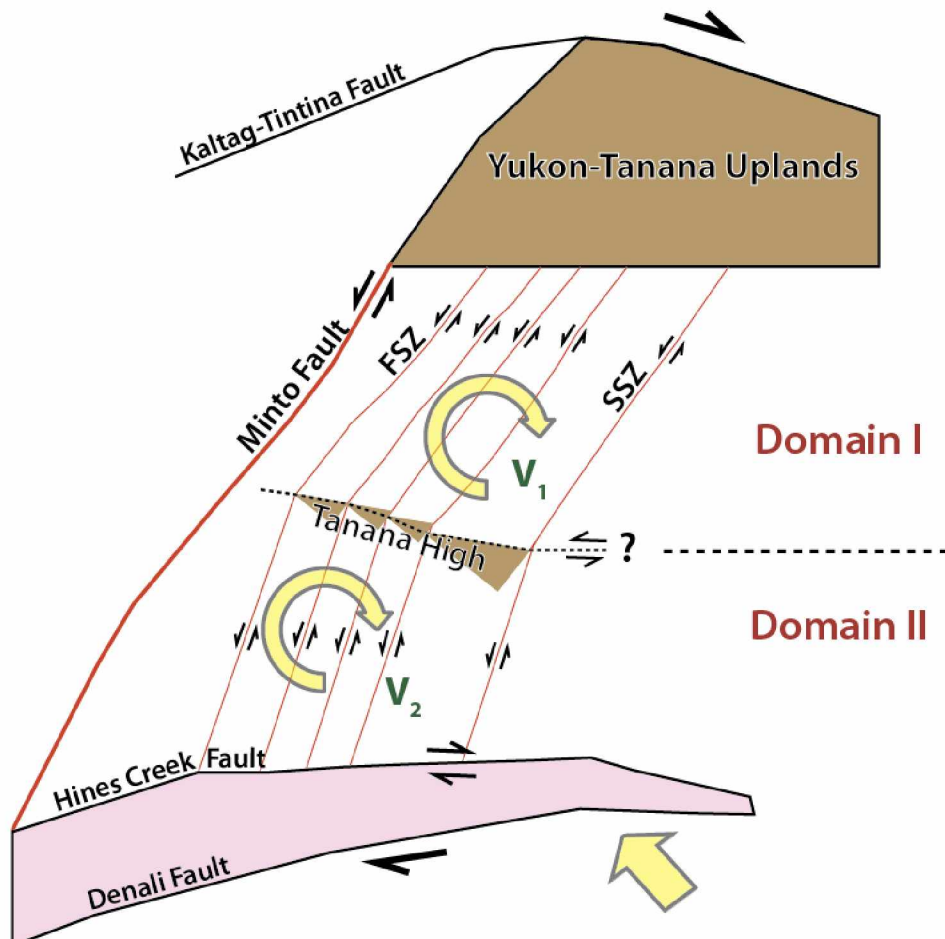
Figure 2-12 Foreland-flexural-type basement deformation model of the Tanana basin

In this model, the thrust belt of the Alaska Range drives north-south directed shortening in the basin. North of the thrust belt, progressive flexural subsidence due to crustal loading causes the development of the foredeep along the northern margin of the foothills of the northern Alaska Range. In this model, the Tanana High is the forebulge of the Alaska Range foreland basin or, alternatively, is a basement high underlain by the leading edge of the Alaska Range fold-and-thrust belt. Compression north of the Tanana High drives clockwise rotation of crustal blocks facilitated by left-lateral motion on northeast-striking faults in Domain I. Rotation is about a vertical axis located in the Yukon-Tanana Upland.
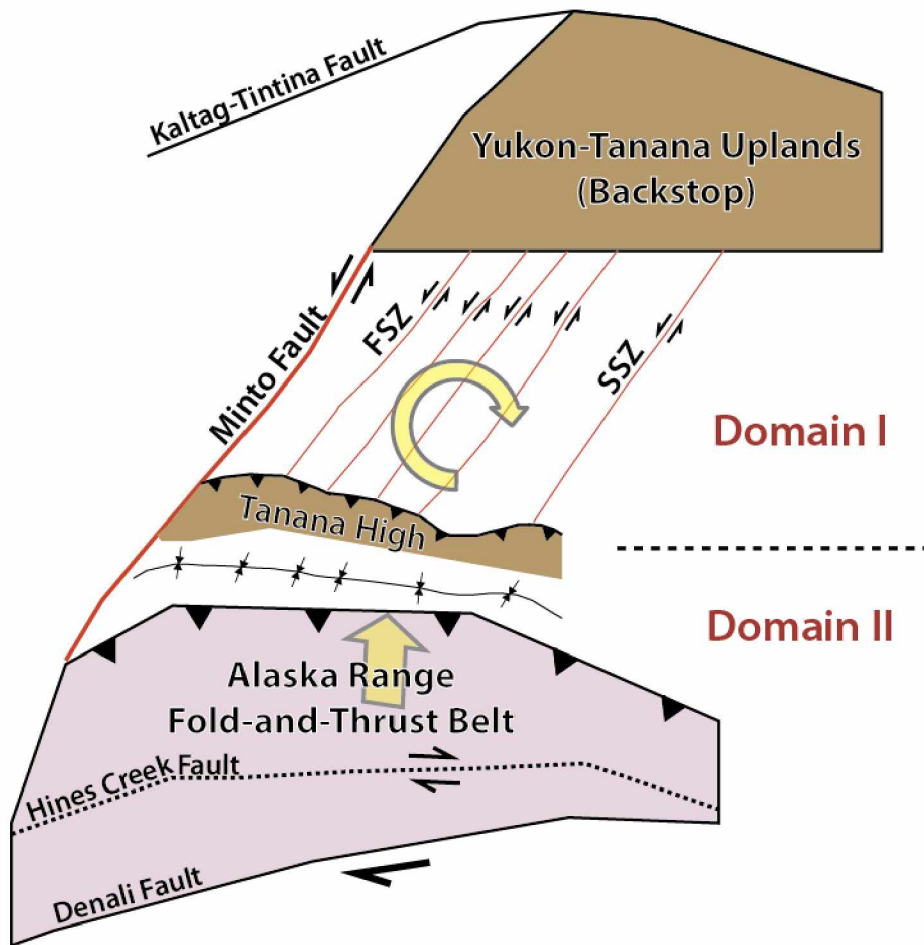
Figure 2-13 Block rotation-type basement deformation model of the Tanana basin

A modified version of Page et al.'s (1995) model in which the regional heterogenous dextral shear between the Denali and Tintina fault systems is divided into two structural domains, Domain I and II. Fault blocks in Domain I rotate clockwise with a higher rotational velocity V_1 whereas the blocks in Domain II rotate clockwise with relatively smaller rotational V_2. Note that the faults in both domains are left-lateral and northeast-striking, in contrast to Model 1.
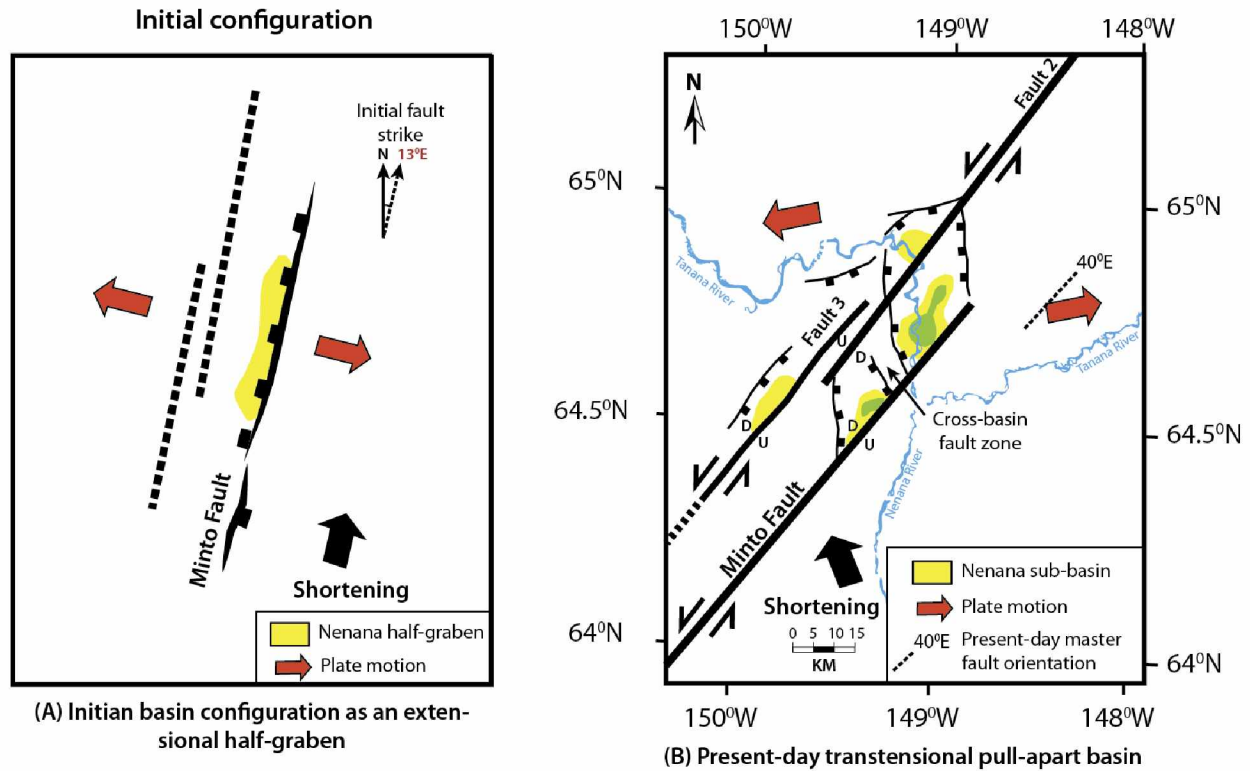
Figure 2-14 Transtensional pull-apart-type basement deformation model of the Nenana basin

(a) In the first phase, the Nenana basin initiates as a single depocenter within an extensional half-graben along the Minto Fault (modified after Dixit and Hanks, 2015). (b) In the second phase, extensional structures are overprinted by deformation associated with NE-SW left-lateral strike-slip tectonics. In this model, two left-lateral, oblique-slip master faults (Minto fault and Fault 2) overlap, forming a releasing bend. Faults 2 and 3 are reactivated normal faults from the extensional phase. A cross-basin transverse fault zone is formed across the basement stepover which further divides the basin into two discrete depocenters. The geometries of these basin depocenters are further controlled by the degree of transtension and rates of relative displacement across the master fault surfaces (See Wu et al., 2009). The sub-basins along the western margin of the Nenana basin are interpreted as incipient pull-apart zones characterized by localized half-grabens parallel to main fault zone.
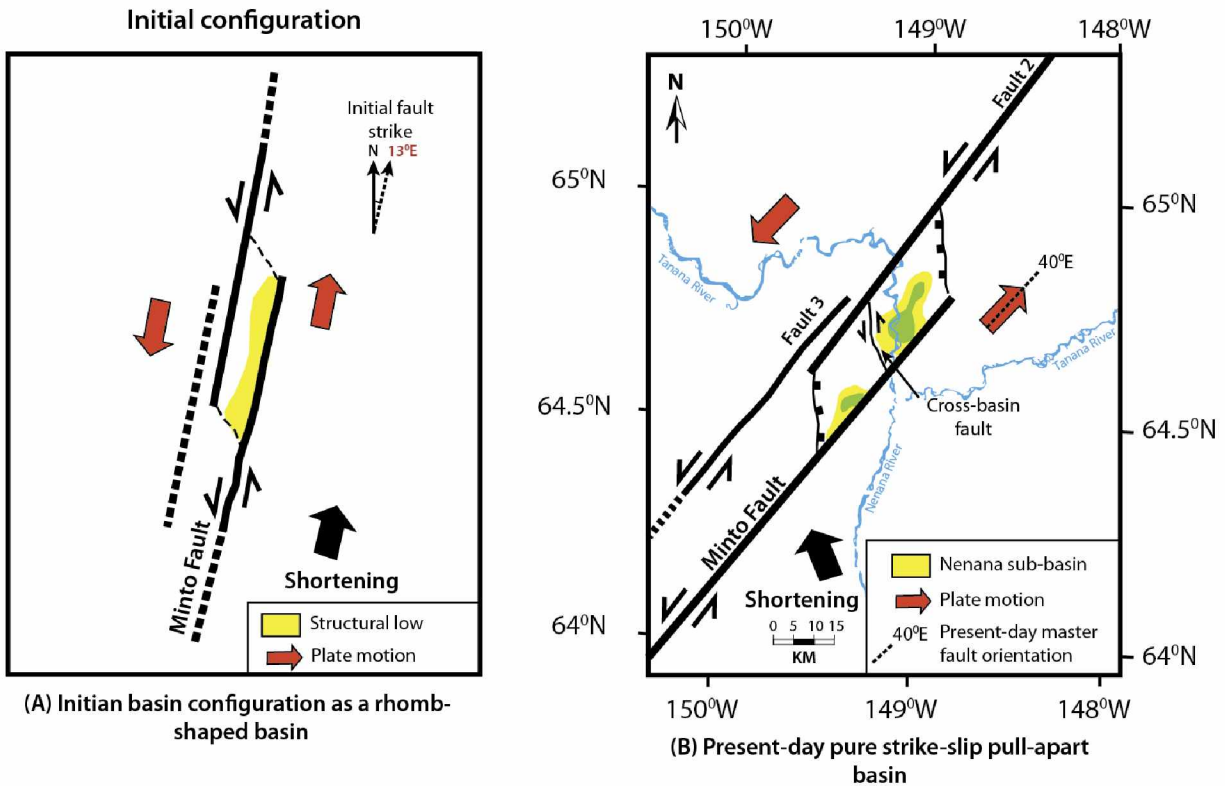
Figure 2-15 Pure strike-slip-type basement deformation model of the Nenana basin

Simplified basin evolution model of the Nenana basin as a pure strike-slip pull-apart basin in the MFFZ (modified from Tape et al., 2015). (a) In the initial phase, the Nenana basin develops as a single asymmetric rhomb-shaped depression between two left-lateral strike-slip master faults. Basin subsidence only occurs locally across an area of fault overlap between two master fault segments. (b) With further strike-slip displacement, a cross-basin left-lateral strike-slip fault forms that links the main basin-bounding faults. Strike-slip strain partitioning and uplift along this oblique cross-basin fault divides the main basin into two isolated and asymmetric depocenters. The elongate shape of the basin is attributed to the presence of a basal ductile decollement similar to Sims et al. (1999).

96

Table 2-1 Generalized stratigraphy and associated rock properties for units in the Nenana and Tanana basins

Period/Epoch	Formation	Major Lithology	Depositional Environment	Assigned Density (kg/m³)	Assigned Susceptibility (SI x 10⁻⁰³)	Color Code
Quaternary	Surficial Deposits	Unconsolidated gravel, sand, silt and clay	Alluvial fan/ flood-plain/ lacustrine/ swamp	1800-1900	0.02	
Pliocene to Miocene	Nenana Gravel	Coarse-grained conglomerate and sandstone	Alluvial fan/ braided fluvial systems	2100-2250	0.22	
Miocene to Late Eocene	Grubstake Formation	Laminated mudstone and sandstone	Lacustrine	2300-2450	0.25	
	Lignite Creek Formation	Conglomerate, sandstone, mudstone and coal	High-sinuosity mixed-load fluvial systems			
	Suntrana Formation	Coarse grained sandstone and coal	Distal sandy braided fluvial systems			
	Sanctuary Formation	Laminated mudstone	Lacustrine			
	Healy Creek Formation	Conglomerate, sandstone, mudstone and coal	Proximal, gravelly braided stream systems			
Early Eocene to Late Paleocene	Late Paleocene Sediments	Siltstone, mudstone and coal	Fluvial/lacustrine/swamp/ alluvial fan	2450-2500	0.29	
Early Mississippian-Middle Devonian	Totatlanika Schist	Metavolcanic and metavolcaniclastic quartzfeldspathic schist, phyllite and gneiss; metamorphic grade varying locally between greenschist, amphibolite and gneissic facies gneiss with phyllite	-	2550-2620	0.4	
Early Paleozoic to Proterozoic	Yukon-Tanana schists	Quartz-mica (pelitic schist) and phyllite, locally calcareous and carbonaceous. Dominant metamorphic grade greenschist facies, varies across high-angle faults in Yukon-Tanana Upland to as high as eclogite facies	-	2650-2750	0.5	
Paleocene to Late Cretaceous	intrusions	Plutons and dikes composed of granodiorite, tonalite, diorite, monzonite, syenite and gabbro	-	2620-2900	3 to 30	

In this study, we measured the density and magnetic susceptibility contrasts for the subsurface rocks from the outcrop exposures of similar rock lithologies along Parks Highway and in the Suntrana Creek area along the northern foothills fold-and-thrust belt of the Alaska Range (Figure 1). In addition, borehole well cuttings of two wells drilled into the Nenana basin (Nenana # 1 and Nunivak # 1 well) were analyzed for rock properties at the Alaska Geologic Materials Center (GMC), Eagle River (Dixit and Tomsich, 2014). A handheld magnetic susceptibility meter was used for the discrete measurements of magnetic susceptibility. Density measurements of rock samples were carried out in the laboratory at the University of Alaska Fairbanks. Average densities and magnetic susceptibilities of individual rock unit were used for 2D modeling of gravity and magnetic data. Data sources include 133 samples from Nunivak # 1 well and 6 samples from Nenana # 1 well collected from the Alaska Geologic Materials Center (GMC); 107 magnetic susceptibility measurements from exposures near the Nenana basin and published data by Athey and others (2006). Our measured rock densities generally increase with age of the rock units and depths (less than 2.1 g/cm^3 for Quaternary sediments to greater than 2.6 g/cm^3 for metamorphic basement rocks). Typical average densities for Cenozoic and Early Cretaceous pluton are greater than 2.8 g/cm^3. Simplified stratigraphic column is adapted from Wahrhaftig (1987) and Ridgway et al. (2007).

3 Cenozoic tectonic and thermal history of the Nenana basin, central Interior Alaska: new constraints from seismic reflection data, fracture history and apatite fission-track analyses [1]

3.1 Abstract

The Nenana basin of interior Alaska forms a segment of the diffuse plate boundary between the Bering and North American plates and is located within a complex zone of crustal-scale strike-slip deformation that accommodates dextral shear stresses related to the regional fault systems and compressional stresses due to oblique plate convergence to the south. The basin is currently the focus of new oil and gas exploration. Integration of seismic reflection and well data, fracture data and apatite fission track analyses with regional data improves our understanding of the tectonic development of this continental strike-slip basin. The Nenana basin formed during the Late Paleocene as a 13-km-wide half-graben, affected by regional intraplate magmatism and localized crustal thinning across the Minto fault in south-central Alaska. The basin was uplifted and exhumed along this faulted margin in Early Eocene through to Late Oligocene time in response to oblique subduction along the southern Alaska margin. This event resulted in the removal of up to 1.5 km of Late Paleocene strata from the basin. Renewed rifting and subsidence during Early Miocene time widened the basin to the west resulting in deposition of Miocene nonmarine clastic rocks in reactivated and newly-formed extensional half-grabens. In Middle to Late Miocene time, left lateral strike-slip faulting was superimposed on this half-graben system, with rapid subsidence beginning in Pliocene time and continuing to the present-day. At present, the Nenana basin is in a zone of transtensional deformation that accommodates

---

[1] Dixit, N.C., Hanks, C.L., Rizzo, A., McCarthy, P., and Coakley, B. J. (2016). Cenozoic tectonic and thermal history of the Nenana basin, central Interior Alaska: new constraints from seismic reflection data, fracture history and apatite fission-track analyses, Canadian Journal of Earth Sciences.

compressional stresses due to oblique plate convergence and allows tectonic subsidence by oblique-extension along major basin-bounding strike-slip faults.

3.2 Introduction

Continental transform boundaries are often narrow zones of tectonic deformation commonly associated with a steeply-dipping strike-slip fault or a complex array of steep strike-slip faults which accommodate the relative plate motion (Mann, 2007; Seeber et al., 2010). The geometry, type and magnitude of relative plate displacement along the transform fault strongly controls the complex morphologies of transpressional basins and transpressional folds developing along a transform margin (Ben-Avraham, 1992; May et al., 1993; Aksu et al., 2000). Continental transform basins often record the tectonic history of the transform plate boundary and related mechanisms of slip along the faults in their sedimentary fill. Investigating the origins and evolutionary histories of these transform basins would constrain the tectonic development of the transform fault systems as well as the structural architecture and thermal histories of transform margins.

The Nenana basin is a prominent structure that overlies the eastern edge of a diffuse plate boundary between the Bering plate to the west and the North American plate to the east (Cross and Freymueller, 2008) (Figure 3-1). The basin is located between two regional right-lateral strike-slip fault zones – the Denali fault system to the south and the Kaltag-Tintina fault system to the north (Figure 3-1) (Page et al., 1995; Ruppert et al., 2008; Tape et al., 2015; Dixit and Hanks, 2015). The northern Alaska fold-and-thrust belt lies to the south of the Nenana basin. It is the northernmost limit of active deformation from the Alaska Range orogenic belt (Lesh and Ridgway, 2007; Bemis et al., 2012). Recent seismological studies indicate that a number of seismically-active NE-striking, left-lateral crustal-scale strike-slip faults cut through the Nenana

basin and show poorly characterized surface scarps (Figure 3-1) (Cross and Freymueller, 2008; Frohman, 2015; Tape et al., 2015). These faults accommodate horizontal dextral shear between the Denali and Kaltag-Tintina fault systems. There is a general agreement that the Nenana basin formed as a consequence of extension by transtension-related deformation along these major, NE-striking faults. Recent studies address the present-day tectonic deformation style of the Nenana basin (Page et al., 1995; Van Kooten et al., 2012; Tape et al., 2015). However, the timing of faulting, the origin and evolution of the basin is speculative and poorly understood. In addition, determining the extent of tectonic deformation in the basin has been difficult due to lack of outcrop, limited exploration well data and scarcity of publicly available seismic reflection data. As a result, it has been difficult to develop a cohesive tectonic model of the evolution of the basin.

The Nenana basin is a promising hydrocarbon exploration area in interior Alaska and may hold as much as 250 million barrels of recoverable oil, up to 28 billion cubic meters of recoverable natural gas and up to 8 billion short tons of identified coal resources (Merritt, 1986; Doyon Limited, 2015). A better understanding of tectonically-induced deformation, sediment accumulation and subsequent thermal regimes in the subsurface over time can constrain the relative timing of trap formation, hydrocarbon generation and migration within the basin (Hubbert, 1953; Hunt, 1996; Van Kooten et al., 2012).

This study investigates the phases of tectonic deformation of the Nenana basin by an integrated analysis of two-dimensional (2D) seismic reflection profiles, well data, surface fracture data and apatite fission track data. This integrated analysis was used to constrain the

thermal history of the basin and illustrate how basin subsidence and uplift events influenced the thermal regime of the basin over time.

3.3   Geological Background

Central interior Alaska is dominated by two continental-scale, dextral strike-slip fault systems: the Denali and Kaltag-Tintina fault systems (Figure 3-1). The Denali fault is an active intraplate, dextral strike-slip fault that arcs through the Alaska Range. This fault accommodates dextral shear strain resulting from the oblique plate convergence to the south (Eberhart-Phillips et al., 2003; Matmon et al., 2006). The Denali fault is reported to have 350 km of right-lateral strike-slip displacement and it extends steeply through the crust to depths as deep as ~30 km (Lanphere, 1978; Fisher et al., 2007; Haeussler, 2008). The Tintina fault is a steeply dipping dextral strike-slip fault that extends through central Alaska and separates deformed Proterozoic-Paleozoic North American crustal rocks from accreted Yukon-Tanana Terrane rocks in our study area (Till et al., 2007). Murphy and Mortensen (2003) suggested at least 450 km of dextral displacement along the Tintina fault in Late Cretaceous or Early Paleocene time. Since Early Paleocene time, slip on the Tintina fault system has been minimal (Brogan et al., 1975). At its western end, the Tintina fault connects with the the Kaltag fault through a set of splays (Till et al., 2007). To the south, the Alaska Range is a dextral transpressional orogen with north-vergent thrusting along the northern foothills fold-and-thrust belt and strike-slip faulting along the Denali fault (Haeussler, 2008; Bemis et al., 2015). At present, the shallow oblique subduction and and collision of the Yakutat microplate along the southern Alaska margin drives the dextral transpressional deformation across the Alaska Range (Figure 3-1) (Bemis and Wallace, 2007; Carver et al., 2008; Haeussler, 2008). To the north of the central Alaska Range, contractional deformation continues into the Nenana pull-apart and Tanana foreland basins (Ridgway et al.,

2007; Dixit and Hanks, 2015). Geologic and seismological evidence suggest that a zone of distributed dextral shear exists between the Denali and Tintina fault systems, driven by N-S directed crustal shortening in response to oblique plate convergence to the south (Ratchkovski and Hansen, 2002; Ruppert et al., 2008; Bemis et al., 2015). Active faults and numerous active seismic zones (e.g. Minto Flats Seismic Zone, Fairbanks Seismic Zone and Salcha Seismic Zone) across this dextral shear zone suggest clockwise rotation of crustal blocks to accommodate N-S directed crustal shortening in the region (Figure 3-1; Page et al., 1995; Bemis et al., 2015).

Regionally, the Nenana Basin is located within the dextral shear zone between the Denali and Tintina fault systems, to the north of the Alaska Range fold-and-thrust belt (Figures 3-1 and 3-2). Two major seismically-active northeast-striking left-lateral strike-slip faults cut through the basin: the Minto fault in the southeast and an unnamed fault in the northwest (Fault 2 on Figure 3-2). These two faults and subsidiary faults have been referred to as the Minto Flats Fault Zone (MFFZ) (Tape et al., 2015). At present, the basin is subsiding due to on-going oblique-strike-slip (transtensional) movement along the major basin-bounding faults and possibly due to crustal loading along the northern foothills of the Central Alaska Range (Lesh and Ridgway, 2007; Dixit and Hanks, 2015; Tape et al., 2015).

Various tectonic models have been proposed to explain the present-day structural setting of the Nenana basin. Based on shallow seismic reflection and residual Bouguer anomaly data, Van Kooten et al. (2012) and Doyon Limited (2015) proposed that the Nenana basin is an extensional half-graben or graben complex that was formed along the Minto Fault. In contrast, Tape et al. (2015) and Dixit and Hanks (2015) interpreted the Nenana basin as a transtensional

pull-apart basin situated between the two basin-bounding active left-lateral faults within the MFFZ (Figure 3-3).

Only four exploration wells have been drilled in the Nenana basin (Figures 3-2 and 3-3). Figure 3-4 outlines the stratigraphy of the basin encountered by the exploration wells. Proterozoic to Early Paleozoic Yukon-Tanana Terrane schist and Late Paleozoic Totatlanika schist underlies the Cenozoic non-marine sedimentary basin. The sedimentary fill of the Nenana basin includes: Late Paleocene sediments (Late Paleocene Formation), a Miocene sequence (Usibelli Group), a Pliocene sequence (Nenana Gravel), and Quaternary surficial deposits (Figure 3-4) (Merritt, 1986; Frost et al., 2002; Van Kooten et al., 2012). The Usibelli Group, the Miocene coal-bearing sequence, is further subdivided into five different formations--the Healy Creek, Sanctuary, Suntrana, Lignite Creek and Grubstake formations. The major thermally mature to marginally mature source rocks of the Nenana basin occur in the Late Paleocene and Healy Creek formations (Figure 3-4) (Van Kooten et al., 2012, Dixit and Tomsich, 2014).

3.4 Data and Methods

The dataset used in this study includes 350-km-long of two-dimensional seismic reflection profiles, borehole logs from four exploration wells and apatite fission track (AFT) data from four rock samples: two collected from the well cuttings of Nunivak 1 well and two samples from an outcrop along the eastern margin of the basin, near the town of Nenana.

3.4.1 Well Data

Borehole logs and lithostratigraphic data from four exploration wells (Nenana 1, Totek Hills 1, Nunivak 1 and Nunivak 2) were used as control points to determine the subsurface geology of the basin (Figures 3-2 and 3-5) (AOGCC, 2015; Doyon Limited, 2015). The age assignments for the observed sedimentary units in Nunivak 1 and Nunivak 2 wells were based on

palynomorph data collected from these exploration wells (Gerry Van Kooten, written communication, 2014). In addition to subsurface stratigraphy, sonic and density logs were further used to establish well-to-seismic ties that allowed the stratigraphic correlation of key seismic reflectors.

Nunivak 1 well was selected to generate a representative one-dimensional tectonic subsidence history model for the basin (Figures 3-3b and 3-5). Nunivak 1 was chosen because it: 1) shows good tectonic history (unconformities and well preserved sedimentary strata); 2) represents most of the stratigraphic sequences that are well documented in outcrop; 3) is drilled at a geographic location which samples the deeper area within the basin; and 4) has reasonable thermal history data needed to calibrate the subsidence history model. The burial history for this well was generated using the BasinMod software program (Platte River Associates Inc.). The BasinMod software program uses decompaction and backstripping techniques to estimate tectonic subsidence according to the method of Steckler and Watts (1978). The main input parameters for the modeling included the ages and depths of each stratigraphic horizon. To generate a useful thermal history for this well, we considered the basal heat flow model published for the Nenana basin by Van Kooten and others (2012) and Dixit and Hanks (2015). Our burial history model is constrained by the subsurface stratigraphy at Nunivak 1 well and the observed present-day temperature data.

3.4.2 Seismic Reflection Data

The seismic reflection data available for this study includes four 2D seismic reflection profiles approximately 350-km-long. These profiles extend down to 4 sec in two-way-travel time (TA02, TA03, TA04 and TA05; Figure 3). Three seismic transects (TA02, TA03 and TA04) are oriented northwest-southeast whereas one seismic transect is oriented northeast-southwest,

105

parallel to the structural trend observed in the region. This 2D seismic grid was acquired and processed by ConocoPhillips and was kindly provided for our research. More recently, Doyon Limited (2015) published a series of additional 2D and 3D seismic reflection profiles that were acquired during hydrocarbon exploration surveys in the Nenana basin. We integrated this more recent published seismic reflection data with the 2D seismic grid provided by ConocoPhillips to evaluate the subsurface geometry, timing of faulting and evolution of the Nenana basin. An integrated seismic interpretation was performed employing the IHS Kingdom Suite. Synthetic seismograms and depth-converted seismic horizons were used for the correlation of stratigraphic units encountered in the wells as well as to generate structural and isopach maps for the selected horizons. The lithological and stratigraphic information derived from the published well data was used to constrain the age and geological interpretation of individual units.

3.4.3 Apatite Fission Track (AFT) Data

Four samples were collected for an AFT analysis to evaluate the thermal history of the Nenana basin. Samples 1 and 2 were collected from well cuttings of Nunivak 1 well stored at the Geological Materials Center in Eagle River, Alaska (Dixit and Tomsich, 2014) (Figure 3-5). Sample 1 was taken from the Late Paleocene sediments (depth interval of 2746 m- 3359 m) whereas Sample 2 was taken from the Miocene Usibelli Group sediments (depth interval of 1695 m- 2252 m). Sample 3 was collected from quartzite of the Yukon-Tanana Terrane exposed along the Parks Highway, in the footwall of the Minto Fault (Figure 3-2). Sample 4 was obtained from schist of the Yukon Tanana Terrane located farther south, near the town of Nenana (Figure 3-2). This sample also marks the footwall of the Minto Fault.

All of the samples were sent to Apatite to Zircon Inc. (A2Z, Idaho) for AFT analysis. The detailed experimental procedures and principles of fission track analysis that are implemented by Apatite to Zircon Inc. are described in Donelick et al. (2005). We used the HeFTy software (Ketcham et al., 2007) to model the time-temperatures histories for each sample. Input parameters for the time-temperature modeling (inverse modeling) of each sample were the fission-track length distribution and the fission-track age with errors of $\pm 1\sigma$. For every inverse model, additional timing constraints such as stratigraphic age, sample depth and present-day temperature were applied to honor the tectonic burial history of the basin. Each inverse model randomly generated (Monte Carlo approach) 10000 independent time-temperature paths and compared the modelled data with measured fission track data. The best-fit solution for each of the inverse models was based on a goodness of fit (GOF) value, in which 'good' and 'acceptable' fit to the measured data corresponded to GOF values of 0.5 and 0.05, respectively. The best-fit time-temperature path (GOF close to 1) provided the most likely thermal history for a given sample in accordance with the measured data.

3.4.4   Fracture Sampling and Calcite Twin Data

In order to investigate the history of fracture formation at the basin scale, we collected fracture data that included fracture orientations (strike and dip), modes of deformation (opening or shearing), the presence or absence of fracture fill (calcite or quartz) and cross-cutting relationships in the outcrop of basement schist rocks of the Yukon Tanana Terrane exposed near the town of Nenana (Figure 3-2). We used the linear scanline fracture survey method to measure the fracture attributes of each fracture (Priest, 1993). Each scanline was set up normal to the strike of a particular fracture set identified at the outcrop. Based on the quality of exposed rocks, at least 25 fractures were measured for each fracture set for further statistical analysis.

At high temperatures and in the presence of reactive fluids, open fractures are completely filled with mineral precipitates such as calcite and quartz (Laubach, 2003). The cemented fractures therefore record fluid migration pathways and can provide information on stress regimes active during fracture filling. To examine the modes of deformation and temperature history of such fractures, we collected oriented rock samples containing well-preserved veins for thin section analysis. Petrographic thin sections (cut parallel as well as normal to the mineralized vein walls) for each of these samples were made by National Petrographic Services, Inc in Houston, Texas. We analyzed these thin sections to interpret vein composition, type of deformation and the direction of shear identified from crystal orientations.

Mechanical e-twinning occurs in calcite crystals that are deformed at low temperatures ($<$ 300^0c) and under high shear stresses (Burkhard, 1993). Thin twins in calcite generally dominate at temperatures below 170^0C whereas above 200^0C, calcite exhibits thick twins (Ferrill et al., 2004). As a result, twin morphologies in calcite from vein fillings can be used to provide information about deformation temperature of a host rock. In this study, we used thin sections from each sample to further analyze twin thickness and extent of deformation within a vein. Resulting calcite twin morphologic interpretations were then integrated with the apatite fission track data in order to constrain the timing of fracture formation within the basin.

3.5   Observations

3.5.1   Major Depositional Sequences and Events
We identified four major seismic sequences from synthetic seismic ties, unconformities and reflection character within Cenozoic strata of the Nenana basin.   These include: 1) Proterozoic to Paleozoic seismic basement; 2) Paleocene syn-rift sequence; 3) Miocene syn-rift sequence; and 4) Pliocene and younger post-rift sequence (Figures 3-6 and 3-7).

Proterozoic to Paleozoic Pre-Rift Seismic Basement

An erosional unconformity marks the top of Proterozoic to Paleozoic metamorphic basement rocks of the Yukon-Tanana Terrane. It is also observed in well data. The basement unconformity dips to the east from Nenana 1 well and to the southeast from Totek Hills 1 well and truncates against a faulted-block along the Minto Fault, near the town of Nenana (Figures 3-2, 3-3 and 3-5). We first interpreted the basement sequence along the basin margins on the seismic profiles and traced it further into the deeper sections of the basin.

The seismic reflection data did not provide a direct reflection at the top of metamorphic basement (Figures 3-6a and 3-7b). Consequently, well logs, truncation patterns of seismic reflectors and upper crustal models of the Nenana basin were defined with the potential field data from gravity and magnetics (see Dixit and Hanks, 2015). These data constrain our interpretation of the top of metamorphic basement within the basin (Figures 3-6b and 3-7b). The interval velocities directly derived from the well data for our interpreted basement sequence are 4.5 - 5.3 km/s, and comparable to velocities of metamorphic bedrock in the Yukon-Tanana Terrane calculated from deep crustal seismic studies (4.9 km/sec; Brocher et al., 2004).

Two major northeast-striking, down-to-west faults bound the basin on the top-of-basement structure (Fault 3 and Minto Fault; Figure 3-6b). Both of these faults offset the basement unconformity and show > 1 km mean fault displacement. In map-view, the distance between the two northeast-striking basin-bounding faults generally increases to the north (Figure 3-3).

The top-of-basement structure map also illustrates the asymmetry of the Nenana basin (Figure 3-3). The basement surface deepens abruptly to >5.5 km deep in the southeast, on the downthrown side of the Minto Fault. The top of basement shallows gradually westward where it is 1079 m at Nenana 1 well (Figure 3-3). The basement on the upthrown side of the Minto Fault is exposed along the northeastern margin of the basin, near the town of Nenana (Figure 3-2).

Paleocene and Older Synrift Sequence

The palynomorph data collected from Nunivak 1 well suggests that > 305 m of Late Paleocene non-marine deposits overlie the seismic basement (Van Kooten et al., 2012, Gerry Van Kooten, written communication, 2016). At the eastern basin margin, growth strata are evident in this sequence where high-amplitude, continuous seismic reflectors expand toward the major, northeast-striking faults that bound the basin (Figure 3-6). This Late Paleocene sequence thickens toward the east and above the deepest parts of the basin (Figure 3-6b). The sequence also pinches out or thins towards the west, along the Nenana High and to the southwest, along the Totek Hills High (Figure 3-7b). At the base of the sequence, seismic reflections onlap onto the irregular and gently sloping basement surface along the western and southwestern margins of the basin (Figures 3-6b and 3-7b). The non-marine character of the sediments, thickening of strata against the major basement-involved faults and progressive onlap onto the underlying basement surface suggests active deposition of these sediments during growth of a normal fault-bounded basin, suggesting that this is a synrift sequence (Schlische, 1991; Contreras et al., 1997).

110

Early Eocene to Late Oligocene Unconformity

At the top of the Late Paleocene sequence, an erosional unconformity truncates underlying seismic reflectors (Figures 3-6b and 3-7b). This surface indicates that the underlying Paleocene sequence experienced a post-depositional exhumation. This unconformity is also evident as a hiatus on well logs (Nunivak 1 and Nunivak 2; Figure 3-5). To the west of the Nenana High, the angular unconformity cannot be traced or identified on the seismic data (Figure 3-6b).

Miocene Synrift Sequence

Seismic reflection ties to well control indicate that the sequence above the Late Paleocene Formation in Nunivak 1 and Nunivak 2 wells based on the palynomorphs data is Early Miocene to Late Miocene in age. This sequence marks deposition of fluvial and lacustrine coal-bearing rocks of the Miocene Usibelli Group (Van Kooten et al., 2012; Gerry Van Kooten, written communication, 2016) (Figure 3-5). On seismic reflection profiles, this sequence downlaps onto the underlying Early Eocene/Late Oligocene angular unconformity (Figures 3-6b and 3-7b). This seismic sequence is characterized by high-amplitude, continuous reflections along the deeper sections of the basin and near the eastern basin margin (Figure 3-6b and 3-7b). These seismic reflections become less continuous to discontinuous across the gently-sloping, western and southwestern basin margins. This discontinuity in seismic reflections suggests laterally heterogenous lithologies or a fractured rock mass along these basin margins (Chopra and Marfurt, 2008).

111

Based on the seismic reflection character, the Miocene sequence can be further divided into two sub-sequences: (1) a Lower Miocene sequence (including the Healy Creek and Sanctuary formations), and (2) an Upper Miocene sequence (including the Suntrana Creek, Lignite Creek and Grubstake formations) (Figure 3-4). Stratigraphically, the Lower Miocene sequence shows a fining-upward trend that reflects a transition from a sand-rich fluvio-deltaic environment of the Healy Creek Formation to a silt-rich lacustrine environment of the Sanctuary Formation (Ridgway et al., 2007, Van Kooten et al., 2012). In the seismic reflection data, the two subsequences are separated by a subaerial unconformity. On seismic reflection profiles, Sanctuary Formation strata progressively onlap the top-of-Healy Creek surface along the hanging wall and indicate a continuous deepening of the basin (Figure 3-6b). This Lower Miocene sequence thickens across the northeast-striking major faults (Fault 3 and Minto Fault) and suggests sedimentation coeval with the development of these faults (Figure 3-6b).

The Upper Miocene sequence consists of extensive braided fluvial-deltaic sediments of the sand-rich Suntrana and Lignite Creek formations that transition upward into the silt-rich, lacustrine facies of the Grubstake Formation (Figure 3-4) (Ridgway et al., 2007; Van Kooten et al., 2012). On seismic profiles, this sequence onlap the underlying Lower Miocene sediments towards the western and southwestern basin margins and also thickens against the northeast-trending major basin faults (Fault 3 and Minto Fault). Deposition of the Upper Miocene sequence, therefore, records a renewed period of basin subsidence.

Locally, a set of northwest-striking negative flower structures are associated with syndeformational growth strata within the Upper Miocene sequence (Figure 3-6b). These

northwest-striking faults generally cut through the basement surface, indicating continuation of basement-involved oblique-extensional faulting in the basin.

Pliocene to Quaternary Post-Rift Sequence

The top of the Miocene Usibelli Group is well defined as an unconformity surface in both outcrop and in wells and is overlain by the Pliocene Nenana Gravel and Quaternary deposits (Figure 3-5). On seismic profiles, the Nenana Gravel downlaps basinward onto the Miocene unconformity surface (Figures 3-6b and 3-7b). This sequence displays a poor seismic reflectivity and/or a lack of continuous stratigraphic reflectors in large parts of the basin. Much of the poor seismic resolution in this section could be due to unconsolidated, fractured or poorly-sorted sediments (Dixit and Tomsich, 2014).

This sequence thickens towards the north and above the deepest section of the basin (Van Kooten et al., 2012; this study) and thins westward and southwestward along the margins of the basin (Figure 3-6b). The surface exposures of the Miocene Usibelli Group and Neogene Nenana Gravel sediments near the Totek Hills High (Figure 3-2) suggest that the southwestward-thinning of Pliocene-Quaternary strata could be due to erosion during the uplift and exhumation of this region (Figure 3-7b). Unlike older basin sequences, the observed thickness variations of Pliocene and younger strata were not controlled by any major basement-involved fault. This suggests filling of the basin in a post-rift setting.

3.5.2   Burial History of Nunivak 1 Well

In order to better understand the subsidence and thermal history of the Nenana basin, we evaluated the tectonic subsidence history of the Nunivak 1 well (Figure 3-8). The Nunivak 1 well was drilled on an intra-basement high in the Nenana basin.

Cenozoic strata encountered in Nunivak 1 well record three distinct phases of tectonic subsidence and a single phase of uplift in the area (Figure 3-8). Subsidence rates are calculated from inferred compacted sediment thicknesses, as interpreted from Nunivak 1 well data. At the Nunivak 1 well site, rapid tectonic subsidence (~0.24km/Ma) occurred from Late Paleocene to Early Eocene and resulted in the deposition of more than 1829 m of Late Paleocene sediment. This was interrupted by a major episode of basement uplift and exhumation from Early Eocene (54.8 Ma) to Late Oligocene (23.8 Ma) that eroded and removed as much as 1524 m of Late Paleocene Formation strata. Renewed tectonic subsidence in the Miocene resulted in the deposition of 2012 m of Usibelli Group strata in gravelly braided streams to high-sinuosity mixed-load streams and lacustrine environments (Figure 3-8) (Buffler and Triplehorn, 1976). The rate of basin subsidence in the Miocene (~0.11 km/ Ma) appears to be much slower than that in the Late Paleocene (~0.24 km/Ma). Our burial history curves further suggest that tectonic subsidence accelerated during Pliocene time (~0.37km/Ma) with the deposition of about 1372 m of Nenana Gravel deposits in gravelly braided streams and alluvial fans (Wahrhaftig, 1987). The basin continued to subside rapidly until the present.

3.5.3   Apatite Fission Track Analysis

A fission-track age is mainly a function of fission track lengths and, for apatite, records the cooling history of the host rock from temperatures $< 120^0 C$ (Green et al., 1989; Gallagher et al., 1998, Ketcham et al., 1999). Apatite fission track ages and fission track length data were determined for 4 samples (Table 3-1). Fission track ages obtained from these 4 samples fall between 41.4 ± 7.8 Ma and 7.79 ± 3.5 Ma (Table 3-1 and Figure 3-9). In general, the AFT ages decrease from west to east (Figure 3-2). Samples 1 and 2 collected from the Nunivak 1 well show the oldest AFT ages (Figure 3-2) while samples 3 and 4 from the exposed basement rocks in the footwall of the Minto fault have the youngest AFT ages. The observed AFT ages and track

lengths indicate that all samples have experienced temperatures >120^{0}C and have been totally annealed in the past (Figure 3-9).

Cooling History of Samples 1 and 2 from the Nunivak 1 Well

The AFT age of 39.41± 4.8 Ma for Sample 1 from the Late Paleocene Formation of Nunivak 1 well is significantly younger than the formation age (Table 3-1; O'Sullivan, 1999). Mean track lengths of 13.9 ± 1.52 μm for this sample are shorter than the standard, unannealed mean track length of 16.3 ± 0.9 μm (Gleadow et al., 1986). These two observations suggest that Sample 1 resided in the apatite partial annealing zone (PAZ, 120^0 C to 60^0 C) for a significant time. The HeFTy inverse model solution for Sample 1 shows a goodness-of-fit (GOF) of 0.94 for the AFT age and 0.82 for the track length (Figure 3-9). This model suggests a bimodal thermal history with two distinct phases of rapid burial and subsequent heating - first in the Late Paleocene to Early Eocene and second during Early Miocene to present day, with an intervening phase of rapid cooling in the Middle Eocene to Late Oligocene.

Sample 2 is from the Miocene Usibelli Group penetrated by the Nunivak 1 well (Figure 3-5). Sample 2 has an AFT age of 41.40 ± 7.8 Ma which is significantly older than the depositional age of the Miocene Usibelli Group (Table 3-1). The older AFT age thus indicates that Sample 2 was clearly not completely reset and contains apatite fission tracks that are inherited from the provenance of sediments deposited (Gleadow et al., 1986). Sample 2 also yields longer mean track lengths (14.28 ± 1.18 μm) compared to Sample 1, indicating rapid cooling of the host rock through the PAZ at 58 Ma – 55 Ma. The HeFTy inverse model solution for Sample 2 indicates a GOF of 0.96 for the AFT age and 0.46 for the track length (Figure 3-9).

The relatively lower GOF for the AFT track length could be due to fission tracks that are inherited from the provenance of sediments deposited and not reset completely (Gleadow et al., 1986; O'Sullivan, 1999). The weighted-mean time-temperature solution for this inherited apatite sample suggests that most of the cooling occurred between 60 Ma to 50 Ma. This sample was then rapidly buried and subsequently heated from surface temperature (15^0 C) to about 65^0 C since Pliocene through to present-day (Figure 3-9).

Cooling History of Samples 3 and 4 from the Outcrops

Sample 3 is from basement rocks (mainly quartzite) of the Nenana Basin exposed along the Parks Highway and in the footwall of the NE-striking, basin-bounding Minto Fault (Figure 2). The observed AFT age of 28.35 ± 4.1 Ma for Sample 3 is much younger than the depositional age and is therefore reset completely (Gleadow et al., 1986) (Figure 3-9). Similar to Sample 2, Sample 3 shows a longer mean fission track length of 14.45 ± 1.44 μm which indicates rapid cooling of the host rock through the PAZ. The HeFTy inverse model for Sample 3 indicates a GOF of 0.98 for the AFT age and 0.99 for the track length (Figure 3-9). The weighted-mean time temperature path for Sample 3 further suggests that the initial cooling of Sample 3 through the PAZ (120^0 C to 60^0 C) occurred from Early Oligocene to Early Miocene and is continuing to the present day. A continuous, gradual cooling history of Sample 3 can be interpreted as being due to continuous uplift of the footwall of the Minto Fault along the eastern basin margin.

Sample 4 is also from the basement rocks (mainly schist) of the Nenana basin, located farther south of Sample 3, near the town of Nenana (Figure 3-2). This sample yielded a much younger pooled age of 7.8 ± 3.5 Ma and mean track length of 14.3 ± 1.2 μm (Figure 3-9). The

116

younger fission track age and longer fission track length of this sample suggest that the sample was reset completely and then uplifted rapidly through the PAZ during the Late Miocene (~10 Ma to 7Ma). The inverse model solution for Sample 4 provides a GOF of 1 and 0.99 for the AFT age and track length distribution, respectively.

Overall, thermal histories for all four samples suggest that the area experienced temperatures in excess of 120^0C during Late Paleocene time. Following an episode of maximum burial, cooling through the PAZ in the deeper parts of the basin occurred in Mid Eocene to Late Oligocene time, whereas along the eastern margin of the basin, rocks were uplifted and cooled through the PAZ during the Early Oligocene to Late Miocene. At present, Samples 1 and 2 are undergoing rapid burial and are situated within the PAZ along the hanging wall of the Minto Fault (Figure 3-2). In contrast, Samples 3 and 4 are undergoing rapid uplift and are situated above the PAZ, along the footwall of the Minto Fault. The difference in the observed cooling histories of Samples 3 and 4 suggests a progressive migration of footwall uplift southward along the eastern margin of the basin over time.

3.5.4 Analysis of Fracture Sets and Fracture Formation Chronology

We identified four main fracture sets in the regional basement schist of the Yukon Tanana Terrane located at an outcrop near the town of Nenana, hereafter referred to as the 'Nenana outcrop' (Figure 3-2). Based on the statistical analysis of fracture orientations, modes of deformation and cross-cutting relationships, these fracture sets were distinguished based on relative age, orientation, mode of opening and fracture fill (Figure 3-10). All of these fracture sets are shear fractures and are filled with calcite and/or quartz. Each of the fracture sets is discussed in detail below.

117

Fracture Set (F1)

Fracture set F1 consists of shear fractures that range in strike from 300° to 320° and have an average dip of 75° SW +/- 30° (Table 3-2). At the Nenana outcrop, all other fracture sets (sets F2 to F4) terminate against this fracture set (Figure 3-10). In thin section, set F1 fracture fill is composed largely of calcite with subsidiary quartz. Calcite crystals appear blocky to fibrous in shape, whereas secondary quartz crystals tend to be elongated and blocky. In thin sections that are parallel to vein walls, the calcite crystals are oriented at 40°-50° angles to the right (91° NE) with respect to the vein wall and suggest right-lateral shear (Table 3-2). However, in thin sections that are normal to vein walls, the calcite crystals are oriented at 30° angles to the left relative to the vein wall showing a dominant dip-slip motion. Combined slip vectors inferred from thin sections of set F1 therefore suggest that the veins in this fracture set exhibit a right-lateral shear displacement with a strong dip-slip component (Table 3-2). The NW-striking right-lateral transfer fault in the Nenana basin shows a similar average orientation to set F1 (325^0 strike with dip of 70^0). We therefore correlate set F1 to the NW-striking oblique-slip fault in the basin.

The morphology and thickness of the calcite twins in set F1 indicate that both thin (Type I, <170 °C) and thick (Type II, 200-300 °C) twins are present (Table 3-2). Under increasing strain at temperatures below 170 °C, new thin twins form instead of widening existing twins (Ferrill et al., 2004). We therefore interpret that thick calcite twins in fracture set F1 were formed when the host rock was exposed to temperatures > 200^0C whereas thin twins were locally developed within thick twins at lower temperatures (<170 °C).

Fracture Set (F2)

Fracture set F2 is a set of en-echelon shear fractures with a strike of 240°-260° and an average dip of 73° SE +/- 30° (Table 3-2). At the Nenana outcrop, slickenfibres on F2 fracture surfaces show dominantly left-lateral motion. In some places, these fractures abut against and postdate, set F1 and cross-cut set F3 (Figure 3-10). We therefore interpret that the fractures in set F2 formed after set F1 and simultaneously with set F3.

In thin section, fracture set F2 consists of extensional veins filled dominantly with quartz and shear veins filled primarily with calcite. The calcite-filled veins show a strong sense of left-lateral shear motion (Table 3-2). In thin sections cut parallel to the vein wall, calcite crystal orientations show two distinct groups. Calcite crystals in the first group are oriented from 65°-75° (311° NW), while the ones in the second group range from 40°-50° (286° NW) in orientation with respect to the vein wall. In thin sections cut normal to the vein walls, calcite crystals are oriented both at 20° and 40° angles. As a result, combined slip vectors for set F2 show that the opening projection of calcite-filled veins has predominantly left-lateral shear sense with a strong dip-slip component.

Both thick (Type II) and thin (Type I) calcite twins were observed in all of the thin sections of shear veins in set F2 (Table 3-2). The calcite twins show signs of deformation with patchy and curved twins.

Fracture Set (F3)

The shear fractures in fracture set F3 range in strike from 340°-360° and have an average dip of 81° E +/- 30° (Table 3-2). In outcrop, these Mode II shear fractures show a right-lateral

119

shear sense. This set clearly abuts against set F1 and crosscuts set F2 (Figure 3-10). F3 fractures are filled primarily with calcite with secondary quartz. In thin sections parallel to vein walls, calcite crystals appear to have grown at a 45°- 60° angle (~125°- 140° SE) with respect to the vein wall (~170°) (Table 3-2). No dip-slip motion was observed across the veins. The crystal orientations therefore indicate that the calcite-filled veins in set F3 were forming and simultaneously deforming in a mainly right-lateral shear-related regime. Thick (Type II) and thin (Type I) calcite twins are also present in all of the thin sections obtained for set F3 (Table 3-2).

Fracture Set (F4)

Fractures from set F4 range in strike from 200°-220° and have an average dip of 74°NW +/- 30° (Table 3-2). In contrast to F3, these Mode II shear fractures show predominant left-lateral strike-slip deformation at the Nenana outcrop. In some places, this fracture set abuts against all of the older fracture sets (F1-F3) and hence postdates all (Figure 3-10). In addition, this is the only fracture set in which filled fractures show a crack-seal texture with calcite crystals appearing to have grown from previously precipitated calcite reflecting incremental strain over time (Durney and Ramsay, 1973). Both calcite and quartz crystals appear to be oriented perpendicular to (~300° NW) and at 45°-60° (~340° NW) with respect to the vein wall (~210°), indicating predominant left-lateral strike-slip deformation in the veins (Table 3-2).

Most thin sections from set F4 fractures show both thick (Type II) and thin (Type I) calcite twins (Table 3-2). However, in some thin sections of fractures that abut on the older sets, only thin calcite twins (Type I, < 170^{0}C) are observed. The shear fractures in set F4 that exhibit only thin calcite twins are interpreted to be youngest in Nenana outcrop. In the Nenana basin,

NE-striking strike-slip faults such as the Minto Fault have a similar average orientation (40^0NE) to set F4 and share a left-lateral shear sense. We interpret that the shear fractures in set F4 are related to these NE-striking strike-slip faults in the basin.

3.6   Discussion

3.6.1   Implications for the Tectonic Evolution of the Nenana Basin

In this study, we integrated the seismic stratigraphy interpretations with the available fission track and fracture data analyses to construct a structural model for the evolution of the Nenana basin that is consistent with all observational data. A schematic structural section that reflects all four stages of basin evolution is shown in Figure 3-11. This section is based on the seismic line TA-02 that extends from the town of Nenana in the southeast to the northwest across the basin (Figure 3-3).

Late Paleocene Basin-scale Extension and Initiation of Graben System

Seismic reflection data interpretations such as the progressive onlap of synrift strata and growth strata patterns suggest that the Nenana basin initiated as a structural half-graben in Late Paleocene time (Figure 3-11a). Growth strata within the Late Paleocene sediments provide an upper age constraint on the initial rifting in the Nenana basin. The formation of this extensional system was dominated by localized early extensional rifting along the north-east striking, westward-dipping Minto Fault.

Based on the seismic and paleomagnetic data, the restored average strike direction for the Minto Fault during this time is approximately $N13^0E$ (Wallace and Ruppert, 2012; this study). This observation highlights a mean regional WNW-directed crustal extension across the Nenana

basin in the Late Paleocene (Figure 3-11). The presence of more than 1.5 km of locally-sourced lacustrine and fluvial deposits (Van Kooten et al., 2012, Doyon Limited, 2015) in the Late Paleocene Formation further confirms that this rifting phase was initiated rapidly and occurred no later than Late Paleocene.

In the deeper parts of the basin, the thermal history of Sample 1 indicates rapid heating from temperatures less then 40^0C to higher than 170^0C associated with the rapid burial of sediments during the Late Paleocene rifting episode (Figure 3-9). Considering that the maximum vertical depth of burial of the Late Paleocene Formation in Nunivak 1 well was ~2012 m after compaction during this time, an estimated geothermal gradient of 66^0C/km would be required. The cooling histories of the basement AFT samples (Samples 3 and 4) located along the footwall of the Minto Fault are also consistent with our interpretation of regionally extensive high heat flow in Late Paleocene time (Figure 3-9).

Eocene to Oligocene Regional Uplift and Erosion of Late Paleocene Strata

An erosional unconformity at the top of the Late Paleocene sequence in the basin suggests a significant uplift occurred during Eocene to Late Oligocene time and marked the end of the initial phase of rifting in the Nenana basin (Figure 3-11b). This unconformity is well documented in the wells located on basement highs and implies that the rift-shoulders of the graben were exposed from the beginning of Eocene time through Oligocene time.

Our AFT data also supports a regional uplift event in the Nenana basin during Early Eocene to Late Oligocene time (Figure 3-9). AFT data from Samples 1 and 2 are located in the deeper parts of the basin and record rapid cooling and exhumation in excess of 0.7 km/Ma

122

beginning in Early to Mid Eocene time. This implies that the Minto Fault was reactivated as a reverse fault with approximately 1.5 km of vertical displacement along its hanging wall during the Eocene uplift and exhumation event. Sample 3 from the Nenana outcrop shows that it was uplifted and exhumed beginning in Mid to Late Eocene time with a slower cooling rate of 3.33^0C/Ma. However, the time-temperature path for Sample 4 located 4 km farther to the south from Sample 3 suggests that this sample was still buried and/or experienced higher heat flows through Eocene to Oligocene time. We therefore propose that the regional uplift and exhumation progressed northeastward on either side of the Minto Fault and towards the Yukon-Tanana Upland during this time.

Transition from Extensional to Transtensional Fault Regime during Miocene time

During the early Miocene, the Nenana basin widened with the formation of a new half-graben on the western shoulder of the basin (Figure 3-11c). Renewed rifting and continued subsidence along major northeast-striking faults allowed deposition of the Lower Miocene sequence (including Healy Creek and Sanctuary formations) in both northeast-trending half-grabens (Figure 3-11c). The Lower Miocene sequence thickens against the Minto fault, suggesting that the Minto fault was reactivated and grew as a normal fault during this early Miocene rifting phase. The depositional settings for the Lower Miocene sequence indicate a transition from proximal braided river deposits of the Healy Creek Formation to lacustrine deposits of the Sanctuary Formation. In addition to the presence of growth strata, this transition suggests that tectonic subsidence due to slip on major graben-bounding faults accelerated during the Mid Miocene and mainly controlled the deposition of the Lower Miocene sequence in the basin.

As the rifting and basin subsidence continued into the mid- to late Miocene, deposition of the Upper Miocene sequence (including Suntrana Creek, Lignite Creek and Grubstake formations) continued along the northeast-striking faults within the graben system (Figure 3-11c). Stratigraphic thickness variations across northwest-striking faults and the presence of minor growth strata within negative flower structures associated with these faults suggest that NW-striking faults were reactivated as oblique-extensional (transtensional) transfer faults, accommodating left-lateral motion along major northeast-striking faults and driving subsidence locally during this phase of rifting.

AFT time-temperature curves for samples 1, 2 and 3 indicate that these samples were outside the partial annealing zone (temperatures < 60^0C) during Early Miocene time (Figure 3-9). Based on the observed thickness of Miocene strata (~1707 m) in Nunivak 1 well, samples 1 and 2 located along the hanging wall of the Minto Fault show slow burial from the Early Miocene to Late Miocene at ~0.1 km/Ma. In the eastern region, along the Nenana outcrop, Sample 3 shows slower cooling (~2.7^0C/Ma) associated with the exhumation of the Yukon-Tanana Upland during Miocene time (Brennan, 2012; Frohman, 2015). In contrast, Sample 4 located 4 km farther away, exhibits a phase of rapid cooling 23.7^0C/Ma in the Late Miocene and suggests that the exhumation of the Yukon-Tanana Upland was migrating to the south during this time. In addition, a correlation of calcite twin paleothermometry with fission track data from Sample 4 suggests that calcite-filled shear fractures in all fracture sets (F1 to F4) formed during Mid to Late Miocene time (Figure 3-12).

124

We interpret that the reactivation of pre-existing NW-striking faults during this time resulted in the formation of conjugate shear fractures of sets F2 and F3 corresponding to a NE-directed shortening. These fractures are overprinted by shear fractures of set F4 that contain thick calcite twins (Type II) and have the same average orientation as Minto Fault and are interpreted to have formed as result of left-lateral strike-slip displacement along the Minto fault during this time.

Pliocene to Present Day Development of Transtensional Pull-apart Basin

Pliocene to present-day growth of the Nenana basin is characterized by a profound change in sediment transport directions marked by the deposition of Nenana Gravel and Quaternary sediments in northerly flowing river systems (Figure 3-11d) (Wahrhaftig et al., 1969; Ridgway et al., 2007).

The nature of faulting and changes in sedimentary thicknesses across the northwest- and northeast-striking faults during this phase are difficult to constrain due to poor seismic reflectivity in younger sections of the basin. However, AFT data (Figure 3-9) suggest that samples 1 and 2 in the basin were undergoing rapid burial ($\sim37\text{-}58^0$C/km) during this time whereas samples 3 and 4 situated along the footwall of Minto Fault are being rapidly uplifted at present. The presence of deformed thin calcite twins in all fracture sets (F1 to F4) identified in this study is consistent with our interpretation that the basement rocks along the footwall of Minto Fault were exhumed and deformed since the Pliocene and now are exposed at the Nenana outcrop. Some shear fractures in set F4 that abut on the older fracture sets and contain only thin

125

calcite twins are interpreted to have formed since the Pliocene and continue to form at the present-day (Figure 3-12).

The present-day stress tensor of the Nenana basin as inferred from seismic and fracture data corresponds to a left-lateral strike-slip regime with the principal maximum horizontal stress axis, S_{Hmax}, oriented N30^{0}E. The NE-striking faults in the basin are oriented N40^{0}E at the present-day and therefore lie oblique to the regional compression axis allowing transfer of a component of strike-slip from crustal shortening of the central Alaska Range in response to plate convergence. This implies a 17^0 clockwise rotation of the stress-field in the Nenana basin since the Late Paleocene (Figure 3-11d).

Implications for the Regional Tectonic Setting of Central Interior Alaska

The Nenana basin is located along a diffuse plate boundary between the Bering plate to the west and the North American plate to the east. The basin occupies a position on the foreland side of the northern Alaska Range thrust system (Figure 3-1). Regional dextral Tintina-Kaltag and Denali strike-slip fault systems that bound the basin to the north and south respectively, accommodate N-S crustal shortening driven by an oblique plate convergence to the south. Our study provides more detailed information on regional intra-plate stress fields that were present during the different phases of basin evolution. These stress regimes likely reflect the tectonic influence of regional structural features that were active during individual phases of basin development in central Alaska.

Paleocene time in central Alaska was dominated by an extensional tectonic regime and was largely marked by high geothermal gradients associated with widespread intra-plate magmatism related to Pacific-Kula slab window subduction, regional-scale strike-slip faulting along the Tintina fault system and local subsidence along basin-scale extensional faults (Bradley et al., 2003; Till et al., 2007). In our study, high geothermal gradients (66^0C/km) and initiation of the Nenana extensional half-graben in the Late Paleocene is consistent with regional intra-plate crustal thinning and associated NW-oriented extension, extensive magmatism and high heat flow. Modern day tectonic settings that show elevated geothermal gradients (40^0C/km to 100^0C/km) due to high regional heat flow occur in regions affected by ridge subduction and near trench magmatism (Groome and Thorkelson, 2009; Benowitz et al., 2012).

The Eocene-Oligocene exhumation event was a regional event in central Alaska (Trop and Ridgway, 2007, Dusel-Bacon et al., 2016). Our results suggest that this regional exhumation episode resulted in uplift and erosion of Paleocene and older sedimentary strata in the Nenana Basin with the formation of a basin-wide angular unconformity. Researchers have suggested a number of different explanations for this regional event, including far-field effects of oblique northwestward subduction of oceanic crust and the Resurrection-Kula spreading ridge (Bradley et al., 1993; Haeussler et al., 2003); major strike-slip movements along the Denali and Tintina fault systems (Plafker and Berg, 1994; Ridgway et al., 2002; Roeske et al., 2003) and counterclockwise rotation of western and southwestern Alaska that was driven by Eurasia-North America convergence (Coe et al., 1985; Plafker, 1987; Lonsdale, 1988). The observed regional unconformity associated with the Eocene-Oligocene thermal cooling and uplift event in the Nenana basin could have been caused by any or all of these geologic processes in central Alaska.

Regional extension resumed during Late Oligocene- Early Miocene with deposition of the Lower Miocene sequence in half grabens within the Nenana basin. During this time, extensional displacement along NE-striking faults that form the basin's major boundaries progressively widened the basin to the west. This model requires major dextral-slip along the Denali and Tintina fault systems to drive NW-directed extension in the basin. Previous studies on central Alaska suggest that such large-scale dextral shear was observed along the Denali and Tintina fault systems during Oligocene through Early Miocene time (Nokleberg et al., 2000; Ridgway et al., 2002; Moore and Box, 2016) and is consistent with previous interpretations of the plate reorganization between the Kula/Pacific oceanic plate and the North American continental margin across south-central Alaska (Wallace and Engebretson, 1984; Lonsdale, 1988).

The development of the Nenana basin from Middle Miocene through Late Miocene was marked by a change from dominantly extensional to a transtensional regime. During this episode of transtension, left-lateral strike-slip shear was superimposed on pre-existing NE-trending half grabens in the basin. The inferred sinistral transtension in the basin was coeval with continuation of NW-directed oblique convergence between the Pacific and North American plates and onset of shallow subduction of the Yakutat microplate beneath the southern Alaskan margin (Wallace and Engebretson, 1984; Plafker and Berg, 1994; Miller et al., 2002). We interpret the initiation of a transtensional fault regime in the Nenana basin during this time as the product of oblique crustal shortening across NE-striking major crustal-scale faults due to plate convergence to the south.

Rapid exhumation and tectonic development of the northern foothills of the central Alaska Range occurred from the Early Miocene to present in response to the far field effects of continuing subduction of the Yakutat microplate beneath south-central Alaska (Benowitz et al., 2011; Brennan, 2012). In our study, the high tectonic subsidence rates observed in the basin during Pliocene to recent time likely reflect the influence of this north-vergent thrusting along the actively uplifting Alaska Range; with basin subsidence mainly controlled by oblique slip on the major basin-bounding faults. This setting continues to the present day.

3.6.2 Implications for the Thermal Maturity and Hydrocarbon Generation

The Nenana basin may have significant hydrocarbon resource potential. A detailed understanding of the thermal history and tectonic development of the basin provides information on source rock maturity, timing of hydrocarbon trap formation and the present-day hydrocarbon generation potential of the basin. The burial and thermal history models developed in this study aid in the general understanding of the hydrocarbon potential of the Nenana basin and complement previous hydrocarbon studies on the basin.

Numerous authors have used Rock-Eval Pyrolysis and vitrinite reflectance data from well cuttings of the Nunivak 1 well to evaluate the petroleum potential of the source rocks of the Nenana basin (Stanley and Lillis, 2011, Van Kooten et al., 2012; Dixit and Tomsich, 2014). These studies suggests that both Healy Creek and Paleocene Formation sediments in Nunivak 1 well have thermally-mature gas-prone coals with mean vitrinite reflectance ranging from 0.57 to 0.74 % R_0 and organic-rich oil-prone shales with total organic content (TOC) up to about 61.32 wt.%. Our results show that the source rocks of the Paleocene Formation in Nunivak 1 well first

entered the early oil maturity zone in Late Paleocene time when they were buried to depths greater than 1.5 km and exposed to paleotemperatures significantly greater than the modern-day temperatures (Figure 3-8). However, subsequent uplift and erosion during Eocene-Oligocene time removed significant volumes of mature Paleocene source rocks and lowered the hydrocarbon generation potential of remaining strata by reducing temperature and overburden pressure, It is likely that the NE-striking faults were reactivated as reverse faults at this time, causing hydrocarbon leakage to the surface and further reducing the hydrocarbon storage capacity of the basin.

Hydrocarbon generation in Early Miocene Healy Creek Formation source rocks began in the Mid Miocene time when the source rocks first entered into the early oil generation window (Figure 3-8). This was followed by rapid subsidence during the Pliocene and a corresponding increase in subsurface temperatures and pressures. At present, the source rocks of both the Early Miocene Healy Creek and Paleocene formations in Nunivak 1 well are in the main oil generation window and are likely sources of oil and gas accumulations in the basin. Our seismic-to-well ties suggest that thick fluvial sandstones with porosities ranging from 16% to 24% commonly occur in tilted fault blocks and within the Healy Creek and Suntrana formations of the Nenana basin (Van Kooten et al., 2012; Doyon Limited, 2015). These Miocene reservoir rocks overlie thermally-mature hydrocarbon generating source rocks of the basin and could be the most important reservoir rocks in the basin. As inferred from seismic data, intra-formational shales in the Healy Creek Formation and siltstones of the Sanctuary and Grubstake formations pinch out against the basement highs and could further seal the reservoir sands against fault contacts (Figures 3-6 and 3-7). The observed growth strata and regional unconformities in the basin

further indicate that the formation of NW- and NE-striking faults predates the Miocene to recent hydrocarbon generation and likely controls formation of structural traps in the Miocene sandstone reservoirs. A good example of such faulted block structural traps within the Nenana basin is an intra-basinal high (Figure 3-1) that has been the focus of an extensive hydrocarbon exploration program in recent years (Doyon Limited, 2015).

The timing of fracture development and their orientation may have significant impact on the direction of hydrocarbon migration and trap integrity. Fractures observed in the Nenana outcrop (Table 3-2 and Figure 3-11d) indicate WNW directed crustal extension since Mid Miocene time and could suggest ENE-trending migration pathways from deeper source rocks charging overlying Miocene sandstone reservoirs within the faulted block traps since this time.

3.7 Conclusion

Integrated analysis of seismic reflection data, borehole logs and surface fracture data yielded a model for the structural evolution of the Nenana basin. The burial history results were then integrated with apatite fission track and calcite twinning thermometry data to further provide thermochronological constraints on the timing of deformation in the basin and to evaluate the petroleum source rock maturation. This integrated analysis reveals three distinct phases of rifting and an episode of regional uplift and exhumation since formation of the basin in Late Paleocene time. The results of our fission track analyses further confirm the episodes of maximum paleotemperature associated with rifting and cooling due to a regional episode of uplift and exhumation. In addition to this, we identified four distinct fracture sets showing fractures of differing character (fracture strike and dip, modes of deformation and the nature of fracture fill) from the outcrop studies and tied them to the major faults in the basin. These

fracture sets show evidence of different faulting mechanisms present within the basin and likely represent the state of stress in the region over time.

During Late Paleocene time, intraplate magmatism and subsequent extension formed and/or reactivated a series of normal faults in central Alaska (Till et al., 2007; Wallace and Ruppert, 2012). The Nenana basin initiated as an extensional half graben along one of these extensional faults, the Minto Fault, during this time. Fault-controlled rapid tectonic subsidence (~0.24 km/Ma) and extension-related regional magmatism resulted in high heat flow with corresponding geothermal gradient of ~66^{0}C/km in the basin. This first major paleothermal episode in the basin was coeval with the deposition of Late Paleocene source rocks. These source rocks entered the oil maturity window at shallow depths due to these increased temperatures during the Late Paleocene.

Beginning in the Early Eocene through Late Oligocene, central Alaska experienced regional-scale uplift and exhumation in response to oblique Resurrection-Kula ridge subduction and associated crustal-scale strike-slip faulting along the major Denali and Tintina fault systems (Trop and Ridgway, 2007, Dusel-Bacon et al., 2016). This regional uplift and exhumation event resulted in the reactivation of the Minto Fault as a reverse fault and removal of up to 1.5 km of Late Paleocene strata from some parts of the Nenana basin. Apatite fission track analyses of all samples indicate rapid cooling through the PAZ (120^{0}C to 60^{0}C) during this time. Uplift and erosion of significant volumes of mature source rocks in the basin at this time may have resulted in significant loss of hydrocarbons to the surface.

Plate reorganization between the Kula/Pacific oceanic plate and the North American plate during Miocene time caused a major change in stress field orientation across most of southern Alaska, including the Nenana basin (Wallace and Engebretson, 1984; Lonsdale, 1988). During Mid to Late Miocene time, crustal shortening oblique to the major NE-striking basin-bounding faults superimposed a left-lateral shear on the pre-existing half-grabens in the basin. NW- and NE-striking faults were reactivated as oblique-extensional (transtensional) faults, further driving basin subsidence locally. Both Paleocene and Miocene source rocks were buried and subsequently subjected to increased temperatures that may have initiated hydrocarbon generation. During Mid to Late Miocene time, fracture sets (F1 to F4) observed along the eastern margin of the basin were formed. Fission track data suggest that the hanging wall of the Minto Fault experienced basin subsidence (~0.1 km/Ma) whereas the footwall was uplifted. This uplift may have been related to the progressive southward exhumation of the Yukon-Tanana Upland during this time (Frohman, 2015).

Starting in Pliocene time and continuing to today, central Alaska experienced north-vergent crustal shortening in response to the far field effects of continuing subduction of the Yakutat microplate to the south. This resulted in uplift and exhumation of the central Alaska Range transpressional orogen (Benowitz et al., 2011; Brennan, 2012). At present the northern part of the Nenana basin is undergoing WNW-directed extensional deformation along a step-over zone between major left-lateral strike-slip faults, further widening the basin in the north. The southern part of the basin is rapidly subsiding (geothermal gradients up to 37 to 58^0C/km) in response to the crustal loading due to the Alaska Range to the south. The major source rocks of the basin are currently within the oil-generation window and likely sourcing a fresh hydrocarbon charge

northwestward in updip structural traps that are controlled by the major fault systems in the basin.

3.8 References

Alaska Oil and Gas Conservative Commission (AOGCC). 2015. Digital well history files, Available from http://doa.alaska.gov/ogc/publicdb.html [Accessed September, 2013].

Aksu, A. E., Calon, T. J., Hiscott, R. N., and Yasar, D. 2000. Anatomy of the North Anatolian fault zone in the Marmara Sea, Western Turkey: Extensional basins above a continental transform. GSA Today, 3-7.

Bemis, S. P. 2004. Neotectonic Framework of the North-Central Alaska Range Foothills, M.S. Thesis, University of Alaska Fairbanks, Fairbanks, AK, USA.

Bemis, S.P., and Wallace, W. K. 2007. Neotectonic framework of the north-central Alaska Range foothills, in K. D. Ridgway, J. M. Trop, J. M. G. Glen, and J. M. O'Neill (Eds.), Tectonic growth of a collisional continental margin: Crustal evolution of southern Alaska. Geological Society of America Special Paper, 431:549-572.

Bemis, S. P., Carver, G. A. and Koehler, R. D. 2012. The Quaternary thrust system of the northern Alaska Range. Geosphere, 8(1):196-205, doi: 10.1130/GES00695.1.

Bemis, S. P., Welon, R. J., and Carver, G. A. 2015. Slip partitioning along a continuously curved

fault: Quaternary geologic controls on Denali fault system partitioning, growth of the Alaska

Range, and the tectonics of south-central Alaska, Lithosphere, L352.1, doi:10.1130/L352.1.

Ben-Avraham, Z. 1992. Development of asymmetric basins along continental transform faults.

Tectonophysics, 215: 209–220.

Benowitz, J. A., Layer, P. W., Armstrong, P., Perry, S., Haeussler, P. J., Fitzgerald, P. G., and

VanLaningham, S. 2011. Spatial variations in focused exhumation along a continental scale

strike-slip fault: The Denali fault of the eastern Alaska Range. Geosphere, 7(2): 455–467,

doi:10.1130/GES00589.1.

Benowitz, J. A., Haeussler, P. J., Wallace, W. K., O'Sullivan, P. B., and Gillis, R. J. 2012.

Cenozoic tectono-thermal history of the Tordrillo Mountains, Alaska: Paleocene–Eocene ridge-

subduction, decreasing relief, and late Neogene faulting. Geochemistry Geophysics Geosystems,

13 (4): Q04009, doi:10.1029/2011GC003951.

Bradley, D. C., Haeussler, P., and Kusky, T. M. 1993. Timing of early Tertiary ridge subduction

in southern Alaska. United States Geological Survey Bulletin, 2068: 163-177.

Bradley, D., Kusky, T., Haeussler, P., Goldfarb, R., Miller, M., Dumoulin, J., Nelson, S., and Karl, S. 2003. Geologic signature of early Tertiary ridge subduction in Alaska, in Session, V.B., Roeske, S.M., and Pavlis, T.L., eds., Geology of a transpressional orogen developed during ridge-trench interaction along the north Pacific margin. Geological Society of America Special Paper, 371: 19-49.

Brennan, P.R.K. 2012. Lithospheric structure and geologic development of a collisional orogen: Insights from the central Alaska Range, Master's Thesis, Purdue University, Indiana, USA.

Brocher, T. M., Fuis, G. S., Lutter, W. J., Christensen, N. I., and Ratchovski, N. A. 2004. Seismic velocity models for the Denali fault zone along the Richardson Highway, Alaska, in 2002 Denali earthquake. Seismological Society of America Bulletin, Special Issue, 94: 85–106.

Brogan, G. E., Cluff, L. S., Korringa, M. K., and Slemmons, D. B. 1975. Active faults of Alaska, Tectonophysics, 29: 73–85.

Buffler, R. T., and Triplehorn, D. M. 1976. Depositional environments of the Tertiary coal-bearing group, central Alaska, in Miller, T.P., ed., Recent and ancient sedimentary environments in Alaska, Proceedings of Symposium, April 2-4, Anchorage: Anchorage, Alaska Geological Survey, H1-H13.

Burkhard, M. 1993. Calcite twins, their geometry, appearance and significance as stress–strain markers and indicators of tectonic regime: a review. Journal of Structural Geology, 15: 351–368.

Carver, G. A., Bemis, S. P., Solie, D. N., and Obermiller, K. E. 2008. Active and potentially active faults in or near the Alaska Highway corridor, Delta Junction to Dot Lake, Alaska. Alaska Division of Geological & Geophysical Surveys Preliminary Interpretive Report, 2008-3D: 1-32.

Chopra, S., and Marfurt, K. J. 2008. Gleaning meaningful information from seismic attributes. First Break, 26: 43–53.

Coe, R. S., Globerman, B. R., Plumley, P. R., and Thrupp, G. 1985. Paleomagnetic results from Alaska and their tectonic implications, in Howell, D.G., ed., Tectonostratigraphic Terranes of the Circum-Pacific Region: Houston, Texas. Circum-Pacific Council for Energy and Mineral Resources, Earth Science Series, 1: 85–108.

Contreras, J., Scholz, C. H., King, G. C. P. 1997. A general model of rift basin evolution, constraints of first order stratigraphic observations. Journal of Geophysical Research, 102: 7673–7690.

Cross, R. S., and Freymueller, J. T. 2008. Evidence for and implications of a Bering plate based on geodetic measurements from the Aleutians and western Alaska. Journal of Geophysical Research, 113: B07405, doi:10.1029/2007JB005136.

Dixit, N. C., and Tomsich, C. S. 2014. Apatite fission track, magnetic susceptibility, and vitrinite reflectance analyses on cuttings from the Nunivak #1 and Nenana #1 wells, Alaska. Division of Geological & Geophysical Surveys Geologic Materials Center Data Report, 422 (1): pp. 891, doi:10.14509/27042.

Dixit, N. C., and Hanks, C. L. 2015. Cenozoic structural framework and tectono-sedimentary evolution of the southern Nenana basin, Alaska [abs]: Implications for conventional and unconventional hydrocarbon exploration. The American Association of Petroleum Geologists Annual Convention and Exhibition, Denver, Colorado, 3 June 2015.

Donelick, R. A., O'Sullivan, P. B., and Ketcham, R. A. 2005. Apatite fission-track analysis. Reviews in Minerology and Geochemistry, 58:49-94. doi:10.2138/rmg.2005.58.3.

Doyon Limited. 2015. Alaska onshore rift basins, Nenana and Yukon Flats. Available from http://doyonoil.com/Content/pdfs/NenanaBasin3DSeismic.pdf [Accessed November, 2015].

Durney, D. W., and Ramsay, J. G. 1973. Incremental strains measured by syntectonic crystal growths. In: De Jong, K. A., Scholten, R. (Eds), Gravity and Tectonics, Wiley, New York, 67-96.

Dusel-Bacon, C., Bacon, C. R., O'Sullivan, P. B., and Day, W. C. 2016. Apatite fission-track
evidence for regional exhumation in the subtropical Eocene, block faulting, and localized fluid
flow in east-central Alaska. Canadian Journal of Earth Sciences, 53: 260–280,
dx.doi.org/10.1139/cjes-2015-0138.

Eberhart-Phillips, D., Haeussler, P. J., Freymueller, J. T., Frankel, A. D. et al. 2003. The 2002
Denali fault earthquake, Alaska: a large magnitude, slip-partitioned event. Science, 300: 1113–
1118.

Ferrill, D. A., Morris, A. P., Evans, M. A., Burkhard, M., Groshong Jr., R. H., and Onasch, C. M.
2004. Calcite twin morphology: a low-temperature deformation geothermometer, Journal of
Structural Geology, 26: 1521–1529.

Fisher, M. A., Pellerin, L., Nokleberg, W. J., Ratchkovski, N. A., and Glen, J. M. G. 2007.
Crustal structure of the Alaska Range orogen and Denali fault along the Richardson Highway.
Geological Society of America Special Papers, 431: 43–53, doi:10.1130/2007.2431(03).

Fletcher, H. 2002. Crustal Deformation in Alaska Measured using the Global Positioning system,
Ph.D. Dissertation, University of Alaska Fairbanks, Fairbanks, Alaska, USA.

Frohman, R. A. 2015. Identification and evolution of tectonic faults in the greater Fairbanks area,
Alaska, Master's Thesis, University of Alaska Fairbanks, Fairbanks, Alaska, USA.

Frost, G. M., Barnes, D. F. and Stanley, R. G. 2002. Geologic and isostatic gravity map of the

Nenana basin area, central Alaska. United States Geological Survey Geologic Investigations

Series Map, 2543 (16), 2 sheets, scale 1:250,000.

Gallagher, K., Brown, R., and Johnson, C. 1998. Fission track analysis and its applications to

geological problems, Annual Review of Earth and Planetary Sciences, 26: 519–572,

doi:10.1146/annurev.earth.26.1.519.

Gleadow, A. J. W., Duddy, I. R., Green, P. F., and Lovering, J. F. 1986. Confined fission track

lengths in apatite: a diagnostic tool for thermal history analysis. Contributions to Minerology and

Petrology, 94: 405-415.

Green, P. F., Duddy, I. R., Laslett, G. M., Hegarty, K. A., Gleadow, A. J. W., and Lovering, J. F.

1989. Thermal annealing of fission tracks in apatite: Quantitative modelling techniques and

extension to geological timescales. Chemical Geology- Isotope Geoscience Section, 79: 155–

182.

Groome, W., and Thorkelson, D. 2009. The three-dimensional thermo-mechanical signature of

ridge subduction and slab window migration. Tectonophysics, 464: 70–83,

doi:10.1016/j.tecto.2008.07.003.

Haeussler, P. J., Bradley, D. C., Wells, R., and Miller, M. L. 2003. Life and death of the Resurrection plate: evidence for an additional plate in the northeastern Pacific in Paleocene–Eocene time. Geological Society of America Bulletin, 115: 867–880.

Haeussler, P. J. 2008. An overview of the neotectonics of interior Alaska: Far- field deformation from the Yakutat microplate collision, in Freymueller, J. T., et al., eds., Active tectonics and seismic potential of Alaska. American Geophysical Union, Geophysical Monograph, 179: 269–285.

Hubbert, M. K. 1953. Entrapment of petroleum under hydrodynamic conditions. AAPG Bulletin, 37: 1954–2026.

Hunt, J. M. 1996. Petroleum Geochemistry and Geology. W. H. Freeman, New York, NY, USA, 2nd edition, pp. 743.

Ketcham, R. A., Donelick, R. A., and Carlson, W. D. 1999. Variability of fission-track annealing kinetics: Extrapolation to geological time scales. American Mineralogist, 84: 1235-1255.

Ketcham, R. A., Carter, A. C., Donelick, R. A., Barbarand, J., and Hurford, A. J. 2007. Improved modeling of fission-track annealing in apatite. American Mineralogist, 92: 799-810.

Koehler, R. D. 2013. Quaternary Faults and Folds (QFF). Alaska Division of Geological & Geophysical Surveys Digital Data Series 3, Available from http://maps.dggs.alaska.gov/qff/ doi:10.14509/24956.

Lanphere, M. A. 1978. Displacement history of the Denali fault system, Alaska and Canada. Canadian Journal of Earth Sciences, 15: 817 – 822.

Laubach, S. E. 2003. Practical approaches to identifying sealed and open fractures. AAPG Bulletin, 87: 561–579.

Lesh, M. E., and Ridgway, K. D. 2007. Geomorphic evidence of active transpressional deformation in the Tanana foreland basin, south-central Alaska, in K. D. Ridgway, J. M. Trop, J. M. G. Glen, and J. M. O'Neill (Eds.), Tectonic growth of a collisional continental margin: Crustal evolution of southern Alaska. The Geological Society of America Special Paper, 431: 573-593.

Lonsdale, P. 1988. Paleogene history of the Kula plate: offshore evidence and onshore implications. Geological Society of America Bulletin, 100: 733–754, doi: 10.1130/0016-7606(1988)1002.3.CO;2.

Mann, P. 2007. Global catalogue, classification, and tectonic origin of restraining and releasing bends on strike-slip faults, in Cunningham, D., and Mann, P., eds., Tectonics of strike- slip restraining bends. Geological Society of London Special Publication.

Matmon, A., Schwartz, D. P., Haeussler, P. J., Finkel, R., Lienkaemper, J. J., Stenner, H. D., and Dawson, T. E. 2006. Denali fault slip rates and Holocene–late Pleistocene kinematics of central Alaska. Geology, 34: 645–648.

May, S. R., Ehman, K. D., Gray, G. G., and Crowell, J. C. 1993. A new angle on the tectonic evolution of the Ridge basin, a "strike-slip" basin in southern California. Geological Society of America Bulletin, 105: 1357–1372.

Merritt, R. D. 1986. Coal geology and resources of the Nenana Basin, Alaska. Alaska Division of Geological & Geophysical Surveys, Public-data File, 086-74, pp. 71.

Miller, M. L., Bradley, D. C., Bundtzen, T. K., and McClelland, W. 2002. Late Cretaceous through Cenozoic strike-slip tectonics of southwestern Alaska. Journal of Geology, 110: 247-270, doi:10.1086/339531.

Moore, T. E., and Box, S. E. 2016. Time-slice maps showing age, distribution, and style of deformation in Alaska north of 60° N. U.S. Geological Survey Open-File Report, 2016–1138, pp. 101, Available from http://dx.doi.org/10.3133/ofr20161138.

Murphy, D. C. and Mortensen, J. K. 2003. Late Paleozoic and Mesozoic features constrain displacement on Tintina fault and limit large-scale orogen-parallel displacement in the northern Cordillera [abs]. Geological Association of Canada-Mineralogical Association of Canada-Society of Economic Geologists, Vancouver, pp. 151.

Nokleberg, W. J., Parfenov, L. M., Monger, J. W. H., Norton, I. O., Khanchuk, A. I., Stone, D. B., Scotese, C. R., Scholl, D. W., and Fujita, K. 2000. Phanerozoic tectonic evolution of the circum-North Pacific. United States Geological Survey Professional Paper, 1626, pp. 122.

O'Sullivan, P. B. 1999. Thermochronology, denudation and variations in palaeosurface temperature: a case study from the North Slope foreland basin, Alaska. Basin Research, 11(3): 191–204.

Page, R. A., Plafker, G., and Pulpan, H. 1995. Block rotation in east-central Alaska: a framework for evaluating earthquake potential. Geology, 23 (7): 629-632.

Plafker, G. 1987. Regional geology and petroleum potential of the northern Gulf of Alaska continental margin, in Scholl, D. W., Grantz,A., and Vedder, J. G., eds., Geology and resource potential of the continental margin of western North America and adjacent ocean basins: Houston, Texas. Circum-Pacific Council for Energy and Mineral Resources, Earth Science Series, 6: 229–268.

Plafker, G., and Berg, H. C. 1994. Review of the geology and tectonic evolution of Alaska, in G. Plafker, and H. C. Berg (Eds.), The Geology of Alaska. Boulder, Colorado, Geological Society of America, The Geology of North America, G-1: 989-1021.

Priest, S. D. 1993. Discontinuity analysis for rock engineering. Chapman & Hill, pp. 473.

Ratchkovski, N. A., and Hansen, R. 2002. New constraints on tectonics of interior Alaska: earthquake locations, source mechanisms, and stress regime. Bulletin of the Seismological Society of America, 92 (3): 998-1014.

Ridgway, K. D., Trop, J. M., Nokleberg, W. J., Davidson, C. M., and Eastham, K. R. 2002. Mesozoic and Cenozoic tectonics of the eastern and central Alaska Range: Progressive basin development and deformation in a suture zone. Geological Society of America Bulletin, 114: 1480-1504.

Ridgway, K. D., Thoms, E. E., Layer, P. W., Lesh, M. E., White, J. M., and Smith, S. V. 2007. Neogene transpressional foreland basin development of the north side of the central Alaska Range, Usibelli Group and Nenana Gravel, Tanana Basin, in K. D. Ridgway, and others (Eds.), Tectonics Growth of a Collisional Continental Margin - Crustal evolution of southern Alaska. Geological Society of America Special Paper, 431: 507–547.

Rizzo, A. J. 2015. Natural fracture character and distribution adjacent to the Nenana basin, central Alaska, Master's Thesis, University of Alaska Fairbanks, Fairbanks, Alaska, USA.

Roeske, S. M., Snee, L. W., and Pavlis, T. L. 2003. Dextral slip reactivation of an arc-forearc boundary during Late Cretaceous-Early Eocene oblique convergence in the northern Cordillera, in Sisson, V. B., Roeske, S. M., and Pavlis, T. L., eds., Geology of a transpressional orogen developed during ridge trench interaction along the North Pacific margin. Geological Society of America Special Paper, 371: 141–170.

Ruppert, N. A., Ridgway, K. D., Freymueller, J. T., Cross, R. S., and Hansen, R. A. 2008. Active tectonics of interior Alaska - Seismicity, GPS geodesy, and local geomorphology, in Freymueller, J. T. , Haeussler, P. J., Wesson, R. L., and Ekström, G. (Eds.), Active tectonics and seismic potential of Alaska: Washington, D.C. American Geophysical Union, Geophysical Monograph, 179: 109-133.

Schlische, R.W. 1991. Half-graben basin filling models: new constraints on continental extensional basin evolution. Basin Research, 3: 123–141.

Seeber, L., Sorlien, C., Steckler, M., and Cormier, M. H. 2010. Continental transform basins: why are they asymmetric?. EOS -Transactions of the American Geophysical Union, 91: 29–31.

Stanley, R. G., and Lillis, P. G. 2011 Preliminary interpretation of Rock-Eval pyrolysis and vitrinite reflectance results from the Nunivak 1 well in the Nenana basin, central Alaska (Abs.), Society of Petroleum Engineers and Pacific Section, American Association of Petroleum Geologists, 87–88.

Steckler, M. S., and Watts, A. B. 1978. Subsidence of the Atlantic-type continental margins off New York. Earth and Planetary Science Letters, 41: 1-13.

Tape, C. H., Silwal, V., Ji, C., Keyson, L., West, M. E., and Ruppert, N. A. 2015. Transtensional tectonics of the Minto Flats fault zone and Nenana basin, central Alaska. Bulletin of the Seismological Society of America, 105 (4): 2081-2100.

Till, A. B., Roeske, S. M., Bradley, D. C., Friedman, R., and Layer, P. W. 2007. Early Tertiary ranstension-related deformation and magmatism long the Tintina fault system. Alaska. In: Till, A. B., Roeske, S. M., Foster, D. A., and Sample, J. (eds.) Exhumation and continental strike-slip fault systems. Geological Society of America Special Paper, 434: 233–264, doi: 10.1130/2007.2434(11).

Trop, J. M., and Ridgway, K. D. 2007. Mesozoic and Cenozoic tectonic growth of southern Alaska—A sedimentary basin perspective, in Ridgway, K. D., Trop, J. M., Glen, J. M. G., and O'Neill, J. M., eds., Tectonic growth of a collisional continental margin- crustal evolution of southern Alaska. Geological Society of America Special Paper, 431: 55–94.

Van Kooten, G. K., Richter, M. and Zippi, P. A. 2012. Alaska's interior rift basins: A new frontier for discovery, Oil and Gas Journal, pp. 10.

Wahrhaftig, C., Wolfe, J. A., Leopold, E. B. and Lanphere, M. A. 1969. The coal-bearing group in the Nenana coal field, Alaska. United States Geological Survey Bulletin, 1274: 1-30.

Wahrhaftig, C. 1987. The Cenozoic section at Suntrana Creek, in M. L. Hill (Eds.), Geological Society of America, Cordilleran Section, Centennial Field Guide, 1: 445–450.

Wallace, W. K., and Engebretson, D.C. 1984. Relationship between plate motions and Late Cretaceous to Pa!cogene magmatism in southwestern Alaska. Tectonics, 3: 295-315.

Wallace, W.K., and Ruppert, N. 2012. Young tectonics of a complex plate boundary zone: Indentation, rotation, and escape in Alaska. American Geophysical Union fall meeting, San Francisco, CA, Abstract T14A-08.

Wilson, F. H., Dover, J. H., Bradley, D. C., Weber, F. R., Bundtzen, T. K., and Haeussler, P. J. 1998. Geologic map of Central (interior) Alaska. U.S. Geological Survey Open-File Report, 98-133-A, 62, 3 sheets.
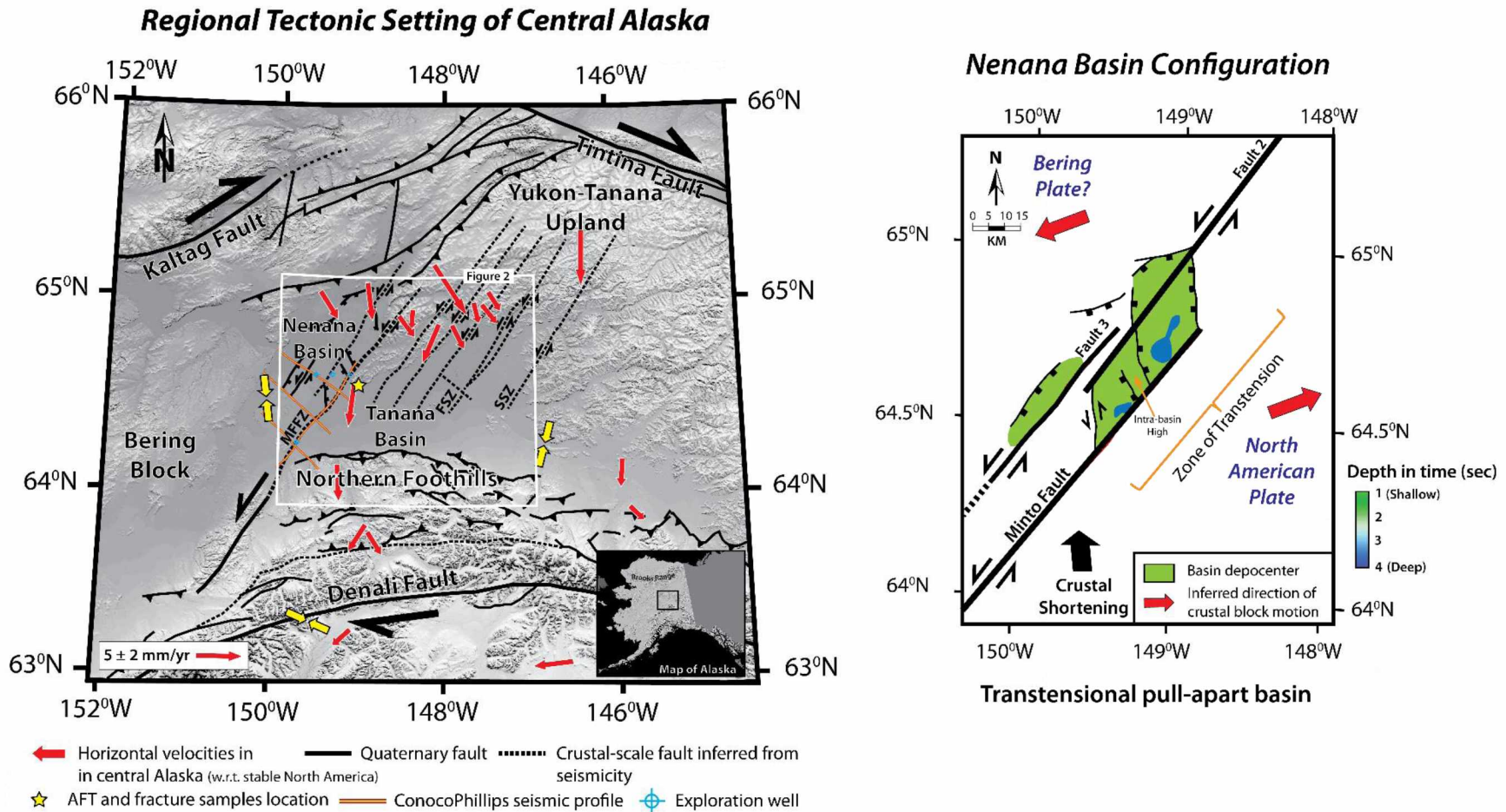
Figure 3-1 Simplified tectonic setting of the Nenana basin, central Interior Alaska

(Left) Simplified tectonic map showing regional tectonic framework of central Interior Alaska and location of the Nenana basin relative to major active faults in the region. Faults are modified from Bemis (2004), Koehler (2013), Frohman (2015) and Tape et al. (2015). the Minto Flats Seismic Zone (MFSZ) , the Fairbanks Seismic Zone (FSZ) and the Salcha Seismic Zone (SSZ). White box indicates the position of Figure 2. (Right) Simplified present-day tectonic model

of the transstensional Nenana pull-apart basin (modified from Dixit and Hanks, 2015). Plate motion velocity vectors are inferred from the GPS velocities available

for the region (Fletcher, 2002).
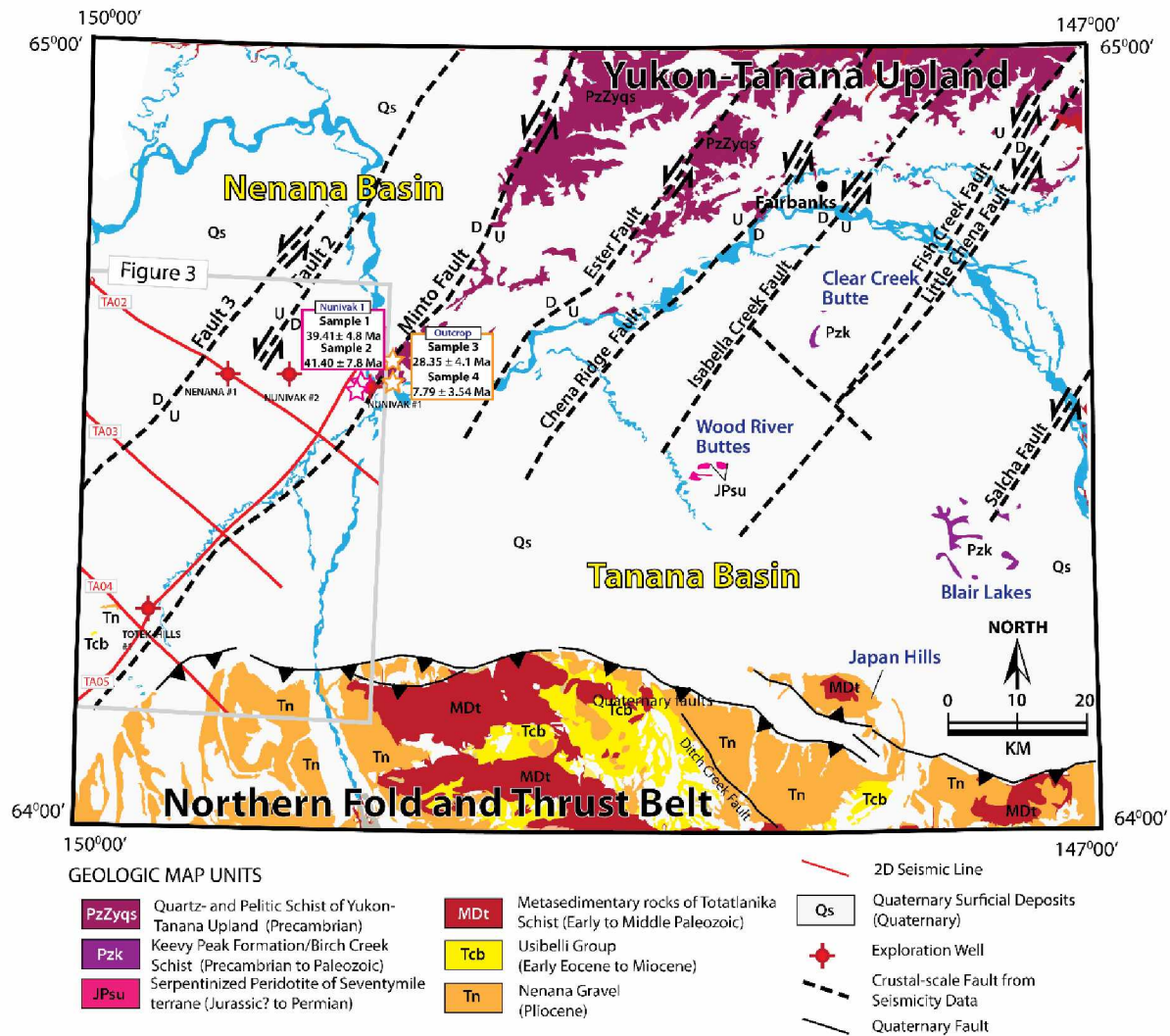
Figure 3-2 Geologic of central Interior Alaska

Geologic map of central Interior Alaska, showing the Cenozoic-age Nenana basin and exposed geology, including major lithologic units and regional fault systems. Dashed black lines indicate high-angle strike-slip faults inferred from active seismicity in the region as well as in surface outcrops in the Fairbanks area, (Ruppert et al., 2008; Frohman, 2015; Tape et al., 2015). Quaternary thrust faults are shown as black lines with thrust symbols and define the northern limit of the Northern Foothills fold-and-thrust belt of the central Alaska Range (Bemis, 2004). Red box indicates the extent of seismic profiles used in this study (Figure 3; courtesy of ConocoPhillips). Map modified from Wilson et al. (1998). Stars indicate location of AFT samples collected from the wells (pink star) and obtained from the Nenana outcrop (orange star) used in this study (Rizzo, 2015).
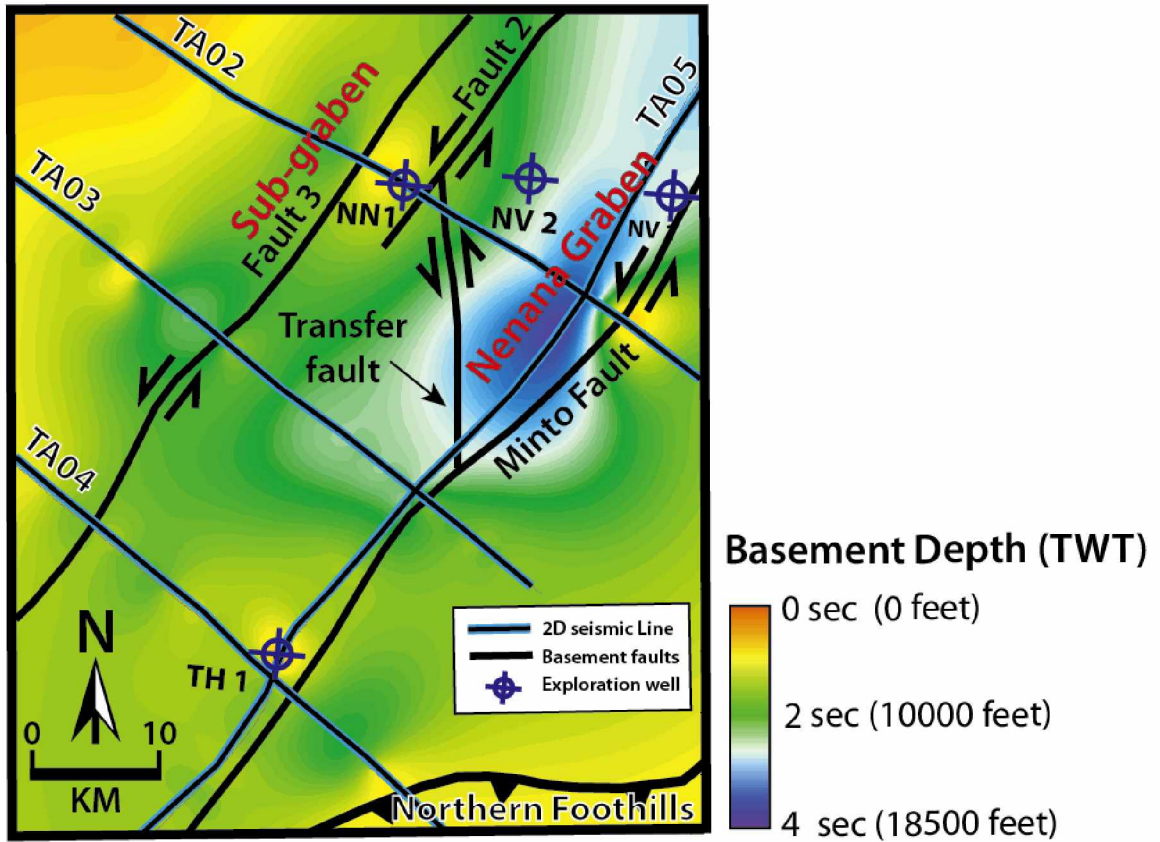
Figure 3-3 Seismic basement depth map of the Nenana basin

Top of basement map for the Nenana basin showing the distribution of faults (solid black lines) and major structural

features discussed in text. Map is in two-way travel time and based on the interpretation of 2D seismic profiles (blue

lines) and published structural data by Dixit and Hanks (2015) and Doyon Limited (2015).

Stratum		Color Code	Thickness (ft) (Nunivak 1)	Lithology (Nunivak 1) GR (gAPI) 0–200	Depositional Setting	Structural Style	Tectonic Phase	Seismic Marker
Age	Formation							
Tertiary — Neogene — Pliocene	Nenana Gravel		4500'		Braided fluvial-alluvial fan	Transtensional	Post-rift	NG
Tertiary — Neogene — Miocene — Late	Grubstake Fm. (Usibelli Group, Upper Miocene)		550'		Lacustrine	Transtensional	Post-rift	GF
Tertiary — Neogene — Miocene — Late	Lignite Creek Fm. (Usibelli Group, Upper Miocene)		840'		High-sinuosity mixed load fluvial			
Tertiary — Neogene — Miocene — Middle	Suntrana Fm. (Usibelli Group, Upper Miocene)		960'		Distal sandy braided fluvial			SUF
Tertiary — Neogene — Miocene — Early	Sanctuary Fm. (Usibelli Group, Lower Miocene)		1020'		Lacustrine	Extensional	Syn-rift II	SNF
Tertiary — Neogene — Miocene — Early	Healy Creek Fm. (Usibelli Group, Lower Miocene)		1990'		Proximal gravelly braided fluvial	Extensional	Syn-rift II	HCF
Tertiary — Paleogene — Oligocene / Eocene	Uplift and exhumation				Uplift and exhumation			
Tertiary — Paleogene — Paleocene	Paleocene Fm.		975'		Fluvial-lacustrine-alluvial fan	Extensional	Syn-rift I	LPF
Paleozoic	Basement Schist							BM

Right-margin annotations: Overburden; Seal/Caprock; Reservoir; Seal/Caprock; Reservoir; Oil source; Gas source; Top of oil window (10345', Nunivak 1 well); Oil source; Gas source. "Formation of fracture set F1, F2, F3 & F4."

Figure 3-4 Generalized stratigraphy of the Nenana basin

Figure 4. Generalized stratigraphy showing lithologies, depositional settings, sedimentary thickness, tectonic evolutionary phases and Cenozoic petroleum system of the Nenana basin (modified after Wahrhaftig, 1987; Ridgway et al., 2007; Doyon Limited, 2015).
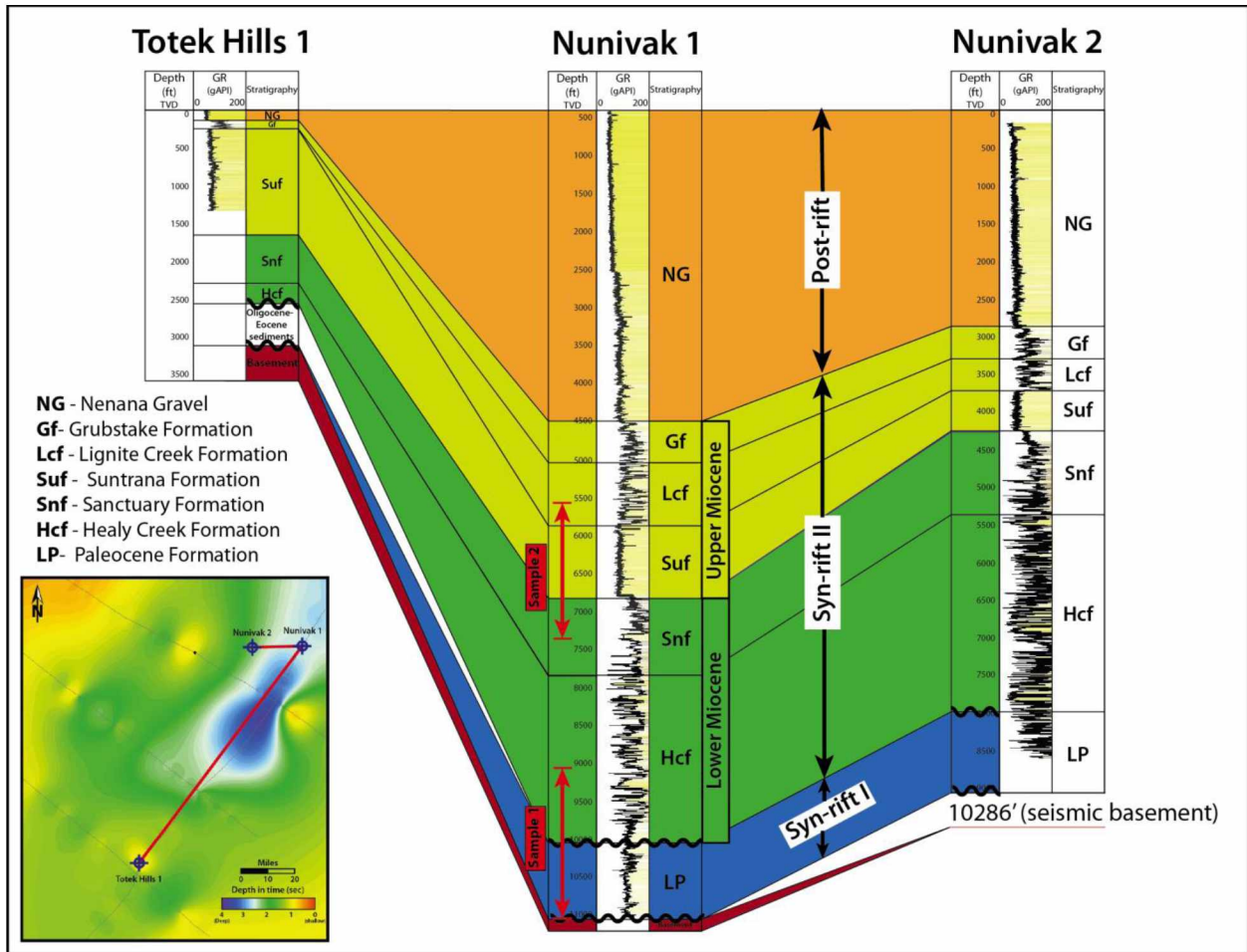
Figure 3-5 Lithostratigraphic well correlation

Location of the wells is shown in Figure 2. The Gamma Ray (GR) borehole logs display a broad lithological overview of strata present in each of the wells. Formation boundaries and ages were based on the published well data by Doyon Limited (2015). Red arrows indicate the depth of samples collected from the well cuttings of Nunivak 1 well for fission-track dating (Dixit and Tomsich, 2014). The sedimentary sequences are further correlated to tectonic deformation episodes that are recognized in the Nenana basin: syn-rift 1, syn-rift 2 and post-rift (See Section 4).
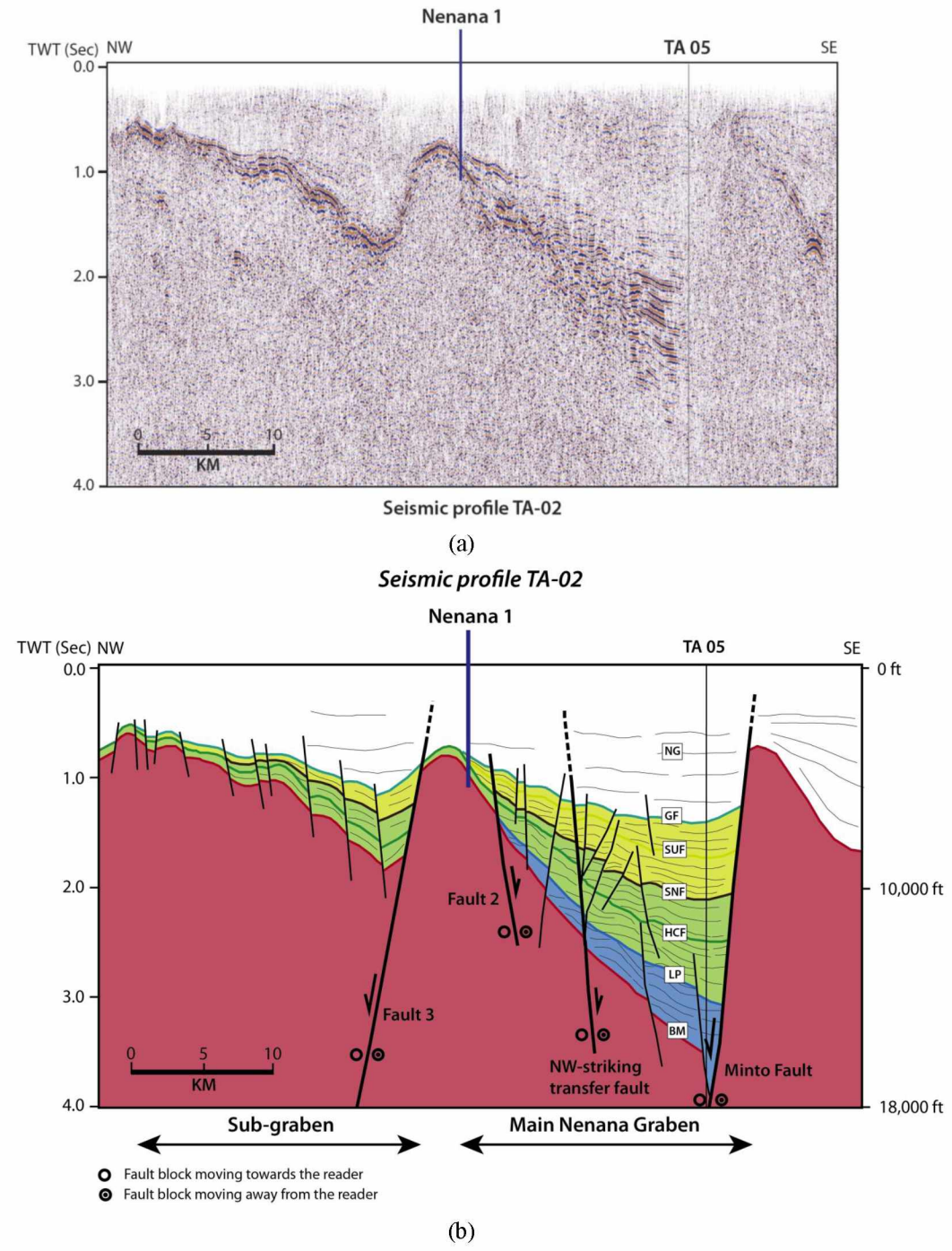
Figure 3-6 Seismic profile TA-02

(A) Uninterpreted seismic profile TA-02 (courtesy of ConocoPhillips), and (b) interpreted seismic profile TA-02 across the Nenana basin. See Figure 3 for the location of seismic profile TA-02. Seismic megasequences and formation boundaries are color coded and match colors of stratigraphic correlation shown in Figure 5.

(a)
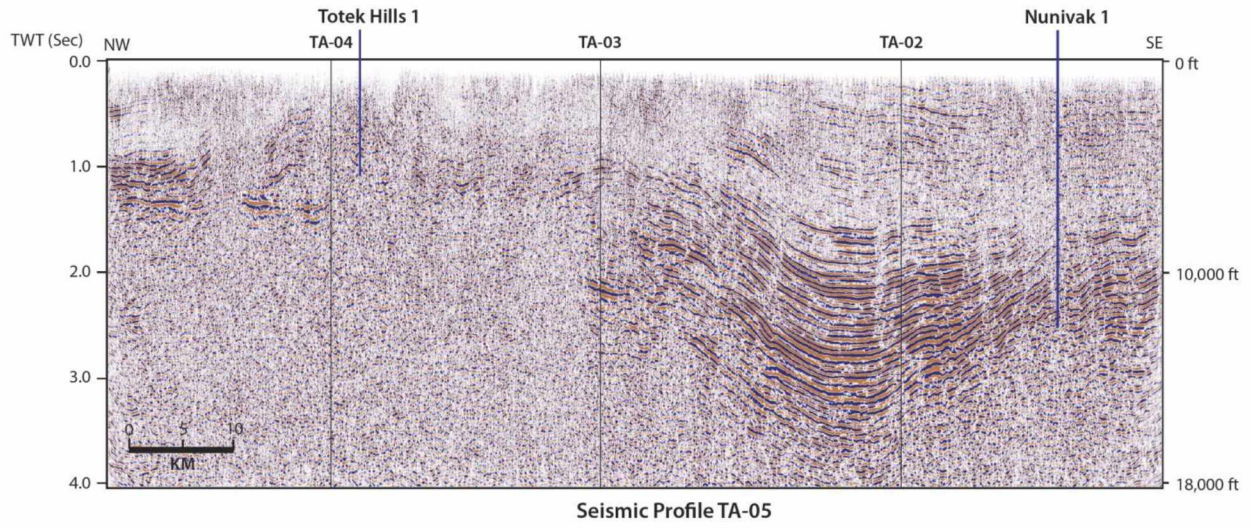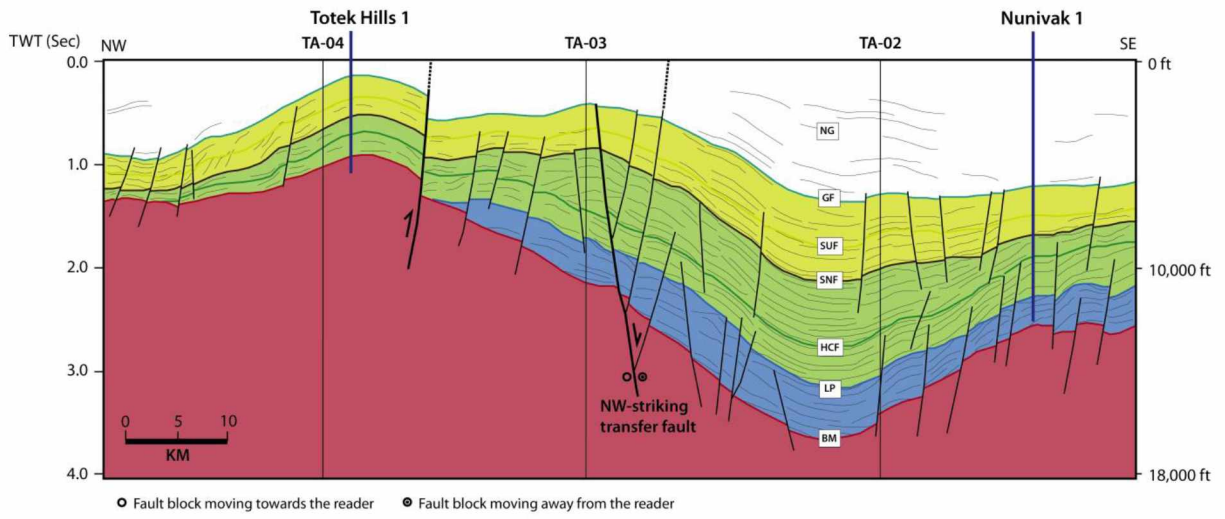
(b)

Figure 3-7 Seismic profile TA-05

(A) Uninterpreted seismic profile TA-05 (courtesy of ConocoPhillips), and (b) interpreted seismic profile TA-05 across the Nenana basin. See Figure 3 for the location of seismic profile TA-05. Seismic megasequences and formation boundaries are color coded and match colors of stratigraphic correlation shown in Figure 5.
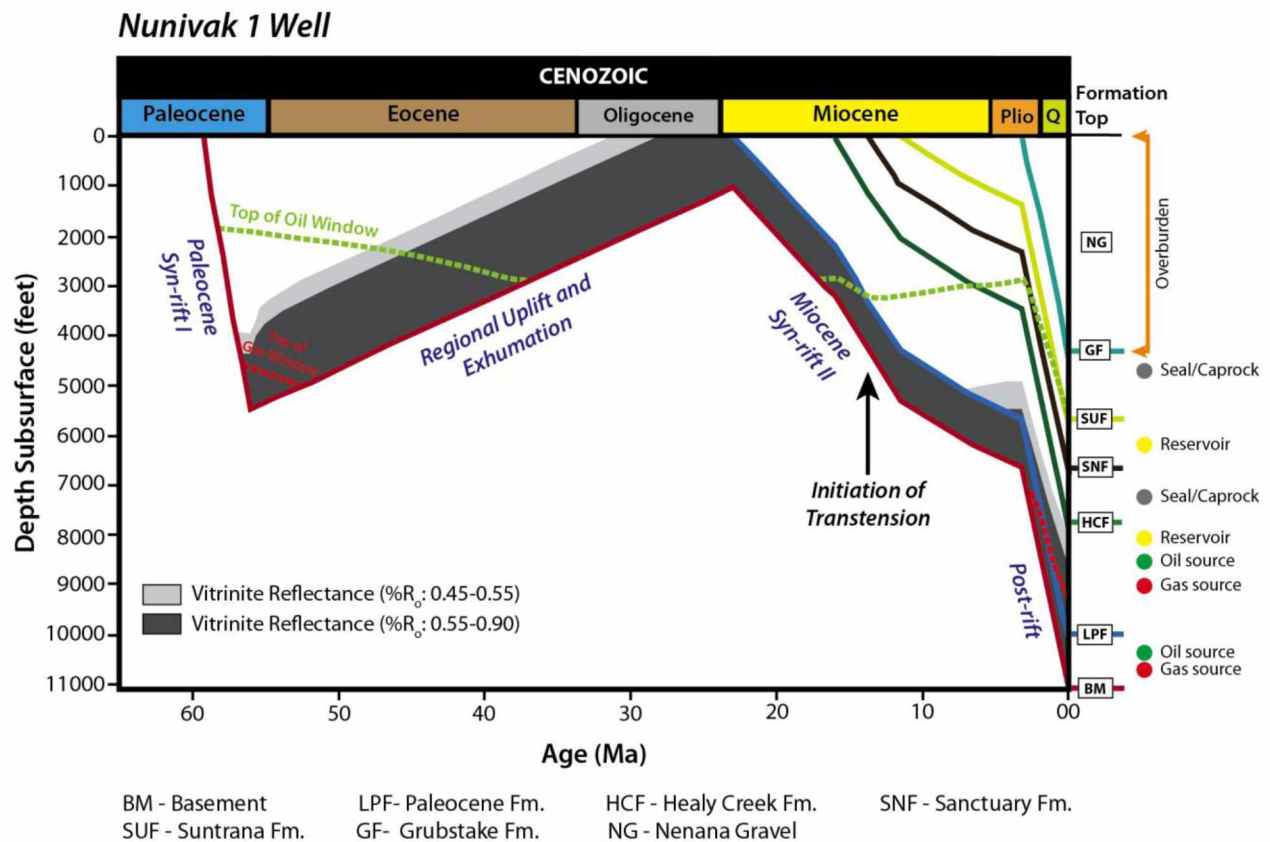
Figure 3-8 Burial and thermal history of Nunivak 1 well, Nenana basin

1D burial history model of the Nunivak 1 well shows the relationship between subsurface depth of the key horizons, formation age and hydrocarbon generation windows. The burial history modeling was performed using BasinMod software developed by Platte River Associates. The model was further calibrated using formation thicknesses identified from Nunivak 1 data (AOGCC, 2015), paleo-heat flow data estimated from fission track analyses and published data by Van Kooten and others (2012), and thermal maturities published by Stanley and Lillis (2011) and Dixit and Tomsich (2014). Estimates of Eocene-Oligocene uplift and erosion are based on geohistory model of Nenana basin pseudowell published by Van Kooten and others (2012).

157
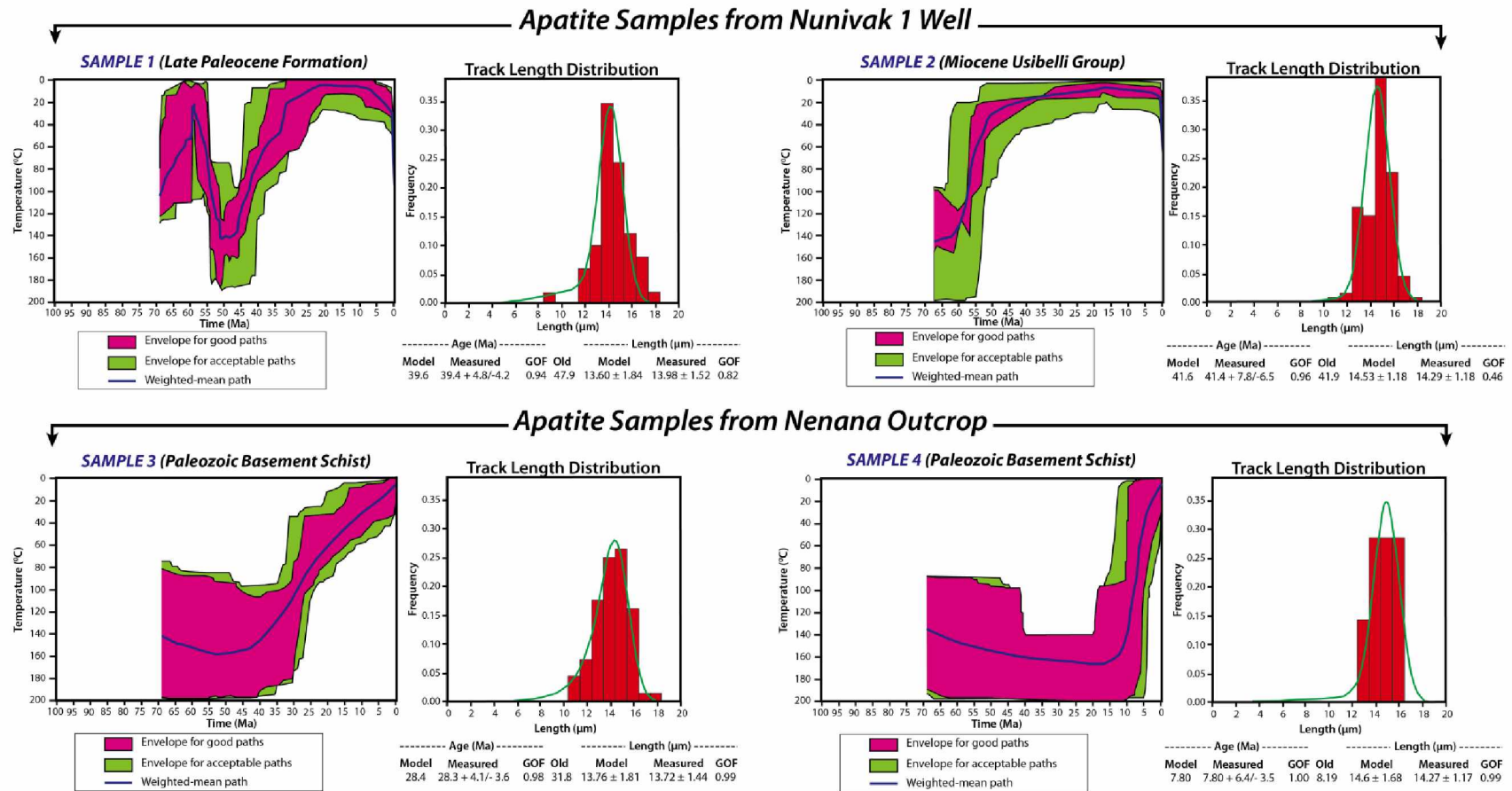
Figure 3-9 Time-temperature (t-T) histories of samples 1 to 4

The t-T pathways were obtained from inverse modeling with HeFTy software (Ketcham, 2007). The main constraints on the possible t-T pathway for each sample include estimates of stratigraphic age, subsurface depth and present-day temperature at a given depth. The goodness-of-fit (GOF) is the fit between the observed and modelled data. Green and pink shaded areas mark envelopes of acceptable fit and good fit solutions (GOF > 0.5) respectively for each sample.
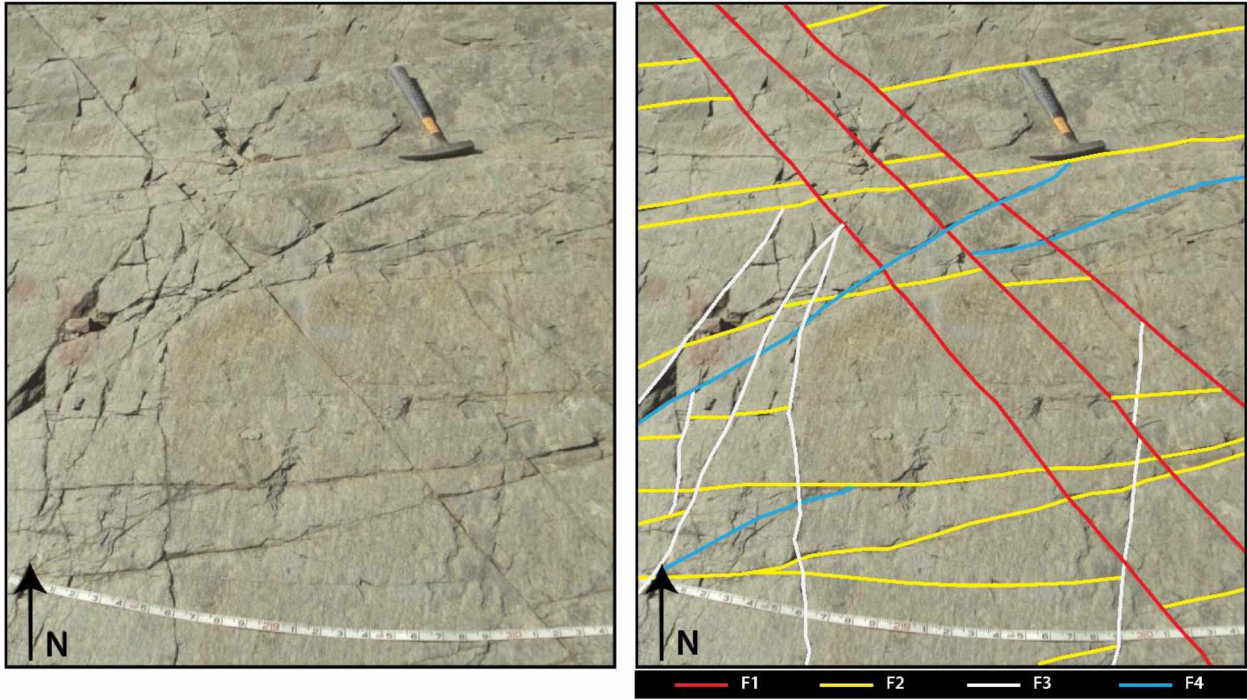
Figure 3-10 Cross-cutting relationships of fracture sets F1 to F4 at the Nenana Outcrop

(Left) Uninterpreted bedding plane surface at the outcrop. (Right) Cross-cutting relationships of fracture sets F1 (red), F2 (green), F3 (orange), and F4 (blue). Set F1 crosscuts all fracture sets and is interpreted to be the earliest fracture set. Sets F2 and F3 commonly cross-cut each other and terminate on set F1. Set F4 terminates on all other fracture sets and is interpreted as the youngest fracture set.
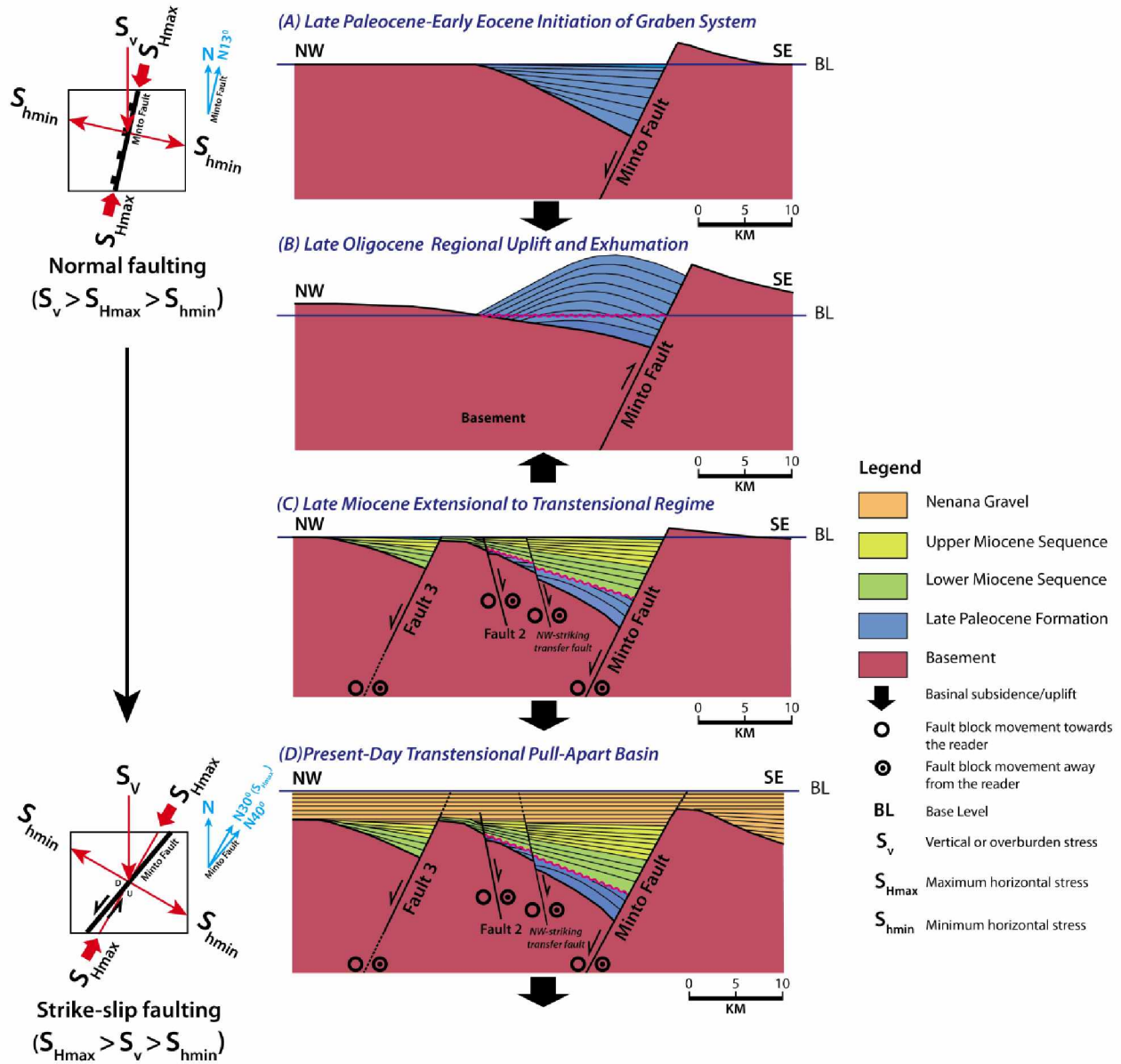
Figure 3-11 Simplified tectonic evolution model of the Nenana basin

(A) Late Paleocene initiation of half-graben; (B) Mid Eocene to Late Oligocene regional uplift and erosion; (C) Early Miocene to Late Miocene transition from extensional to transtensional basin, (D) Pliocene-present day transtensional pull-apart basin. See Section 5.0 for more detailed discussion. Compressional trends are inferred from paleomagnetic, seismic and fracture data studies (Wallace and Ruppert, 2012; this study).

Time-temperature path for the fracture area (Sample 4)
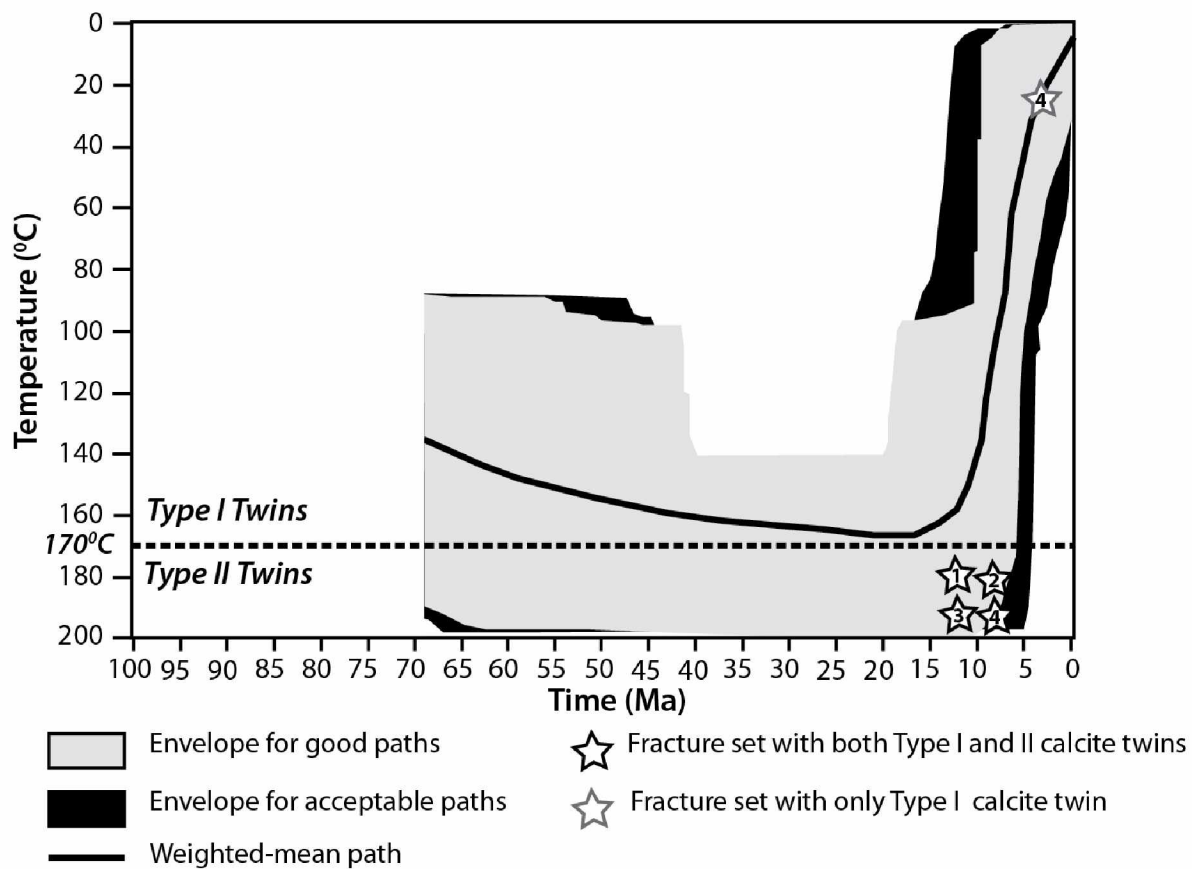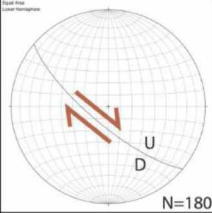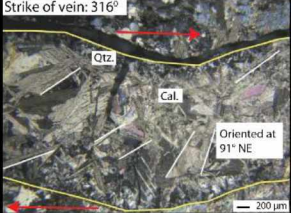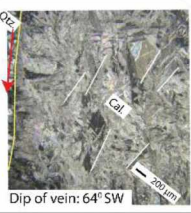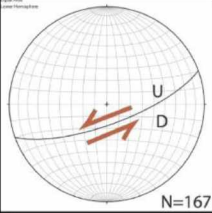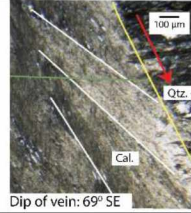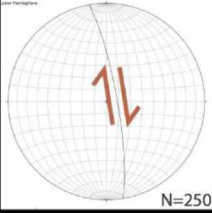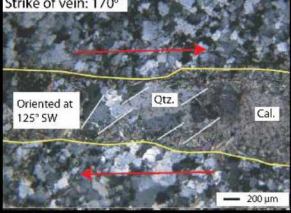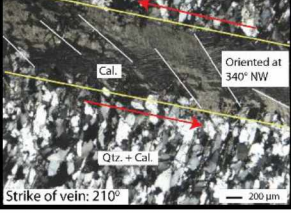
Figure 3-12 Timing of fracture formation for sample 4

Time-temperature path for Sample 4 located at the Nenana outcrop is based on apatite fission track modeling. Stars show the proposed timing of fracture formation based on character and texture of calcite fracture fill. All of the fracture sets indicated they formed under shear conditions and contain calcite fill with Type II calcite twins, suggesting that the fractures were cemented and deformed during the early phase of transtension in Middle to Late Miocene time. Some fractures from set F4 that contain only Type I calcite twins and are interpreted as forming more recently, in Pliocene through present-day time.

161

Table 3-1Apatite fission track data for the Nenana basin samples

Sample	total spots	accepted spots	sum Ns	[U]m ppm	[Th]m ppm	[Sm]m ppm	pooled age	Mean Track Length (μm)	Std. dev (μm)	95%- CI	95%+ CI
Sample 1	40	20	365	27.24	108.47	66.73	39.41	13.98	1.52	4.25	4.76
Sample 2	40	33	604	17.62	22.82	68.31	41.40	14.29	1.18	6.54	7.76
Sample 3	40	24	245	15.06	39.43	75.37	28.35	13.72	1.44	3.57	4.09
Sample 4	40	10	11	11.82	10.56	33.36	7.79	14.27	1.17	3.54	6.4

Table 3-2 Results of fracture analyses showing the orientations and characteristics of fracture sets F1 to F 4.

Set	Orientation	Fracture Character		Sense of Motion (Slip Vector)	Thin Section Analysis (Parallel to the Strike)	Thin Section Analysis (Parallel to the vein)
		Outcrop	Thin Section			
F1	N=180	- Shear fractures - Right-lateral shear - In basement schist	- Quartz with secondary calcite - Right-lateral crystals angled at 40^0-50^0 along strike - Crystals are angled at 30^0 along dip - Type I and Type II calcite twins present	- Strike: 300^0-325^0 - Average dip: $75^0 \pm 30^0$ SW - Dominantly dip-slip with right-lateral component - Slip vector $>40^0$, $<80^0$ SW		
F2	N=167	- Shear fractures - Left-lateral shear - In basement schist	- Quartz and calcite veins - Right-lateral crystals angled at 65^0-70^0 and 40^0-50^0 along strike - Crystals are angled at 50^0 to 70^0 along dip - Type I and Type II calcite twins present	- Strike: 240^0-260^0 - Average dip: $73^0 \pm 30^0$ SE - Dominantly dip-slip with left-lateral component - Slip vector $>40^0$, $<80^0$ SE		
F3	N=250	- Shear fractures - Right-lateral shear - In basement schist	- Quartz and calcite veins - Right-lateral crystal arrangement along strike - Type I and Type II calcite twins present	- Strike: 340^0-360^0 - Average dip: $81^0 \pm 30^0$ E - Dominantly right-lateral with no dip-slip component - Slip vector N/A		
F4	N=217	- Shear fractures - Left-lateral shear - In basement schist	- Quartz and calcite veins - Left lateral crystal arrangement along strike - Type I and Type II calcite twins present	- Strike: 200^0-220^0 - Average dip: $74^0 \pm 30^0$ NW - Dominantly left- lateral with no dip-slip component - Slip vector N/A		

163

4   In situ stress variations associated with regional changes in tectonic setting, Northeastern Brooks Range and eastern North Slope of Alaska[1]

4.1   Abstract

The northeastern Brooks Range of northern Alaska is an active, north-directed fold-and-thrust belt that is advancing on the Barrow Arch and the north-facing passive margin of the Arctic Basin. Density logs, leak-off tests and mud weight profiles from fifty seven wells from the northeastern North Slope were used to determine the magnitude of the present-day in situ stresses and document significant regional lateral and vertical variations in relative stress magnitude. Preliminary analysis of the in situ stress magnitudes indicates two distinct stress regimes across this region of Alaska. Areas adjacent to the eastern Barrow Arch exhibit both strike-slip and normal stress regimes. This in situ stress regime is consistent with fault patterns in the subsurface and with north-south extension along the Barrow Arch and the north Alaska margin. To the south in and near the northeastern Brooks Range thrust front, in situ stress magnitudes indicate an active thrust fault regime is present at depths up to 6000 ft (1829 m). This is consistent with the fold and thrust structures in surface exposures and in the subsurface. However, at depths greater than 6000 ft (1829 m), the relative in situ stress magnitudes indicate a change to a strike-slip regime. This observation is consistent with the few earthquake focal mechanisms in the area and suggests deep north-northeast oriented strike-slip faults may underlie the western margin of the northeastern Brooks Range.

4.2 Introduction

Knowledge of the present-day state of stress is critical to understanding regional-scale tectonic problems as well as the local and regional distribution and character of faults and fractures. Fracture and fault systems can control the delivery of subsurface fluids to wellbores and facilitate the migration of hydrocarbons from source rocks. Regional in situ stress conditions reflect the current tectonic setting and can indicate areas and depths where the crust is critically stressed, and faults and fractures are more likely to act as conduits rather than barriers to fluid flow. Understanding in situ stress conditions is also key to addressing subsurface engineering problems such as wellbore instability, hydraulic fracture stimulation and lost circulation (Zoback, 1992; Martin et al., 2003).

In low-permeability reservoir rocks such as shales, faulting and fault-related fractures play an important role in enhancing reservoir permeability. Natural fractures parallel to the regional maximum principal horizontal in situ stress tend to be open and more permeable than the fractures oriented perpendicular to the maximum horizontal in situ stress (Hubbert and Willis, 1957). In hydraulic fracturing, induced fractures propagate parallel to the maximum principal horizontal stress (Brudy and Zoback, 1999). Consequently, a detailed understanding of the relationship between the present-day stress and the orientation of natural and hydraulically induced fractures is essential to successfully develop a shale reservoir. Estimates of stress magnitudes can be made through the integration of data derived from observations of borehole breakouts, mini-frac tests, density logs and earthquake focal mechanism solutions (Bell and Babcock, 1986; Bell, 1996; Zoback, 2007).

The Alaska North Slope is a physiographic province that extends some 50,000 square miles inland from the Beaufort Sea coastal margin to the crest of the Brooks Range (Shideler and Hechtel, 2000). In this study, we examine the in situ stress state of the northeastern section of the North Slope located between the National Petroleum Reserve, Alaska (NPRA) and the Arctic National Wildlife Refuge (ANWR) (Figure 4-1). This area contains the two largest oil fields in North America, Prudhoe Bay and Kuparuk River fields, and many smaller satellite oil and gas fields such as Alpine and Pt. Thompson fields. In recent years, the primary source rock for these conventional accumulations, the Triassic Shublik Formation, has been the focus of an unconventional shale resource play (Scheirer et al., 2014). Reliable estimations of the in situ stress state is crucial in evaluating the success of hydraulic fracture stimulation treatments, which in turn, strongly affect the productivity of potential shale wells in unconventional reservoirs.

We use data from fifty seven petroleum exploration wells drilled in the northeastern North Slope province to constrain the local and regional changes in in situ stress state to a depth of 9000 ft (2743 m) (Figure 4-2). We examine the available density logs, formation leak-off tests and mud weight profiles, in addition to published data on stress orientations and fault patterns to quantitatively estimate components of the in situ stress state.

4.3   Geological Setting of the Northeastern North Slope, Alaska
The northeastern North Slope of Alaska encompasses three major tectonic provinces. From south to north, these are: the northeastern Brooks Range, the Arctic Foothills of the Brooks Range, and the Arctic coastal plain (Figure 4-3) (Wahrhaftig, 1965). The northeastern Brooks Range consists of the leading edge of the Brooks Range thrust system and includes a thick sequence of folded and thrusted Devonian to Early Cretaceous sedimentary rocks. The initiation

of Brooks Range orogenesis occurred in the late Jurassic to Early Cretaceous, when a south-facing passive continental margin represented by the late Devonian to Triassic Ellesmerian Sequence and pre-Mississippian Franklinian Sequence collided with one or more intraoceanic arc-related terranes (Figure 4-4; Moore et al., 1994). During the Jurassic-Early Cretaceous, opening of the Canada Basin to the north initiated rifting and deposition of the Beaufortian Sequence (Figure 4-4) (Grantz and May, 1983; Houseknecht and Bird, 2011). The present-day North Slope is a fragment of the Paleozoic south-facing passive continental margin (Grantz and May, 1983).

The northward-migrating Brooks Range thrust front formed an east-west-trending foredeep, the Colville Basin, which accumulated large volumes of Late Cretaceous to Quaternary sediments shed from the Brooks Range (the Brookian sequence, Figure 4-4; Bird and Molenaar, 1992). To the north, the basin thins onto a southeast plunging subsurface structural high, the Barrow Arch. Sediments entered the Colville basin from west to east, eventually filling the basin and spilling over the Barrow Arch. Active deposition today is on the north side of the arch, beneath the present-day continental margin.

The current day configuration of the Barrow arch is a product of multiple extension and rift events (Moore et al., 1994). The northern flank of the Barrow Arch is the present-day continental margin that formed during Jurassic rifting and whose northern limit is marked by a series of down-to-the-north, east-west trending graben complexes, the largest of which is the Dinkum Graben (Figure 4-3; Hubbard et al., 1987). The southern flank of the Barrow Arch slopes gently to the south beneath the Colville basin where its shape is modified by several

basement highs. The Fish Creek Platform is a southeast-plunging basement high bounded to the

north by a southeast-striking, basement-involved fault that accommodated post-Aptian dextral

strike-slip displacement. This is the Fish Creek Platform boundary fault (Figure 4-3; Homza,

2004). The Umiat basin is a sub-basin that predates the Colville basin and formed in response to

the northeast-southwest directed Late Paleozoic extension and rifting (Figure 4-3; Fulk, 2010).

Further northeast, the Canning Displacement Zone has been interpreted as an active strike-slip

shear zone of earthquake epicenters (Figure 4-3) and represents a northern extension of the

Aleutian arc Benioff Zone from central Alaska to the Beaufort Sea shelf (Grantz et al., 1983).

4.4   Previous Work on In Situ Stress Distribution

A number of previous studies have investigated the in situ stress field in the North Slope

region. Griffin (1985) first determined the direction of maximum horizontal stress, S_{Hmax} in the

Kuparuk Formation from wellbore ellipticity, sonic velocity and differential strain data collected

from 12 wells in the Kuparuk River Unit, west of Prudhoe Bay. That study found three distinct

local S_{Hmax} directions above the Barrow Arch at 5700 ft (1737 m) – 6800 ft (2073 m): northwest-

southeast, north-south and northeast-southwest oriented. He suggested that this highly variable

local stress pattern differed from the northwest-southeast oriented regional horizontal stresses

due to the influence of pre-existing faults in the area. Blundell and Hallam (1991) later examined

the hydraulic fracture directions in the Kuparuk Formation using wellbore breakouts and

formation micro-scanner (FMS) images. Their interpretation also indicated three different

directions of fracture orientations (northwest-southeast, north-northwest-south-southeast and

northeast-southwest trending) for the Kuparuk Formation above the Barrow Arch that were

consistent with S_{Hmax} directions documented by Griffin (1985).

More recently, Hanks et al. (2000) used borehole breakouts in 30 wells from the northeastern North Slope to determine S_{Hmax} orientations (Figure 4-5A). Their study suggests that S_{Hmax} orientations across the Arctic Foothills and southern Colville basin are dominantly northwest-southeast trending; orthogonal to, and related to, the northeastern Brooks Range thrust front (Figure 4-5B). In contrast, the local stresses above the Barrow Arch show a more complex bimodal stress pattern where S_{Hmax} orientations are generally either northwest or northeast-trending (Hanks et al., 2000). They attribute this bimodal behavior above the Barrow Arch to the complex extensional faulting along the northern Alaska continental margin.

Only a few earthquake focal mechanisms are available from this part of Alaska (Grantz et al., 1983; Biswas et al., 1986; Ruppert, 2008). Stress tensor inversion results from a small subset of earthquakes across the Canning River Displacement zone suggest a strike-slip stress regime with regional S_{Hmax} oriented northeast-southwest (Grantz et al., 1983; Biswas et al., 1986). This contrasts markedly with exposed structures in the northestern Brooks Range, which are dominated by north and northwest directed thrust faults.

4.5   Estimation of In Situ Stress State

The present-day stress state is characterized by five components: (1) the overburden stress (vertical stress, S_v) magnitude; (2) the minimum horizontal stress (S_{hmin}) magnitude; (3) the maximum horizontal stress (S_{Hmax}) magnitude; (4) the maximum horizontal stress (S_{Hmax}) orientation; and (5) the formation pore pressure (P_p) (Bell, 1990 and 1996). As noted, petroleum exploration data comprising density logs, mini-fracture tests, leak-off tests, and borehole breakouts collected during drilling and logging of oil and gas wells can be used to constrain the present-day stress field. The S_{Hmax} orientations in the North Slope region have already been

emphasized in previous studies mentioned earlier. Here we evaluate each of the four remaining components of the present-day stress state.

4.5.1 Vertical Stress or Overburden Stress, S_v

The magnitude of the vertical or overburden stress (S_v) at any point is generally equal to the pressure exerted by the weight of the overlying rocks and the contained fluids above that point. It can be calculated by integrating rock bulk densities from the surface to a given depth (Engelder, 1993) as shown in equation 1.

$$S_v = \int_0^Z \rho(Z)g\,dz \ldots \ldots \ldots \ldots (1)$$

Where $\rho(z)$ is the bulk density of the overlying rocks at depth Z and g is the acceleration due to gravity. We evaluated density logs from 57 vertical oil and gas wells to determine vertical stress magnitudes at the northeastern North Slope. Density logs were corrected for three issues (Rider, 2000) before estimation of vertical stress magnitudes: (1) depths of density logs were corrected for vertical subsea depths (TVDSS) to obtain an accurate density trend at a given depth; (2) the mean density above surface casing for unlogged section was calculated by linear extrapolation of the density log to the surface or from nearby wells that also have the similar density trend; and (3) the density logs were corrected to remove spurious data caused by poor hole conditions. In some cases where no density log was available for a well, average mean density of about 2.3 g/cm^3 (2300 kg/m^3) was assumed for the Paleogene to Neogene sediments, whereas for Cretaceous and older sediments the assumed average rock density was 2.4 g/cm^3 (2400 kg/m^3) based on the density trends of the surrounding wells. These assumed rock densities are close to the modelled rock densities for the northeastern Brooks Range region reported by Giovannetti and Bird (1979). Cross-plotting density and sonic logs from the wells further provided a cluster

of real data points which were then filtered for suspect data from their density and velocity

values. The final density corrected data were used in calculating vertical stress magnitudes for 57

wells (Equation 1).

The vertical stress profile shown on Figure 4-6 illustrates a non-linear stress variation

down to a depth of 6000 ft (1829 m). This non-linear behavior of the vertical stress reflects

continuous increases in bulk densities from surface down to 6000 ft (1829 m) that can be

attributed to a number of factors including the consolidation states, lithology and the deformation

characteristics of the sedimentary formations (Karig and Hou, 1992; Bjørlykke, 2010; Dugan and

Sheahan, 2012).

At greater depths (> 6000 ft (1829 m)), the vertical stress profile is almost linear, (S_v=

6.93×10^{-03} x depth) indicating that the sediment bulk densities are nearly constant.

4.5.2 Minimum Horizontal Stress Magnitude, S_{hmin}

The most reliable method for determining the minimum horizontal stress magnitude

(S_{hmin}) employs data from hydraulic mini-frac tests, leak-off tests (LOTs) and fracture gradients

(Figure 4-7) (Enever et al., 1996). Unfortunately, no hydraulic mini-frac tests were performed for

the 57 wells available for this study. However, a large number of leak-off tests were conducted in

the northeastern North Slope to determine the maximum drilling fluid weights required to drill

the next section of the wellbore (AOGCC, 2014). In a leak-off test, as drilling fluid is pumped

into the wellbore after the casing is set, the pressure of the drilling fluid in a small section of

wellbore is increased linearly until it induces a fracture at the borehole wall. Fracture initiation is

marked by a point of departure (fluid leak-off pressure, LOP) on a pressure versus time plot

(Figure 4-7B). This leak-off pressure is an approximate lower bound estimate of the minimum horizontal stress, S_{hmin} (Bell, 1990; Zoback, 2007).

In our study, the magnitudes of S_{hmin} were estimated from a number of leak-off tests available for the northwestern North Slope (Figure 4-8). Where leak-off data was not available, we used the available fracture gradient data to estimate the S_{hmin} magnitudes for a given well. The fracture gradient is considered to be approximately equal to the leak-off pressure from the leak-off test (Bai, 2011).

4.5.3 Pore Pressure, P_p

Pore pressure (also known as formation pressure, P_p) is the in-situ pressure of the fluids in the pores of a rock formation at a depth of interest. If the pore fluids support the weight of overlying pore fluids, pore pressure equals the hydrostatic pressure of the formation ($P_{hydrostatic}$) (Zoback, 2007). The pore pressures for relatively permeable formations are generally derived from seismic reflection data in advance of drilling or from post-drill methods such as drill stem tests (DSTs), repeat formation testers (RFTs), hydrostatic pressure gradients and drilling mud weights (Zimmerman et al., 1990). In terms of drilling operations, hydrostatic pore pressure at a given depth is calculated as:

$$P_{hydrostatic} = 0.052 * P_w * Z \dots \dots \dots \dots (2)$$

Where, P_w = Equivalent mud weight in lb/gal

Z = Vertical height of fluid column in feet

When pore pressure is equal to lithostatic pressure (overburden stress, S_v), the pore fluids support weight of overlying sediments in addition to the pore fluids (Zoback, 2007).

In this study, nearly all the hydrostatic pore pressure measurements were made using the equivalent mud weight data and available pore pressure gradients derived from seismic velocities (AOGCC, 2014) in the northeastern North Slope. In addition, several pore pressure values were obtained from DST data available for the area.

Figure 4-9 shows that the pore pressure gradient in the northeastern North Slope is generally hydrostatic, with an average gradient of 0.434 psi/ft (9.81 MPa/km). Overpressured intervals are observed below 12000 ft (3658 m) in some wells (See Appendix 7-A). All magnitudes of P_p estimated for these intervals are derived from mud weight data.

4.5.4 Maximum Horizontal Stress Magnitude, S_{Hmax}
The magnitude of the maximum horizontal stress (S_{Hmax}) completes the stress characterization and is generally the most difficult component to determine. The S_{Hmax} magnitude can be determined from borehole breakouts for which the compressive rock strength is known or from hydraulic fractures where the tensile rock strength is available (Brudy and Zoback, 1999). Unfortunately, no rock strength data is available for wells in the northeastern North Slope. However, hydraulic fractures provide a good constraint on the magnitude of the maximum horizontal stress in a vertical well. These fractures form parallel to S_{Hmax} when the tensile strength of rock is greater than the minimum circumferential stress (stress tangential to the wellbore) (Brudy and Zoback, 1999; Zoback, 2007). For this study, we have used empirical formulas related to fracture formation in a vertical wellbore to estimate the magnitudes of S_{Hmax} in the northeastern North Slope. The criteria for the formation of drilling-induced tensile fracture in elastic rocks in a vertical well is represented by,

$$\sigma_{\theta\theta} = S_{Hmax} + S_{hmin} - 2(S_{Hmax} - S_{hmin})\cos2\theta - P_p - P_w \leq T \dots \dots \dots \dots (3)$$

Where, $\sigma_{\theta\theta}$ = the effective hoop stress at the wall of a vertical wellbore

θ = the angle measured from the direction S_{Hmax} around the wellbore wall

P_p = the pore pressure at the depth of drilling induced tensile fracture

P_w = the mud weight at the depth of drilling induced tensile fracture

T = the tensile rock strength (Hubbert and Willis, 1957)

Assuming tensile strength of reservoir rocks to be negligible ($T = 0$), Equation 3 can be reduced to,

$$\sigma_{\theta\theta} = S_{Hmax} + S_{hmin} - 2(S_{Hmax} - S_{hmin}) \cos 2\theta - P_p - P_b \leq 0 \dots \dots \dots \dots (4)$$

where, $P_b = P_w$ = the fracture breakdown pressure (when $T = 0$)

As tensile fracture forms in the direction of maximum horizontal stress ($\theta = 0°$),

$$S_{Hmax} \geq 3\, S_{hmin} - P_p - P_b \dots \dots \dots \dots (5)$$

Substitution of the in situ stress state components (S_{hmin}, P_p and P_b) determined from the Leak-off Tests and mud weight profiles in Equation 5, we were able to constrain a lower bound estimate for the magnitude of S_{Hmax} in the northeastern North Slope.

The S_{Hmax} magnitudes for the northeastern North Slope are summarized in Figure 4-10. The depth profile of S_{Hmax} magnitudes shows a departure from a linear trend. The observed deviation from the general linear trend in the S_{Hmax} values can occur due to uncertainities arising from estimations of all constraining parameters including the formation pore-pressure, P_p, the fracture breakdown pressure, P_b, and the S_{hmin} magnitudes.

4.6   The Spatial Distribution of Stress Fields

The in situ stress magnitudes derived from these fifty seven wells in the northeastern North Slope are summarized in Figure 4-11. Following Anderson's theory of faulting (Figure 4-

12) (Anderson, 1951), the relative magnitudes of S_v, S_{hmin} and S_{Hmax} were then used to define the three distinct tectonic stress regimes:

1. Thrust or reverse fault stress regime ($S_{Hmax} > S_{hmin} > S_v$)

2. Strike-slip fault stress regime ($S_{Hmax} > S_v > S_{hmin}$), and

3. Normal fault stress regime ($S_v > S_{Hmax} > S_{hmin}$)

In order to visualize the regional changes in tectonic stress regimes defined by Anderson's fault types, we used the generalized Angelier's shape parameter ($A_\emptyset$) (Simpson, 1997) methodology to develop indexed stress field maps for depths of 3000 ft (914 m), 6000 ft (1829 m) and 9000 ft (2743 m) for our study area (Figures 4-13, 4-14 and 4-15). The Angelier's shape parameter $\emptyset$, is a ratio of principal stress magnitude differences and determines the slip direction on a specified fault plane which is controlled by relative magnitudes of the principal stresses (Angelier, 1975). Based on the relative magnitudes of the three principal stresses (S_v, S_{Hmax} and S_{hmin}) of situ stress tensor, we calculated Angelier's shape parameter ($\emptyset$) for each of the in situ stress regime at our depths of interest using Equation 6:

$$\emptyset = [\sigma_2 - \sigma_3]/[\sigma_1 - \sigma_3] \ldots \ldots \ldots \ldots (6)$$

Where, σ_1 = the magnitude of maximum principal stress

σ_2 = the magnitude of intermediate principal stress

σ_3 = the magnitude of minimum principal stress

For example in a normal fault regime ($S_v > S_{Hmax} > S_{hmin}$), we considered σ_1, σ_2 and σ_3 to be representative of the magnitudes of S_v, S_{Hmax} and S_{hmin}, respectively. In order to generate stress maps for our study area, we then assigned index numbers, p = 0, 1, 2, and 3 on a stress scale to the normal (0 to 1), strike-slip (1 to 2) and thrust stress (2 to 3) regimes, respectively (Figure 4-

12) (Hurd and Zoback, 2012). Finally, to visualize stress fields at a depth of interest, we

calculated the generalized Angelier's shape parameter, $A_\emptyset$ for each well using Equation 7.

$$A_\emptyset = [p + 0.5] + (-1)^p (\emptyset - 0.5) \ldots \ldots \ldots \ldots (7)$$

Where, p = stress index number

The numerical values of $\emptyset$ and $A_\emptyset$ used in the visualization of stress regimes in our study

area are listed in Appendix 7-A. Note the lack of well data in the area lying immediately

northwest of the Brooks Range deformation front (Figure 4-2). We used a minimum curvature

(biharmonic) gridding algorithm (max residual- 0.029, max iteration- 10,000 and relaxation

factor- 1) available in Surfer 12 (Golden Software, Inc.) with a grid spacing of approximately

6200 ft (1890 m) for the interpolation of the in situ stress fields for depths of 3000 ft (914 m),

6000 ft (1829 m) and 9000 ft (2743 m).

4.7   Discussion

4.7.1   Implications for the Regional Stress Regimes in the Northeastern North Slope

Variations in S_v

The magnitude of vertical stress, S_v, in the northeastern North Slope is dominantly

controlled by the current depth of the sediments (Figures 4-6 and 4-11). The linear increase in

the S_v values to deeper depths up to 12000 ft (3658 m) is best explained by sediment compaction

and the corresponding increase in densities with burial depth. However, there are spatial

variations of S_v across the study area. The estimated vertical stress magnitudes are highest in the

wells drilled near the foothills of the Brooks Range fold-and-thrust belt (See Figure 4-2 and

Appendix 7-A). These higher S_v values could be the result of higher than expected rock densities

177

due to the uplift of deeper, older rocks near the foothills of the Brooks Range fold-and-thrust belt (Moore et al., 1994).

Alternatively, the lower S_v magnitudes in the wells drilled above the eastern end of the Barrow Arch may be due to a greater volume of low density rocks in this area, independent of uplift history. This situation can be explained by lateral facies variations in the subsurface (Bell and Bachu, 2003). Regional facies maps of Ellesmerian and upper Beaufortian sequences indicate that the shaly sedimentary units from these sequences (such as the Shublik Formation and Kingak Shale) pinch out on the south-eastern flank of the Barrow Arch (Moore et al., 1994). The absence of higher density shales and the presence of younger, lower density rocks from the Brookian Sequence above the Barrow Arch could generate lower vertical stress magnitudes.

Regional variations in relative magnitude of S_v, S_{Hmax} and S_{hmin}

Figures 4-13, 4-14 and 4-15 show the spatial distribution of stress regimes in the northeastern North Slope calculated from Anderson's fault types for depths of 3000 ft (914 m), 6000 ft (1829 m) and 9000 ft (2743 m), respectively. Three distinct patterns of in situ stress distribution can be observed in the subsurface of northeastern Alaska at a depth of 3000 ft (914 m) (Figure 4-13). At this depth, an active thrust fault regime ($S_{Hmax}>S_{hmin}>S_v$) occurs in the south, near the deformation front of the eastern Brooks Range. This is consistent with both the observed thrust-related deformation in the northeastern Brooks Range fold-thrust belt and the north-northwest S_{Hmax} orientations from borehole breakout data (Wallace and Hanks, 1990; Hanks et al. 2000, Hanks, 2013). In contrast, a normal fault regime ($S_v>S_{Hmax}>S_{hmin}$) dominates the area north of the thrust front, above the eastern end of the Barrow Arch, and near the Umiat

sub-basin. This is consistent with seismic reflection studies (e.g., Casavant et al., 2004) that suggest that Cretaceous and younger rocks along the eastern portion of the Barrow Arch have been extensively deformed by north- and northwest-striking normal faults to depths up to ~4500 ft (1372 m). A normal fault regime above the Umiat sub-basin is consistent with the extensional dominated fault zone observed in the Umiat sub-basin (Fulk, 2010).

At this depth, strike-slip faulting ($S_{Hmax}>S_v>S_{hmin}$) is limited to the Fish Creek Platform and to the transition zone between the northeastern Brooks Range thrust front and the extensional Barrow Arch, as S_{Hmax} decreases relative to S_v. High angle faults bounding the Fish Creek Platform may have a component of strike slip motion; however, no shallow strike slip faults have been documented at the leading edge of the northeastern Brooks Range deformation front.

At depths in between 6000 ft (1829 m) to 9000 ft (2743 m) (Figure 4-14), the region of thrust faulting is reduced to a small area north of the eastern Brooks Range fold and thrust belt. A normal fault regime continues to dominate across the eastern Barrow Arch region and towards the Umiat sub-basin. Strike-slip fault regimes expand and become better developed north of the Barrow Arch in the Dinkum Graben, over the Fish Creek Platform and across the Canning River Displacement Zone.

At depths >9000 ft (2743 m), the thrust stress regime associated with the range front of the northeastern Brooks Range observed at shallower depths has changed to a strike-slip fault regime (Figure 4-15). Biswas and others (1986) modeled the fault-plane solutions for the 1968 M_w 4.9 earthquake located in the vicinity of the Canning River Displacement Zone (CRD)

(Figure 4-5b). They suggested predominant left-lateral strike-slip solutions for this event, with depths ranging from 5 to 9 km. The change from a thrust regime to a strike-slip fault regime at depths greater than 9000 ft (2743 m) as inferred from our stress state is consistent with the observed fault plane focal mechanisms along the Canning River Displacement Zone (Figure 4-5; Biswas et al., 1986; Grantz et al., 1983). The observed changes in the stress regimes at deeper depths, therefore, exhibit a complex interaction between the tectonic convergence that is oblique to the main structural trends and strike-slip faulting in the eastern North Slope region.

The change in in situ stress regimes from surface to depth is not uncommon in fold-and-thrust belts. In the Alberta basin, Canada, the stress regime changes from thrust faulting in the shallow parts of the foreland fold-and-thrust belt of the Rocky Mountains to a strike-slip fault stress regime at greater depths up to 9000 ft (2743 m) to 12000 ft (3658 m) (Reiter and Heidbach, 2014). Hydraulic fracture tests performed in an oil well at the center of the Michigan basin (an intracratonic sedimentary basin) revealed a similar change in the in situ stresses: a change of stress regime from shallow thrust faulting to strike-slip faulting at depths greater than 600 ft (183 m) (Haimson, 1978). In addition, Plumb (1994) performed over 1000 stress measurements from 30 hydrocarbon fields using hydraulic fracture tests and concluded that, in sedimentary basins such as the Appalachian, East Texas and Piceance basins, the thrust fault stress regime is more dominant at depths down to 1000 ft (304.8 m) and changes to strike-slip and normal fault stress regimes at greater depths. These interpreted changes in the stress regimes could be a result of a variety of factors that can affect the principal stress magnitudes, including vertical stress reduction due to tectonic uplift and erosion (Couzens-Schultz and Chan, 2010), changes in the reservoir pore pressures (Plumb, 1994; De Bree et al., 1993; Zoback, 2007,

Tingay et al., 2012) and, reservoir depletion and fluid injection processes (Streit and Hillis, 2002; Bell and Grasby, 2012).

North of the thrust front, at >9000 ft (2743 m), most of the northeastern North Slope is in a strike slip regime with a normal stress regime above the Barrow Arch. Strike-slip faulting is common in the areas near Fish Creek Platform and Dinkum graben. The observed basement topography and southeast-trending structural grain (Beikman, 1980; Homza, 2004) in these areas appear to strongly influence the present-day gravity-induced stress regimes at greater depths.

North of the Barrow Arch, near the Dinkum Graben, the strike-slip stress regime is poorly constrained and is calculated for only one exploration well. Although, the Mesozoic Dinkum Graben is an extensional rift structure that exhibits a regional normal fault stress regime (Grantz and May, 1983; Grantz et al., 1990), it is possible that this stress regime trends into a strike-slip stress regime in highly overpressured rock sequences (De Bree et al., 1993; Zoback, 2007, Tingay et al., 2012). Moderately overpressured rock intervals are observed at depths > 9000 ft (2743 m) in some exploration wells drilled in the vicinity of the Dinkum Graben (Wells 22 and 23 in Appendix 7-A). This implies that the northern margin of Alaska, along the Dinkum Graben, may be an extensional margin regionally but has a component of strike slip at a local scale, especially in the areas where overpressured rock sequences exist.

4.7.2   Implications for the Induced Hydraulic Fractures in the Shublik Shale Play
Understanding the regional stress field at the northeastern North Slope is critical in order to develop effective drilling and completion strategies for the Shublik Formation. Specifically, the in situ stress regime has a significant impact on the orientation and character of hydraulically

induced fractures and reactivated natural fractures during hydraulic fracturing stimulation operations. For example, hydraulically induced fractures form parallel to the direction of present day maximum horizontal stress, S_{Hmax} (Zoback, 2007). Further, natural fractures are reactivated in tensile or shear failure if they are oriented parallel or sub parallel to the maximum in situ horizontal stress.

Figure 4-16 shows the spatial distribution of the present-day stress field at the top of the Shublik Formation beneath the eastern North Slope. Petroleum exploration of the Shublik Formation as an unconventional shale oil play will target the area where the Shublik is in the oil window (Bird, 1991; Peters et al., 2006; Hanks, 2013). As seen in Figure 4-16, the Shublik maturity window straddles the two major in situ stress regimes identified in this study: the extensional regime across the Barrow Arch and north Alaska margin; and transitional compressional to strike-slip regime near the foothills of the northeastern Brooks Range. Figure 4-17 illustrates how the predicted strike and orientation of induced fractures in Shublik wells could vary depending upon the stress regime. For a hypothetical exploration well A drilled in the Shublik Formation within the thrust fault regime (Figure 4-16), hydraulically induced fractures will propagate horizontally in a direction parallel to the S_{Hmax} orientation, in this case striking north-northwest (Figures 4-17; Zoback, 2007). However, at depths greater than 6000 ft, where S_v is greater than S_{Hmax} and the stress regime is strike-slip, induced fractures would be vertical at the same location. For the wells B and C drilled in strike-slip and normal fault regimes respectively (Figure 4-16), hydraulically induced fractures will be vertical to sub-horizontal and strike parallel to the S_{Hmax} direction (i.e., perpendicular to the active thrust front). In either case,

natural fractures oriented northwest, parallel to the present-day maximum horizontal stress (i.e.,

perpendicular to the present day thrust front) would be expected to be open or easily reactivated.

4.8   Conclusions

The northeastern Brooks Range of northern Alaska is a northern salient of the Jurassic to

modern Brooks Range fold-and-thrust belt that is currently actively advancing toward the

Barrow Arch and the north-facing passive margin of the Arctic Basin. Structures observed in the

exposed parts of the range and in the subsurface thrust front are all north or north-northwest

directed thrust related folds (Wallace and Hanks, 1990). However, the only available fault plane

focal solutions yield a strike-slip mechanism (Grantz et al., 1983; Biswas et al., 1986).

Density logs, leak-off tests, and mud profiles from 57 wells from the northeastern North

Slope were used to determine the magnitude of present-day in situ stresses and document

significant regional lateral and vertical variations in relative stress magnitude.

Preliminary analysis indicates two distinct stress regimes across this region of Alaska.

Areas adjacent to the eastern Barrow Arch and the present day passive margin exhibit both

strike-slip ($S_{Hmax} > S_v > S_{hmin}$) and normal stress regimes ($S_v > S_{Hmax} > S_{hmin}$). This in situ stress

regime is consistent with observed fault patterns in the subsurface and with the north–south

extension along the Barrow Arch and the north Alaska margin.

To the south, within and near the northeastern Brooks Range thrust front, in situ stress

magnitudes indicate that an active thrust fault regime ($S_{Hmax} > S_{hmin} > S_v$) is present at depths

down to approximately 6000 ft (1829 m). This finding is consistent with the fold and thrust

structures observed in surface exposures and in the subsurface. However, at depths greater than 6000 ft (1829 m), relative in situ stress magnitudes indicate a change to a strike-slip regime. This change in in situ stress regime is probably due to increasing S_v and a relatively low magnitude S_{Hmax}, and is facilitated by the strongly mechanically stratified sedimentary rocks in this part of the fold-and-thrust belt.

The orientations of hydraulically induced fractures in the Shublik Formation will depend on the nature of the stress regime and will vary by location. Induced fractures are likely to be horizontal in the southeastern portion of the study area at depths less than 6000 ft (1829 m) where relative in situ stress magnitudes suggest that a thrust faulting regime is active. However, at depths greater than 6000 ft (1829 m), induced fractures are likely to be vertical and oriented northwest, as the in situ stress regime becomes strike-slip. In the extensional regime associated with the Barrow Arch, hydraulically induced fractures will be vertical and oriented in northwest and northeast directions.

4.9   References

Alaska Oil and Gas Conservative Commission (AOGCC). (2014). Digital well history files, doa.alaska.gov/ogc/publicdb.html (accessed May 14, 2014).

Anderson, E. M. (1951). The Dynamics of Faulting: Oliver and Boyd, Edinburgh, 206 p.

Angelier, J. (1975). Sur l'analyse de mesures recueilles dans des sites faillès: l'utilitè d'une confrontation entre les mèthodes dynamiques et cinèmatiques, C.R. Academy of Science, Paris, D1895-1808.

Bai, M. (2011). Risk and uncertainties in determining fracture gradient and closure pressure :
American Rock Mechanics Association.

Beikman, B. M. (1980). Geologic map of Alaska: U.S. Geological Survey, scale 1:2,500,000.

Bell J. S., and Babcock, E. A. (1986). The stress regime of the Western Canadian Basin and
implications for hydrocarbon production: Bulletin of Canadian Petroleum Geology, v.34, p.
364–378.

Bell, J. S. (1990). Investigating stress regimes in sedimentary basins using information from oil
industry wireline logs and drilling records, in Hurst, A., Lovell, M.A., and Morton, A.C.,
ed., Geological applications of wireline logs: Geological Society Special Publications, v. 48,
p. 305–325.

Bell, J. S. (1996). In situ stresses in sedimentary rocks (part 2): applications of stress
measurements: Geoscience Canada, v. 23, p. 135-153.

Bell, J. S., and Bachu, S. (2003). In situ stress magnitude and orientation estimates for
Cretaceous coal-bearing strata beneath the plains area of central and southern Alberta:
Bulletin of Canadian Petroleum Geology, v. 51, p. 1-28.

Bell, J., and Grasby, S. (2012). The stress regime of the Western Canadian Sedimentary Basin:
Geofluids, v. 12, p. 150–165.

Bird, K. J. (1991). Geology, play descriptions, and petroleum resources of the Alaskan North

    Slope, petroleum provinces 58-60, USGS Open File Report 88-450Y.

Bird, K. J., and Molenar, C. M. (1992). The North Slope foreland basin, Alaska: American

    Association of Petroleum Geologists Memoir, v.55, p. 363-393.

Bird, K. J., and Houseknecht, D. W. (2002). U.S. Geological Survey 2002 petroleum resource

    assessment of the National Petroleum Reserve in Alaska (NPRA): USGS Fact Sheet 045-02,

    6 p.

Biswas, N., Pujol, J., Tytgat, G., and Dean, K. (1986). Synthesis of seismicity studies for

    western Alaska: Tectonophysics, v. 131, p. 369 – 392.

Bjørlykke, K. (2010). Petroleum Geoscience: From Sedimentary Environments to Rock Physics,

    Springer, Berlin, Germany, 346 p.

Blundell, J. S., and Hallam, R. J. (1991). Determination of hydraulic fracture orientation in the

    Kuparuk River field, Alaska (abstract) in The integration of geology, geophysics,

    petrophysics, and petroleum engineering in reservoir delineation, description and

    management: American Association of Petroleum Geologists, p. 202–203.

Brudy, M., and Zoback, M. D. (1999). Drilling- induced tensile wall-fractures: implications for

    determination of in situ stress orientation and magnitude: International Journal of Rock

    Mechanics and Mining Sciences, v. 36, p. 191-215.

Casavant, R., Hennes, A., Johnson, R. and Collett, T. (2004). Structural analysis of a proposed

   pull-apart basin: Implications for gas hydrate and associated free-gas emplacement, Milne

   Point Unit, Arctic Alaska, Vancouver, BC, Canada: The American Association of Petroleum

   Geologists, Hedberg Research Conference, September, 12-16.

Couzens-Schultz, B. A., and Chan, A. W. (2010). Stress determination in active thrust belts: an

   alternative leak-off pressure interpretation: Journal of Structural Geology, v. 32, p. 1061–

   1069.

De Bree, P., Hydendaal, H. G., and Van De Hoek, P. J. (1993). Rock mechanical investigations

   for improved fracture closure gradient prediction, Champion Field, Brunei: Shell

   International Research Report, RKGR.93.030.

Dugan, B., and Sheahan, T. C. (2012). Offshore sediment overpressures of passive margins:

   Mechanisms, measurement, and models: Reviews of Geophysics, v. 50, p. 1-20,

   doi:10.1029/2011RG000379.

Enever, J. R., Yassir, N., Willougby, D. R., and Addis, M. A. (1996). Recent experience with

   extended leak-off tests for in situ stress measurements in Australia: Australian Petroleum

   Production and Exploration Association Journal, v.36, p. 528 -534.

Engelder, T. (1993). Stress Regimes in the Lithosphere: Princeton University Press, Princeton,

   N. J., 451 p.

Fulk, B. (2010). Seismic analysis of the Ikpikpuk-Umiat basin, NPRA, North Slope, Alaska,

    MSc Thesis, San Diego State University, San Diego, California, 49 p.

Garrity, C. P., Houseknecht, D. W., Bird, K. J., Potter, C. J., Moore, T. E., Nelson, P. H., and

    Schenk, C. J. (2005). U.S. Geological Survey 2005 oil and gas resource assessment of the

    central North Slope, Alaska: Play maps and results: U.S. Geological Survey Open-File

    Report, 2005-1182, http://pubs.usgs.gov/of /2005/1182/2005-1182.pdf (accessed May 20,

    2014).

Giovannetti, D. M., and Bird, K. J. (1979). Gravity and magnetic profiles and rock property data

    for the Shaviovik-Echooka rivers area, North Slope, Alaska: U.S. Geological Survey Open-

    File Report 79-1504, 14 p., 1 sheet.

Grantz, A., Dinter, D. A., and Biswas, N. N. (1983). Map, cross-sections, and chart showing late

    Quaternary faults, folds, and earthquake epicenters on the Alaskan Beaufort shelf: U.S.

    Geological Survey Miscellaneous Investigations Map I-1182-C, 7 p., 3 sheets, scale

    1:500,000.

Grantz, A., and May, S. D. (1983). Rifting history and structural development of the continental

    margin north of Alaska, in Watkins, J.S., and Drake, C.L., ed., Studies in continental margin

    geology: American Association of Petroleum Geologists Memoir, v.34, p. 77–100.

Grantz, A., May, S. D., and Hart, P. E. (1990). Geology of Arctic continental margin of Alaska, in The Geology of North America, The Arctic Ocean region., edited by Grantz, A., L. Johnson and J. F. Sweeney: Geological Society of America. Boulder, Colorado, p. 257-288.

Griffin, K. W. (1985). Induced Fracture Orientation Determination in the Kuparuk Reservoir: Society of Petroleum Engineers, doi:10.2118/14261-MS.

Haimson, B. C. (1978). Crustal stress in the Michigan Basin: Journal of Geophysical Research, v. 83, p. 5857–5863, doi:10.1029/JB083iB12p05857.

Hanks, C. L., Parker, M., and Jemison, E. B. (2000). Borehole breakouts and implications for regional in situ stress patterns of the northeastern North Slope, Alaska, in Pinney, D.S., and P.K. Davis, ed., Short Notes on Alaska Geology 1999: Alaska Division of Geological & Geophysical Surveys Professional Report 119C, p. 33-43. doi:10.14509/2685.

Hanks, C. L. (2013). In situ stresses in northern Alaska and impact on natural fractures in the Shublik Formation: Alaska Division of Geological and Geophysical Surveys.

Homza, T. X. (2004). A structural interpretation of the Fish Creek Slide (Lower Cretaceous), northern Alaska: American Association of Petroleum Geologists Bulletin, v.88, p. 265–278.

Houseknecht, D. W., and Bird, K. J. (2011). Geology and petroleum potential of the rifted

    margins of the Canada basin, in A. M. Spencer, A.F. Embry, D.L. Gautier, A.V. Stoupakova

    and K. Sørensen, eds, Arctic Petroleum Geology, Geological Society of London Memoir,

    v.35, p. 509-526.

Hubbard, R. J., Edrich, S. P., and Rattey, R. P. (1987). Geologic evolution and hydrocarbon

    habitat of the 'Arctic Alaska Microplate', in Tailleur, I., and P. Weimer, ed., Alaskan North

    Slope Geology: Bakersfield, California and Anchorage, Alaska, Pacific Section, Society of

    Economic Paleontologists and Mineralogists and Alaska Geological Society, p. 797–830.

Hubbert, M. K., and Willis, D. G. (1957). Mechanics of Hydraulic Fracturing: Petroleum

    Transactions, 210 p.

Hurd, O., and Zoback, M. D. (2012). Regional stress orientations and slip compatibility of

    earthquake focal planes in the New Madrid seismic zone: Seismological Research Letters, v.

    83, doi: 10.1785/0220 110122.

Karig, D. E., and Hou, G. (1992). High-stress consolidation experiments and their geologic

    implications: Journal of Geophysical Research, v.97, p. 289–300, doi:10.1029/91JB02247.

Martin C. D., Kaise, P. K., and Christiansson, R.(2003). Stress, instability and design of

    underground excavations: International Journal of Rock Mechanics & Mining Science, v.40,

    p. 1027-1047.

Moore, T. E., Wallace, W. K., Bird, K. J., Karl, S. M., Mull, C. G., and Dillon, J. T. (1994). Geology of northern Alaska, in Plafker, George, and H.C. Berg, ed., The Geology of Alaska, the Geology of North America: Boulder, Colorado, Geological Society of America, v. G-1, p. 49–140.

Peters, K. E., Magoon, L. B., Bird, K. J., Valin, Z. C., and Keller, M. A. (2006). North Slope Alaska: source rock distribution, richness, thermal maturity, and petroleum charge, AAPG Bulletin, v.90, p. 261-292.

Plumb R. (1994). Variations of the least horizontal stress magnitude in sedimentary rocks: American Rock Mechanics Association, North American rock mechanics symposium, June, 1-3, Austin, Texas.

Reiter, K., and Heidbach, O. (2014). 3-D geomechanical–numerical model of the contemporary crustal stress state in the Alberta Basin (Canada): Journal of Geophysical Research-Solid Earth, v.5, p. 1123-1149, doi: http://doi.org/10.5194/sed-6-2423-2014.

Rider, M. (2000). The Geological Interpretation of Well Logs: Whittles Publishing, Caithness, Scotland, 280 p.

Ruppert, N. A. (2008). Stress Map for Alaska from Earthquake Focal Mechanisms, in Active

 Tectonics and Seismic Potential of Alaska, ed., J. T. Freymueller, P. J. Haeussler, R. L.

 Wesson and G. Ekström: American Geophysical Union, Washington, D. C..

 doi: 10.1029/179GM20.

Scheirer, A. H., Magoon, L. B., Bird, K. J., Duncan, E. A., and Peters, K. E. (2014). Toward

 successful petroleum production from unconventional and conventional reservoirs in the

 central Alaska North Slope: Society of Petroleum Engineers. doi:10.15530/urtec-2014-

 1934939.

Shideler, R., and Hechtel, J. (2000). Grizzly bear, in J. C. Truett and S.R. Johnson, The natural

 history of an Arctic oil field: development and the biota, Academic Press, San Diego,

 California, p. 105-132.

Simpson, R. W. (1997). Quantifying Anderson's fault types: Journal of Geophysical Research,

 v.102, p. 17909–17919.

Streit, J., E. and Hillis, R. R. (2002). Estimating fluid pressures that can induce reservoir failure

 during hydrocarbon depletion, SPE/ISRM Rock Mechanics Conference, 20-23 October,

 Irving, Texas.

Tingay, M., Morley, C., Laird, A., Limpornpipat, O., Krisadasima, K., Pabchanda, S., and Macintyre, H. (2012). Overpressures in the Northern Malay Basin: Part 1 - Origin and distribution: Proceedings of the Society of Petroleum Engineers, International Petroleum Technology Conference, p. 3260-3271.

Wahrhaftig, C. (1965). Physiographic divisions of Alaska: U.S. Geological Survey Professional Paper, v.482, 52 p., 6 sheets, scale 1:2,500,000.

Wallace, W. K., and Hanks, C. L. (1990). Structural provinces of the northeastern Brooks Range, Arctic National Wildlife Refuge, Alaska: American Association of Petroleum Geologists Bulletin, v. 74, p. 1100-1118.

Zimmerman, T., MacInnis, J., Hoppe, J., Pop, J. J., and Long, T. (1990). Application of emerging wireline formation testing technologies: 8th Offshore South East Asia Conference, p. 1-7.

Zoback, M. L. (1992). First and second order patterns of stress in the lithosphere: the World Stress Map Project: Journal of Geophysical Research, v. 97, p. 11703- 11728.

Zoback, M. D. (2007). Reservoir Geomechanics, Cambridge University Press, 464 p.

Figure 4-1 Basemap of northern Alaska

Basemap of Northern Alaska showing the study area (in red box) (modified from Bird and

Houseknecht, 2002). The Trans-Alaska Pipeline System (TAPS, dark red line) runs

approximately 800 miles and connects the oil and gas fields of Prudhoe Bay to the port of Valdez

in the south.
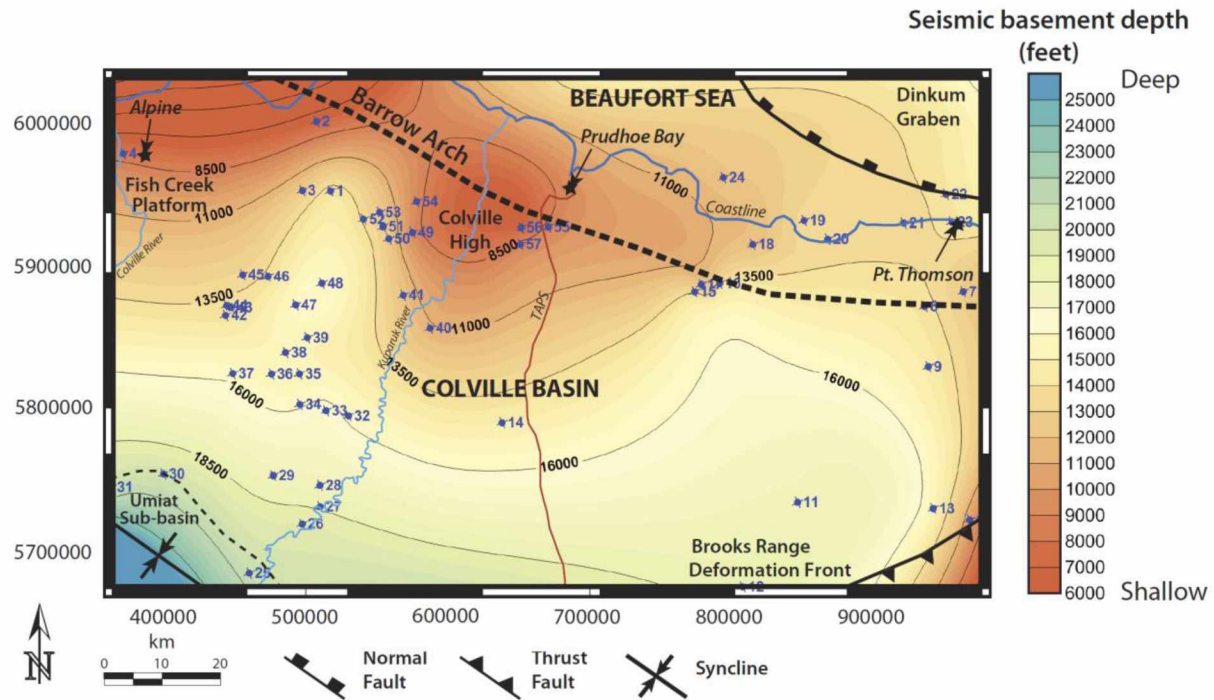
Figure 4-2 Seismic basement depth map of the study area

A depth-to-seismic basement map of the study area with the locations of the 57 wells used in this study (AOGCC, 2014). The area corresponds with the red box marked in Figure 1. Coordinate system is the North American Datum of 1927 (NAD 27) - Alaska zone 4.
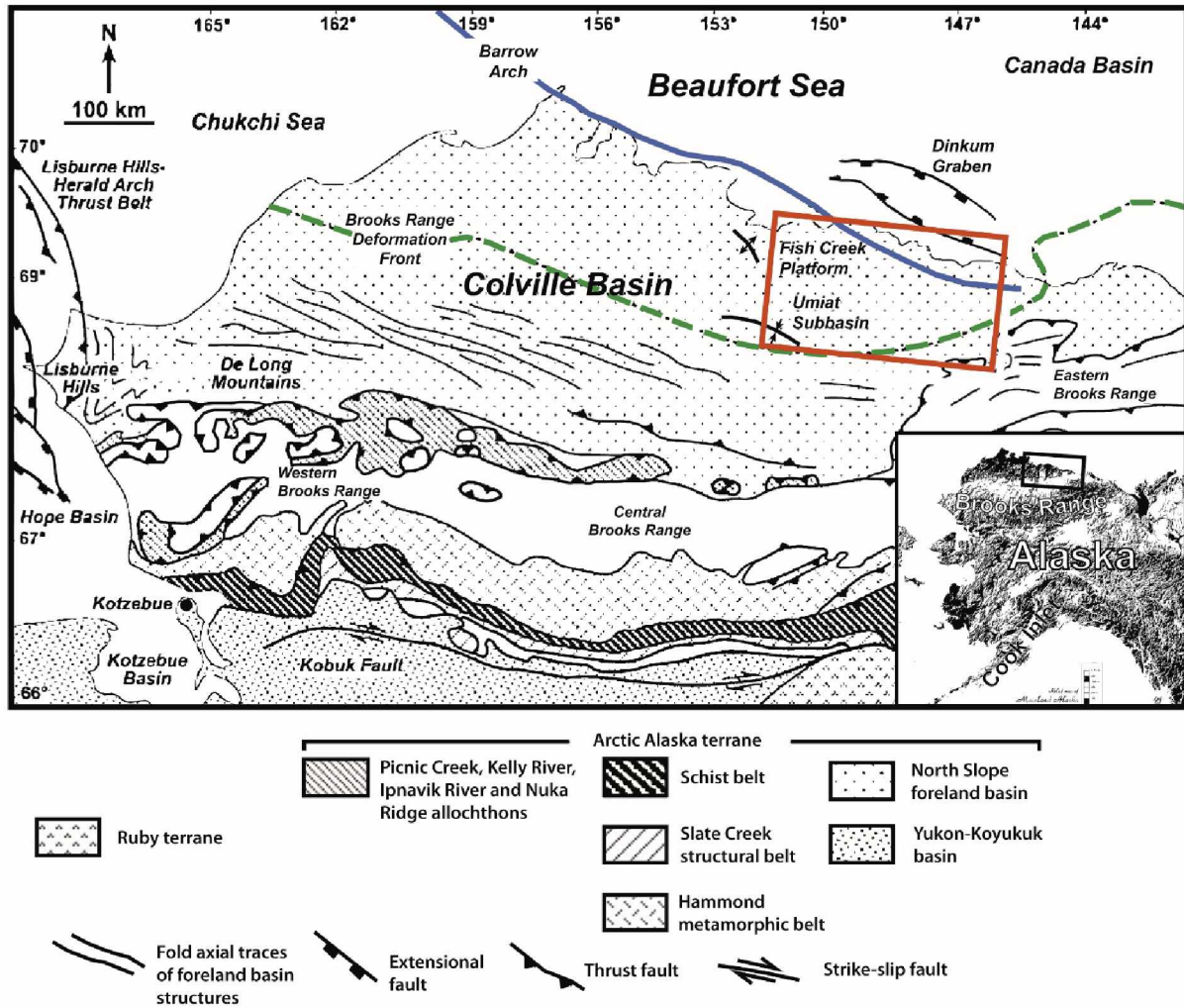
Figure 4-3 Tectonic setting of northern Alaska

Simplified structural map of northern Alaska, showing major structural features and location of study area (red box) The study area includes two major structural regimes: the subsurface northern limit of deformation related to the northeastern Brooks Range fold-and -thrust belt in the southeast (solid green line); and the present-day Alaska extensional margin along the Barrow Arch to the north (solid blue line). Currently, the Barrow Arch and north Alaska margin exhibit extensional stresses set up by active thrust front interacting with the structural high beneath the Barrow Arch. To the south and near northeastern Brooks Range front, compressional stresses exist due to active thrust faulting. Map modified from Moore et al. (1994).

NORTH SLOPE STRATIGRAPHY
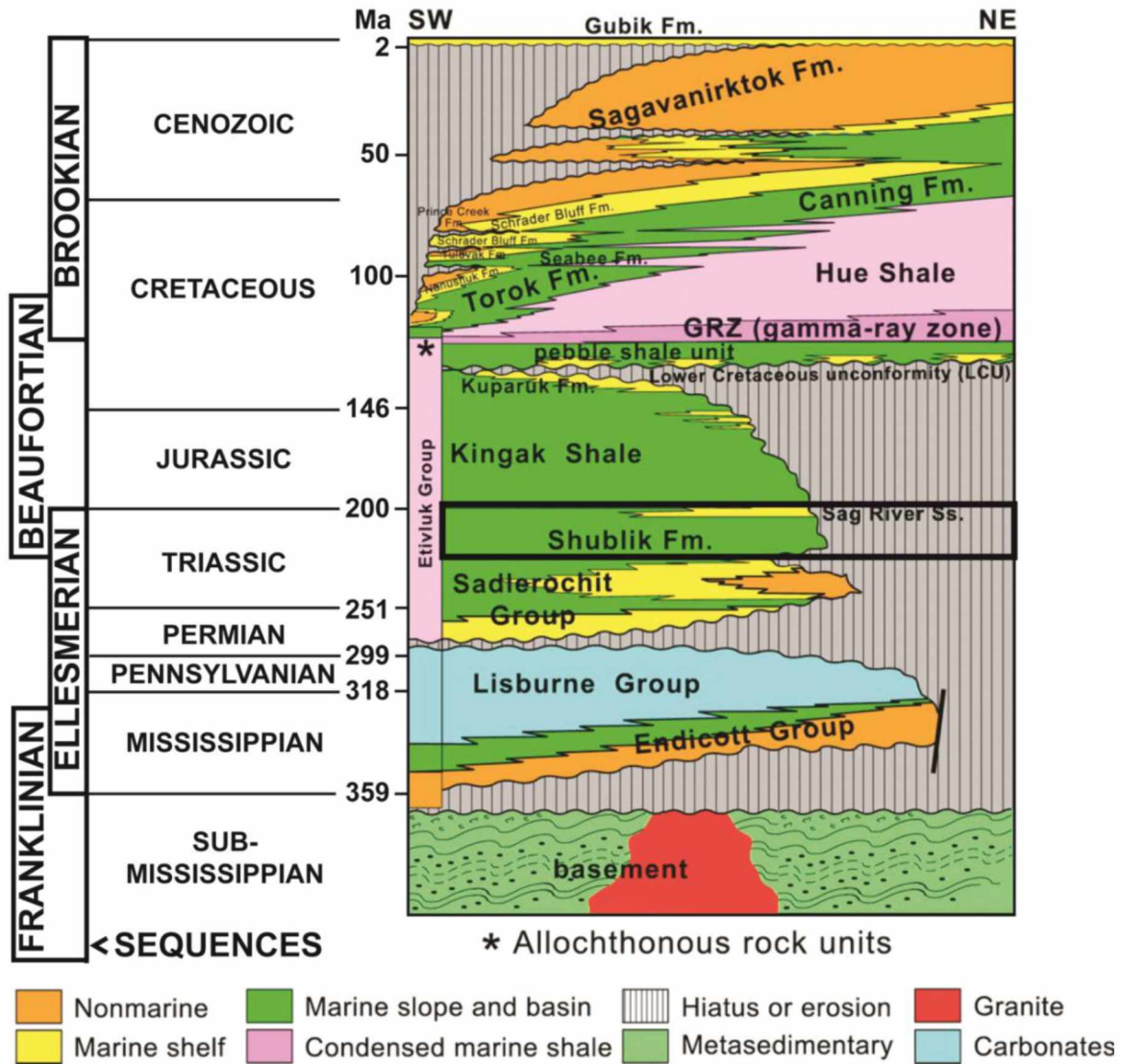
Figure 4-4 Generalized stratigraphy of the North Slope of Alaska

The Middle to Upper Triassic Shublik Formation (marked in black box) is one of the main petroleum source rocks of the North Slope and is currently being evaluated for its unconventional economic potential (Scheirer et al., 2014). Modified from Garrity and others (2005).
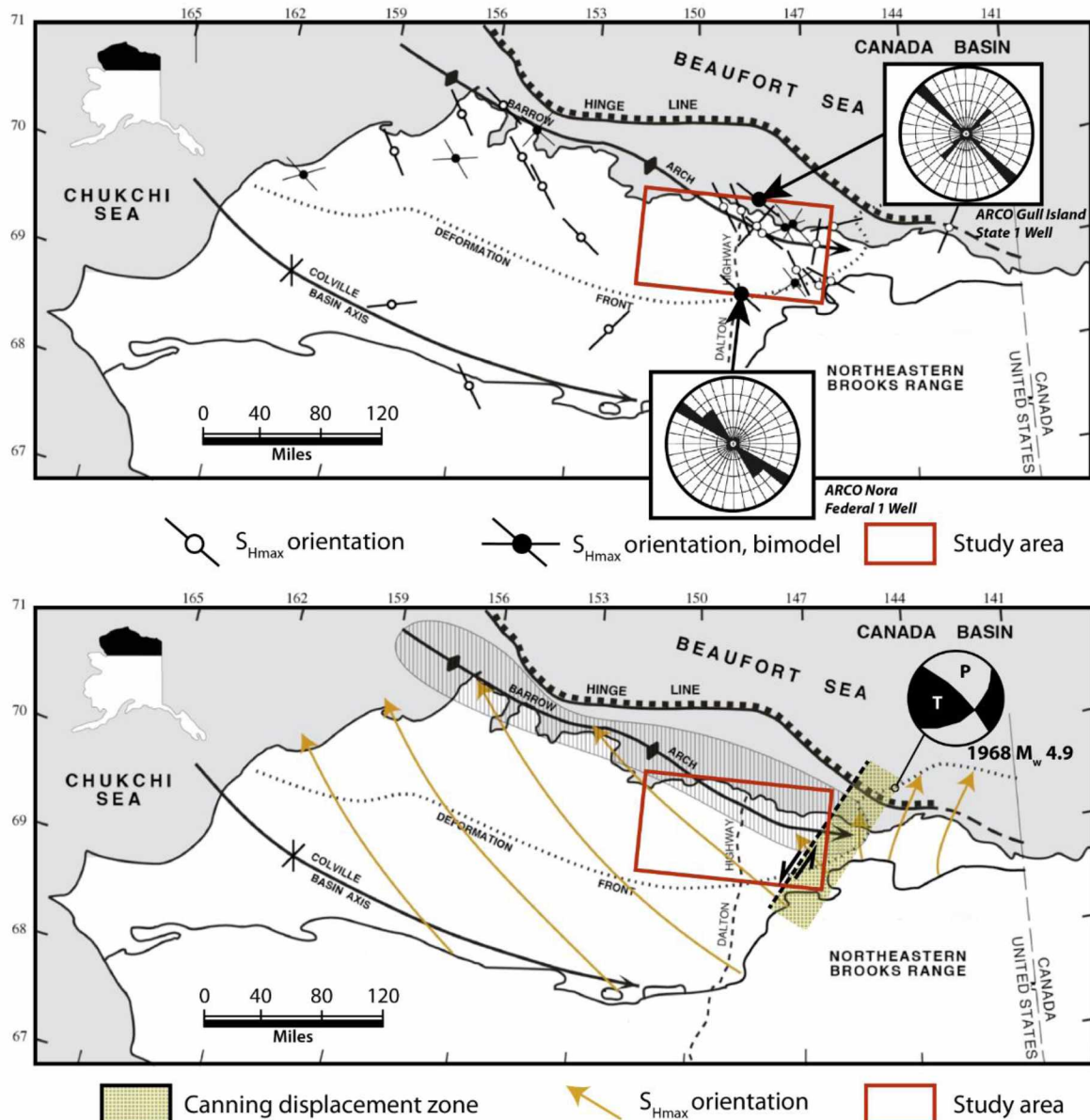
Figure 4-5 Map of northern Alaska showing the orientation of maximum horizontal stresses

The orientations of maximum horizontal stress (S_{Hmax}) were derived from the borehole breakout data available for 30 selected North Slope wells. The S_{Hmax} orientations suggest two distinct in situ stress regimes. Throughout much of the southern Colville basin S_{Hmax} is oriented northwest and approximately perpendicular to the Brooks Range fold-and-thrust front. Borehole breakouts in wells more distal to the thrust front and above the Barrow arch are bimodal and are generally northwest and northeast trending. (B) The map shows that the present-day horizontal maximum

principal stress, S_{Hmax}, directions are generally perpendicular to the deformation front of the Brooks Range fold-and-thrust belt. Along the Barrow Arch, the inferred S_{Hmax} orientations are vary from northwest to northeast trending. The focal plane solution for the 1968 M_w 4.9 earthquake (P for pressure axis, T for tension axis), occurred 30 km offshore of Barter Island, suggests a sinistral slip on a northeast-striking fault plane, reflecting active strike-slip faulting along the Canning River Displacement Zone (Grantz et al., 1983; Biswas et al., 1986). Maps are modified from Hanks et al., (2000) and Hanks (2013).
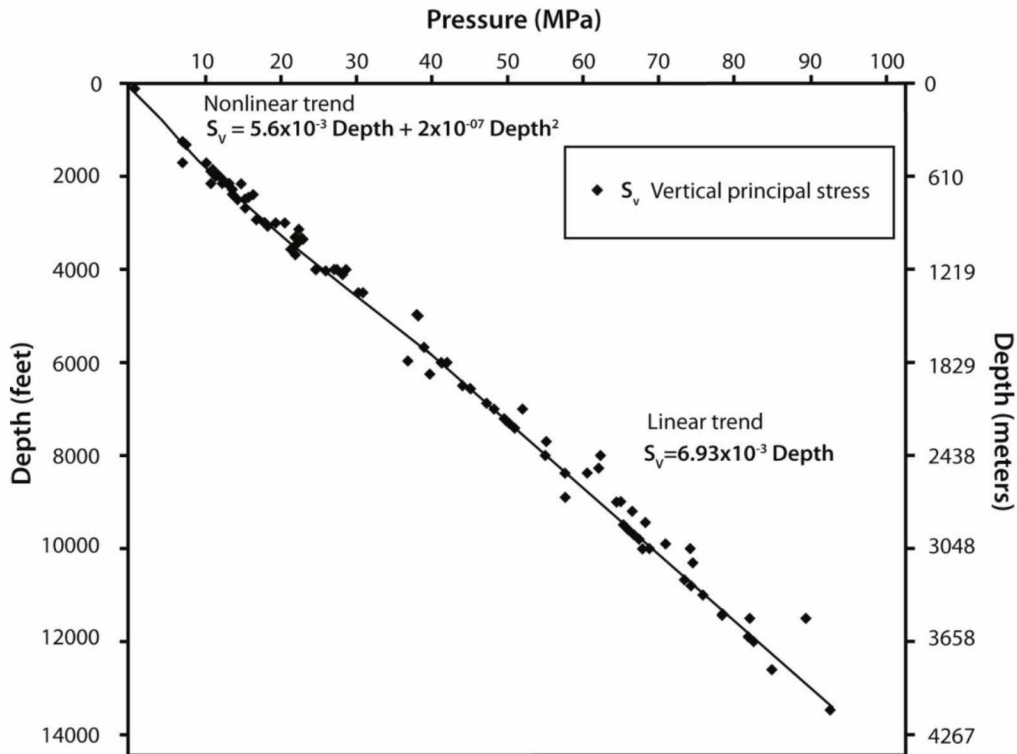
Figure 4-6 Vertical stress magnitudes in the study area

Vertical stress (S_v) magnitudes with depth inferred from density logs from 57 wells drilled in the study area.
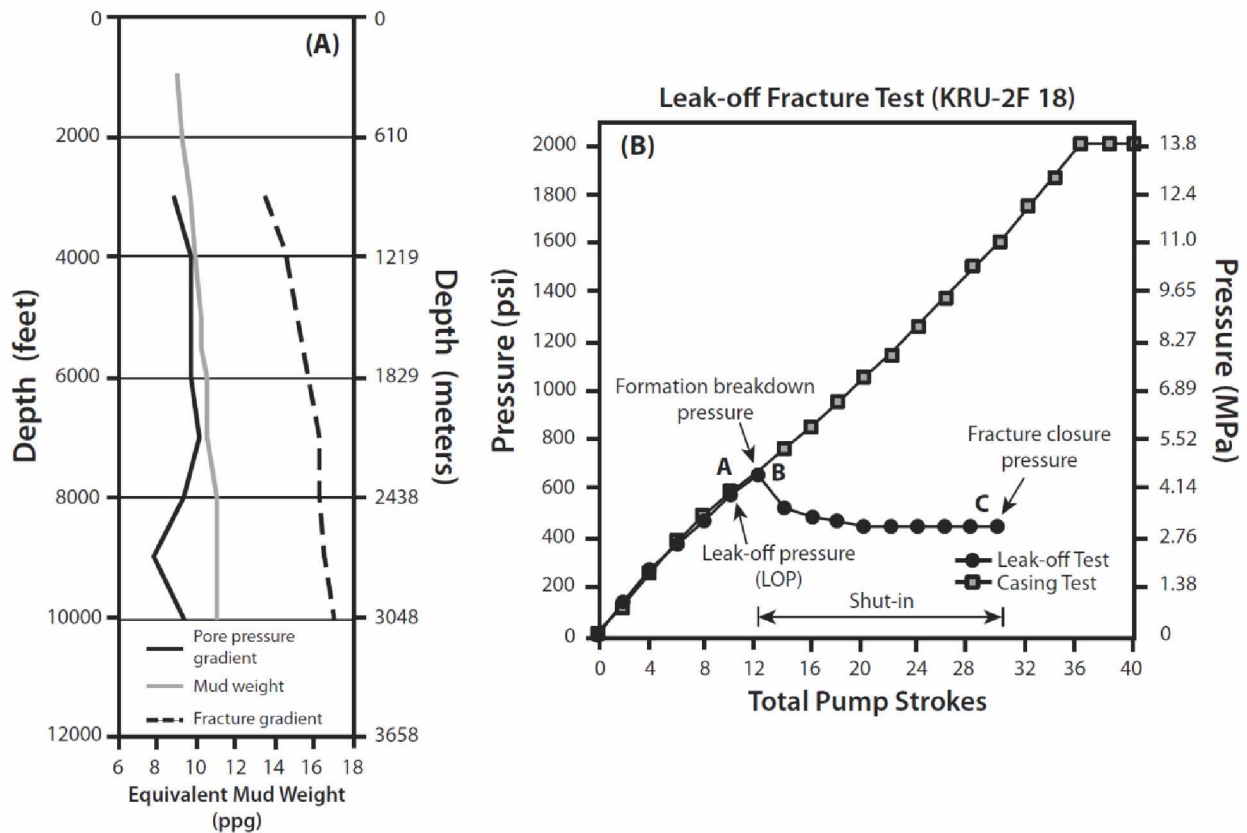
Figure 4-7 Subsurface pressure and leak-off test profiles of Kuparuk River Unit 2F-18 well (A) Subsurface pressure profiles for Kuparuk River Unit 2F-18 well showing hydrostatic pore pressure and fracture gradient data with depth (AOGCC, 2014). (B) Example of a leak-off test (LOT) (marked in solid black circles) conducted in Kuparuk River Unit 2F-18 well. Graph shows a linear pressure build up. As fractures initiate (Point A), the data trend line starts to deviate from linearity, and the corresponding pressure is referred as leak-off pressure (LOP). The maximum test pressure (Point B) is achieved when the pump is stopped. As the pump is stopped, the pressure decreases rapidly and levels off at a pressure called the fracture closure pressure. The leak-off pressure is interpreted as the magnitude of S_{hmin} (Bell and Babcock, 1986).
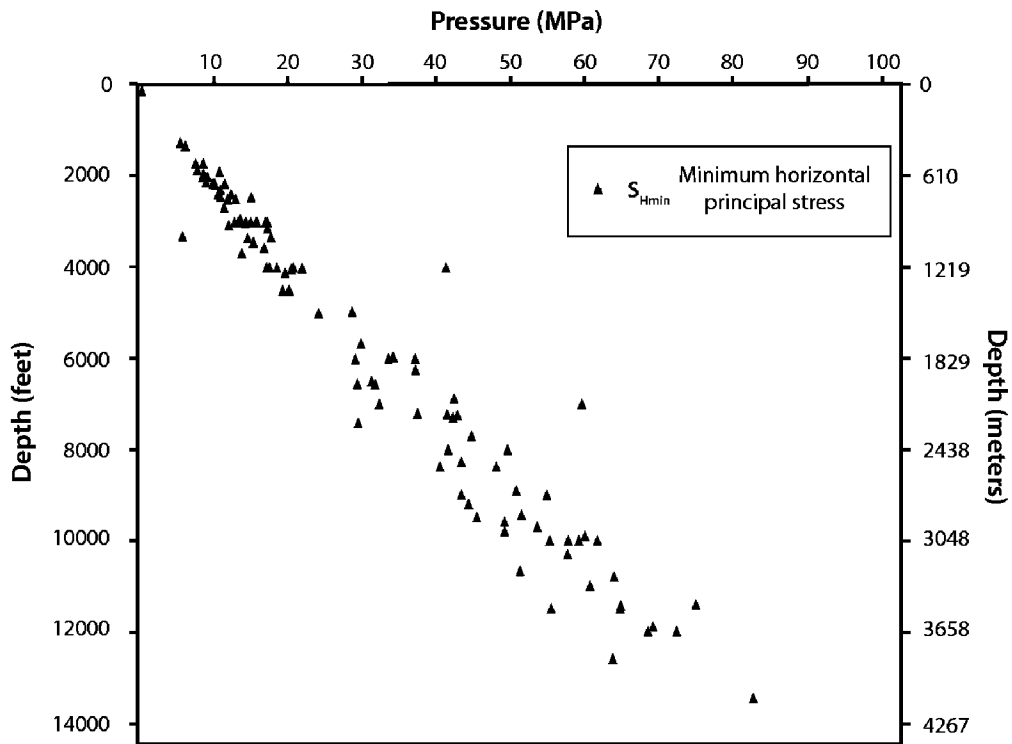
Figure 4-8 Minimum horizontal stress magnitude in the study area

Minimum horizontal stress (S_{hmin}) magnitudes with depth inferred from formation leak-off tests

and fracture gradient data available from the 57 wells in the study.
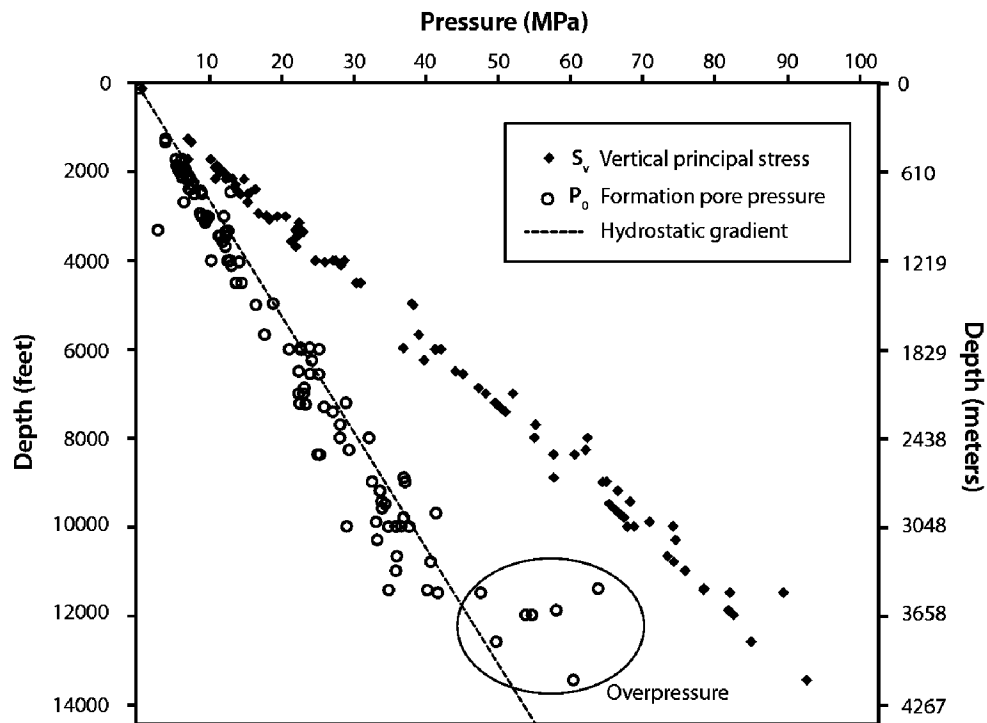
Figure 4-9 Pore pressure magnitudes in the study area

Depth plot of the pore pressure (P_p) magnitudes derived from drilling mud weights and pore

pressure gradients available for the 57 wells in the study. The pore pressure values indicate that

they are mainly hydrostatic . However, overpressured formations are observed at depths greater

than approximately 12, 000 feet (3658 m).

202
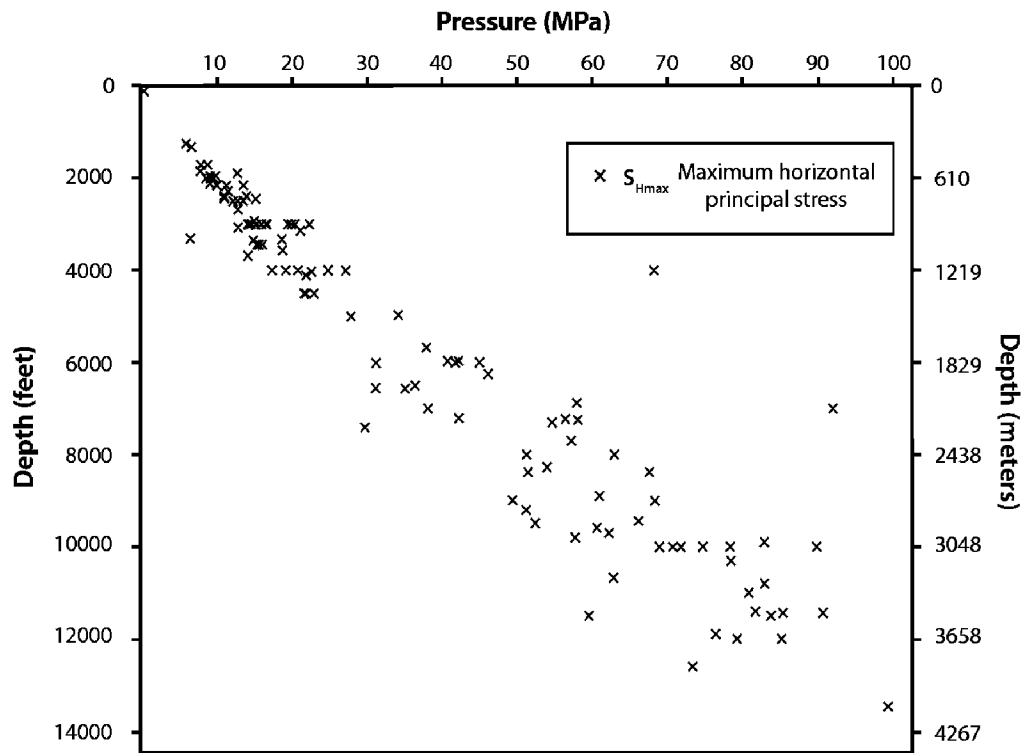
Figure 4-10 Maximum horizontal stress magnitudes in the study area

Magnitude of S_{Hmax} versus depth showing distribution of calculated lower limit estimates for

maximum principal horizontal stress (S_{Hmax}) from the 57 wells in the study. For a vertical

borehole, the constrained magnitude of maximum principal horizontal stress is a function of the

magnitudes of minimum principal horizontal stress (S_{hmin}), formation pore-pressure (P_p) and the

formation breakdown pressure (P_b). Dispersion of the S_{Hmax} values with depth reflects, in part,

dispersion of measured S_{hmin} (Figure 8).
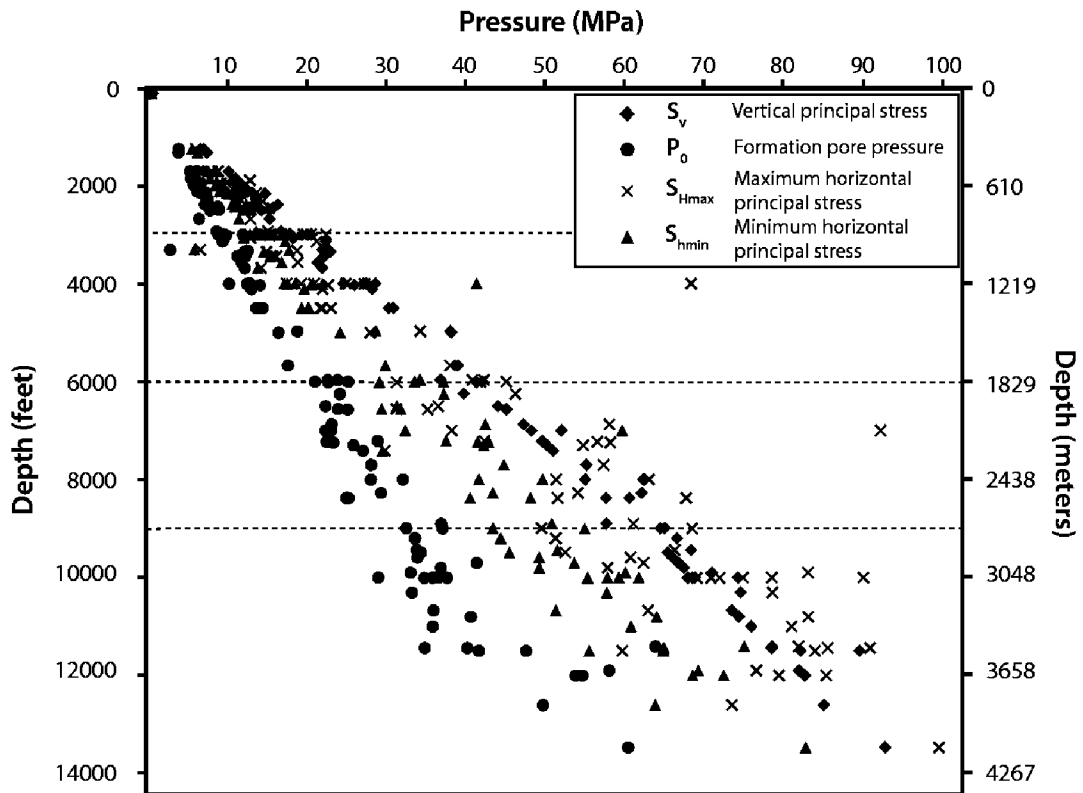
Figure 4-11 Depth profile of in situ stress magnitude derived for the study area

The dotted horizontal lines indicate the depths (3000 ft (914 m), 6000 ft (1829 m) and 9000 ft

(2743 m)) at which in situ stress distribution maps were generated in this study. These depths

were selected to show the distribution of stress regimes in the area, both spatially and laterally,

based on the availability of well data and on the basement topography.
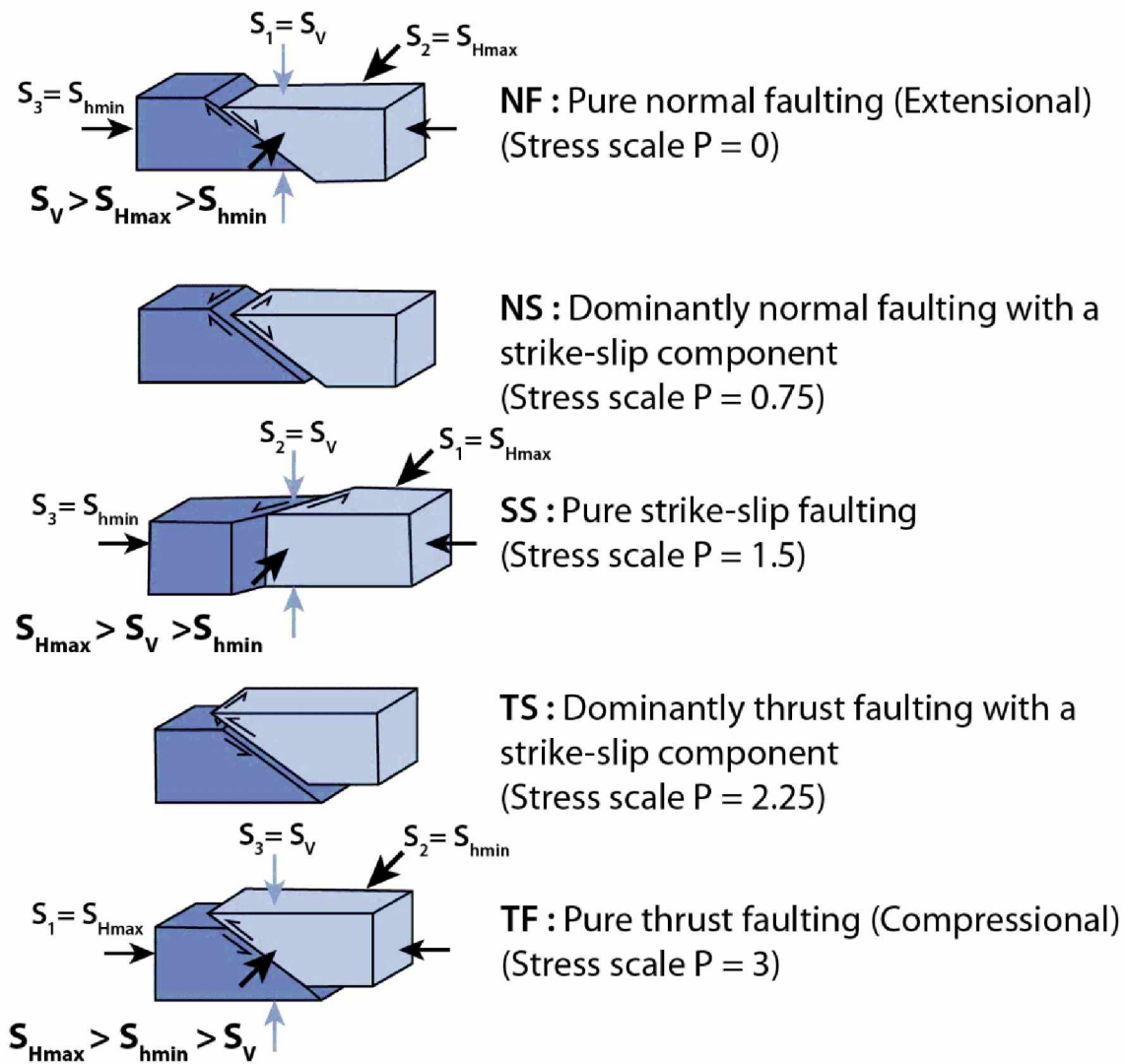
Figure 4-12 Anderson's fault classification criteria

A range of possible stress states (normal, strike-slip and thrust faulting) at a depth of interest was estimated using Anderson's fault classification system and the relative stress magnitudes (Anderson, 1951; Simpson, 1997). In the sedimentary basins with normal faulting or strike-slip stress regime, S_{hmin} is the smallest principal stress relative to S_{Hmax} and S_v. In thrust fault stress regime, the vertical stress, S_v, is expected as the smallest principal stress. Stress index values are based on a stress index scale, P = 0, 1, 2, and 3 (Hurd and Zoback, 2012).
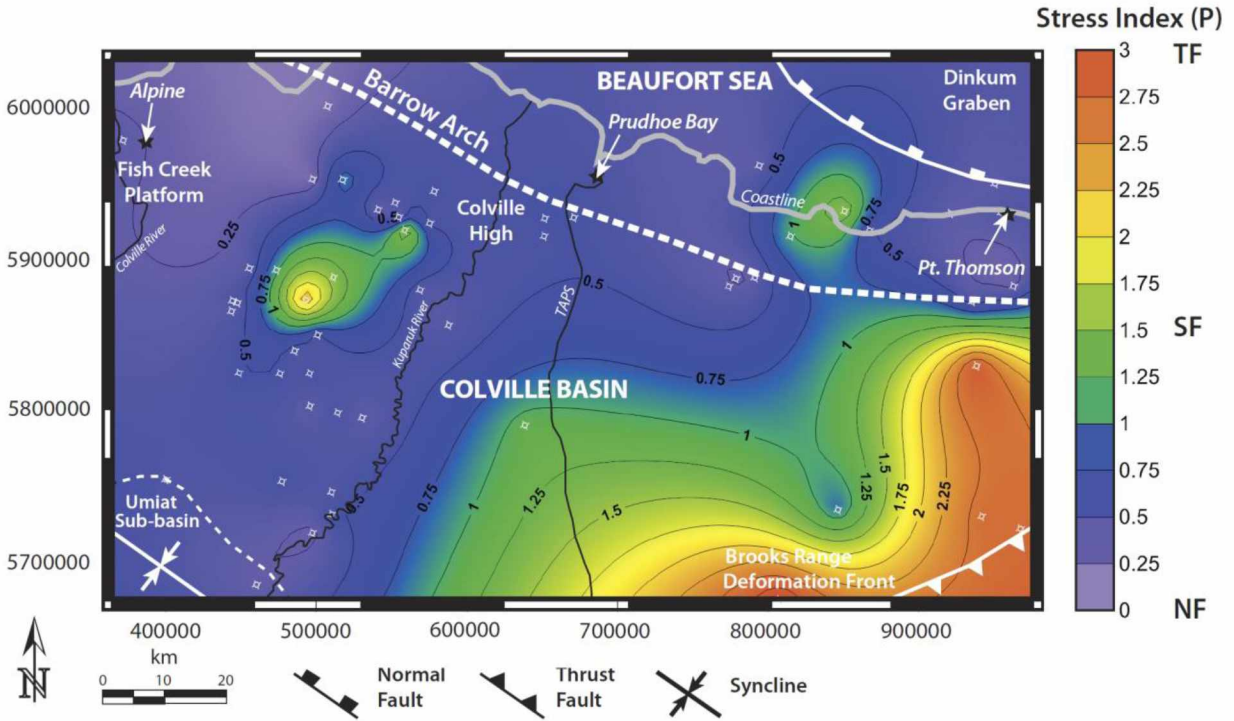
Figure 4-13 Map of in situ stress regimes present at a depth of 3000 ft

Spatial variations in normal faulting (NF), strike-slip faulting (SS) and thrust faulting (TF) stress regimes in the study area at a depth of 3000 ft (914 m). The reverse faulting regime in the southeast corner is probably related to north-northwestward oriented active compression from the northeastern Brooks Range fold-thrust belt. The normal faulting regime adjacent to the Barrow arch suggests an extensional stress regime, probably related to the present day passive margin, which includes large, young extensional faults. The small areas of strike-slip faulting may be associated with Fish Creek Platform and Colville High.
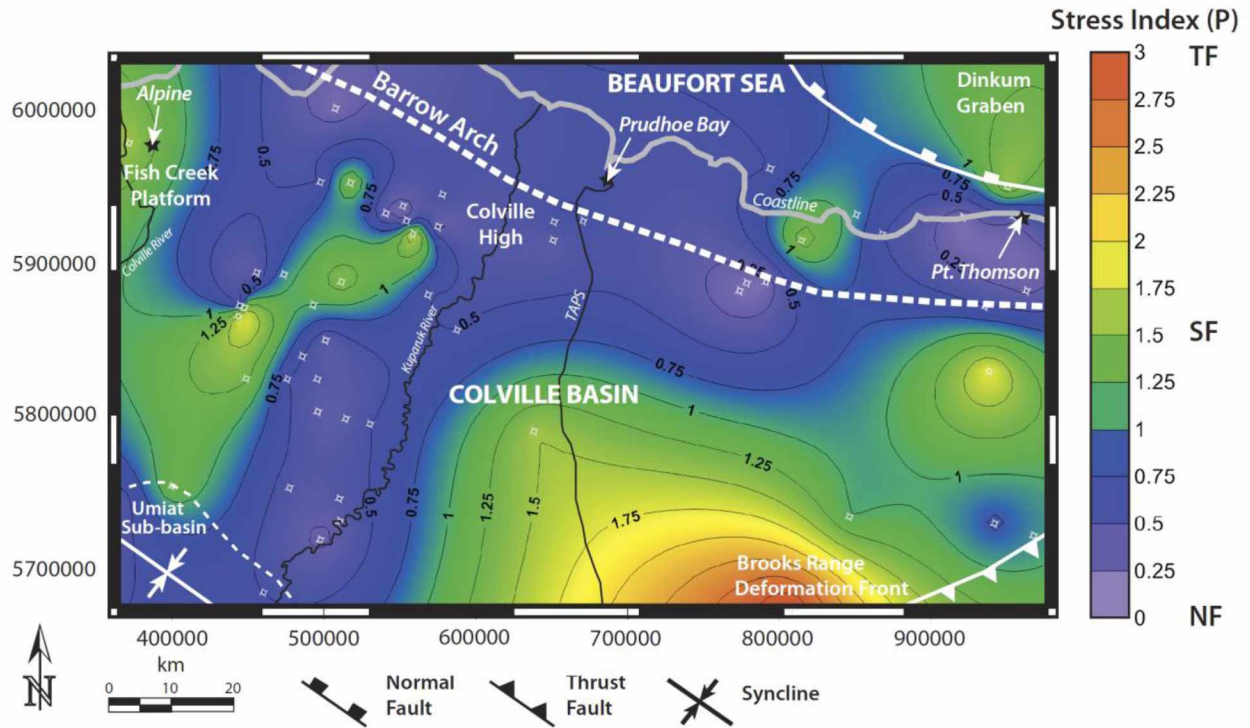
Figure 4-14 Map of in situ stress regimes present at a depth of 6000 ft

Spatial variations in normal faulting (NF), strike-slip faulting (SS) and thrust faulting (TF) stress regimes in the study area at a depth of 6000 ft (1829 m). The area of thrust faulting is reduced in size immediately north of the northeastern Brooks Range fold-and-thrust belt. Normal faulting is dominant above the Barrow Arch. Strike-slip faulting becomes more obvious across the Fish Creek Platform and becomes evident to the north at the eastern end of the Barrow Arch and in the Dinkum Graben.
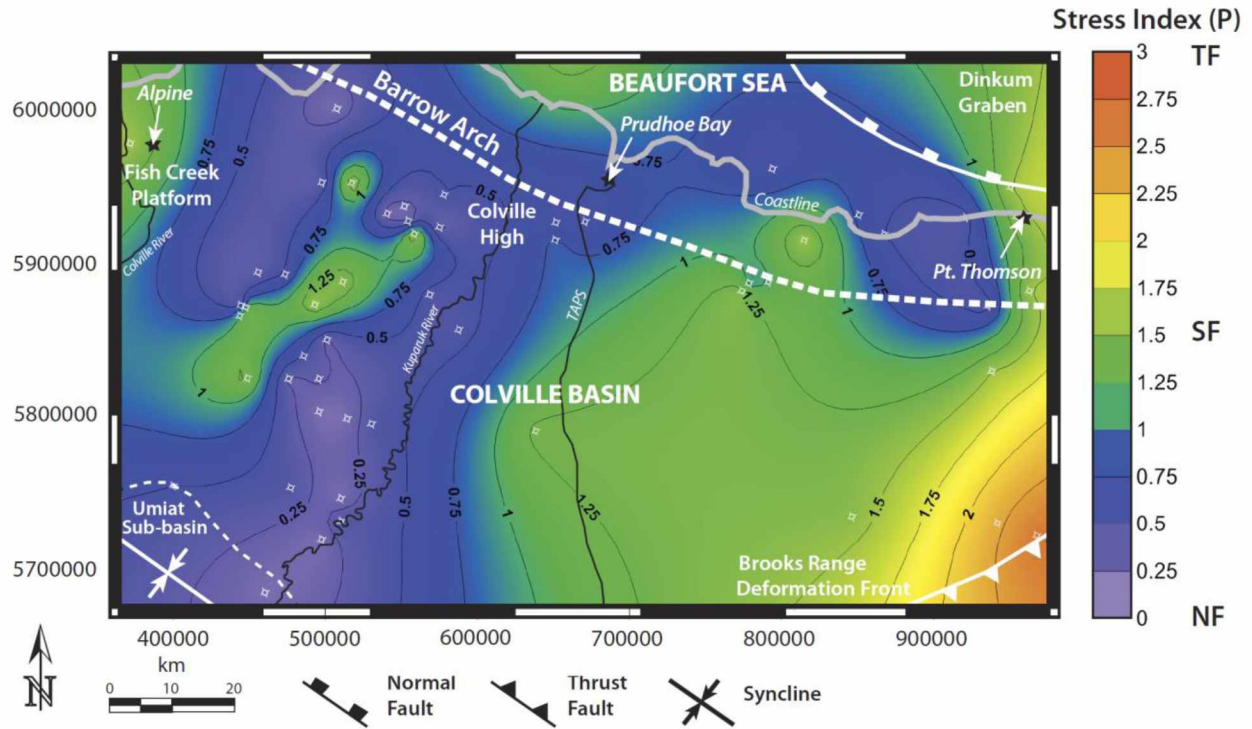
Figure 4-15 Map of in situ stress regimes present at a depth of 9000 ft

Spatial variations in normal faulting (NF), strike-slip faulting (SS) and thrust faulting (TF) stress

regimes in the study area at a depth of 9000 ft (2743 m). A strike-slip stress regime replaces the

thrust stress regime in the southeastern corner as vertical stress increases. This observation is

consistent with the local earthquake focal mechanisms and suggests deep north-northeast

oriented strike-slip faults may underlie the northeastern front of the Brooks Range fold-and-

thrust belt. A similar explanation may hold for the area of strike-slip near the Fish Creek

Platform. Thus, basement topography and structures appear to strongly influence present-day in

situ stress regimes in the area.
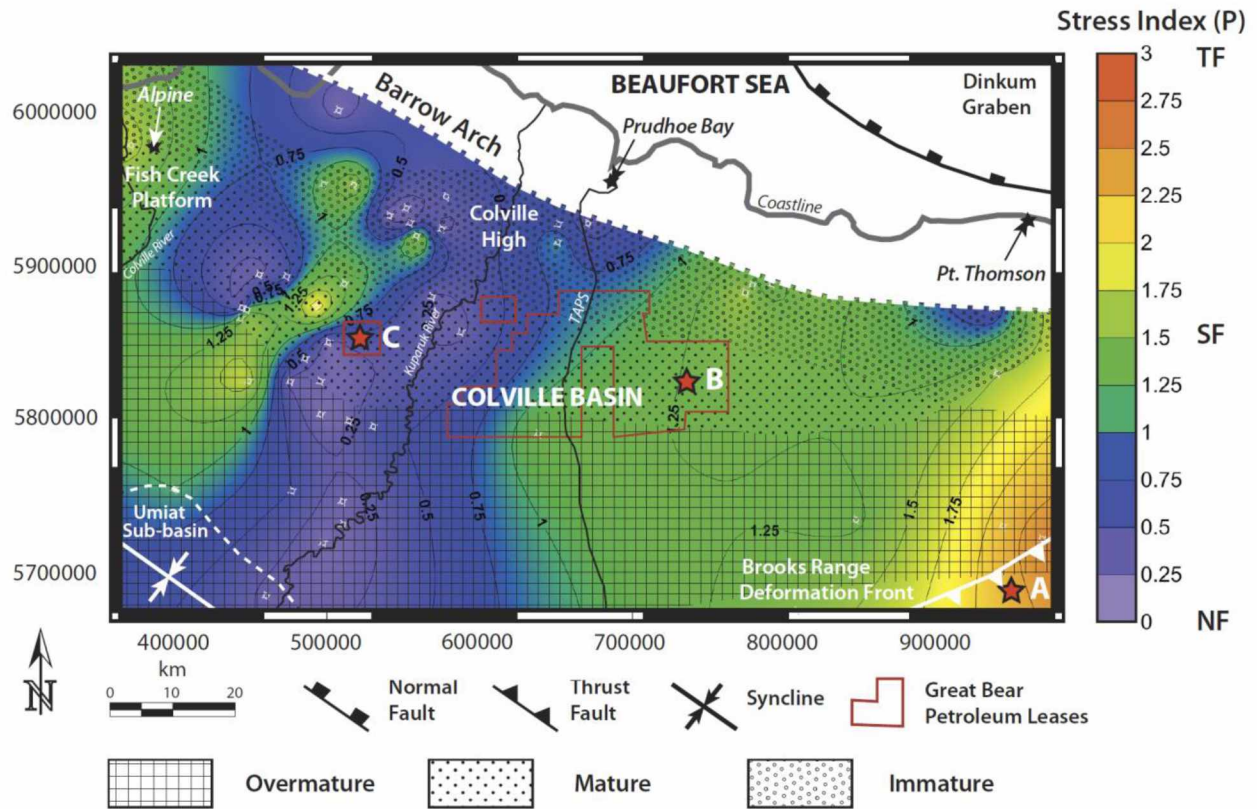
Figure 4-16 Map of in situ stress regimes present at the top of the Shublik Formation
Regional thermal maturity windows of the Shublik Formation are superimposed on the stress regime map (modified from Hanks, 2013). Hypothetical wells B and C (marked as red stars) show the areas of variable stress regimes where the Shublik has been identified as being mature.
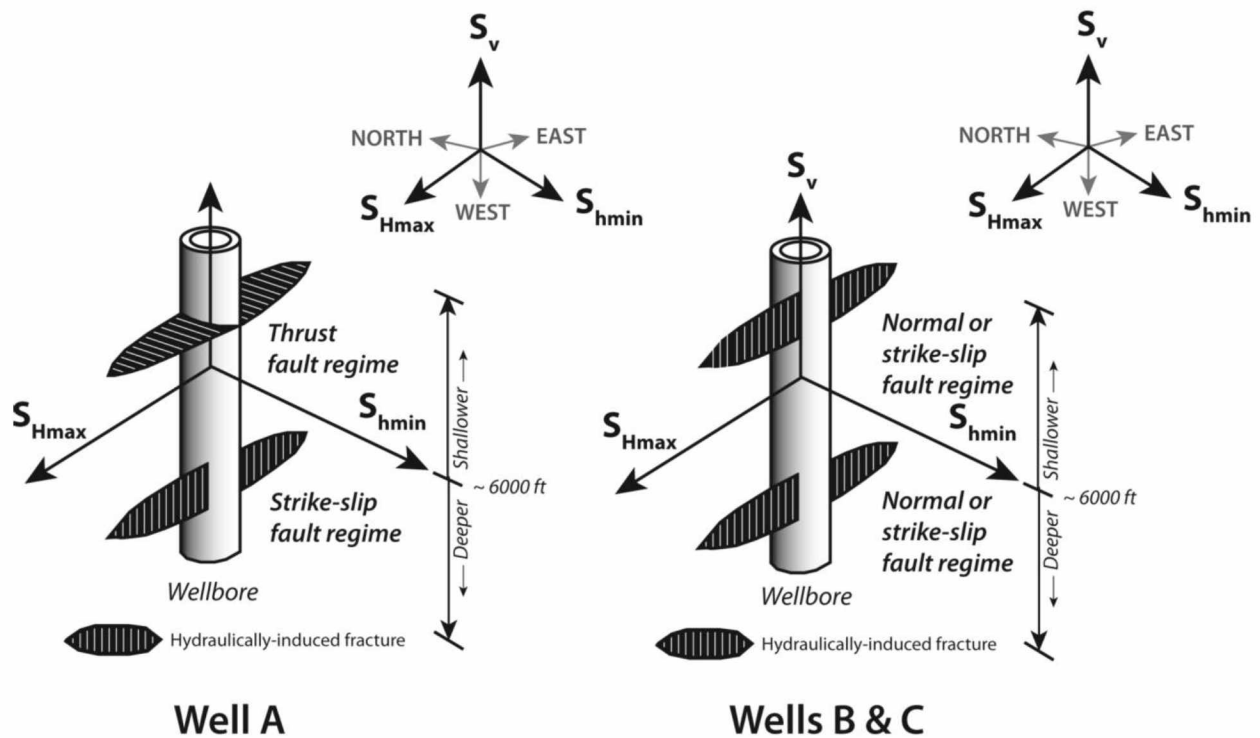
Figure 4-17 Models for the hydraulic fracture geometries

Simplified models for the hydraulic fracture geometries in hypothetical exploration wells A, B and C (locations shown on Figure 16). Hydraulic fractures in well A at shallow depths where a thrust fault regime would be active will be horizontal; at depths greater than 6000 ft (1829 m) where the in situ stress regime would be strike slip, hydraulic fractures would be vertical and northwest-oriented. In locations B & C, hydraulic factures will be vertical and either northwest-oriented or northeast-oriented, depending upon the orientation of local S_{Hmax}.

5 A preliminary study of the carbon sequestration and enhanced coal bed methane production potential of subbituminous to high-volatile bituminous coals of the Healy Creek Formation, Nenana Basin, Interior Alaska[1]

5.1 Abstract

Naturally fractured, unmineable coal seam reservoirs are attractive targets for geological sequestration of CO_2 because of their high CO_2-adsorption capacity and possible cost offsets from enhanced coal bed methane production. In this study, we have investigated the CO_2 sequestration and CH_4 production potential of the subbituminous to high-volatile C bituminous Healy Creek Formation coals through preliminary sensitivity analyses, experimental design methods, and fluid flow simulations. Our primary sensitivity analyses indicate that the total volumes of CO_2 sequestered and CH_4 produced from the Healy Creek coals are mostly sensitive to bottomhole injection pressure, coal matrix porosity, fracture porosity, fracture permeability, coal compressibility and coal volumetric strain. The results of Plackett-Burman experimental design were used to further generate proxy models for probabilistic reservoir forecasts. Our probabilistic estimates for the mature, subbituminous to high-volatile C bituminous Healy Creek coals in the entire Nenana Basin indicate that it is possible to sequester between 0.41 TCF (P10) and 0.05 TCF (P90) of CO_2 while producing between 0.36 TCF (P10) and 0.05 TCF (P90) of CH_4 at the end of a 44 year forecast. Fluid flow scenarios show that CO_2 sequestration through a primary reservoir depletion method is the most effective way to inject CO_2 in the coals of the Nenana Basin. Including a horizontal well instead of the vertical well resulted in relatively high average gas production rates and subsequent total cumulative gas production. Our CO_2 buoyancy

---

[1] Dixit, N.C., Ahmadi, M., Hanks, C.L., and Awoleke, O. (2016). Preliminary study of the carbon sequestration and enhanced coal bed methane production potential of subbituminous to high-volatile bituminous coals of the Healy Creek Formation, Nenana basin, Interior Alaska, Natural Resources Research (in press).

scenario suggests that the effect of CO_2 buoyancy and the nature of caprock should be considered in identifying potential geologic sites for CO_2 sequestration.

5.2   Introduction

In Interior Alaska, local communities rely on coal as a major energy source for electricity generation, with over 30% of the electricity generated by six coal-fired power plants (McDowell Group Inc., 2013). In 2007, greenhouse gases emitted from the coal-fired power sources in the Fairbanks North Star Borough (FNSB) were equivalent to over 1.61 million short tons of CO_2 (Holdmann and Murphy, 2008). Long term sequestration of CO_2 in Interior Alaska will be desirable to reduce CO_2 emissions from power generating stations under the Clean Power Plan (CPP) if coal is to continue to be a viable energy source. Several recent geological studies have showed that CO_2 can be stored as a compressed gas, liquid or in supercritical phase within a geological media such as depleted oil and gas reservoirs, deep unmineable coal seams and deep saline aquifers (Bachu, 2000; Davison et al., 2001). The abundance of coal-bearing strata in Interior Alaska provides an attractive and significant CO_2 storage option, with the additional advantage of the CO_2 sequestration costs being offset by the enhanced coal bed methane recovery (ECBM).

The Nenana coal province is the most promising area for long-term storage of CO_2 in the Interior Alaska area. These thick, Tertiary-age coal resources are located relatively close to the largest coal-fired power plants (Figure 5-1A and 5-1B). Estimates of the total identified coal resource that occurs at depths up to 3000 ft within the Nenana coal province are 7.7 billion short tons, with an additional 10 billion short tons of undiscovered resources in the subsurface of the Nenana Basin (Wahrhaftig, 1973; Merritt, 1986; Stevens and Bank, 2007).

This paper focuses on the CO_2 sequestration capacity of subbituminous to high-volatile C (HVC) bituminous coals from a portion of the Tertiary coal-bearing section in the central part of the Nenana Basin. The primary objective of our study is to use reservoir simulation to determine the CO_2 storage potential of these coals and subsequent recovery estimates of coal bed methane (ECBM).

5.3   Background

The Nenana Basin is a Cenozoic northeast-southwest-oriented pull-apart basin in central Interior Alaska with the Yukon-Tanana Upland to north and north-east, and the Alaska Range fold-and-thrust belt to the south (Van Kooten et al., 2012; Tape et al., 2015) (Figures 5-1 and 5-2). The basin is structurally asymmetric with a steeply dipping southeastern margin bounded by a major, active strike-slip fault, the Minto fault, and a relatively gently dipping northwestern flank (Van Kooten et al., 2012; Dixit and Hanks, 2015; Doyon Limited, 2015). Several recent seismic-reflection and potential-field studies of the basin suggest that most basin subsidence and basin growth has been accommodated along northwest- and northeast-striking intrabasinal transverse and normal faults that further allowed depocenters to develop in northern and southern parts of the basin (Dixit and Hanks, 2015, Doyon Limited, 2015; Rizzo, 2015). The central part of the basin is marked by an intrabasinal structural high that provides potential structural traps; these traps have been the focus of an extensive hydrocarbon exploration program in recent years (Doyon Limited, 2015) (Figure 5-2).

213

5.3.1 Coal Stratigraphy

The basin contains up to 24000 ft of Tertiary non-marine sedimentary strata deposited uncomfortably on Proterozoic to early Paleozoic Yukon-Tanana Terrane basement schist (Van Kooten et al., 2012, Doyon Limited, 2015) (Table 5-1). The Tertiary sedimentary sequences are mainly composed of: 1) Late Paleocene and older sediments, 2) Miocene Usibelli Group sediments, 3) Pliocene Nenana Gravel, and 4) Quaternary surficial and unconsolidated deposits. The Usibelli Group is further subdivided into five formations: the Healy Creek, Sanctuary, Suntrana, Lignite Creek and Grubstake formations (Wahrhaftig et al., 1969). The major thermally mature to marginally mature coal-bearing units of the Nenana Basin occur in the Late Paleocene and Healy Creek formations (Van Kooten et al., 2012).

The Healy Creek Formation (late Oligocene to early Miocene in age) is the focus of this study and is the oldest unit within the coal-bearing Usibelli Group. The Healy Creek Formation in the exposed Nenana coal province consists of fine-to-medium-grained sandstone, conglomerate, carbonaceous claystone and thinly to thick bedded coals deposited in a proximal to gravelly braided fluvial environment adjacent to peat-forming wetlands (Wahrhaftig et al., 1969; Ridgway et al., 2007; Dixit and Tomsich, 2014). Coal thicknesses in the Healy Creek Formation vary significantly across the exposed Nenana province, reaching up to 70 ft thick (Ridgway et al., 2007). In the Nenana coal province, the Tertiary coal seams appear to be laterally continuous and cover an area over 2500 mi^2 (Merritt, 1986).

The Healy Creek Formation is overlain comfortably by thick lacustrine grey siltstone and mudstone "caprock" of the early Miocene Sanctuary Formation. The Sanctuary Formation is up to 1000 ft thick in the Nenana Basin (Doyon Limited, 2015) (Figure 5-3). The Healy Creek

Formation uncomformably overlies Late Paleocene coals and coaly mudstones in the deeper parts of the basin (Van Kooten et al., 2012; Doyon Limited, 2015).

In the Nunivak 1 and Nunivak 2 wells, Healy Creek Formation coal seams range from 5ft to 20 ft in thickness and are considered saturated with coal bed methane, making them viable candidates for CO_2 sequestration and ECBM in the central Nenana Basin (AOGCC, 2015; Doyon Limited, 2015) (Figure 5-4). These Healy Creek Formation coals are subbituminous to HVC bituminous coals with Type III kerogen (78-98%) and occur at depths of about 5340 ft to 10100 ft in the central part of the basin (Van Kooten et al., 2012; Dixit and Tomsich, 2014; Doyon Limited, 2015). The mean vitrinite reflectance of the coals ranges from 0.43 to 0.74%R_0 and suggests that the coals are in the early oil generation window in the basin (Stanley and Lillis, 2011; Doyon Limited, 2015). Petrographic analyses of the Healy Creek Formation coal samples from the Nunivak 1 well indicate that the coals contain between 78% to 90% vitrinite (huminite) with around 7% to 20% liptinite contents, making them ideal candidates for geological CO_2 sequestration (White et al., 2005; Dixit and Hanks, 2015). Rock-Eval pyrolysis analyses of these coaly units from the Nunivak 1 well further indicate that the coals have up to about 61.32 wt.% of total organic content (TOC) (average about 37.17 wt.%) and show excellent hydrocarbon source potential (Stanley and Lillis, 2011).

5.3.2 Previous CO_2 Sequestration Estimates

Several studies have investigated the CO_2 storage potential of the Tertiary-age low-rank lignite and subbituminous coals that occur at depths less than 3000 ft in the Nenana coal province. Stevens and Bank (2007) first evaluated CO_2 storage capacity of Tertiary coals of the Usibelli Group that occur at depths less than 3000 feet in the Nenana coal fields using the U.S.

Geological Survey (USGS) estimates of coal resources for Central Alaska. Their estimates were based on the assumption that the low-rank Tertiary coals of the Nenana coal fields had initial gas contents of 100 scf/ton with the ratio of 3:1 for CO_2/CH_4 adsorption capacity. They concluded that the coals in the Nenana coal province could sequester about 0.063 gigatons (Gt) (1.1 trillion cubic feet (TCF)) of CO_2.

Based on recent CO_2 sequestration studies of lower rank coals in the Williston Basin of North Dakota and the Powder River Basin in Colorado, Shellenbaum and Clough (2010) found that the lower rank coals located at depths less than 3000 ft in the Nenana coal fields had a potentially higher CO_2/CH_4 adsorption capacity, on the order of 10:1. They revised the estimate of CO_2 sequestration potential in Nenana coal seams to about 0.41 Gt (9.02 TCF).

Recent seismic, drilling and outcrop studies of the Nenana Basin, one of the major sub-basins in the Nenana coal province near the northern foothills of the Alaska Range, have identified fairly thick and extensive lignite to high-rank bituminous deposits (up to 1200 ft thick on average) in the Usibelli Group and Late Paleocene Formation at depths up to 21000 ft (Van Kooten et al., 2012; Hanks and Holdmann, 2013; Doyon, 2015). Based on the thickness, distribution and rank of these Middle to Early Tertiary coal beds, Hanks and Holdmann (2013) suggest that these coals are a potential candidate for geologic CO_2 sequestration and simultaneous coal bed methane production. Their preliminary analysis of the CO_2 storage potential of the lignite to high-rank bituminous coals located at deeper depths in the Nenana Basin was based on the total pure coal mass, and coal adsorption capacity and suggests that these coals could sequester up to 4.36 Gt of CO_2 (~96 TCF) at a depth greater than 5110 ft.

5.3.3 Evaluating the Effect of Uncertainty in Coal Properties on CO_2 Sequestration and ECBM Production Estimates

Evaluating the technical feasibility and economic viability of a coal bed as a candidate CO_2 sequestration reservoir requires a detailed knowledge of: 1) in-situ gas content, 2) water saturation, 3) coal porosity and permeability, 4) CO_2 adsorption capacity, 5) in situ stress, 6) cleat spacing and 7) overlying caprock (Flores, 2004; Hernandez et al., 2006; Pashin et al., 2009; Seidle, 2011; Pashin, 2016). It is important to account for this complexity associated with the coal properties to provide better constraints on the CO_2 sequestration capacity and ECBM production estimates of a coal-bearing area.

Most of the previous CO_2 sequestration feasibility studies for the Nenana coal province were based on the assumptions that the coal parameters such as coal rank and coal density remain unchanged both laterally and with depth, and that the total mass of the coal is available for CO_2 sequestration. However, laboratory and field pilot-scale studies during the last few decades have shown that coal seams are highly variable in terms of their physical and chemical properties (McKee et al., 1988; Pashin, 1998, Siriwardane et al., 2009; Pashin et al., 2015). In addition, due to the heterogeneity in coal properties such as permeability, adsorptive capacity, and gas composition, not all of the coal seams in the subsurface are suitable for CO_2 sequestration and coal bed methane production.

With limited field data, reservoir heterogeneities can result in a wide range of uncertainty in reservoir input variables that are a source of inaccuracy in reservoir forecasts. Over the last decades, numerical modeling and reservoir characterization studies have demonstrated the utility

of experimental design methods and Monte Carlo analysis in reducing these uncertainties in reservoir properties and quantifying their effect on reservoir performance (Damsleth et al., 1992; Friedmann et al., 2003; Yeten et al., 2005; Arinkoola and Ogbe, 2015).

5.4   Methods

A top-Healy Creek Formation structure map was used to construct a three-dimensional (3D) reservoir model of the candidate coal reservoirs. The Computer Modeling Group's Generalized Equation-of-State Model (GEM) compositional simulator was used to perform multi-component (CO_2, CH_4 and water) compositional flow simulations associated with CO_2 sequestration and coal bed methane recovery. The input parameters for the stochastic reservoir simulations were obtained from newly published petroleum exploration data, field data collected in this study and suitable data from other analogue coal-bearing basins. We performed sensitivity analyses to identify the most influential reservoir variables that had a maximum impact on the CO_2 sequestration and CH_4 production estimates at the end of a 44 year simulation period (24 years of primary CH_4 production followed by 20 years of CO_2 injection). The results of our sensitivity analyses were used as an input for the two-level Plackett-Burman (PB) experimental design to model the interactions between the most important reservoir input variables and the reservoir response and to generate proxy models. Monte Carlo analysis using these regression models as inputs allowed us to determine a probabilistic range (P10 to P90) of the total cumulative volumes of CO_2 sequestered and CH_4 produced at the end of the 44 year forecast. We also investigated the effects of producer well spacing, reservoir pressure depletion, well orientation and caprock lithology on CO_2 sequestration and enhanced coal bed methane estimates through a series of fluid flow simulations. The following sections discuss our approach in detail.

5.4.1 Constructing a Reservoir Model of the Healy Creek Formation Coals

Publicly available gamma ray logs and core data from two exploration wells (Dixit and Tomsich, 2014; AOGCC, 2015) along with 2-dimensional (2D) seismic data collected during the 1980's by ARCO were used to build the geological model. A drainage area of 160 acres in the central part of the Nenana Basin was selected for the geologic model based on the availability of well data and its vicinity to infrastructure that could be used in future to transport anthropogenic CO_2 to the basin (Figure 5-1). We identified three coal seams (CS1, CS2 and CS3), with ranks ranging from subbituminous to HVC bituminous within the Healy Creek Formation as our target seams for CO_2 sequestration (Figures 5-3 and 5-4). Well data were tied to 2D seismic profiles using synthetic seismograms to create time-to-depth curves for the target coal seams. A 3-dimensional orthogonal corner point grid was then developed using CMG Builder, based on the structure map of the Healy Creek coals (Figure 5-5).

In the absence of nitrogen isotherm data for low-permeability HVC bituminous coals, a "dual-porosity" reservoir model was built in GEM for a two-component system (CO_2 and CH_4). The coal seams were simulated as uniform and continuous in our base model. The face cleats were modeled in a NW-SE direction (I-direction), following the trend of maximum principal horizontal stress inferred from the fracture data collected from an outcrop along the eastern margin of the Nenana basin (Rizzo, 2015). Initial reservoir simulations were run using one injection well and one production well (a quarter of a 5-spot vertical well pattern) with a 160 acre drainage area. The model was subdivided into five vertical layers to better constrain the fluid flow behavior in the coal seams. The base case simulation model consists of 4805 blocks (31 in I-direction, 31 in J-direction and 5 in K-direction) with an individual block size of 71 ft x 97 ft x 15 ft (Figure 5-5). This grid setting was chosen based on a grid size sensitivity study that

identified the coarsest grid model possible with a minimal loss of detail and optimized the simulation running time. The coal seam was considered sealed, homogeneous, and isotropic to focus more on the uncertainty in the parameters under investigation.

5.4.2 Reservoir Properties

Constructing a 3D reservoir model that realistically represents reservoir heterogeneity requires a detailed measure of the geologic and related reservoir properties. Many of the initial reservoir properties for the Healy Creek coals are not known. A key part of this study was to qualitatively investigate the effect of the uncertainty in these reservoir properties. In this study, most of the initial reservoir properties of the candidate Healy Creek coals were calculated from the previously published well log data and coal analyses from the Nenana coal province, and/or used reservoir properties from coal-bearing basins that had a similar coal character. A list of the resulting input reservoir parameters used in this study are summarized in Table 5-2.

5.4.3 Probabilistic Reservoir Simulation through Experimental Design

Reservoir Sensitivity Analysis

The main objective in this part of the analysis was to find the most influential input variables on the total volumes of CO_2 sequestered and CH_4 produced from the Healy Creek Formation coals. To do this, we varied one input variable at a time using its low value (P90) or high value (P10) while keeping other input variables constant at their base-level values (P50) (Table 5-3). The sensitivity of each parameter was analyzed and discussed by observing key indicators such as CO_2 breakthrough times and peak gas rates. The most important reservoir variables identified in the sensitivity analyses were then used as an input for two-level (low and high-level) Placket-Burman experimental design.

The simulation input parameters used in the base model are given in Tables 5-2 and 5-3. In the base model scenarios, we ran the simulation for 24 years of primary methane production and an additional 20 years of CO_2 injection with 160 acres of well spacing. During the primary methane production period, a vertical production well was placed in the center of our reservoir grid with a drainage area of 160 acres. After 24 years of primary methane production, one vertical injection well and one vertical production well were placed in opposite corners of the grid with a well spacing of 160 acres (Figure 5-6). The initial 24 years of primary production time was included in our models because the peak gas production rate starts to decline after 24 years. A single vertical injector well was modeled under two constraints: pure CO_2 injection, and a maximum bottom-hole pressure of 3100 psia. The injection pressure was kept below the formation fracture pressure (4368 psia) at these depths to avoid accidental fracturing of coal close to the injection well (Dixit et al., 2014). The vertical production well was set for a routine minimum bottom-hole pressure (BHP) of about 300 psia (Ross et al., 2009). The extended Palmer and Mansoori equation (1998) was used to model the coal matrix shrinkage and swelling using the parameters in Table 5-2.

For our study, we assumed CO_2 breakthrough time as the time at which 1% of total injected CO_2 gas moles were produced (Ross et al., 2009). It means approximately 99% of CO_2 injected was stored in the coal.

Experimental Design Approach for Probabilistic Reservoir Forecasting

After identifying the most influential input variable in the reservoir sensitivity analysis, we used a two-level (low and high) Plackett-Burman (PB) experimental design to capture the interactions between the input variables and estimate their effects on the reservoir response with a minimal number of simulation runs. In PB design, the total cumulative volumes of CO_2 sequestered and CH_4 produced were considered as dependent variables or the reservoir response. A traditional two-level PB experimental design involves 4n simulation runs (where n = 1, 2, 3…) where the maximum numbers of reservoir input variables that can be studied are 4n-1 (Plackett and Burman, 1946). Using PB design, we developed the 8-run experimental matrix for the reservoir input variables (a full-factorial design would consist of 2^5=32 runs), as shown in Table 5-4.

Based on the results of the PB experimental design and in order to determine a probabilistic suite of reservoir forecasts, we first generated first-order polynomials for each of the dependent variables using multivariate regression analyses. The PB approach limits the reservoir response to a first-order polynomial regression model. These first-order polynomials were then used as proxy models for Monte Carlo simulations. Monte Carlo simulations were performed on the given proxy model with 2000 realizations to generate the cumulative probability distributions of the total volumes of CO_2 sequestered and CH_4 produced. The resulting distribution of the reservoir response (P90 to P10) from the deterministic estimation (P50) shows the effect of uncertainty in each input parameter.

5.4.4 Fluid Flow Simulation Scenarios

In this study, we also investigated the effects of producer well spacing, reservoir pressure depletion, well orientation and caprock lithology on CO_2 sequestration and enhanced coal bed methane estimates. For our fluid flow simulation scenarios, reservoir simulations were performed over a 44 year period for a well spacing of 160 acres and with a single injection well and production well located in opposite corners of the grid.

Primary CH_4 Production with no CO_2 Injection

Here, primary production simulations were performed over a 44 year period to determine the total cumulative volumes of CH_4 produced with no CO_2 injection. The simulations were run for a well spacing of 160 acres (1 production well in the center) and 40 acres of well spacing (4 producing wells) to analyze the effects of dewatering and reservoir pressure depletion on the total cumulative primary CH_4 production (Figure 5-7). In addition, we also investigated the time to reach peak gas production and water production rates for future production forecasting.

Enhanced CH_4 Production with CO_2 Injection

Pure CO_2 was injected into the coal seams via a vertical injection well and desorbed methane from the coal surface was produced through a vertical production well with a well spacing of 160 acres in two scenarios: Case 1--CO_2 was injected into the coal as soon as the production well was opened for CH_4 production; and Case 2--CO_2 was injected into the coal after 24 years of primary CH_4 production. Case 2 was considered the base case against which the results from all other scenarios were compared. In Case 2, primary methane production for 24 years was allowed to deplete the reservoir pressure before injection of CO_2.

223

In both scenarios, the CO_2 was injected at an injection rate of 200,000 SCF/day. In these scenarios, we consider injection of CO_2 within a small drainage area of 160 acres using only one injection well, resulting in a lower rate of CO_2 injection. However, it is possible to inject large volumes of CO_2 within a relatively short period of time using a larger number of injection wells if a production-scale field size is considered. Such a full-field reservoir study is beyond the scope of this study and should be considered for future work. The simulations were run to further determine the time when the breakthrough of CO_2 would occur in the production wells and the total cumulative volumes of CO_2 that could be stored in the coal seams at the time of breakthrough. The injection pressure was set to be 3100 psia, less than the formation fracture pressure of 4368 psia in the area (Dixit et al., 2014).

Vertical vs Horizontal Well Injection

Traditionally, most CO_2 injection wells are vertical wells (Ayers, 2002; Reeves et al., 2003). However, recent studies of low-permeability coals from the Alberta basin of Canada, and Ordos basin of China have shown that much higher well productivity is obtained with a horizontal well due to the greater wellbore contact with the coal surface and increased intersection with high conductivity fractures in the coal (Gentzis et al., 2008; Pan et al., 2013). In this study, we investigated the effect of a horizontal well drilled in the I-direction (i.e., the primary fluid migration pathway in a fractured coal reservoir). A horizontal well was placed in the bottom layer of the model to take advantage of the vertical upward sweep of gas (buoyancy effect). We modeled a single-lateral well with a short horizontal length of 600ft; the drainage area was kept constant relative to the base case (160 acres). We placed the injector well and producer well at the corners of the simulation domain of 160 acres. We then investigated the

total cumulative volumes of CO_2 sequestered and CH_4 produced at the time of CO_2 breakthrough using the horizontal well and compared it to our base-case simulation results. In these scenarios, pure CO_2 was injected for 20 years after 24 years of primary CH_4 production. Coal matrix shrinkage and swelling was incorporated in the model.

Effect of CO_2 Buoyancy and Caprock Lithology

The main objective of this simulation was to investigate the effect of gas migration into the caprock overlying the target coal seams on the amount of CO_2 trapped within the coal seams. For simplicity, we assumed a sandstone-shale sequence (individual layer thickness of 25 ft) overlying the Healy Creek coals. Sand porosity and permeability values were obtained from the Totek Hills 1 well data (Doyon Limited, 2015). Shale porosity and permeability values were from the Powder River Basin (This study; Ross et al., 2009). For the leakage scenario, pure CO_2 was injected for 20 years after 24 years of primary CH_4 production. Coal matrix shrinkage and swelling was included.

5.5 Results

5.5.1 Preliminary Sensitivity Analyses

Figure 5-8 shows the results of our primary sensitivity analyses for varying one reservoir input parameter at a time at the end of a 44 year forecast. In our base case simulation, we kept all the reservoir parameters at the P50 level. For all other simulation scenarios, we varied one parameter at a time to its P90 or P10 level. Below we discuss the most influential reservoir input parameters to which the reservoir response was most sensitive.

Injector Bottom-hole Pressure (BHIP)

The bottom hole pressure of an injector well is a key parameter that determines the peak injection rate for CO_2 at a given reservoir pressure. We found that the BHP constraint for the injector well had a significant effect on the total cumulative volumes of CO_2 sequestered and CH_4 produced (Figure 5-8). Both the total cumulative volumes of CO_2 sequestered and CH_4 produced increased by 89% and 66% respectively for a BHIP constraint of 4000 psia (P10) compared to the base case (P50 value of 3100 psia) (Table 5-3).

Increasing the BHIP allowed more CO_2 to be injected, causing more CH_4 to be desorbed from the matrix in exchange for CO_2. The higher BHIP also allowed a 95% increase in peak gas injection rate compared to the base case peak gas injection rate of 1.12 MMSCF/day. The final average reservoir pressure observed after gas breakthrough in the production well increased by 34% as compared to the base case value of 1655 psia.

Lowering the BHIP constraint to 2000 psia (P90) had a negative effect on the total cumulative CO_2 sequestration and CH_4 production volumes (Figure 5-8). Twenty years after initiation of CO_2 injection, CO_2 sequestration decreased by 71% and CH_4 production decreased by 46% relative to the base case volumes (Table 5-3). CO_2 breakthrough was not observed. In this case, the peak gas injection rate decreased by 82% and the final average reservoir pressure decreased by 29%.

Coal Matrix Porosity

A matrix porosity of 0.01% was used in the base case scenario. Using a higher matrix porosity of 1% (P10) increased the total cumulative CH_4 production by 39% and CO_2 sequestration volumes by 32%, whereas a lower matrix porosity of 0.001% (P90) decreased both the cumulative CH_4 production and CO_2 sequestration capacity by 8% and 6% respectively (Figure 5-8 and Table 5-3). The peak gas injection rate increased by 11% with an increase in the matrix porosity whereas it decreased by 2.4% with a decrease in the matrix porosity.

These values indicate that increasing the value for coal matrix porosity increased the pore volume and the free CH_4 in the matrix pores. More CH_4 flowed from the pores of the matrix to fractures compared to the base case.

Coal Fracture Porosity

The fracture porosity was simulated at 0.001% (P90) and 0.1% (P10) with the base case value of 0.01%. Fractures were assumed to be fully saturated with water.

Decreasing the fracture porosity to 0.001% increased cumulative CH_4 production by 24% and CO_2 sequestration volumes by 15%, whereas increasing the fracture porosity to 0.1% decreased cumulative CH_4 production by 70% and total CO_2 sequestered by 24% (Figure 5-8 and Table 5-3). By increasing the cleat porosity we introduced more water into the cleats (since we assumed that the cleats were 100% water saturated), making it harder for the gas to flow through the cleats and requiring additional water to be produced.

Coal Fracture Permeability

The permeability of natural fractures within the coal is a key constraint on the CO_2 sequestration capacity of the coal. Our simulations showed that cumulative CO_2 injection and CH_4 production volumes increased with increasing fracture permeability (Figure 5-8). Increasing the fracture permeability to 1 md (P10) increased the total cumulative CH_4 production by 37% and CO_2 sequestration volumes by 18%. However, CO_2 breakthrough occurred at 15776 days due to increased gas injection rate. The peak gas injection rate increased by 174% compared to the base case value. Decreasing the fracture permeability to 0.001 md (P90) reduced cumulative CH_4 production by 99% and CO_2 sequestration volumes by 98%, but there was no CO_2 breakthrough after 20 years of injection (Figure 5-8 and Table 5-3).

These results indicate that an increase in fracture permeability increases the total gas flow through the fractures. This means more CO_2 can be injected and more CH_4 produced at a higher injection rate over a short time. However, because of the higher permeability of coal fractures, CO_2 could move through the fractures at a faster rate, decreasing the breakthrough time at the production well.

We also examined the effect of permeability anisotropy by varying permeability just in the direction of the face cleats (I-direction). In this scenario, we increased the fracture permeability in the I-direction to 1 md, while keeping the fracture permeabilities in all other directions at the base case value of 0.1 md. We found that there was a moderate increase in the total cumulative volumes of CO_2 sequestered by 21% and CH_4 produced by 16% (Table 5-3).

These results suggest that high permeability in the face cleat direction dominates gas flow to the production wells and influences the gas sweep patterns.

Matrix Shrinkage and Swelling Parameters

In GEM, an extended Palmer and Mansoori equation was used to calculate fracture permeability changes due to desorption and adsorption of gases in the coal matrix and changes in effective stress. Fracture compressibility defines the linear effective stress term in the Palmer and Mansoori equation, whereas volumetric strain at infinite pressure was incorporated in the shrinkage and swelling term (CMG, 2015). Our simulation results indicate that the geomechanical behavior of the reservoir due to desorption and adsorption of gases during production can influence reservoir response significantly.

Fracture Compressibility

Our simulations showed that, by decreasing the fracture compressibility to 1×10^{-06} /psi (compared to 1.38×10^{-04} 1/psi in the base case) both the total cumulative volumes of CO_2 sequestered and the CH_4 produced decreased significantly by 69% and 85% respectively (Figure 5-8 and Table 5-3). Increasing the fracture compressibility to 1×10^{-3} significantly increased both the total cumulative volumes of CO_2 sequestered and CH_4 produced by 47% and 84% respectively.

It is likely that, at lower fracture compressibility values, the fractures become stiffer and become harder to open, resulting in a reduction in the fracture permeability and a decrease in the total cumulative volumes of CO_2 sequestered and CH_4 produced.

Volumetric Strain (CH_4)

For increased CH_4 volumetric strain of 0.005 (compared to base case value of 0), we found that the total volumes of CO_2 sequestered and CH_4 produced increased by 34% and 29%, respectively (Figure 5-8 and Table 5-3).

Increase in the volumetric strain for CH_4 caused a large, negative change in the matrix volume. Matrix shrinkage dominated and fracture permeability increased, further enhancing the CO_2 sequestration and cumulative CH_4 production.

5.5.2 Experimental Design Method and Monte Carlo Analysis

Our sensitivity analyses suggest that six reservoir parameters have the most significant effect on the total cumulative volumes of CO_2 sequestered and CH_4 produced: injector bottomhole pressure, coal matrix porosity, fracture porosity, fracture permeability, fracture compressibility and CH_4 volumetric strain. Using these six parameters, a two-level (low and high), 8-run experimental matrix for Plackett-Burman design was generated to capture the effects of linear interactions between the input parameters on the reservoir response (Table 5-4). Eight additional fluid-flow simulations for a six-variable matrix were performed using the CMG-GEM reservoir simulator. The corresponding total cumulative volumes of CO_2 sequestered and CH_4 produced for each simulation run at the end of the 44 year forecast were reported in Table 5-4.

A multivariable linear regression analysis of the simulation results from the Plackett-Burman design generated the following two first-order polynomials of the reservoir response (Tables 5-5 and 5-6).

Total cumulative volumes of CH_4 produced = 0.001 (BHIP) - 9.594 (MPorosity) + 4.801 (FPorosity) + 1.503 (FPermeability) + 3489.515 (FCompressibility) – 222.852 (VStrain) - 1.379

Total cumulative volumes of CO_2 sequestered = 0.001 (BHIP) - 8.273 (MPorosity) + 10.868 (FPorosity) + 1.998 (FPermeability) + 3542.373 (FCompressibility) - 332.308 (VStrain) – 1.682

Where BHIP is injector bottomhole pressure, MPorosity is coal matrix porosity, FPorosity is fracture porosity, FPermeability is fracture permeability, FCompressibility is fracture compressibility and VStrain is CH_4 volumetric strain.

The R-squared statistic suggests that the model explains 99.9% of the variability in the total volumes of CH_4 produced while the adjusted R-square is 99.7 % (Table 5-5). For the variability in the total volumes of CO_2 sequestered, the fitted model R-square was 99.9% and adjusted R-square was 99.4% (Table 5-6). Based on the results of our regression analysis, the injector bottomhole pressure (BHIP), fracture permeability (FPermeability) and CH_4 volumetric strain (VStrain) had a significant effect (assuming 95% confidence level) on both the total volumes of CO_2 sequestered and CH_4 produced at the end of the 44 year forecast. Coal matrix porosity (Mporosity) had a significant effect on the estimation of CH_4 production volumes. Fracture porosity (FPorosity) and fracture compressibility (FCompressibility) became insignificant on reservoir response towards the end of this simulation period.

Using these first-order polynomials as proxy models in Monte Carlo simulations, we generated the cumulative probability distributions and probability density functions for the total

volumes of CH_4 produced and CO_2 sequestered (Figure 5-9). The probability distribution of

reservoir response was calculated from 2000 iterations in Monte Carlo simulations. Since no data

was available for the probability distributions of the individual input variables, probability

functions used in the PB design (low and high levels) were applied in Monte Carlo analysis

(Table 5-4). The cumulative probability distribution of the total volumes of CH_4 produced at the

end of 44 years has P10 of 3.81 BCF, P50 of 1.89 BCF and P90 of 0.53 BCF. Furthermore, the

cumulative probability distribution of the total volumes of CO_2 sequestered at the end of this

period suggests P10 of 4.35 BCF, P50 of 2.06 BCF and P90 of 0.50 BCF.

5.5.3   Fluid Flow Simulated Production Scenarios

Primary CH_4 Production with no CO_2 Injection
       The results of our primary production scenarios are shown in Figure 5-10. At the end of

44 years and with no CO_2 injection, our simulations suggest that well spacing of 40 acres yielded

the total cumulative primary CH_4 recovery 211% higher than one with a larger well spacing of

160 acres. With smaller well spacing (40 acres), the final reservoir pressure reduced to 445 psia

with a peak gas production rate of 237 MSCF/day. In contrast, a higher well spacing (160 acres)

reduced the final reservoir pressure only to 952 psia with a lower peak gas production rate of 51

MSCF/day. The cumulative water production was higher (590 Mbbl) in 40 acres of well spacing

than in 160 acres (269 Mbbl).

       By increasing the number of injection wells in the same drainage area, we accelerated the

reservoir pressure reduction process, resulting in faster CH_4 desorption from the matrix to the

fracture system and an improved dewatering process in the coal bed reservoir (Figure 5-10).

However, the gas decline rate was observed to be higher in the 40 acres of well spacing scenario

than in the 160 acres. Our simulations showed that the total cumulative primary CH_4 recovery would be much higher in a multiple-well production system than using only one production well for the same drainage area.

Enhanced Coal Bed Methane Production with Pure CO_2 Injection

In this scenario, pure CO_2 was injected into the coal seams via a vertical injection well and desorbed methane from the coal surface was produced through a vertical production well with a well spacing of 160 acres. Two cases were evaluated--Case 1 where CO_2 injection was simultaneous with CH_4 production and Case 2 where CO_2 injection begins after 24 years of CH_4 production.

Results show that total cumulative volumes of CO_2 sequestered in Case 1 decreased by 30% compared to the total cumulative volumes in Case 2 (1.46 BSCF) (Figure 5-11). The total cumulative volumes of CH_4 produced in Case 1 decreased by 73% compared to Case 2 (0.8 BSCF). CO_2 breakthrough occurred at 5173 days for Case 1, but no CO_2 breakthrough was observed for Case 2. At the time of CO_2 breakthrough in the production well, the reservoir pressure reached 1497 psi in Case 1 whereas the reservoir pressure was reduced to 1206 psi in Case 2 after 20 years of CO_2 injection with no CO_2 breakthrough (Figure 5-11).

In Case 1, total cumulative volumes of CO_2 injected and sequestered in the coal reservoir were limited by initial water within the coal system and relatively high in situ reservoir pressures. In Case 2, primary cumulative production of CH_4 reduced the reservoir pressure and subsequent CH_4 desorption from the coal surface, further providing more surface area for CO_2

adsorption within the coal. In addition, higher volumes of free CO_2 injected in the coal fractures in Case 1 resulted in CO_2 breakthrough at the production well much earlier than in Case 2 (no CO_2 breakthrough).

This suggests that, in water-saturated coal, water content in the coal system and reservoir pressure are the most important parameters that should be considered when determining the timing for CO_2 injection in the coal reservoir.

Vertical vs Horizontal Well Injection

In this scenario, pure CO_2 was injected using a horizontal well after 24 years of primary CH_4 production and the results compared to Case 2. As seen from Figure 5-12, the average gas production rate using a horizontal well increased by 99% compared to the vertical well. The higher initial gas production rate resulted in a significant increase in the CH_4 production volumes and hence, a shorter production life of the horizontal well at the end of the simulation period.

Using the horizontal well, we increased the contact area of the wellbore with the coal surface as compared to the vertical well. The corresponding increased gas production could be due to initial higher CO_2 injectivity. Figure 5-13 shows the CO_2 gas sweep pattern observed with the horizontal injection well in comparison with the vertical well. It is clear from Figure 5-13 that the horizontal injection well provides a more efficient CO_2 gas sweep as the gas migrates vertically and laterally to the top of the coal, allowing more CH_4 to be produced.

Effect of CO_2 Buoyancy and Caprock Lithology

In this scenario, pure CO_2 was injected in a coal that was overlain by a sandstone-shale sequence after 24 years of primary CH_4 production. After 20 years of CO_2 injection, only 36% of the total volume of injected CO_2 was sequestered within the coal (Figure 5-14). A gas saturation of up to 63.5% was observed with the sand layer directly overlying the coalbed and with less than 1% in the shale layer.

This could happen if the rate of gas flow within the coal was greater than the rates of gas diffusion and adsorption in the coal. Buoyant gas could move faster in the coal fractures and migrate vertically into the overlying sand unit (Figure 5-15). If no caprock was present or if the caprock was highly fractured, gas would continue to migrate into the overlying rock units rather than flowing towards the production well. Our results therefore suggest that the CO_2 migrated vertically through the coalbeds into the overlying porous sand, then to the top of sand and was trapped by a highly impermeable (0.009 md) shale unit (Figures 5-14 and 5-15).

These results suggest that it is critical to determine the composition and nature of overlying rock formations as well as the coal in order to accurately estimate the volumes of CO_2 sequestration and identify suitable sites for potential geologic sequestration.

5.6   Discussion

5.6.1   Most Influential Reservoir Parameters

The results of our reservoir sensitivity analyses suggest that gas injection pressure (BHIP), coal matrix porosity (MPorosity), fracture porosity (FPorosity), fracture permeability (Fpermeability), fracture compressibility (FCompressibility) and CH_4 volumetric strain (VStrain)

235

have a maximum impact on the total cumulative volumes of CO_2 sequestration through enhanced coal bed methane recovery (Figure 5-8).

Despite the potential for higher CO_2 sequestration and CH_4 production volumes, using a higher IBHP is not an optimal choice if a long-term CO_2 injection is the main objective. The observed fracture pressures through leak-off tests or formation breakdown tests along with the optimum CO_2 injection rates can be used to accurately constrain the IBHP values for the CO_2 injector well (Reeves et al., 2003; Reeves and Oudinot, 2005).

Our preliminary analysis suggests that if the fracture permeabilities are close to 0.1 md, then a well spacing of 160 acres is ideal for the long-term CO_2 injection practices in the study area. For higher fracture permeabilities (> 1 md), the CO_2 breakthrough times would be lower. For high permeability coal reservoirs, we recommend increasing well spacing for the purpose of improving CO_2 sequestration capacity.

As a large volume of methane can be stored as free gas within the porous structure of the coal matrix, high initial coal matrix porosity can effectively improve primary CBM production (Bachu, 2000; Seidle, 2011). In addition, high total pore area due to high porosity of the coal matrix allows storage of a large part of the CH_4 volume as an adsorbed gas in the coal matrix. Therefore, coals with higher matrix porosities would allow increased CBM recovery during the later stages of CO_2 sequestration processes.

In water-saturated coal systems such as Healy Creek coals, the fracture porosity is also important in order to accurately determine the volumes of water produced during the dewatering phase. The prediction of water volumes is critical for determining the best schemes for produced water disposal.

Higher volumetric strain of CH_4 and fracture compressibility would enhance the fracture permeability through coal shrinkage and promote the efficiency of CO_2 sequestration and CH_4 production in the coal. Actual data on the geomechanical properties for Healy Creek coals are not available; an accurate measure of it would help improve prediction of change in permeability and gas flow characteristics within the coal.

5.6.2 Using Plackett-Burman Experimental Design to Develop Probabilistic Reservoir Forecasts

The results of our PB design along with regression analysis suggested that only injector bottomhole pressure, coal matrix porosity, fracture permeability and CH_4 volumetric strain had a significant effect on the reservoir response whereas fracture porosity and fracture compressibility became insignificant at the end of the 44-year forecast (Tables 5-5 and 5-6).

The effect of uncertainties in these main reservoir variables on the resulting reservoir response was quantified in a Monte Carlo analysis (Figure 5-9). For 160 acres of reservoir area, these results indicate that the total cumulative volumes of CH_4 produced would range from 3.81 BCF (P10) to 0.53 BCF (P90), whereas the total cumulative volumes of CO_2 sequestered would be 4.35 BCF (P10) to 0.50 BCF (P90). On the basis of a structure map of the Healy Creek formation (Figure 5-2), thermally-mature subbituminous coal seams (CS1, CS2 and CS3; depths greater than 5340 ft) located within the Nenana Basin cover an area of approximately 15,000

acres. Probabilistic estimates for the Healy Creek coals in the entire Nenana Basin would therefore result in total cumulative volumes of CH_4 produced between 0.36 TCF (P10) and 0.05 TCF (P90), and total cumulative volumes of CO_2 sequestered between 0.41 TCF (P10) and 0.05 TCF (P90) at the end of the 44 year forecast. Estimates of CO_2 sequestration and ECBM capacity of the Nenana Basin obtained in this study are significantly lower than that of previous studies by Stevens and Bank (2007), Shellenbaum and Clough (2010), and Hanks and Holdmann (2013). The spread in the cumulative probability distributions of the total CO_2 sequestration and CH_4 production volumes (P10 to P90 interval) suggests a large range of uncertainty within the most influential reservoir variables. To reduce this uncertainty, it is necessary to more accurately constrain the extreme values (low and high values) of the main reservoir variables--injector bottomhole pressure, matrix porosity, fracture permeability and coal volumetric strain.

5.6.3   CO₂ Sequestration and Methane Production Scenarios

Effect of the Producer Well Spacing
For the primary methane production scenario, the cumulative production volumes of CH_4 largely depend on the producer well spacing. When the producer wells are closely spaced (40 acres), the decline of the reservoir pressure is faster and greater volumes of formation water are removed from the fracture system, further enhancing the CH_4 desorption process in the coal matrix. This observation is supported by the well spacing studies from the San Juan Basin which concluded that, with the small well spacing, gas and water recovery factors from the coals were higher (Young et al., 1991; Agrawal, 2007). However, results of our simulations also indicate that the peak gas rate is much higher with a higher gas decline rate when wells are closely spaced. Despite the positive impact of the smaller well-spacing in these models, the actual

number of producer wells depends on the cost of drilling, the rate at which the field is being developed, the depth of the reservoir and the time limitations for the sequestration operations.

Effect of CO_2 Injection Timing

The results of our ECBM recovery scenarios show that the ECBM recovery under Case 2 (CO_2 injection after 24 years of primary CH_4 production) is the most effective option to inject CO_2 in the coal seams of the Healy Creek Formation in the Nenana Basin. Using this approach, it may be possible to sequestrate 1.46 BSCF of CO_2 while producing 0.8 BSCF of CH_4 over 44 years with a well spacing of 160 acres. No CO_2 breakthrough was observed and, therefore, a long-term CO_2 injection could be achieved.

Effect of Horizontal Well Injection

We found that if we use a horizontal injection well instead of the vertical well, there would be a significant increase in the CH_4 production volumes. The observed increase in the CH_4 production volumes could be due to the increased contact surface between the coal and the wellbore. Our simulations further show a shorter production life for the horizontal well compared to the vertical well, possibly due to the high initial gas production rates. However, the CO_2 injection by a horizontal well will create an effective gas-flow pathway through the coal reservoir by creating more surface contact between the coal surface and the horizontal wellbore. We suggest that a horizontal well may be advantageous if large volumes of CO_2 must be sequestered in over a shorter time period. However, it offers no significant advantage for long-term CH_4 production.

Effect of CO_2 Buoyancy and Caprock Lithology

Last, our simulation scenarios show that the CO_2 sequestration within coal also depends on the permeabilities and porosities of the rock formations overlying the target coal beds. Injected CO_2 will migrate as a free gas vertically and laterally away from the well bore to the top of the coal layer due to gas-buoyancy and reservoir pressure build-up. In the areas where the Healy Creek coals are overlain by highly porous and permeable sands, up to 63.5% of the gas will migrate preferentially through the sands, rather than being adsorbed on the coal surface. However, if the coal beds are overlain by impermeable caprock (rock permeabilities less than 0.002 md), up to 99% of the injected CO_2 would be trapped in the coal. The effect of CO_2 buoyancy and the nature of the caprock should therefore be considered in identifying potential geologic sites for CO_2 sequestration and in CO_2 storage capacity estimates for the coals.

5.7 Conclusion

This study used a preliminary reservoir model of the subbituminous to HVC bituminous coals of the Healy Creek Formation in the Nenana Basin to investigate the feasibility of geologic CO_2 sequestration in these coals and associated coal bed methane recovery. A 3D reservoir model of the Healy Creek Formation coals was developed and populated with coal properties using the Computer Modeling Group's GEM compositional simulator.

Primary sensitivity analyses and experimental design methods were used to assess the effects of uncertainty within major reservoir input parameters on the CO_2 sequestration and CH_4 production volumes. Although there are many variables to consider when developing a CO_2 sequestration/CH_4 production strategy for coals, Plackett-Burman experimental design methods allowed us to determine that bottomhole injection pressure, matrix porosity, fracture porosity and permeability, coal compressibility and coal volumetric strain have the largest impact on the CO_2

sequestration and CH_4 producibility of these particular coals. Our work indicates that the heterogeneity in the reservoir data greatly influences the range of CO_2 sequestration and CH_4 production estimates for the Healy Creek Coals.

Several fluid-flow simulation scenarios were investigated to understand the effect of well spacing on the primary CH_4 recovery, effect of CO_2 injection timing, effect of horizontal well injection, and the effect of caprock lithology on CO_2 migration pathways. Closer well spacing allows faster dewatering of the coal reservoir during the primary gas production phase. Initial peak gas rates are high using a small well-spacing and therefore, greater gas decline rates. With a horizontal injection well, almost 99% additional total cumulative volumes of CH_4 can be produced with a better sweep efficiency, compared to the vertical well. Injected CO_2 will migrate vertically and laterally through the coal beds as free gas away from the injection well due to its buoyancy and pressure build-up in the reservoir. If coals are overlain by a permeable layer such as sand, 63.5% of injected CO_2 will migrate into the overlying sand layer and potentially to the surface if no caprock is present. Proper characterization of the nature and composition of overlying rock units are equally important for the identification of proper geologic storage sites for the CO_2.

We also used the PB design approach and the results of sensitivity analyses to generate proxy models for probabilistic reservoir forecasting of the total volumes of CO_2 sequestered and CH_4 produced. The cumulative probability distributions obtained from the proxy models for our reservoir suggest that the total cumulative volumes of CO_2 sequestered at the end of the 44 year forecast range from 4.35 BCF (P10) to 0.50 BCF (P90) whereas the total volumes of CH_4

produced range from 3.81 BCF (P10) to 0.53 BCF (P90). On the basis of our probabilistic

reservoir estimates for a 160-acre pattern, the mature subbituminous Healy Creek Formation

coals in the entire Nenana Basin could sequester between 0.41 TCF (P10) and 0.05 TCF (P90) of

CO_2 while producing between 0.36 TCF (P10) and 0.05 TCF (P90) of CH_4. These probabilistic

reservoir estimates for the Nenana Basin are significantly less than that of previous studies and

indicate the effect of the uncertainties in reservoir rock properties. The uncertainty in these

forecasts can be reduced, however, by more accurate measures of key Healy coal properties such

as the matrix porosity, fracture porosity and permeability, and coal volumetric strain.

5.8 Acknowledgment

5.9 References

Agrawal, A. (2007). The economic feasibility of enhanced coalbed methane recovery using CO_2

sequestration in the San Juan Basin. Master's thesis, Texas A&M University, College Station,

Texas.

Alaska Oil and Gas Conservative Commission (AOGCC). (2015). Digital well history files, doa.alaska.gov/ogc/publicdb.html. Accessed September, 2015.

Arinkoola, A. O., and Ogbe, D. O. (2015). Examination of experimental designs and response surface methods for uncertainty analysis of production forecast: A Niger Delta case study. Journal of Petroleum Engineering, vol. 2015, doi:10.1155/2015/714541.

Ayers, W. B. (2002). Coalbed Methane Systems, Resources, and Production. AAPG Bulletin, 86(11),1853- 1890.

Bachu, S. (2000). Sequestration of CO_2 in geological media: Criteria and approach for site selection in response to climate change. Energy Conversion and Management, 41 (9), 953 -970.

Computer Modelling Group, (CMG). (2015). GEM - Compositional & Unconventional Oil & Gas Reservoir Simulator, Calgary, Canada.

Damsleth, E., Hage, A., and Volden, R. (1992). Maximum information at minimum cost: A North Sea field development study with an experimental design. Journal of Petroleum Technology, 44 (12), 1350-1356.

Davison, J., Freund, P., and Smith, A. (2001). Putting carbon back in the ground. IEA Greenhouse Gas R&D Programme, Cheltenham, UK.

Dixit, N. C., Hanks, C. L., and Ahmadi, M. (2014). Preliminary reservoir characterization of Late Paleocene coals in the southern Nenana Basin, Interior Alaska: CO_2 sequestration and enhanced coal bed methane recovery [abs]. Alaska Geological Society Technical Conference, Anchorage, Alaska.

Dixit, N. C., and Hanks, C. L. (2015). Cenozoic structural framework and tectono-sedimentary evolution of the southern Nenana Basin, Alaska [abs]: Implications for conventional and unconventional hydrocarbon exploration. The American Association of Petroleum Geologists Annual Convention and Exhibition, Denver, Colorado, 3 June 2015.

Dixit, N. C., and Tomsich, C. S. (2014). Apatite fission track, magnetic susceptibility, and vitrinite reflectance analyses on cuttings from the Nunivak #1 and Nenana #1 wells, Alaska. Division of Geological & Geophysical Surveys Geologic Materials Center Data Report, 422 (1), p. 891, doi:10.14509/27042.

Doyon Limited. (2015). Alaska onshore rift basins, Nenana and Yukon Flats. http://doyonoil.com/Content/pdfs/NenanaBasin3DSeismic.pdf. Accessed November, 2016.

Flores, R. M., (2004). Coalbed methane in the Powder River Basin, Wyoming and Montana: An assessment of the Tertiary-Upper Cretaceous coalbed methane total petroleum system. U.S. Geological Survey Digital Data Series, DDS-69-C, Chapter 2.

Frohman, R. A. (2015). Identification and evolution of tectonic faults in the greater Fairbanks area, Alaska, Master's Thesis, University of Alaska Fairbanks, Fairbanks, Alaska, USA.

Friedmann, F., Chawathe, A., and Larue, D. K. (2003). Assessing uncertainty in channelized reservoirs using experimental designs. SPE Reservoir Evaluation and Engineering, 6(4), 264-274.

Gentzis, T., Goodarzi, F., Cheung, F. K., and Laggoun-Defarge, F. (2008). Coalbed methane producibility from the Manville coals in Alberta, Canada: a comparison of two areas. International Journal of Coal Geology, 74, 237-249.

Hanks, C. L, and Holdmann, G. (2013). Using modeling to assess CO_2 sequestration, engineering, environmental and economic issues related to a proposed coal-to-liquids plant in Interior Alaska, Prepared for the U.S. Air Force by the Geophysical Institute and the Alaska Center for Energy and Power, University of Alaska Fairbanks, Alaska, 1-222.

Hernandez, G., Bello, R., McVay D., et al. (2006). Evaluation of the technical and economic feasibility of CO_2 sequestration and enhanced coal-bed-methane recovery in Texas low-rank coals. Society of Petroleum Engineers Journal, doi:10.2118/100584-MS.

Holdmann, G., and Murphy, J. (2008). Fairbanks North Star Borough baseline greenhouse gas emission inventory: Base year 2007. Alaska Center for Energy and Power, University of Alaska Fairbanks, Alaska.

Koehler, R. D. (2013). Quaternary Faults and Folds (QFF). Alaska Division of Geological & Geophysical Surveys Digital Data Series 3, http://maps.dggs.alaska.gov/qff/ doi:10.14509/24956.

Laubach, S. E., Marrett, R. A., Olson, J. E., and Scott, A. R. (1998). Characteristics and origins of coal cleat: A review. International Journal of Coal Geology, 35, 175 – 207.

McDowell Group Inc. (2013). Energy and economic impacts of coal in Interior Alaska.

McKee, C. R., Bumb, A. C., and Koenig, R. A. (1988). Stress-dependent permeability and porosity of coal and other geologic formations. Society of Petroleum Engineers, 3 (01), 81-91, doi:10.2118/12858-PA.

McVay, D. A., Hernandez, G. A., Bello, R. O., Ayers,W. B., Jr., Rushing, J. A., Ruhl, S. K., Hoffmann, M. F., and Ramazanova, R. I. (2009). Evaluation of the technical and economic feasibility of CO_2 sequestration and enhanced coal bed methane recovery in Texas low-rank coals. AAPG Studies in Geology, 59, 665-688.

Merritt, R. D. (1986). Coal geology and resources of the Nenana Basin, Alaska. Alaska Division of Geological & Geophysical Surveys, Public-data File 086-74, p. 71.

Montgomery, S. L., Barker, C. E., Seamount, D., Dallegge, T. A., and Swenson, R. F. (2003). Coalbed methane, Cook Inlet, south-central Alaska: a potential giant gas resource. AAPG Bulletin, 87(1), 1-13.

Palmer, I., and Mansoori, J. (1998). How permeability depends on stress and pore pressure in coalbeds- a new model. In. SPE Reservoir Evaluation and Engineering, 1 (6), 539–544.

Pan, Z., Connell, L., Shangzhi, M., Sander, R., Camilleri, M., Down, D. I., Carras, J., Lu, M., Xiaokang, F., Wenzhong, Z., Benguang, G., Jianping, Y., Briggs, C., and Lupton, N. (2013) CO_2 injectivity in a multi-lateral horizontal well in a low permeability coal seam: results from a field trial. Energy Procedia, 37, 5834-5841, ISSN 1876-6102, http://dx.doi.org/10.1016/j.egypro.2013.06.507.

Pashin, J. C. (2016). Geologic considerations for CO2 storage in coal. In: Vishal, V., and Singh, T.N., eds., Geologic carbon sequestration: Understanding reservoir behavior, Springer, 137-159, 10.1007/978-3-319-27019-7.

Pashin, J. C., Clark, P. E., McIntyre-Redden, M. R., Carroll, R. E., Esposito, R. A., Oudinot, A. Y., and Koperna, G. J., Jr. (2015). SECARB CO_2 injection test in mature coalbed methane reservoirs of the Black Warrior Basin, Blue Creek Field, Alabama. International Journal of Coal Geology, 144, 71-87, http://dx.doi.org/10.1016/j.coal.2015.04.003.

Pashin, J. C., McIntyre, M. R., Carroll, R. E., Groshong, R. H., Jr., and Bustin, R. M. (2009). Carbon sequestration and enhanced recovery potential of mature coalbed methane reservoirs in the Black Warrior Basin, In: Globe, M., Pashin, J. C. and Dodge, R. L., eds., Carbon dioxide sequestration in geological media: State of the science, AAPG Studies in Geology, 59, 125-147.

Pashin, J. C. (1998). Stratigraphy and structure of coalbed methane reservoirs in the United States: An overview. International Journal of Coal Geology, 35 (1-4), 209-240, http://dx.doi.org/10.1016/S0166-5162(97)00013-X.

Plackett, R. L., and Burman, J. P. (1946). The design of optimum multifactorial experiments. Biometrika, 33, 305-325.

Reeves, S. R., Taillefert, A., Pekot, L., and Clarkson, C. (2003). The Allison unit CO_2 - ECBM pilot: A reservoir modeling study. Topical Report (DE-FC26-0NT40924), U.S. Department of Energy.

Reeves, S., and Oudinot, A. (2005). The Allison CO_2-ECBM Pilot, a reservoir and economic analysis coal. Proceedings of the International Coalbed Methane Symposium, Tuscaloosa, Alabama.

Ridgway, K. D., Thoms, E. E., Layer, P. W., Lesh, M. E., White, J. M., and Smith, S. V. (2007). Neogene transpressional foreland basin development of the north side of the central Alaska Range, Usibelli Group and Nenana Gravel, Tanana Basin. In K. D. Ridgway, and others (Eds.), Tectonic Growth of a Collisional Continental Margin—Crustal evolution of southern Alaska, Geological Society of America Special Paper, 431, 507–547.

Rizzo, A. J. (2015). Natural fracture character and distribution adjacent to the Nenana Basin, central Alaska. Master's Thesis, University of Alaska Fairbanks, Fairbanks, Alaska.

Ross, H. E., Hagin, P., and Zoback, M. D. (2009). CO_2 storage and enhanced coalbed methane recovery: Reservoir characterization and fluid flow simulations of the Big George coal, Powder River Basin, Wyoming, USA. International Journal of Greenhouse Gas Control, 3(6), 773-786.

Seidle, J. (2011). Fundamentals of Coalbed Methane Reservoir Engineering. PennWell Corporation, Tulsa, Oklahoma.

Shellenbaum, D. P., and Clough, J. G. (2010). Alaska geologic carbon sequestration potential estimate: Screening saline basins and refining coal estimates. West Coast Regional Carbon Sequestration Partnership, DOE Contract No. DE-FC26-05NT42593.

Siriwardane, H., Haljasmaa, I., McLendon, R., Irdi, G., Soong, Y., and Bromhal, G. (2009). Influence of carbon dioxide on coal permeability determined by pressure transient methods. International Journal of Coal Geology, 77 (1), 109-118.

Stanley, R. G., and Lillis , P. G. (2011). Preliminary interpretation of Rock-Eval pyrolysis and vitrinite reflectance results from the Nunivak 1 well in the Nenana Basin, central Alaska (abs.). Program with Abstracts, PSAAPG Western Region Meeting, May 6–14, Anchorage, Alaska.

Stevens, S., and Bank, G. (2007). Alaska geologic CO_2 storage potential: Preliminary scoping estimate for deep coal seams, WESTCARB Project draft report, p. 7.

Tape, C. H., Silwal, V., Ji, C., Keyson, L., West, M. E., and Ruppert N. A. (2015). Transtensional tectonics of the Minto Flats fault zone and Nenana Basin, central Alaska. Bulletin of the Seismological Society of America, 105 (4), 2081-2100.

Usibelli Coal Mine, Inc. (2015). Coal:Data sheet. http://www.usibelli.com/Coal-data.php. Accessed December, 2015.

Van Kooten, G. K., Richter, M., and Zippi P. A. (2012). Alaska's Interior rift basins: A new frontier for discovery, Oil and Gas Journal, 110(1a), 48-57.

Wahrhaftig, C., Wolfe, J. A., Leopold, E. B., and Lanphere, M. A. (1969). The coal-bearing group in the Nenana coal field, Alaska. U.S. Geological Survey Bulletin, 1274, 1-30.

Wahrhaftig, C. (1973). Coal reserves of the Healy Creek and Lignite Creek coal basins, Nenana coal field, Alaska. U.S. Geological Survey Open-File Report 73-355, p. 7, 28 sheets, scale 1:63,360.

White, C. M., Smith, D. H., Jones, K. L., Goodman, A. L., Jikich, S. A., LaCount, R. B., DuBose, S. B., Ozdemir, E., Morsi, B. I., and Schroeder, K. T. (2005). Sequestration of carbon dioxide in coal with enhanced coal bed methane recovery — A review. Energy and Fuels, 19(3), 659-724.

Yeten, B., Castellini, A., Guyaguler, B., and Chen, W. H. (2005). A comparison study on experimental design and response surface methodologies,In Proceedings of the SPE Reservoir Simulation Symposium, 93347, 465–479.

Young, G. B. C., McElhiney, J. E., Paul, G. W., and McBane, R. A. (1991). An Analysis of Fruitland Coalbed Methane Production, Cedar Hill Field, Northern San Juan Basin, SPE 22913, presented at the Annual Technical Conference, Dallas, Texas.

A. Regional Tectonic Setting of Central Alaska

Quaternary fault .... Crustal-scale fault inferred from seismicity ⊕ Exploration well
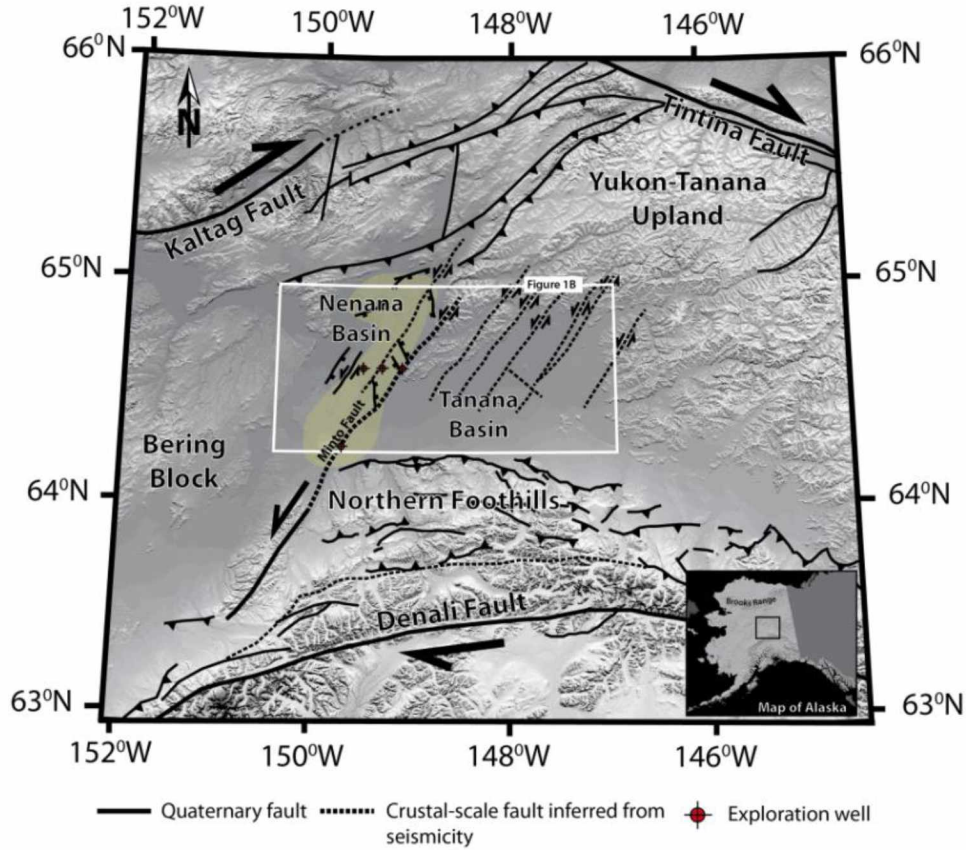
B. Location of the Coal-fired Power Plants
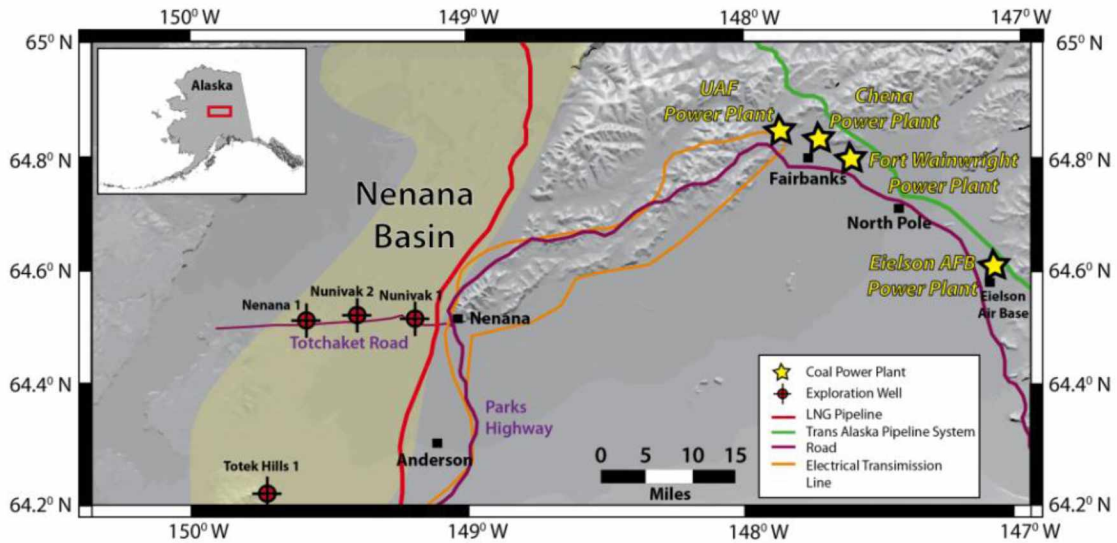
Figure 5-1 Tectonic map of the central Interior Alaska and relative location of the coal-fired plants

(A) Simplified tectonic map showing regional tectonic framework of the central Interior Alaska

and location of the Nenana basin relative to the major active faults in the region. Faults are

inferred from the published maps by Koehler (2013), Frohman (2015) and Tape et al. (2015).

White box indicates the position of Figure 1B. (B) Location map of the Nenana Basin relative to

the coal-fired power plants in Interior Alaska (modified from Doyon Limited, 2015).

253
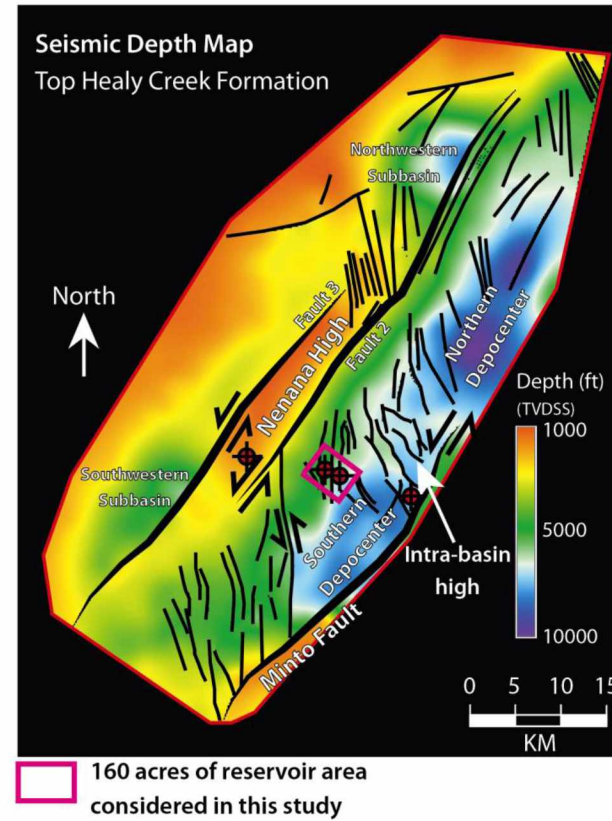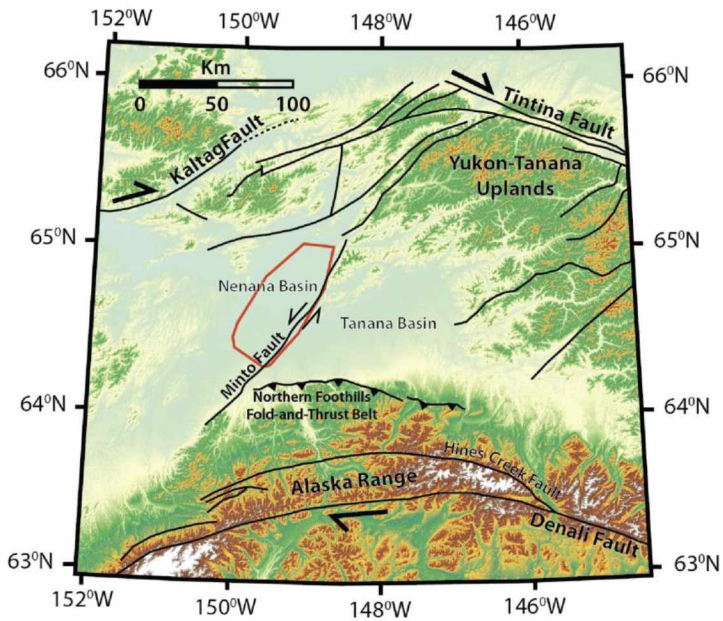
Figure 5-2 Seismic depth map at the top of the Healy Creek Formation, Nenana basin

(Left) Simplified tectonic map of the central Interior Alaska, showing the location of seismic survey area (marked in red) (modified

from Koehler, 2013). (Right) Seismic depth map and fault patterns at the top of the Healy Creek Formation in the Nenana Basin. Tom

Morahan, written communication, 2015). Pink box corresponds to the 160 acres used in the 3D reservoir model built in this study.
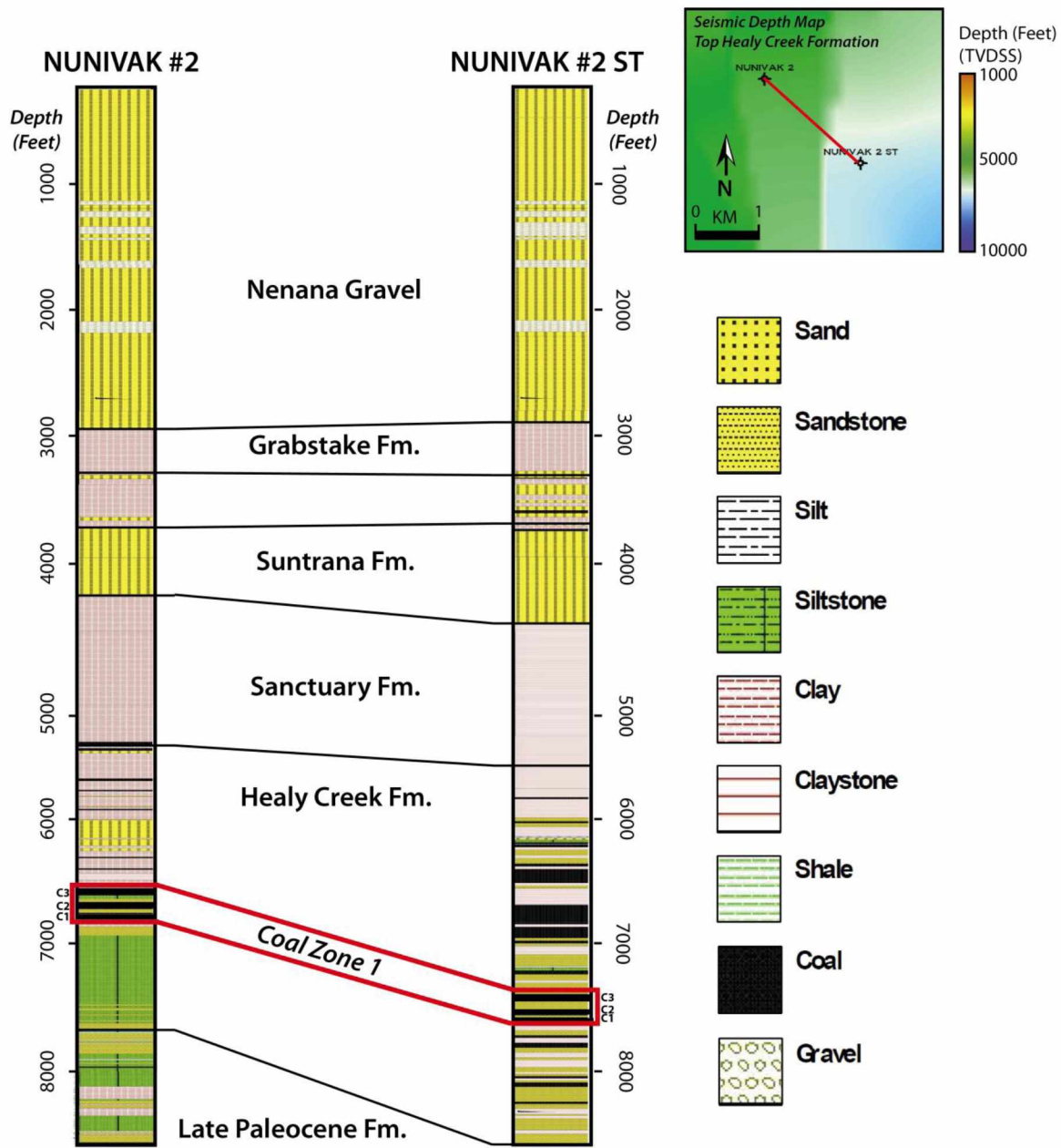
Figure 5-3 Generalized coal stratigraphy of the basin

Coal stratigraphy and stratigraphic correlation between the Nunivak #2 and Nunivak #2 ST wells

drilled in the Nenana Basin (AOGCC, 2015). The red polygon indicates the location of Coal

Zone 1 within the Healy Creek Formation that is the focus on the simulation in this study
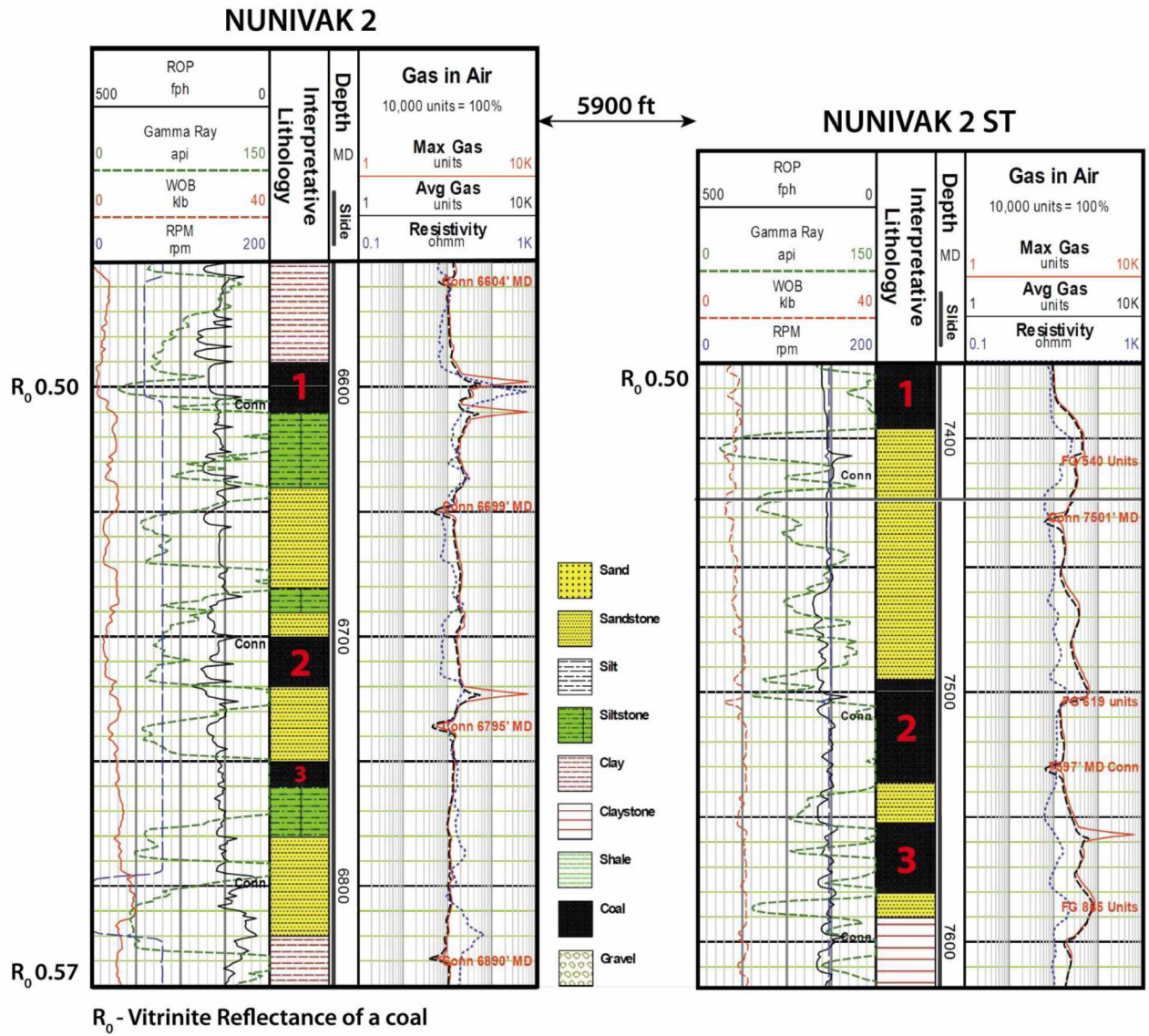
Figure 5-4 Lithostratigraphy of Coal Zone 1 identified in Nunivak 2 and Nunivak 2 ST wells

The average thickness of three coal seams considered in this study varies from 50 ft in Nunivak #2 well to 100ft in Nunivak #2 ST well (AOGCC, 2015). An average coal thickness of 75ft is considered for our simulation domain. These coals are overlain by impermeable claystones and shales from the Healy Creek Formation and Sanctuary Formation locally. The vitrinite reflectance and Rock-Eval properties of the coal seams indicate these coals can produce

256

thermogenic coal gas (up to 99% methane) in the basin (Stanley and Lillis, 2011; Van Kooten et al., 2012; Dixit and Tomsich, 2014).
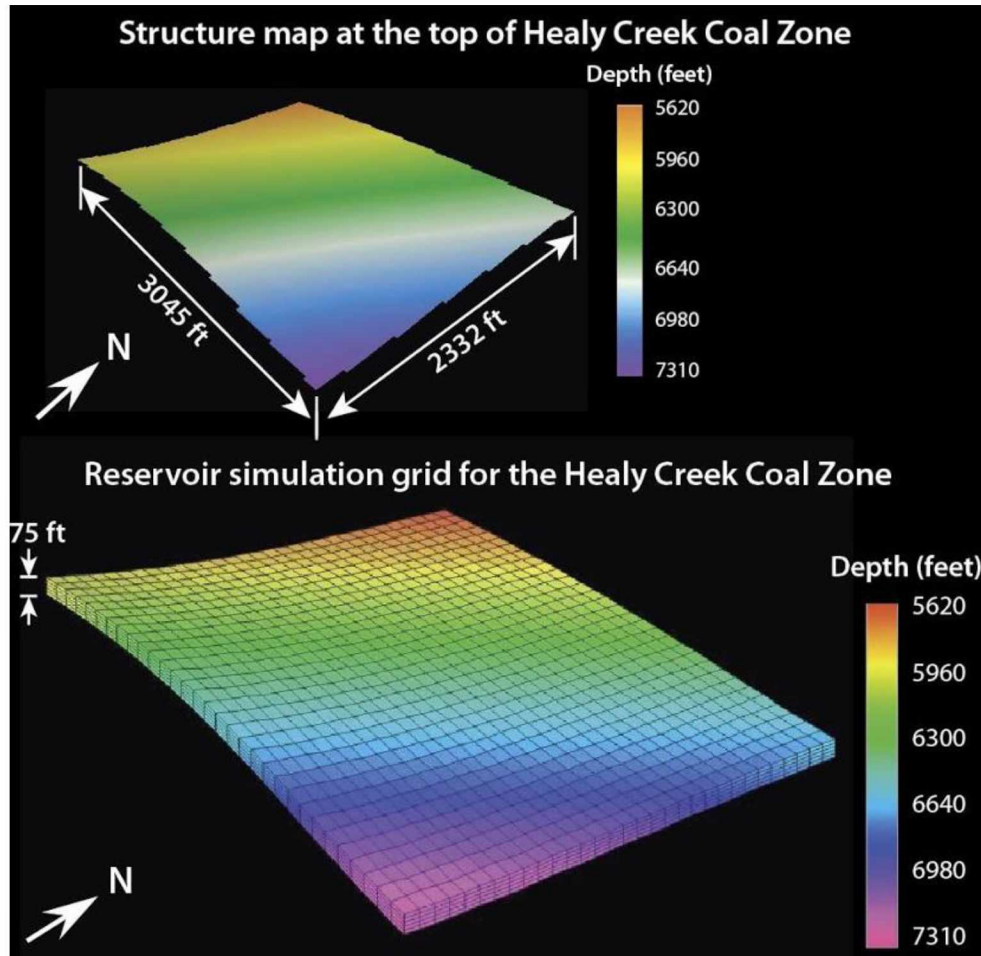
Figure 5-5 Reservoir simulation grid developed for the Healy Creek Coals of the basin The model represents a 160 acres drainage area of equally spaced grids with 31*31 * 5 grid system (individual grid block size of 71 ft x 97 ft x 15 ft) developed using CMG's Builder software. The coal depth in our study area varies from 5620 ft along the intra-basin high to 7310 ft in deeper part of the basin. A total thickness of 75 ft was considered for the target coal seams in Coal Zone 1. The maximum permeability trends (I-direction) were considered in northwest-southeast direction, following the present-day orientation of maximum horizontal stress in our study area (Dixit and Hanks, 2015; Rizzo, 2015).
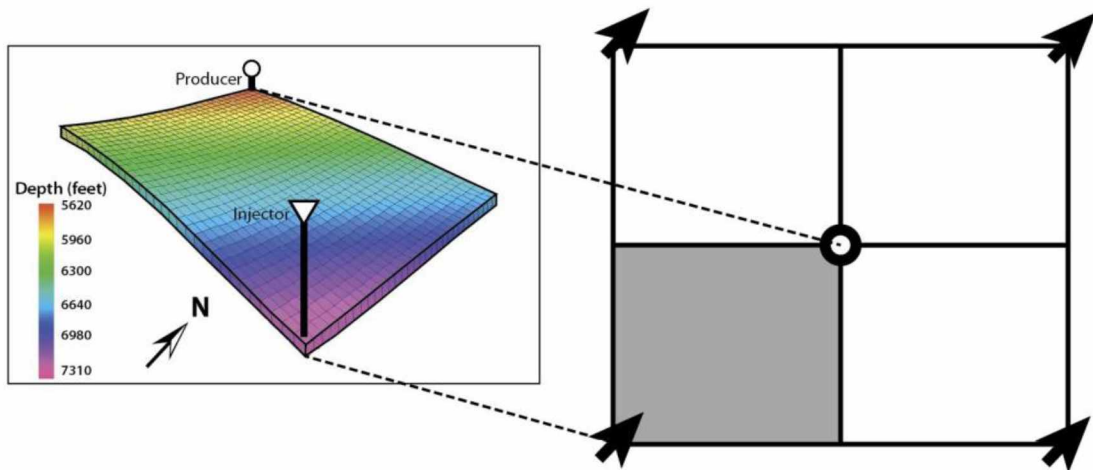
Figure 5-6 The base case well configuration used in the model

The base case reservoir simulation model of a ¼ 5-spot pattern used for our sensitivity analysis. A pair of one injecting and one producing vertical wells was modeled with 160 acres of well spacing between them.
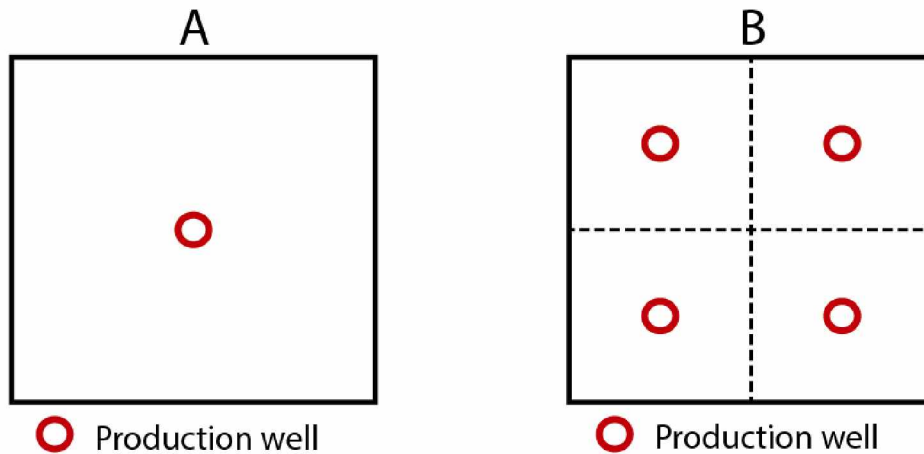
Figure 5-7 Well spacing with 160 acres of the drainage area

Primary production simulation scenario showing, (A) 160 acres of reservoir with 160 acres of well spacing and , (B) 160 acres of reservoir with 40 acres of well spacing.
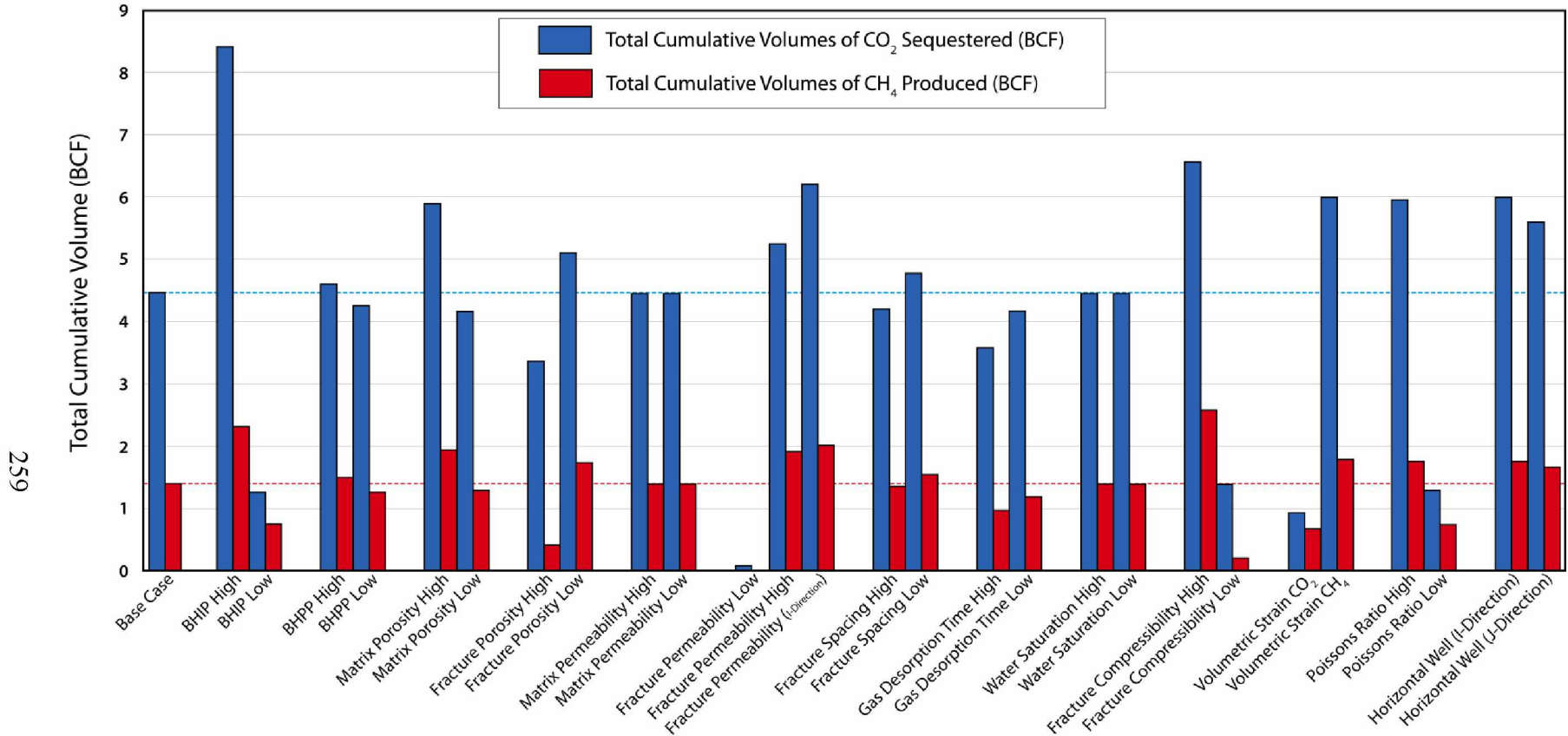
Figure 5-8 Results of the primary sensitivity analyses

Results of our sensitivity analysis in terms of the total cumulative volumes of CO_2 sequestered and CH_4 produced, compared to the base case. The total cumulative volumes of CO_2 sequestered and CH_4 produced were estimated at the end of 44-year simulation period.
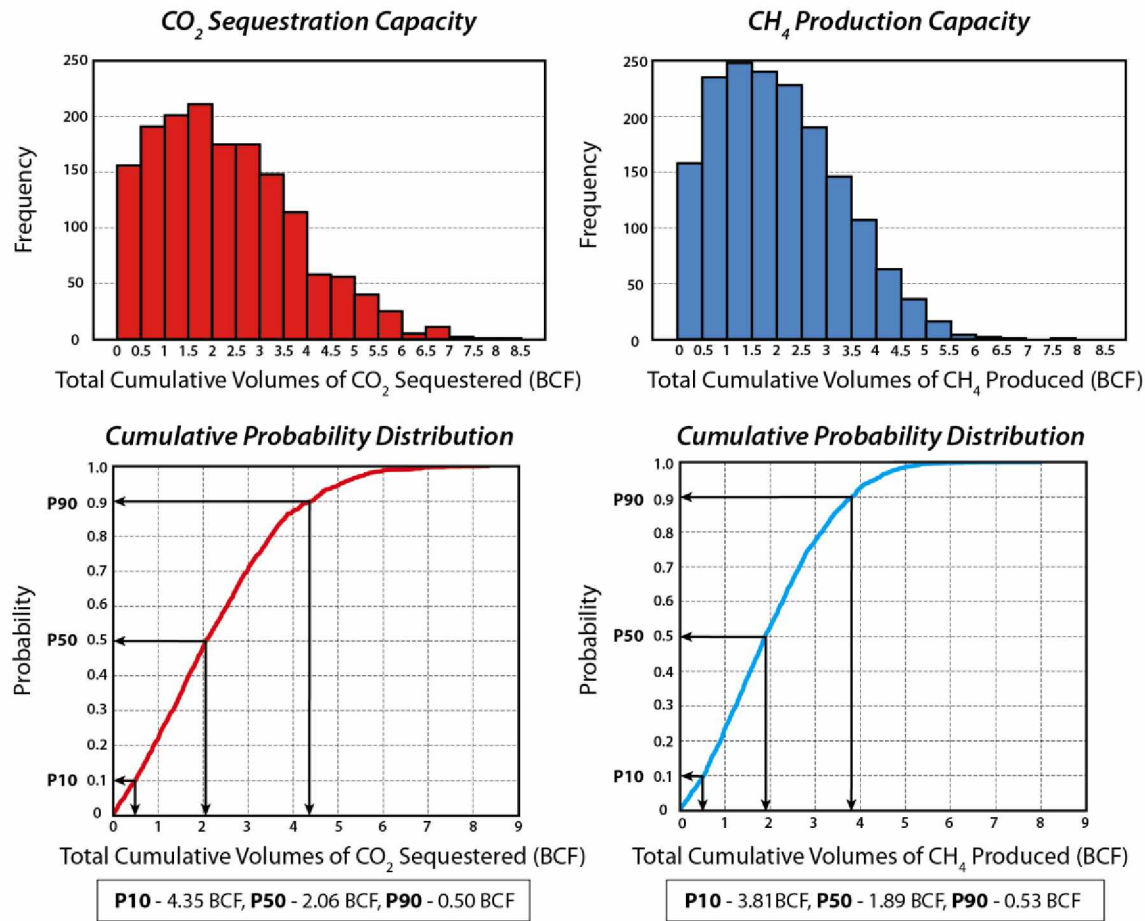
Figure 5-9 Result of Monte Carlo analyses

Probability density and cumulative probability distributions of the total volumes of CO_2 sequestered in and CH_4 produced from the

Healy Creek Formation coals at the end of 44 year forecast. Probabilistic resource assessment was carried out on the proxy models

(See Section 5.2) using Monte Carlo analysis.
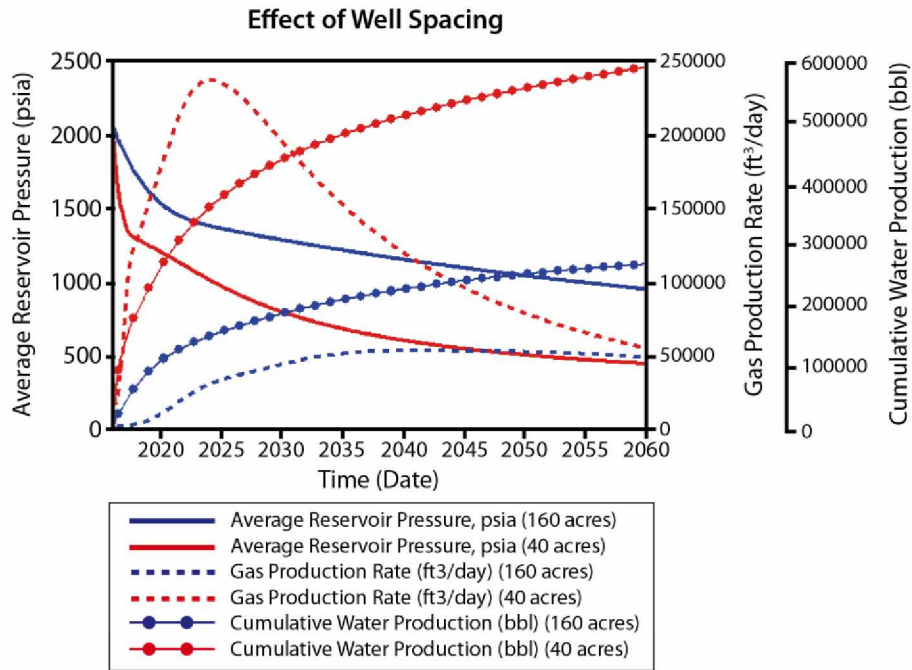
Figure 5-10 Effect of well spacing on the reservoir response

Results of our primary CH$_4$ production scenarios for a well spacing of 160 acres and 40 acres

showing the effect of dewatering and reservoir pressure on the gas production rates over 44

years.
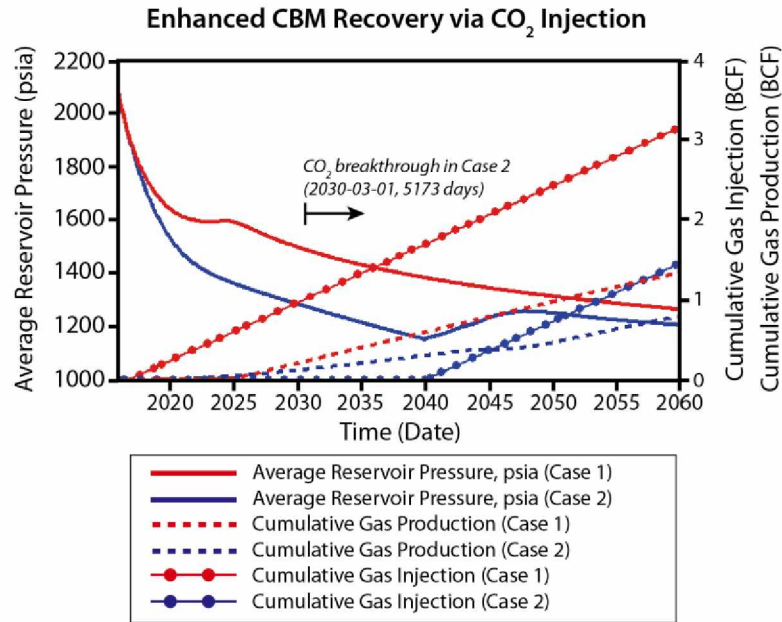
Figure 5-11 Effect of the timing of CO₂ injection on the reservoir response

The results of our enhanced coal bed methane simulation scenarios for Case 1 (CO₂ injection at

the start of CH₄ production) and, Case 2 (CO₂ injection after 24 years of primary CH₄
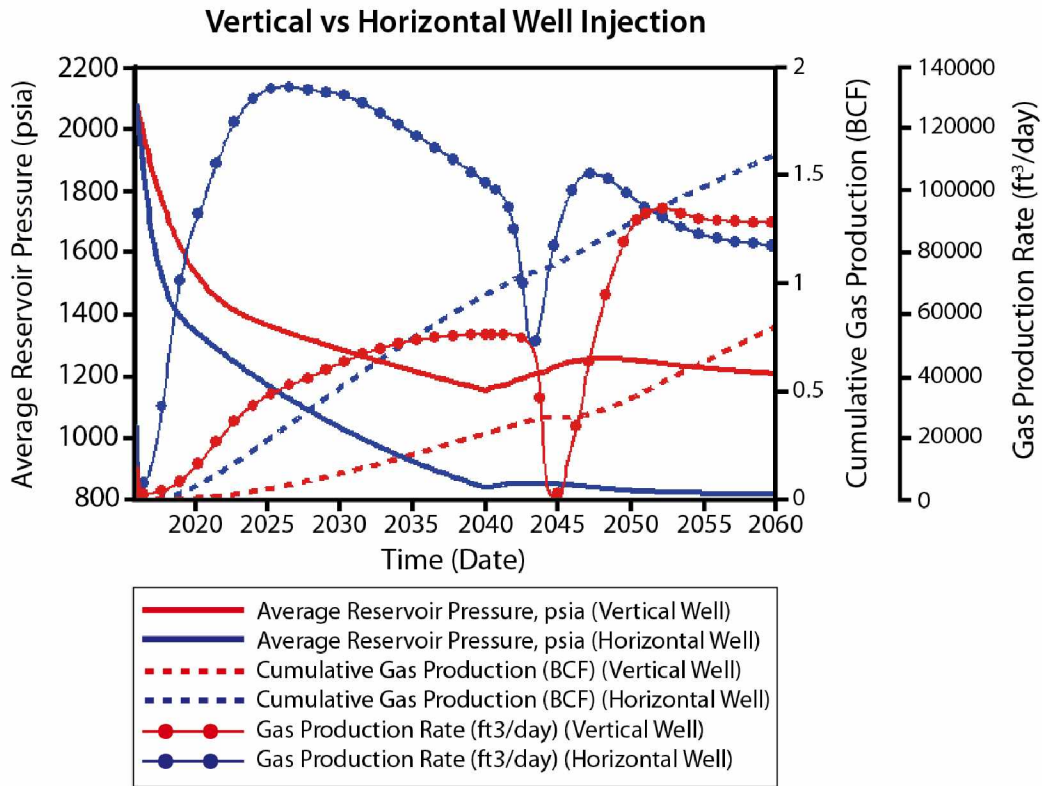
production).

Figure 5-12 Effect of the vertical vs horizontal well injection on the reservoir response

CH_4 production rates and cumulative gas volumes produced through a horizontal well compared to the vertical well at the end of 44 year forecast.
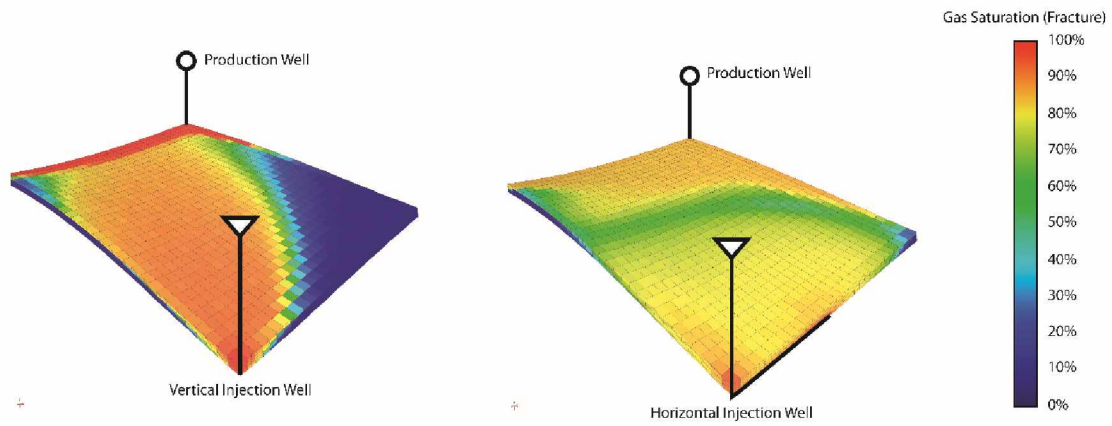
Figure 5-13 Vertical vs horizontal well sweep efficiency

Average gas saturation in the fractures showing more efficient CO_2 sweep pattern in a horizontal

well (compared to a vertical well) at the end of 44 year forecast.
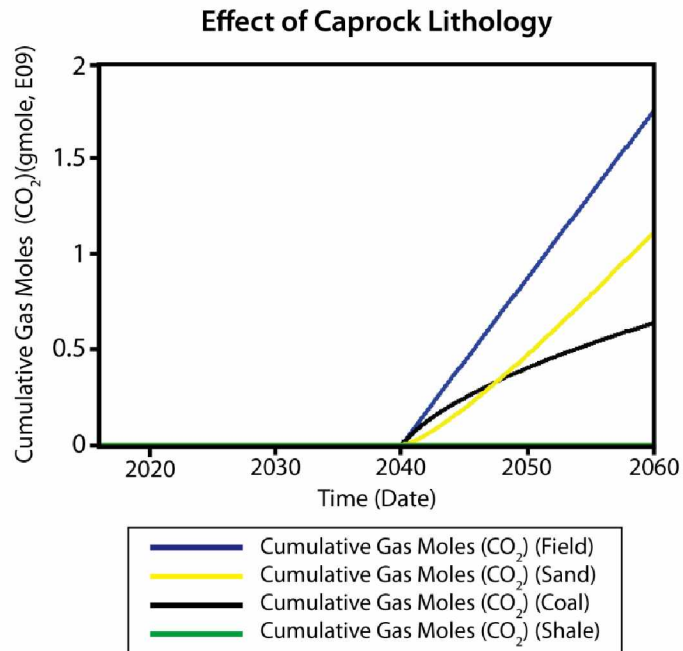
Figure 5-14 Effect of caprock lithology on the reservoir response

The cumulative volumes of CO_2 trapped in a coal (36%), sand (63.5%) and shale (<1%), relative

to the total cumulative CO_2 injected volumes through a vertical well at the end of 44 year

forecast.
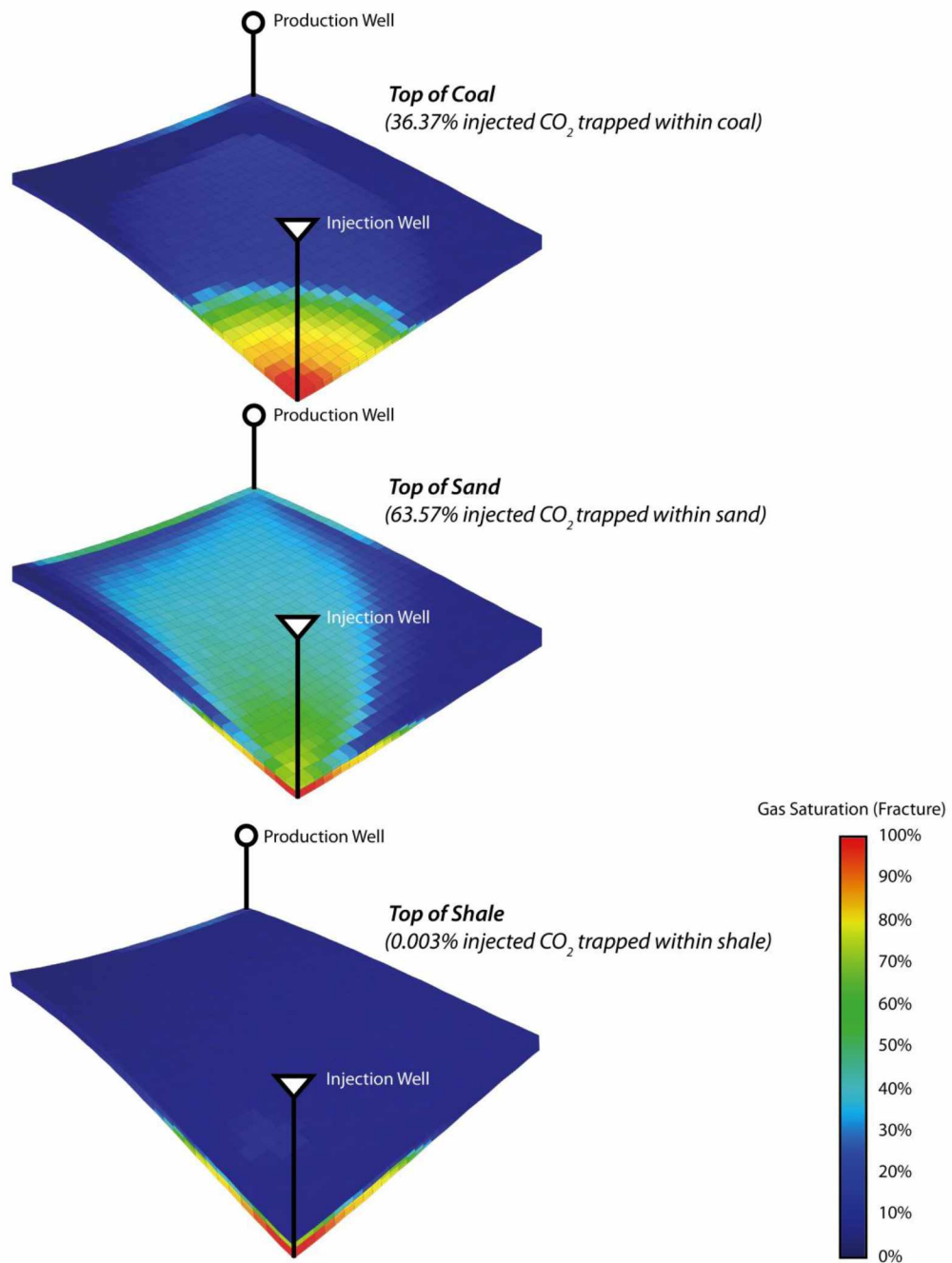
Figure 5-15 CO$_2$ saturation across the different lithologies after 44 years of simulation

The simulation results of our caprock leakage scenario showing the gas saturation and migration

in the fractures across the coal, sand and shale layer after 44 years.

Table 5-1 Generalized stratigraphy of the Nenana basin

Period/Epoch	Formation	Major Lithology	Depositional Environment
Quaternary	Surficial Deposits	Unconsolidated gravel, sand, silt and clay	Alluvial fan/ flood-plain/ lacustrine/ swamp
Pliocene to Miocene	Nenana Gravel	Coarse-grained conglomerate and sandstone	Alluvial fan/ braided fluvial systems
Miocene to Late Eocene	Grubstake Formation	Laminated mudstone and sandstone	Lacustrine
	Lignite Creek Formation	Conglomerate, sandstone, mudstone and coal	High-sinuosity mixed-load fluvial systems
	Suntrana Formation	Coarse grained sandstone and coal	Distal sandy braided fluvial systems
	Sanctuary Formation	Laminated mudstone	Lacustrine
	Healy Creek Formation	Conglomerate, sandstone, mudstone and coal	Proximal, gravelly braided stream systems
Early Eocene to Late Paleocene	Late Paleocene Sediments	Siltstone, mudstone and coal	Fluvial/lacustrine/swamp/ alluvial fan
Early Mississippian-Middle Devonian	Totatlanika Schist	Metavolcaniclastic schist and gneiss with phyllite	-
Proterozoic to early Paleozoic	Yukon-Tanana Schist (Birch Hill Schist)	Greenschist facies sequence with quartzite, phyllite and muscovite	-

Generalized stratigraphy and depositional environments for stratigraphic units in the Nenana Basin (summarized from Wahrhaftig et al., 1969; Van Kooten et al., 2012 and this study).

Table 5-2 Reservoir input parameters used in the base case simulations

Parameter	Units	Parameter Values			References
		Low (P90)	Base Case (P50)	High (P10)	
Coal Formation			Healy Creek Coal		Van Kooten et al., 2012; Dixit and Tomsich, 2014
Reservoir pressure	psi		2820		AOGCC, 2015
Reservoir temperature	°F		144.5		Van Kooten et al., 2012
Coal depth	ft		6000		AOGCC, 2015; Doyon Limited, 2015
Coal thickness	ft		75		AOGCC, 2015
Coal rank			Subbituminous to HVC Bituminous		Dixit and Tomsich, 2014
Average coal density	g/cm3		1.342		This study
Coal gas composition	%		100% CH_4		Van Kooten et al., 2012; Usibelli Coal Mine, 2015
Water saturation	%	100% fracture, 0% matrix	100% fracture, 30% matrix	100% fracture, 30% matrix	Ross et al., 2009, McVay et al., 2009, Agrawal, 2007
Fracture spacing	cm	0.5	2	6	Laubach et al., 1998, Gentzis et al., 2008; McVay et al., 2009
Matrix permeability	md	0.001	0.01	1	Laubach et al., 1998, Ross et al., 2009
Matrix porosity	%	0.001	0.01	1	McVay et al., 2009, Ross et al., 2009
Fracture permeability	md	0.001	0.1	1	McKee et al., 1988; Gentzis et al., 2008; McVay et al., 2009
Fracture porosity	%	0.001	0.01	0.1	McVay et al., 2009, Ross et al., 2009
Initial gas content	SCF/Ton		250		Montgomery et al., 2003; Gentzis et al., 2008; McVay et al., 2009
Adsorption isotherm			Wilcox Coal, TX		McVay et al., 2009
VL, CO_2 Langmuir Volume Constant	SCF/Ton		961.9		
PL, CO_2 Langmuir Pressure Constant	psi		697.5		
VL, CH_4	SCF/Ton		363.6		
PL, CH_4	psi		608.5		
Gas diffusion time	Days	1	1	100	McVay et al., 2009
Coal compressibility	1/psi	1.00E-06	1.38E-04	0.001	McVay et al., 2009, Ross et al., 2009
Poisson's ratio		0.15	0.39	0.45	Agrawal, 2007; Ross et al., 2009

Strain at Pinfinity, CH_4		0	0.005	0.005	Agrawal, 2007; Ross et al., 2009
Injector BHP constraint	psi	2000	3100	4000	Dixit and Hanks, 2015
Producer BHP constraint	psi	100	300	500	Ross et al., 2009

Table 5-3 Results of the primary sensitivity analyses

No	Reservoir Parameter	Value	CO$_2$ Injected (E+09, SCF)	CH$_4$ Produced (E+09, SCF)	Peak gas injection rate (MMSCF/DAY)
1	Base Case		4.46	1.40	1.12
2	Injector Bottomhole Pressure (BHIP)	2000 psi	1.28	0.76	0.21
		4000 psi	8.42	2.33	2.17
3	Producer Bottomhole Pressure (PBHP)	100 psi	4.62	1.51	1.17
		500 psi	4.26	1.27	1.05
4	Matrix Porosity	0.001 %	4.17	1.29	1.09
		1 %	5.9	1.94	1.24
5	Fracture Porosity	0.001 %	5.12	1.74	1.60
		0.1 %	3.38	0.42	0.41
6	Matrix Permeability	0.001 md	4.46	1.40	1.12
		1 md	4.46	1.40	1.12
7	Fracture Permeability	0.001 md	0.09	0.02	0.01
		1 md	5.26	1.92	3.05
		1 md (I-direction)	6.22	2.02	1.59
8	Fracture Spacing	0.5 cm	4.78	1.56	1.09
		2 cm	4.21	1.36	1.17
9	Gas Diffusion Time	10 days	4.18	1.20	1.13
		100 days	3.59	0.98	0.75
10	Matrix Water Saturation	0 %	4.46	1.39	1.11
		70 %	4.46	1.39	1.11
11	Coal Compressibility	0.000001 1/psi	1.40	0.21	0.03
		0.001 1/psi	6.57	2.58	2.55
12	Volumetric Strain, CH$_4$	0	4.46	1.40	1.55
		0.005	6	1.81	2.71
13	Poisson's Ratio	0.15	3.69	1.24	0.92
		0.45	5.06	1.56	1.21
14	Horizontal Well Orientation	I-direction)	6.01	1.77	1.92
		J-direction)	5.61	1.66	1.18

The results of our sensitivity analysis showing the effect of each reservoir parameter on the total cumulative volumes of CO_2 sequestered and CH_4 produced during CO_2 breakthrough for a well spacing of 160 acres at the end of 44 year forecast.

Table 5-4 Plackett-Burman experimental design using six variables and 44-year simulation forecast

Run	BHIP	Matrix Porosity	Fracture Porosity	Fracture Permeability	Fracture Compressibility	Volumetric Strain	Total CO_2 Sequestered (BCF)	Total CH_4 produced (BCF)
	A	B	C	D	E	F		
1	4000	0.001	0.001	1	0.000001	0.005	2.16	2.06
2	2000	0.001	0.001	0.001	0.000001	0	0	0.10
3	2000	0.001	0.1	0.001	0.001	0.005	0	0
4	4000	0.001	0.1	1	0.001	0	5.28	4.07
5	4000	1	0.1	0.001	0.000001	0.005	0.32	0.03
6	2000	1	0.001	1	0.001	0.005	0	0.02
7	4000	1	0.001	0.001	0.001	0	1.49	1.20
8	2000	1	0.1	1	0.000001	0	2.366	1.19

Table 5-5 Results from the linear regression analysis (CH_4 produced)

Model	R	R Square	Adjusted R Square	Std. Error of the Estimate
1	1	0.999	.997	.08240

Model		Unstandardized Coefficients		Standardized Coefficients	t	Sig.
		B	Std. Error	Beta		
1	(Constant)	-1.379	.113		-12.173	.052
	A	.001	.000	.566	25.930	.025
	B	-9.594	.589	-.356	-16.301	.039
	C	4.801	.589	.178	8.157	.078
	D	1.503	.058	.562	25.767	.025
	E	3489.515	426.457	.178	8.183	.077
	F	-222.852	11.653	-.417	-19.125	.033

Summary of the analysis of multiple linear regressions performed using the SPSS software to analyze relationships between the total volumes of CH_4 produced (dependent variable) and reservoir independent variables.

Table 5-6 Results from the linear regression analysis (CO_2 sequestered)

Model	R	R Square	Adjusted R Square	Std. Error of the Estimate
1	1.000	.999	.994	.14348

Model		Unstandardized Coefficients		Standardized Coefficients	t	Sig.
		B	Std. Error	Beta		
1	(Constant)	-1.682	.197		-8.525	.074
	A	.001	.000	.502	16.987	.037
	B	-8.273	1.025	-.239	-8.073	.078
	C	10.868	1.025	.313	10.605	.060
	D	1.998	.102	.581	19.677	.032
	E	3542.373	742.637	.141	4.770	.132
	F	-332.308	20.292	-.484	-16.376	.039

Summary of the analysis of multiple linear regressions performed using the SPSS software to analyze relationships between the total volumes of CO_2 sequestered (dependent variable) and reservoir independent variables.

6   Conclusions

The Nenana basin is located along a transform plate boundary between the Bering and North American plates and occupies a critical yet poorly understood continental part of Interior Alaska. This region is characterized by complex tectonic interactions between a northward prograding fold-and-thrust belt to the south and a shear zone between two basin-bounding crustal scale strike slip fault systems. A better understanding of the origin and evolutionary history of the basin would clarify the tectonic development of the transform boundary at this location and will greatly improve our knowledge about the complex interactions of these tectonic processes through time.

This dissertation presents the first integrated study of the upper crustal structure of the Nenana and Tanana basins. Further analysis of the Nenana basin revealed the distinct tectonic deformation phases and subsequent thermal regimes of the Nenana basin since its initiation in Late Paleocene time. In this study, a workflow for estimating the magnitudes of in situ stress components was tested and validated for the northeastern North Slope of Alaska. The workflow was then used to determine the magnitude of in situ stress in the Nenana basin. These data and interpretations were used to evaluate the CO_2 sequestration and coal bed recovery estimates of the Nenana basin using a series of sensitivity analyses, experimental design methods and fluid simulation scenarios. The conclusions of each study are summarized in the following discussion.

6.1   The present-day crustal geometry of the Nenana and Tanana basins in interior Alaska

The Nenana basin and adjacent Tanana basin are located in a complex zone of intraplate deformation in which compressional stresses due to collision of the Yakutat block are accommodated by oblique-slip faulting along the major crustal-scale strike-slip faults. In Chapter 1, I integrated the regional gravity, magnetic and seismic data with the geological data available for the region and developed nine 2D potential field models. These models provide new insights into the internal geometry and crustal structure of both basins. These forward models also help to refine and validate existing models of basin formation proposed by earlier researchers. The integrated study further underscores the importance of gravity and magnetic modeling as an

273

efficient way to assist exploration efforts in an area with limited data by allowing testing and validation of basin formation theories with local as well as regional data constraints.

Integrated seismic, gravity and magnetic field models indicate that both the Nenana and Tanana basins are underlain by high density basement rocks of similar compositions. These crustal rocks are thicker immediately north and underlying the fold-and-thrust belt of the central Alaska Range. However, these integrated potential field models suggest that the basins are significantly different in their age, basement structure and tectonic origin. The Nenana basin is a narrow (12-15 km wide) and deep (up to 8 km) depression that holds Tertiary sediments as old as Paleocene age (Figures 6-1 & 6-2). In contrast, the Tanana basin exhibits a significantly wider and shallower (up to 2 km) basin that is probably filled with Miocene and younger sediments (Figures 6-1 & 6-2).
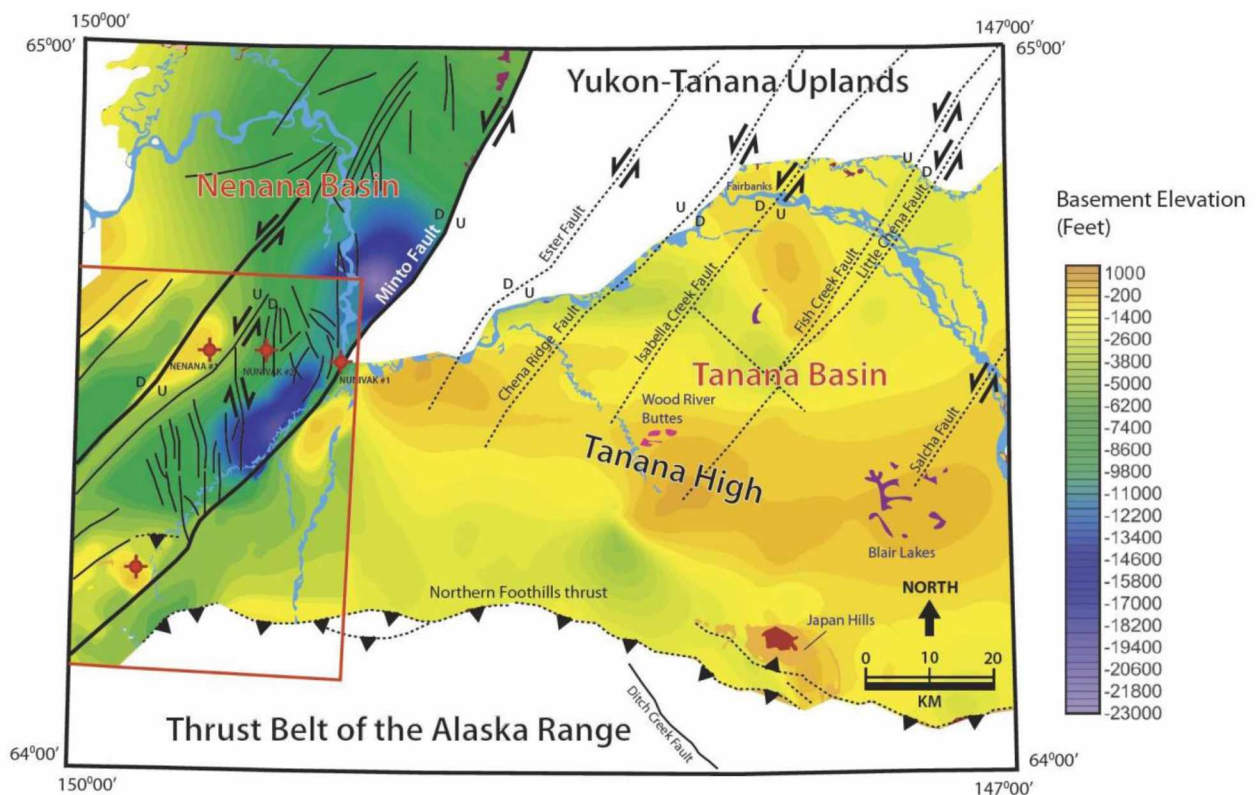
Figure 6-1 Modelled basement depth map using integrated seismic and potential field models of the basins

Based on the integrated potential field models, the Tanana basin is divided into three distinct structural provinces. The northern province represents a region to the south of the Yukon-Tanana Upland that is characterized by northeast-striking crustal-scale strike-slip faults. The central province is a region associated with high-amplitude gravity and magnetic anomalies and is interpreted to represent a roughly east-west striking basinal basement high, the Tanana High. The southern province is characterized by thrust faults and folds and represents the active thrust front of the central Alaska Range. I propose three alternative models that explain this variation in structural geometry: 1) crustal-scale chevron folding across a vertical axis with the hinge region correlating with the Tanana High; 2) a foreland basin with the Tanana High either a forebulge or a blind thrust (Figure 6-3); and 3) differential dextral shear along crustal scale left lateral strike slip faults. Although all three of the proposed models provide an explanation for the existence of the Tanana High, more data is needed to constrain our observations to the best possible model for Tanana basin formation.
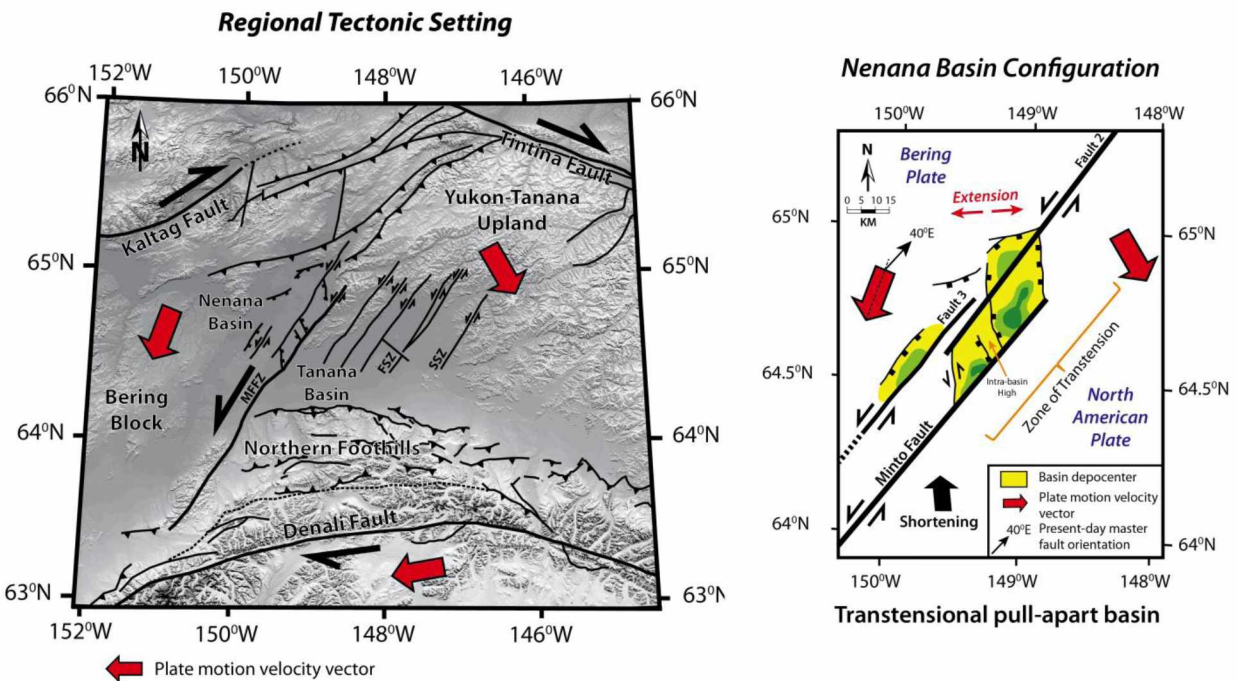
Figure 6-2 Transensional pull-apart-type basement deformation model of the Nenana basin

In contrast to the Tanana basin, results of this study suggest the modern-day Nenana basin is a transtensional pull-apart basin (Figure 6-2) that is forming above and within the left-lateral Minto Flats fault zone. These results further indicate that the structural setting of the Nenana basin is significantly different from the compressional-type setting seen in the Tanana basin. Both basins therefore highlight two separate zones and styles of crustal deformation in central Interior Alaska.
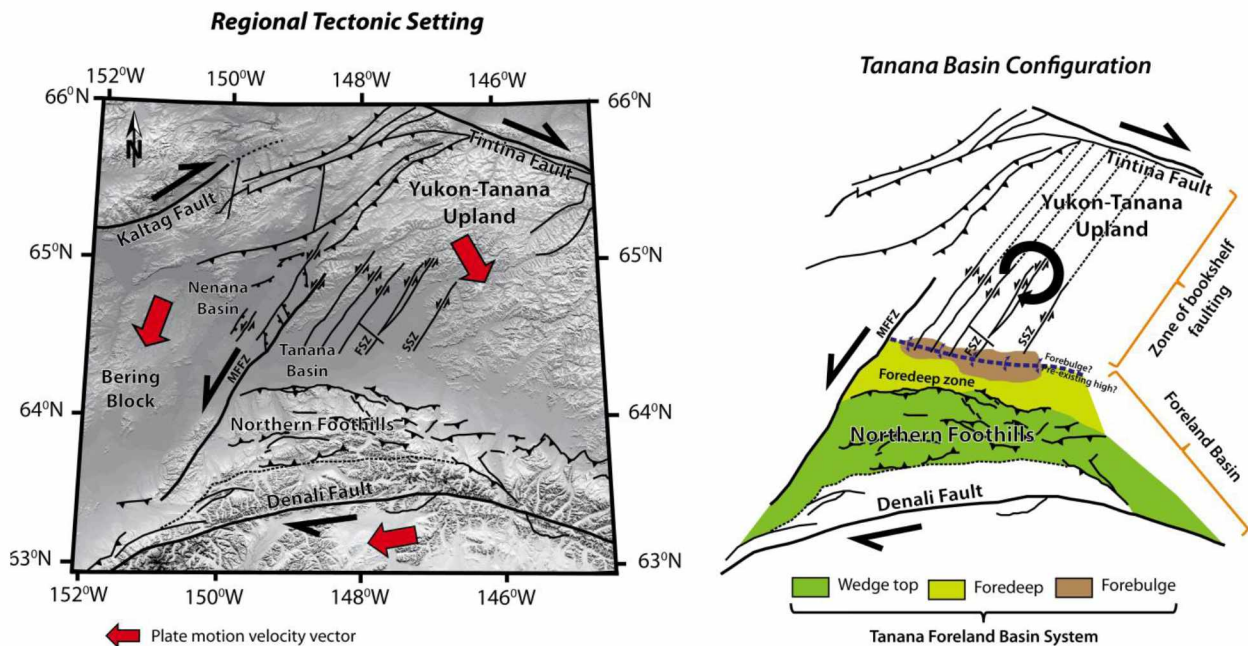
Figure 6-3 Foreland flexural-type basement deformation model of the Tanana basin

6.2 Tectonic development and thermal evolution history of the Nenana basin

The Nenana basin may have enormous hydrocarbon resource potential. Consequently, a detailed understanding of the thermal history and tectonic development of the basin is particularly significant in order to assess the source rock maturity, hydrocarbon traps and hydrocarbon generation potential of the region. In Chapter 2, I investigated the Cenozoic tectonic burial and exhumation history of the Nenana basin by integrating data from apatite fission track analyses, fracture sets, well logs and seismic reflection profiles.

This integrated analysis reveals three distinct phases of rifting and an episode of regional uplift and exhumation since Late Paleocene time (Figure 6-4). The initial rifting in the basin occurred during Late Paleocene time when the organic-rich fluvio-lacustrine sediments of Late

Paleocene age were deposited in an extensional half-graben, bounded to its eastern side by a steep normal fault, the Minto Fault. Fault-controlled rapid tectonic subsidence in the basin resulted in higher heat flow (estimated geothermal gradient of 66^0C/km). This rifting episode is interpreted to be the result of extension-related tectonic processes associated with slab-widow subduction beneath southern Alaska and/or widespread intra-late magmatism and faulting along the Tintina fault system that occurred during Late Cretaceous to Paleocene time.
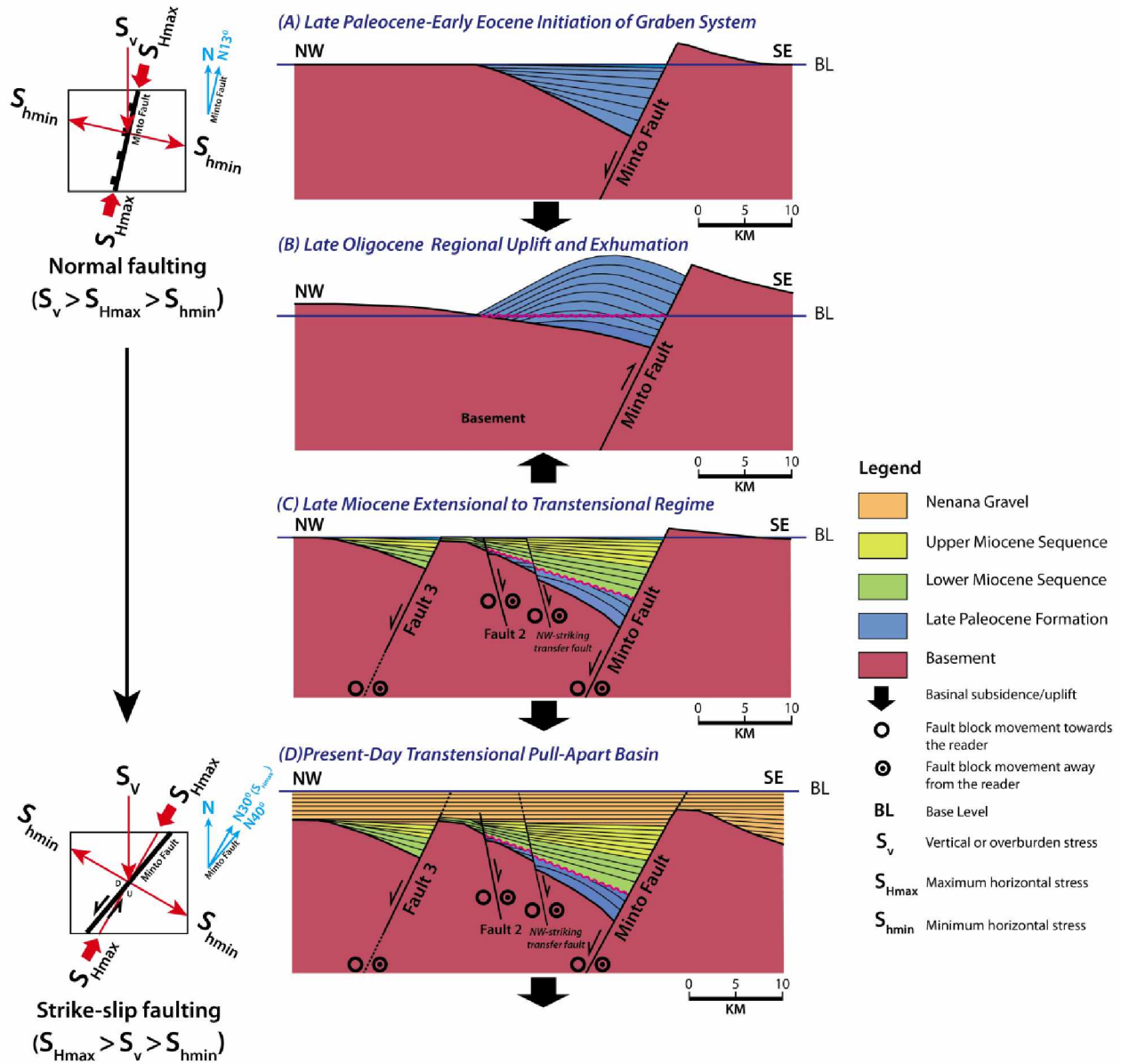
Figure 6-4 Simplified tectonic evolution model of the Nenana basin

Beginning in Early Eocene and continuing into Late Oligocene time, the basin was uplifted. Exhumation resulted in the removal of up to 1.5 km of Late Paleocene strata from parts of the basin. During this period, fission track analyses indicate a phase of rapid cooling where samples were rapidly cooled to the surface temperatures in the basin. This exhumation event was coeval with the widespread uplift and exhumation of the Yukon-Tanana Upland in central Interior Alaska. This regional uplift event has been attributed to oblique plate subduction along the southern Alaskan margin, major dextral strike-slip motion along the Denali and Tintina fault systems and counterclockwise rotation of western Alaska during the Eocene-Oligocene.

A renewed phase of faulting and subsidence initiated in Early Miocene time with the deposition of organic-rich source and reservoir rocks from Miocene fluvial-lacustrine sequences (Usibelli Group) in the basin. This Miocene rifting episode was characterized by relatively slower subsidence and a significantly lower geothermal gradient of ~6^0C/km. During Mid to Late Miocene time, NW-SE crustal shortening associated with the uplift of the Alaska Range to the south resulted in transtensional movements along the major NE-striking basin-bounding faults in the Nenana basin. Timing of uplift and exhumation within the central Alaska Range, coincides? with the transition from dominantly extensional to transtensional tectonics in the Nenana basin.

Since Pliocene time, the Nenana basin has exhibited a rapid post-rift subsidence with a relatively high geothermal gradient (~$37-58^0$C/km). This is reflected in the deposition of overburden rocks as braided fluvial-alluvial post-rift deposits (Nenana Gravel and Quaternary sediments) in a transtensional pull-apart setting. My work also suggests that the present-day subsidence in the basin is driven by oblique-slip motion along reactivated NE-striking major basin-bounding faults and newly formed NW-striking transfer faults which accommodate transtensional stresses resulting from the northward propagating fold-and-thrust belt of the Alaska Range. This episode of rapid subsidence has provided significant overburden with resulting temperatures sufficient for hydrocarbon generation from Miocene and Late Paleocene source rocks.

6.3 Characterizing the state of in situ stress and associated tectonic stress regime in a basin

In Chapter 3, I revised and implemented a published methodology to quantify the magnitudes of individual components of the in situ stress state in a basin using well data. I selected the northeastern Brooks Range of northern Alaska as a test site due to availability of large volumes of petroleum exploration data in this region. I used density logs, leak-off tests, and mud profiles from 57 wells from the northeastern North Slope to determine the magnitude of the overburden stress (vertical stress, S_v), the minimum horizontal stress (S_{hmin}), the maximum horizontal stress (S_{Hmax}) and the formation pore pressure (P_p). Based on the relative magnitude of these stress components, I determined regional lateral and vertical variations in tectonic stress regimes.

Preliminary stress analysis indicates two distinct stress regimes across this region of Alaska. Areas adjacent to the eastern Barrow Arch and the present day passive margin exhibit both strike-slip ($S_{Hmax} > S_v > S_{hmin}$) and normal stress regimes ($S_v > S_{Hmax} > S_{hmin}$). This in situ stress regime is correlates well with the observed fault patterns in the subsurface and with the north–south extension along the Barrow Arch and the north Alaska margin.

To the south, within and near the northeastern Brooks Range thrust front, in situ stress magnitudes indicate that an active thrust fault regime ($S_{Hmax} > S_{hmin} > S_v$) is present at depths down to approximately 6000 ft (1829 m) (Figures 6-5 and 6-6). This finding is consistent with the fold and thrust structures observed in surface exposures and in the subsurface. However, at depths greater than 6000 ft (1829 m), relative in situ stress magnitudes indicate a change to a strike-slip regime (Figure 6-7). This change in in situ stress regime is probably due to increasing S_v and a relatively low magnitude S_{Hmax}, and is facilitated by the strongly mechanically stratified sedimentary rocks in this part of the fold-and-thrust belt. This result is consistent with the observed focal plane mechanisms available in the region.

As the Triassic Shublik Formation has been the focus of a potential unconventional shale resource play, I interpreted the tectonic stress regime at the top of the Shublik Formation using this refined method. The orientations of hydraulically-induced fractures in the Shublik Formation will depend on the nature of the stress regime and will vary by location. Induced fractures are

likely to be horizontal in the southeastern portion of the study area at depths less than 6000 ft (1829 m) where relative in situ stress magnitudes suggest that a thrust faulting regime is active. However, at depths greater than 6000 ft (1829 m), induced fractures are likely to be vertical and oriented northwest, as the in situ stress regime becomes strike-slip. In the extensional regime associated with the Barrow Arch, hydraulically-induced fractures will be vertical and oriented in the northwest and northeast directions.
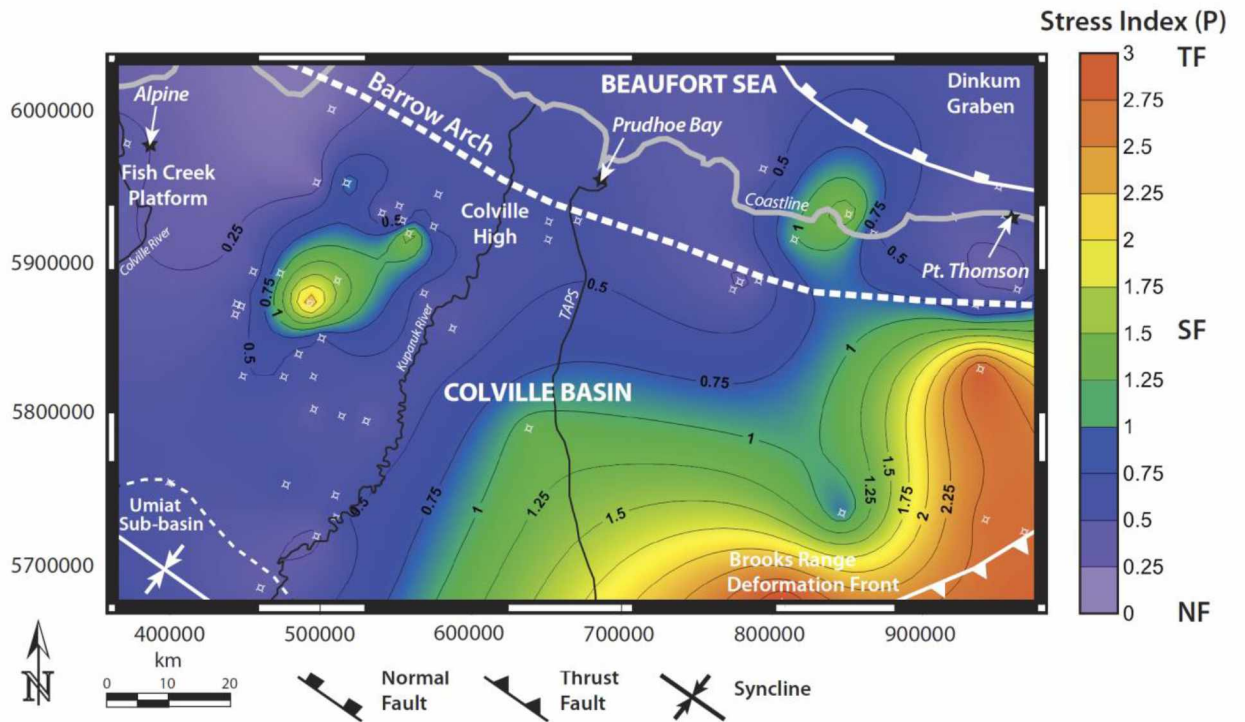
Figure 6-5 Spatial variations in the study area at a depth of 3000 ft (914 m)
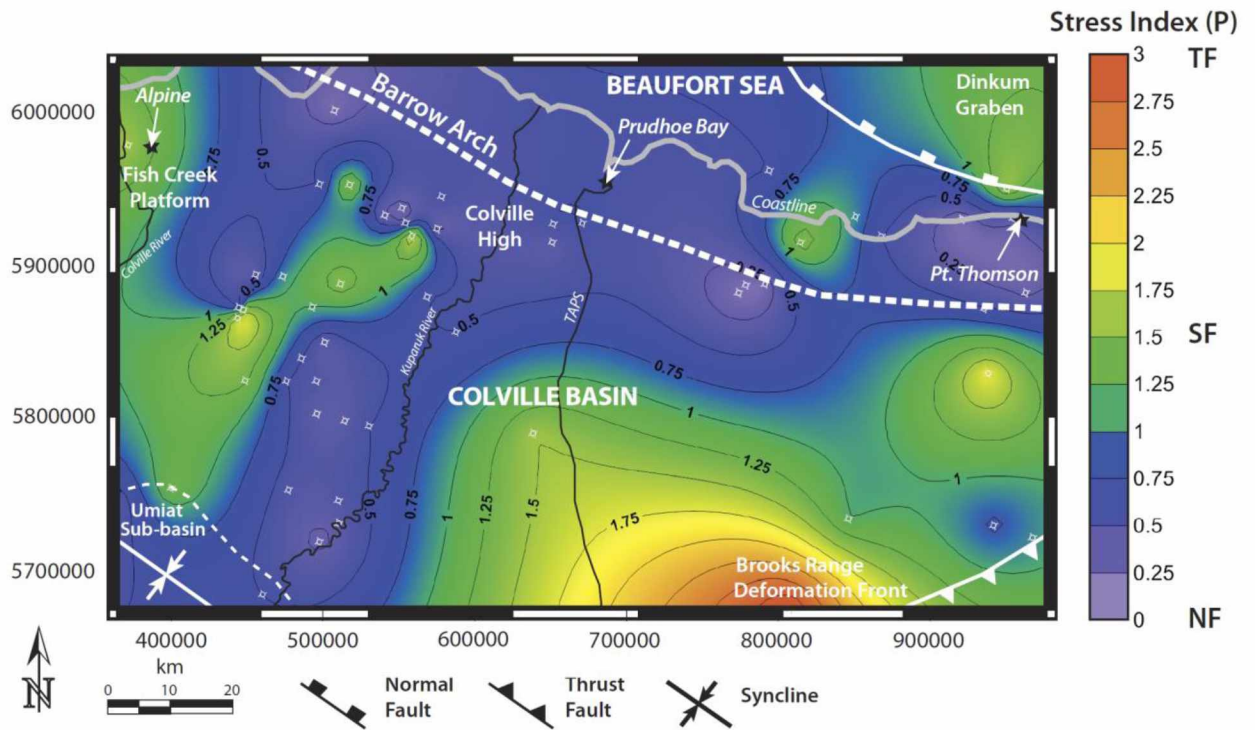
Figure 6-6 Spatial variations in the study area at a depth of 6000 ft (1829 m)
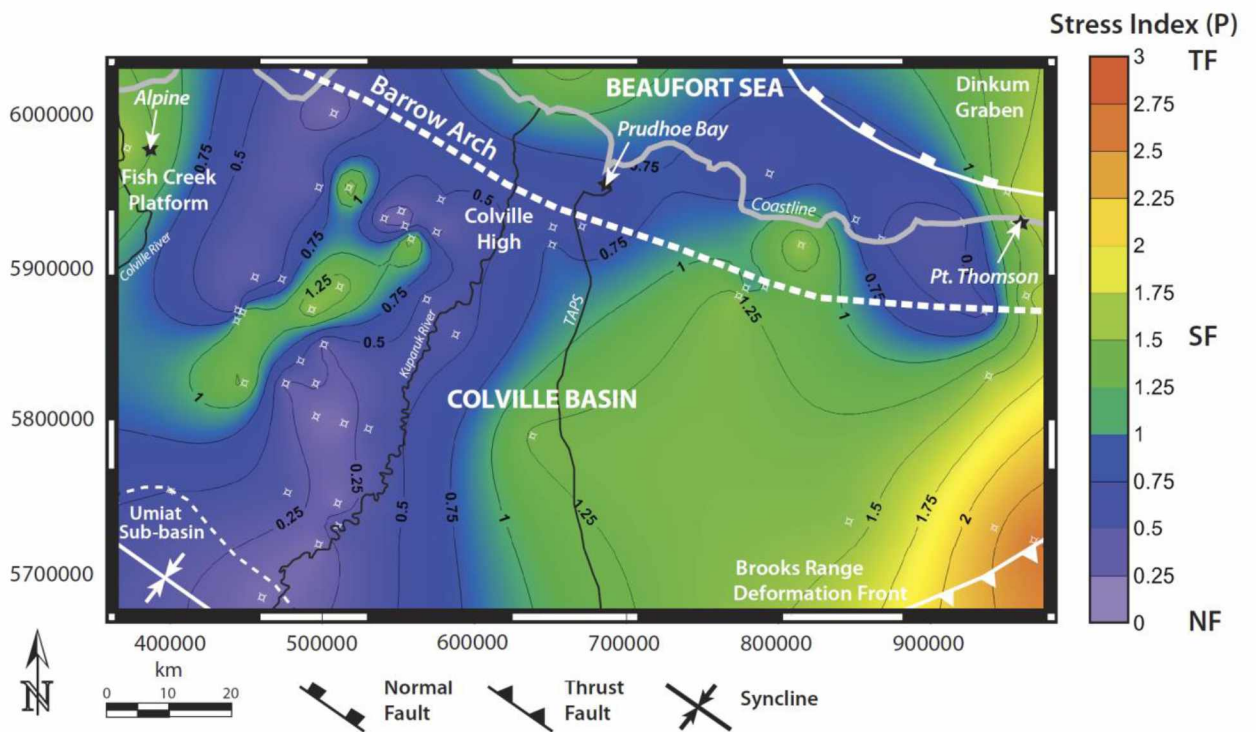
Figure 6-7 Spatial variations in the study area at a depth of 9000 ft (2743 m)

The results presented in Chapter 3 show that ths in situ stress measurement method is a promising technique and can be applied to in situ stress-related studies on hydrocarbon exploration and production such as the Nenana basin where necessary data are available.

6.4   Estimation of CO_2 sequestration and CH_4 production capacity of the Nenana basin

In Chapter 4, I used a preliminary reservoir model of the subbituminous coals of the Healy Creek Formation in the Nenana basin in a series of sensitivity analyses to investigate the effects of uncertainties in reservoir properties on the CO_2 sequestration and CH_4 production estimates of the Nenana basin. I further used the experimental design method and Monte Carlo analysis to determine a probabilistic range (P10 to P90) of the total cumulative volumes of CO_2 sequestered and CH_4 produced from these coals for the entire basin.

Although there are many variables to consider when developing a CO_2 sequestration/CH_4 production strategy for coals, I identified five major coal parameters that have the largest impact on the CO_2 sequestration and CH_4 producibility of the Healy Creek coals. These factors include bottomhole injection pressure, matrix porosity, fracture porosity and permeability, and coal volumetric strain (Figure 6-8).

Several fluid-flow simulation scenarios were used to understand the effect of well spacing on the primary CH_4 recovery, effect of CO_2 injection timing, effect of horizontal well injection, and the effect of caprock lithology on CO_2 migration pathways. Through these simulation scenarios, I found that closer well spacings allowed faster dewatering of coal reservoirs during the primary gas production phase. Initial peak gas rates were high using a small well-spacing and therefore resulted in greater gas decline rates. With a horizontal injection well, an additional ~4% total cumulative volumes of CH_4 were produced, compared to a vertical well. However, the total cumulative volumes of CO_2 sequestered with a horizontal injection well were found to be less due to the negative effect of coal swelling near the horizontal wellbore. Injected CO_2 migrated vertically and laterally through the coal beds as free gas away from the injection well due to its buoyancy and pressure build-up in the reservoir. When coals were overlain by a permeable layer such as sand, ~84% of injected CO_2 migrated into the overlying sand layer.

Proper characterization of the nature and composition of caprock units is therefore important for the identification of specific geologic storage sites for CO_2 in the basin.

I used the experimental design method through Plackett-Burman design to generate proxy models for probabilistic reservoir forecasting of the total volumes of CO_2 sequestered and CH_4 produced from the Nenana basin. The cumulative probability distributions obtained from the proxy models for a 160-acre reservoir of the total cumulative volumes of CO_2 sequestered at the end of a 20-year forecast range from 9.23 BCF (P10) to 2.015 BCF (P90) whereas the total volumes of CH_4 produced range from 3.068 BCF (P10) to 0.975 BCF (P90). On the basis of our probabilistic reservoir estimates for a 160-acre pattern, the mature subbituminous Healy Creek Formation coals in the entire Nenana basin could sequester between 0.87 TCF (P10) and 0.2 TCF (P90) of CO_2 while producing between 0.29 TCF (P10) and 0.1 TCF (P90) of CH_4.

Results of this study suggest that these probabilistic reservoir estimates for the Nenana basin are significantly less than that of previous carbon sequestration studies, probably due to the effect of the uncertainties in reservoir rock properties. However, the uncertainty in these forecasts can be reduced by more accurate measures of key Healy coal properties such as the matrix porosity, fracture porosity and permeability, and coal volumetric strain.
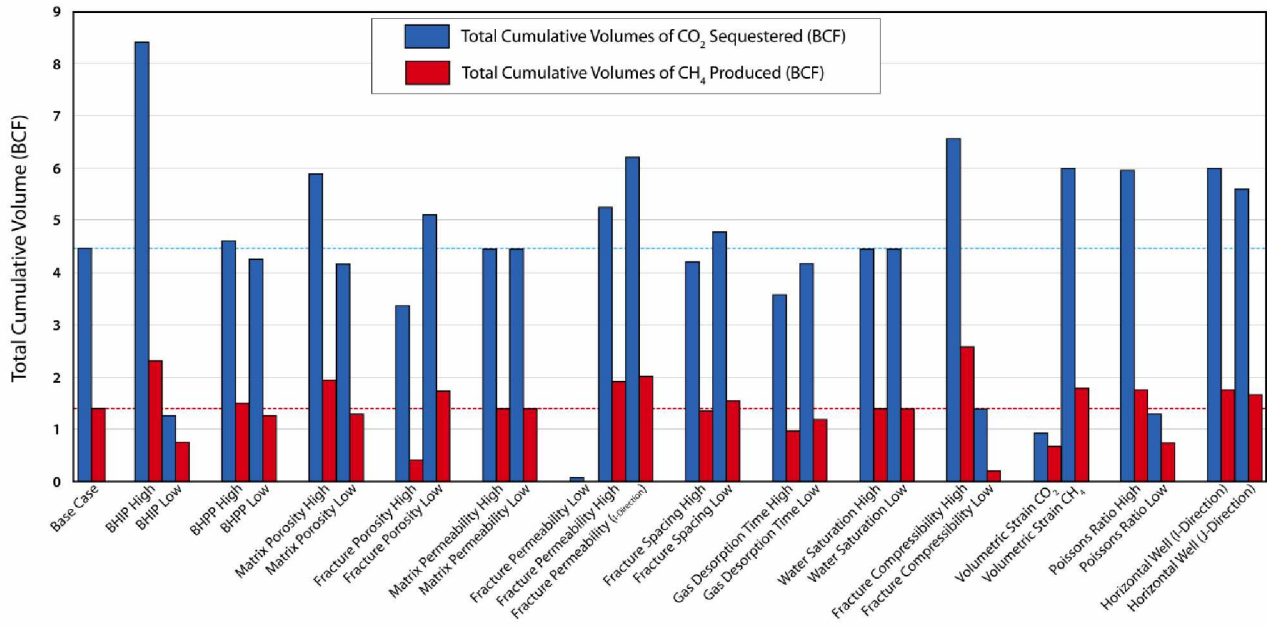
Figure 6-8 Results of the primary sensitivity analyses

7   Appendix

Appendix A

Wells used to calculate the present-day in-situ magnitudes in this study. Stress index values are based on a stress index scale developed by Hurd and Zoback (2012). [Stress Index: 0 ($S_v \gg S_{Hmax} = S_{hmin}$); 0.5 ($S_v > S_{Hmax} > S_{hmin}$); 1 ($S_{Hmax} = S_v > S_{hmin}$); 1.5 ($S_{Hmax} > S_v > S_{hmin}$); 2 ($S_{Hmax} > S_v = S_{hmin}$); 2.5 ($S_{Hmax} > S_{hmin} > S_v$); and 3 ($S_{Hmax} \gg S_{hmin} = S_v$)]. NA-Not available. P_p- Formation pore pressure. S_{Hmax}- Maximum horizontal stress. S_{hmin}- Minimum horizontal stress. S_v- Vertical stress or overburden stress. Ø - Angelier's shape parameter. and A(Ø)- Generalized Angelier's shape parameter.

Well No.	Well Name	Depth (ft)	Depth (m)	Pp (psi)	Pp (MPa)	S_Hmax (Mpa)	S_hmin (Mpa)	S_v (Mpa)	Ø	Stress Index, A(Ø)
1	KUPARUK RIV UNIT 2F-18	3138	956	9.5	0.07	21.3	17.4	22.5	0.8	0.8
		7700	2347	28.1	0.19	57.3	44.8	55.2	0.8	1.2
		9900	3018	33.1	0.23	82.9	60.1	70.9	0.5	1.5
2	KUPARUK RIV UNIT 3A-17	3309	1009	2.9	0.02	6.7	6.0	22.0	0.0	0.0
		6000	1829	NA	NA	12.1	10.8	41.3	0.0	0.0
		9000	2743	NA	NA	18.2	16.2	61.9	0.0	0.0
3	KUPARUK RIV UNIT 2H-17	6013	1833	22.8	0.16	31.4	29.2	41.4	0.2	0.2
		9000	2743	NA	NA	46.9	43.7	61.9	0.2	0.2
4	COLVILLE RIV UNIT CD2-21	114	35	0.4	0.00	0.5	0.5	0.8	0.1	0.1
		2390	728	7.5	0.05	14.1	12.5	16.4	0.4	0.4
		7228	2203	22.6	0.16	56.5	41.5	49.7	0.5	1.5
		9000	2743	NA	NA	70.4	51.7	61.9	0.5	1.5
5	NORTHSTAR UNIT NS-10	4500	1372	13.8	0.10	23.1	20.3	30.3	0.3	0.3
		7000	2134	22.4	0.15	38.3	32.4	48.3	0.4	0.4
		11000	3353	35.9	0.25	80.9	60.7	75.8	0.7	1.3
6	BP SOURDOUGH 1	4500	1372	14.5	0.10	22.0	20.2	31.0	0.2	0.2
		6000	1829	NA	NA	29.4	27.0	41.3	0.2	0.2
		10000	3048	35.9	0.25	78.4	59.2	68.8	0.5	1.5
7	BP YUKON GOLD 1	4000	1219	12.9	0.09	17.5	17.3	27.5	0.0	0.0
		6000	1829	NA	NA	26.3	25.9	41.3	0.0	0.0

#	Name								
		10000	3048	36.6	0.25	74.8	57.8	68.8	0.6	1.4
		12000	3658	54.6	0.38	85.2	72.4	82.5	1.3	1.3
8	UNION OIL E DE K LEFFINGWELL 1	4030	1228	14.2	0.10	22.8	20.6	26.0	0.4	0.4
		6000	1829	NA	NA	33.9	30.7	38.8	0.4	0.4
		9000	2743	NA	NA	50.9	46.0	58.1	0.4	0.4
		12604	3842	49.7	0.34	73.4	63.8	85.0	0.5	0.5
9	EXXON ALASKA ST K 1XX	1704	519	6.2	0.04	9.0	8.8	7.1	0.9	2.9
		6250	1905	24.2	0.17	46.3	37.3	39.8	0.3	1.7
		9000	2743	NA	NA	66.6	53.7	61.9	0.6	1.4
10	EXXON CANNING RIV U BLK A 1	2153	656	7.4	0.05	13.7	11.6	10.9	0.3	2.3
		6000	1829	NA	NA	38.3	32.5	41.3	0.7	0.7
		9000	2743	NA	NA	57.4	48.7	61.9	0.7	0.7
11	ARCO GYR1	4000	1219	12.8	0.09	25.0	20.9	27.1	0.7	0.7
		6000	1829	21.1	0.15	41.9	33.6	42.1	1.0	1.0
		9000	2743	37.1	0.26	68.4	54.9	64.4	0.7	1.3
12	MCCULLOCH OIL FIN CK UNIT 1	4000	1219	10.3	0.07	68.3	41.4	28.7	0.3	2.3
		7000	2134	23.1	0.16	92.1	59.6	52.0	0.2	2.2
		10000	3048	29.0	0.20	89.9	61.7	74.2	0.4	1.6
13	ARCO KAVIK UNIT 3	4970	1515	18.9	0.13	34.3	28.8	38.1	0.6	0.6
		9000	2743	NA	NA	62.1	52.1	68.9	0.6	0.6
14	ARCO PIPELINE STATE 1	8900	2713	36.9	0.25	61.0	50.8	57.7	0.7	1.3
		6000	1829	NA	NA	41.2	34.3	38.9	0.7	1.3
		3000	914	NA	NA	20.6	17.1	19.4	0.7	1.3
15	ANADARKO JACOB'S LADDER C	3442	1049	11.4	0.08	15.8	15.5	22.3	0.0	0.0
		6000	1829	NA	NA	27.6	27.0	40.7	0.0	0.0
		10006	3050	34.8	0.24	71.9	55.3	67.9	0.8	1.2
		11437	3486	34.9	0.24	90.7	64.9	78.4	0.5	1.5
16	TEXACO KAD RIV 1	3442	1049	11.6	0.08	16.3	15.5	22.3	0.1	0.1
		6000	1829	NA	NA	28.3	27.0	40.7	0.1	0.1
		10006	3050	37.7	0.26	69.0	55.3	67.9	1.1	1.1
17	SHELL LAKE 79 FED 1	3442	1049	12.3	0.09	15.5	15.5	22.3	0.0	0.0
		6000	1829	NA	NA	27.1	27.0	40.7	0.0	0.0
		10006	3050	35.9	0.25	70.8	55.3	67.9	1.2	1.2
		11437	3486	40.2	0.28	85.4	64.9	78.4	0.7	1.3
18	UNION OIL ALPENGLOW STATE 1	2450	747	13.0	0.09	15.4	15.2	15.8	0.3	0.3
		6000	1829	25.2	0.17	45.1	37.2	41.3	0.5	1.5
		8000	2438	32.1	0.22	63.0	49.6	55.0	0.4	1.6
19	CONOCO BADAMI 2	5672	1729	17.7	0.12	38.0	30.0	39.0	0.9	0.9
		9700	2957	41.4	0.29	62.3	53.6	66.7	0.7	0.7
		12000	3658	53.8	0.37	79.3	68.5	82.5	0.8	0.8

		3000	914	NA	NA	20.1	15.8	18.0	0.5	1.5
20	**BP BADAMI 4**	4500	1372	13.7	0.09	21.8	19.4	31.0	0.2	0.2
		3000	914	NA	NA	14.5	13.0	18.0	0.3	0.3
		9800	2987	36.9	0.25	57.8	49.3	67.4	0.5	0.5
		10800	3292	40.7	0.28	83.0	64.0	74.3	0.5	1.5
21	**EXXON PT THOMSON UNIT 4**	3350	1021	12.3	0.08	15.0	14.7	23.0	0.0	0.0
		7412	2259	27.1	0.19	29.9	29.6	51.0	0.0	0.0
		11897	3626	58.0	0.40	76.5	69.2	81.8	0.6	0.6
22	**EXXON ALASKA ST F 1**	2160	658	7.0	0.05	11.5	10.3	14.9	0.3	0.3
		7244	2208	23.4	0.16	58.1	42.9	49.8	0.5	1.5
		9000	2743	NA	NA	72.2	53.3	61.9	0.5	1.5
		13470	4106	60.4	0.42	99.4	82.7	92.6	0.6	1.4
23	**EXXON PT THOMSON UNIT 1**	3328	1014	12.6	0.09	18.8	17.9	22.9	0.2	0.2
		6000	1829	NA	NA	34.0	32.2	41.3	0.2	0.2
		11407	3477	63.8	0.44	81.8	75.0	78.5	0.5	1.5
24	**SAVANT KUPCAKE 1**	4110	1253	13.1	0.09	22.0	19.8	28.3	0.3	0.3
		6000	1829	NA	NA	32.2	28.9	41.3	0.3	0.3
		10672	3253	36.0	0.25	62.9	51.3	73.4	0.5	0.5
25	**UNION AMETHYST STATE 1**	6500	1981	22.4	0.15	36.5	31.4	44.1	0.4	0.4
		3000	914	NA	NA	16.9	14.5	18.0	0.7	0.7
		11500	3505	47.6	0.33	59.6	55.5	82.0	0.2	0.2
26	**UNION OIL MASTODON 6-3-9**	2000	610	6.2	0.04	8.8	8.7	12.0	0.0	0.0
		6000	1829	NA	NA	26.4	26.0	41.3	0.0	0.0
		9000	2743	NA	NA	39.6	39.0	61.9	0.0	0.0
27	**BP MALGUK 1**	3010	917	9.9	0.07	15.4	14.4	18.1	0.3	0.3
		6000	1829	NA	NA	30.7	28.7	41.3	0.2	0.2
		9000	2743	NA	NA	46.0	43.1	61.9	0.2	0.2
28	**UNION OIL SMILODON 9-4-9**	1710	521	5.4	0.04	8.1	7.7	10.3	0.1	0.1
		6000	1829	NA	NA	28.4	27.1	41.3	0.1	0.1
		9000	2743	NA	NA	42.6	40.7	61.9	0.1	0.1
29	**CONOCO HEAVENLY 1**	3566	1087	11.9	0.08	18.9	16.9	21.4	0.4	0.4
		6000	1829	NA	NA	38.0	30.8	41.3	0.7	0.7
		9590	2923	33.9	0.23	60.7	49.2	66.0	0.7	0.7
30	**CONOCO GRIZZLY 1**	2282	696	7.6	0.05	11.7	11.1	13.7	0.2	0.2
		6000	1829	NA	NA	46.1	29.0	41.3	0.7	1.3
		8380	2554	25.3	0.17	51.6	40.6	57.6	0.6	0.6
31	**ARCO TULAGA 1**	1250	381	4.0	0.03	6.1	5.7	7.1	0.3	0.3
		5000	1524	16.5	0.11	28.0	24.3	38.2	0.3	0.3
		8000	2438	28.1	0.19	51.4	41.7	62.3	0.5	0.5

No.	Name									
		11500	3505	41.6	0.29	83.8	64.8	89.4	0.8	0.8
32	TEXACO WOLFBUTTON 25-6-9	2490	759	8.0	0.06	13.0	12.1	15.4	0.3	0.3
		6000	1829	NA	NA	33.2	28.8	41.3	0.4	0.4
		9490	2893	34.4	0.24	52.5	45.5	65.3	0.4	0.4
33	UNION OIL PANTHERA 28-6-9	2119	646	6.3	0.04	9.3	9.1	12.7	0.1	0.1
		6000	1829	NA	NA	26.3	25.8	41.3	0.0	0.0
		9000	2743	NA	NA	39.5	38.7	61.9	0.0	0.0
34	UNION OIL STEGODON 24-6-8XX	1850	564	5.5	0.04	8.0	8.0	11.1	0.0	0.0
		6000	1829	NA	NA	26.0	25.8	41.3	0.0	0.0
		9000	2743	NA	NA	39.0	38.7	61.9	0.0	0.0
35	UNION OIL MUSKOXEN 36-7-8	1950	594	5.8	0.04	10.1	8.7	11.7	0.4	0.4
		6000	1829	NA	NA	30.9	26.9	41.3	0.3	0.3
		9000	2743	NA	NA	46.4	40.3	61.9	0.3	0.3
36	TEXACO WOLFBUTTON 32-7-8	2490	759	9.0	0.06	13.7	13.1	14.3	0.5	0.5
		6000	1829	NA	NA	33.0	29.0	43.4	0.3	0.3
		8990	2740	32.5	0.22	49.5	43.4	65.0	0.3	0.3
37	ARCO MELTWATER SOUTH 1	2932	894	8.8	0.06	15.2	13.7	16.9	0.5	0.5
		8377	2553	25.0	0.17	67.7	48.1	60.6	0.6	1.4
38	BP NARVAQ 1	2500	762	8.0	0.06	12.4	12.1	14.4	0.1	0.1
		8272	2521	29.4	0.20	54.1	43.4	62.1	0.6	0.6
39	UNION OIL BLUEBUCK 6-7-9	1950	594	6.8	0.05	9.3	8.8	11.2	0.2	0.2
		6000	1829	NA	NA	28.6	27.1	41.3	0.1	0.1
		9000	2743	NA	NA	42.9	40.6	61.9	0.1	0.1
40	ENI MAGGIORE 1	2000	610	6.0	0.04	9.4	9.0	11.5	0.1	0.1
		2385	727	7.3	0.05	11.2	10.8	13.7	0.1	0.1
		4000	1219	12.9	0.09	19.4	17.7	24.7	0.2	0.2
		9000	2743	NA	NA	43.6	39.7	61.9	0.2	0.2
41	ENI MAGGIORE 3XX	2000	610	6.5	0.04	9.8	9.3	11.5	0.2	0.2
		4000	1219	12.9	0.09	21.0	18.6	24.7	0.4	0.4
		9000	2743	NA	NA	47.2	42.0	61.9	0.3	0.3
42	CONOCO MELTWATER NORTH 1	2150	655	7.4	0.05	10.2	10.0	13.3	0.1	0.1
		5968	1819	23.9	0.17	40.9	34.2	36.9	0.4	1.6
		9000	2743	NA	NA	61.6	51.6	61.9	1.0	1.0
43	ARCO MELTWATER NORTH 2	2150	655	6.9	0.05	10.2	10.1	12.4	0.1	0.1
		5968	1819	22.7	0.16	42.3	34.3	36.9	0.3	1.7
		9000	2743	NA	NA	63.8	51.7	61.9	0.8	1.2
44	CONOCO KUPARUK RIV U MELT 2P-06	2678	816	6.6	0.05	13.0	11.6	15.4	0.4	0.4
		6000	1829	NA	NA	29.1	25.9	41.3	0.2	0.2

#	Name									
		9000	2743	NA	NA	43.7	38.9	61.9	0.2	0.2
45	CIRQUE 3	2432	741	8.9	0.06	11.2	11.1	14.0	0.0	0.0
		6567	2002	25.2	0.17	35.2	31.9	45.2	0.3	0.3
		9000	2743	NA	NA	48.3	43.7	61.9	0.3	0.3
46	HOT ICE 1	1320	402	3.9	0.03	6.8	6.4	7.6	0.4	0.4
		3000	914	9.0	0.06	19.7	16.0	20.6	0.8	0.8
		6000	1829	NA	NA	39.3	32.0	41.3	0.8	0.8
		9000	2743	NA	NA	59.0	47.9	61.9	0.8	0.8
47	UNION OIL RUBY STATE 1	1889	576	6.1	0.04	12.9	10.9	10.9	0.0	2.0
		6000	1829	NA	NA	41.1	34.8	34.5	0.0	2.0
		9000	2743	NA	NA	73.4	52.1	51.8	0.0	2.0
48	CONOCO RAVIK ST 1	7301	2225	25.9	0.18	54.7	42.3	50.2	0.6	1.4
		3000	914	NA	NA	22.5	17.4	18.0	0.1	1.9
		9000	2743	NA	NA	67.5	52.1	61.9	0.6	1.4
49	ENI ROCK FLOUR 3	2000	610	6.0	0.04	9.4	9.0	11.5	0.1	0.1
		6000	1829	NA	NA	28.2	27.1	41.3	0.1	0.1
		9000	2743	NA	NA	42.3	40.6	61.9	0.1	0.1
50	CONOCO ANTIGUA 1	4005	1221	12.6	0.09	27.3	22.0	24.7	0.5	1.5
		6875	2096	23.2	0.16	58.0	42.5	47.3	0.3	1.7
		9000	2743	NA	NA	76.0	55.6	61.9	0.3	1.7
51	ARCO KUPARUK RIV UNIT WT-01	3070	936	9.7	0.07	13.0	12.2	18.4	0.1	0.1
		6000	1829	NA	NA	25.5	23.8	41.3	0.1	0.1
		9000	2743	NA	NA	38.2	35.7	61.9	0.1	0.1
52	ARCO KUPARUK RIV UNIT WT-04	3682	1122	12.3	0.08	14.3	13.9	22.0	0.0	0.0
		6000	1829	NA	NA	23.4	22.7	41.3	0.0	0.0
		9000	2743	NA	NA	35.0	34.0	61.9	0.0	0.0
53	ARCO KRU STATE 2 16-10-10	6558	1999	24.0	0.17	31.3	29.5	45.1	0.1	0.1
		3000	914	NA	NA	14.3	13.5	18.0	0.2	0.2
		9000	2743	NA	NA	43.0	40.4	61.9	0.1	0.1
54	ARCO ROCK FLOUR 1	3000	914	12.0	0.08	16.1	15.1	17.9	0.4	0.4
		7210	2198	29.0	0.20	42.4	37.6	49.6	0.4	0.4
		9000	2743	NA	NA	52.9	46.9	61.9	0.4	0.4
55	ALASKAN CRUDE ACC F-03XX	9200	2804	33.6	0.23	51.3	44.4	66.5	0.3	0.3
		3000	914	NA	NA	16.7	14.5	18.0	0.6	0.6
		6000	1829	NA	NA	33.5	29.0	41.3	0.4	0.4
56	ALASKAN CRUDE ACC F-02XX	9200	2804	33.6	0.23	51.3	44.4	66.5	0.3	0.3
		6000	1829	NA	NA	33.5	29.0	43.4	0.3	0.3
57	PIONEER HAILSTORM 1	2995	913	9.7	0.07	14.8	13.4	17.9	0.3	0.3
		6000	1829	NA	NA	29.6	26.9	41.3	0.2	0.2

		9440	2877	33.8	0.23	66.2	51.5	68.2	0.9	0.9
		10306	3141	33.3	0.23	78.5	57.7	74.5	0.8	1.2

Appendix B

Wells used to calculate the present-day in-situ magnitudes at the top of Shublik Formation in this study. Stress index values are based on a stress index scale developed by Hurd and Zoback (2012). [Stress Index: 0 ($S_v >> S_{Hmax} = S_{hmin}$); 0.5 ($S_v > S_{Hmax} > S_{hmin}$); 1 ($S_{Hmax} = S_v > S_{hmin}$); 1.5 ($S_{Hmax} > S_v > S_{hmin}$); 2 ($S_{Hmax} > S_v = S_{hmin}$); 2.5 ($S_{Hmax} > S_{hmin} > S_v$); and 3 ($S_{Hmax} > S_{hmin} = S_v$)]. S_{Hmax}- Maximum horizontal stress. S_{hmin}- Minimum horizontal stress. S_v- Vertical stress or overburden stress. Ø - Angelier's shape parameter. and A(Ø)- Generalized Angelier's shape parameter.

Well No.	Well Name	Depth (ft)	Depth (m)	S_{Hmax} (Mpa)	S_{hmin} (Mpa)	S_v (Mpa)	Ø	Stress Index, A(Ø)
1	KUPARUK RIV UNIT 2F-18	9601	2926	78.1	57.6	68.8	0.5	1.5
2	KUPARUK RIV UNIT 3A-17	7837	2389	15.8	14.1	53.9	0.0	0.0
3	KUPARUK RIV UNIT 2H-17	9196	2803					NA
4	COLVILLE RIV UNIT CD2-21	8588	2618	66.9	49.3	59.1	0.6	1.6
5	NORTHSTAR UNIT NS-10	14291	4356	110.0	81.0	99.0	0.6	1.6
6	BP SOURDOUGH 1	13890	4234	120.1	87.5	95.5	0.2	1.2
7	BP YUKON GOLD 1	13546	4129	103.2	83.1	93.2	0.5	1.5
8	UNION OIL E DE K LEFFINGWELL 1	13422	4091	77.8	68.1	89.8	0.4	0.4
9	EXXON ALASKA ST K 1XX	12706	3873	96.6	76.8	89.1	0.6	1.6
10	EXXON CANNING RIV U BLK A 1	3116	950	19.9	16.8	18.5	0.4	2.4
11	ARCO GYR1	11405	3476	89.2	71.2	82.4	0.6	1.6
12	MCCULLOCH OIL FIN CK UNIT 1	13606	4147	118.6	81.4	101.7	0.5	1.5
13	ARCO KAVIK UNIT 3	2964	903					NA
14	ARCO PIPELINE STATE 1	11526	3513	79.1	65.8	74.7	0.7	1.7
15	ANADARKO JACOB'S LADDER C	10989	3349	83.7	61.5	75.1	0.6	1.6
16	TEXACO KAD RIV 1	11517	3510	80.6	64.0	78.5	0.9	1.9
17	SHELL LAKE 79 FED 1	11084	3378	80.9	62.1	75.7	0.7	1.7

18	UNION OIL ALPENGLOW STATE 1	12464	3799	100.9	77.3	86.7	0.4	1.4
19	CONOCO BADAMI 2	13627	4154	89.1	77.3	94.6	0.7	0.7
20	BP BADAMI 4	13773	4198	101.8	79.4	95.7	0.7	1.7
21	EXXON PT THOMSON UNIT 4	14684	4476	95.8	86.0	101.0	0.7	0.7
22	EXXON ALASKA ST F 1	15141	4615	117.1	93.1	104.1	0.5	1.5
23	EXXON PT THOMSON UNIT 1	14787	4507	108.0	98.7	101.7	0.3	1.3
24	SAVANT KUPCAKE 1	13330	4063	79.4	64.1	91.7	0.6	0.6
25	UNION AMETHYST STATE 1	12794	3900	66.8	61.7	91.7	0.2	0.2
26	UNION OIL MASTODON 6-3-9	12443	3793	54.7	53.9	86.8	0.0	0.0
27	BP MALGUK 1	12336	3760	63.1	59.1	86.8	0.1	0.1
28	UNION OIL SMILODON 9-4-9	12036	3669	57.0	54.4	83.7	0.1	0.1
29	CONOCO HEAVENLY 1	11809	3599	76.7	61.3	82.9	0.7	0.7
30	CONOCO GRIZZLY 1	11771	3588	82.0	57.0	82.5	1.0	1.0
31	ARCO TULAGA 1	11931	3637	84.5	65.9	93.4	0.7	0.7
32	TEXACO WOLFBUTTON 25-6-9	11042	3366	61.4	52.9	76.7	0.4	0.4
33	UNION OIL PANTHERA 28-6-9	11007	3355	48.3	47.4	76.6	0.0	0.0
34	UNION OIL STEGODON 24-6-8XX	10925	3330	47.3	47.0	75.9	0.0	0.0
35	UNION OIL MUSKOXEN 36-7-8	10555	3217	54.4	47.3	73.3	0.3	0.3
36	TEXACO WOLFBUTTON 32-7-8	10610	3234	58.4	50.8	78.3	0.3	0.3
37	ARCO MELTWATER SOUTH 1	10657	3248	91.5	63.2	78.8	0.6	1.6
38	BP NARVAQ 1	10355	3156					NA
39	UNION OIL BLUEBUCK 6-7-9	10156	3096	48.4	45.9	70.6	0.1	0.1
40	ENI MAGGIORE 1	9525	2903	46.2	42.0	65.5	0.2	0.2
41	ENI MAGGIORE 3XX	9167	2794	48.1	42.7	62.9	0.3	0.3
42	CONOCO MELTWATER NORTH 1	9976	3041	69.7	58.0	67.7	0.8	1.8
43	ARCO MELTWATER NORTH 2	9863	3006	71.5	57.4	67.1	0.7	1.7
44	CONOCO KUPARUK RIV U MELT 2P-06	9857	3004	47.8	42.6	68.7	0.2	0.2

45	CIRQUE 3	9486	2891	51.3	46.2	65.9	0.3	0.3
46	HOT ICE 1	9604	2927	63.4	51.3	66.4	0.8	0.8
47	UNION OIL RUBY STATE 1	9882	3012	78.8	57.1	56.8	0.0	2.0
48	CONOCO RAVIK ST 1	9727	2965	72.9	56.3	67.6	0.7	1.7
49	ENI ROCK FLOUR 3	8614	2626	40.4	38.8	59.5	0.1	0.1
50	CONOCO ANTIGUA 1	8898	2712	76.1	55.4	61.6	0.3	1.3
51	ARCO KUPARUK RIV UNIT WT-01	8945	2726	38.0	35.5	62.0	0.1	0.1
52	ARCO KUPARUK RIV UNIT WT-04	9277	2828	36.1	35.1	64.6	0.0	0.0
53	ARCO KRU STATE 2 16-10-10	9028	2752	43.1	40.6	62.5	0.1	0.1
54	ARCO ROCK FLOUR 1	8795	2681	51.8	45.9	60.7	0.4	0.4
55	ALASKAN CRUDE ACC F-03XX	9382	2860	52.3	45.3	67.9	0.3	0.3
56	ALASKAN CRUDE ACC F-02XX	8409	2563					NA
57	PIONEER HAILSTORM 1	8768	2672	61.7	47.2	62.8	0.9	0.9